

**Surfactant Assisted Synthesis and Characterization of High Surface Area Mesoporous Nanocrystalline Pure,  $\text{Eu}^{3+}$  and  $\text{Sm}^{3+}$  doped Ceria for Selected Applications**

**Bappaditya Mandal**



Department of Chemistry

**National Institute of Technology Rourkela**

**Surfactant Assisted Synthesis and Characterization of High  
Surface Area Mesoporous Nanocrystalline Pure, Eu<sup>3+</sup> and Sm<sup>3+</sup>  
Doped Ceria for Selected Applications**

*Dissertation submitted in partial fulfillment  
of the requirements of the degree of*

*Doctor of Philosophy*

*in*

*Chemistry*

*by*

***Bappaditya Mandal***

(Roll Number: **509CY608**)

*based on research carried out  
under the supervision of*

***Prof.(Ms.) Aparna Mondal***



September, 2016

Department of Chemistry

**National Institute of Technology Rourkela**



Department of Chemistry

**National Institute of Technology Rourkela**

---

September 21, 2016

## Certificate of Examination

Roll Number: 509CY608

Name: Bappaditya Mandal

Title of Dissertation: Surfactant Assisted Synthesis and Characterization of High Surface Area Mesoporous Nanocrystalline Pure,  $\text{Eu}^{3+}$  and  $\text{Sm}^{3+}$  doped Ceria for Selected Applications

We the below signed, after checking the dissertation mentioned above and the official record book (s) of the student, hereby state our approval of the dissertation submitted in partial fulfillment of the requirements of the degree of Doctor of Philosophy in Department of Department of Chemistry National Institute of Technology Rourkela. We are satisfied with the volume, quality, correctness, and originality of the work.

---

Prof.(Ms.) Aparna Mondal  
Principal Supervisor

---

Prof. Garudadhvaj Hota  
Member, DSC

---

Prof. Kalipada Maity  
Member, DSC

---

Prof.(Mrs.) Sabita Patel  
Member, DSC

---

External Examiner

---

Prof. V. Siva Kumar  
Chairperson

---

Prof. Saurav Chatterjee  
Head of the Department



Department of Chemistry

**National Institute of Technology Rourkela**

---

September 21, 2016

**Prof.(Ms.) Aparna Mondal**  
Assistant Professor

### **Supervisor's Certificate**

This is to certify that the work presented in the dissertation entitled *Surfactant Assisted Synthesis and Characterization of High Surface Area Mesoporous Nanocrystalline Pure, Eu<sup>3+</sup> and Sm<sup>3+</sup> Doped Ceria for Selected Applications* submitted by *Bappaditya Mandal*, Roll Number Roll No.509CY608, is a record of original research carried out by him under my supervision and guidance in partial fulfillment of the requirements of the degree of *Doctor of Philosophy* in *Department of Chemistry*. Neither this dissertation nor any part of it has been submitted earlier for any degree or diploma to any institute or university in India or abroad.

---

Prof.(Ms.) Aparna Mondal

# **Dedication**

*Dedicated to my family*

*Signature*

# Declaration of Originality

I, *Bappaditya Mandal*, Roll Number 509CY608 hereby declare that this dissertation entitled *Surfactant Assisted Synthesis and Characterization of High Surface Area Mesoporous Nanocrystalline Pure,  $\text{Eu}^{3+}$  and  $\text{Sm}^{3+}$  doped Ceria for Selected Applications* presents my original work carried out as a doctoral student of NIT Rourkela and, to the best of my knowledge, contains no material previously published or written by another person, nor any material presented by me for the award of any degree or diploma of NIT Rourkela or any other institution. Any contribution made to this research by others, with whom I have worked at NIT Rourkela or elsewhere, is explicitly acknowledged in the dissertation. Works of other authors cited in this dissertation have been duly acknowledged under the sections “Reference” or “Bibliography”. I have also submitted my original research records to the scrutiny committee for evaluation of my dissertation.

I am fully aware that in case of any non-compliance detected in future, the Senate of NIT Rourkela may withdraw the degree awarded to me on the basis of the present dissertation.

September 21, 2016

NIT Rourkela

Bappaditya Mandal

# Acknowledgment

*First and foremost, I would like to express my deep sense of gratitude and reverence to my advisor **Prof. Aparna Mondal** for her patient guidance, excellent advice, consistent support and unflinching encouragement throughout the entire period of my research work.*

*I would like to express my sincere thanks to all my Doctoral Scrutiny Committee (DSC) members **Prof. K. P. Maity** (Department of Mechanical Engineering), **Prof. G. Hota**, and **Prof. S. Patel** along with DSC Chairperson **Prof. V. Siva Kumar** for their valuable comment and discussion during the entire course of my work.*

*I would like to thank **Prof. Saurav Chatterjee**, Head, Department of Chemistry, NIT Rourkela, for allowing me to avail all the facilities of the Department of Chemistry.*

*I am also thankful to all the distinguish professors of Department of Chemistry, NIT Rourkela for their constructive suggestions.*

*I owe a depth gratitude to **Prof. B. B. Nayak** Head, Department of Ceramic Engineering, NIT Rourkela, for his inspiring advice and valuable suggestion.*

*I wish to express my deep regard to all non-teaching staff of NIT Rourkela for their constant practical assistance and help whenever required throughout the period.*

*I express my sincere thanks to the, **Council of Scientific & Industrial Research**, India for financial support.*

*I have been blessed to be surrounded by many caring and loving friends, seniors and juniors like **Sarita, Arnab, Apu, Nihar bhai, Soumen, Animesh, Pijush, Avijit, Smruti**.*

*I wish to express my thanks to my lab mates, **Priyadarshini, Amar, Prakash, Shraban, Tapaswini** and all the research scholars of ours department. Their support and help during my research work make my stay in this institute a memorable one.*

*Finally I would like to thank my parent and family members. Without their inspiration, help and encouragement this work would not have been possible. A special thank goes to my elder brother **Kailash pati Mandal** and elder sister **Dr. Banashree Ghosh** for all their affection and for uplifting my spirit in need.*

**Date:**  
**NIT Rourkela, India**

**(Bappaditya Mandal)**

# Abstract

CeO<sub>2</sub> is one of the most interesting oxides industrially because it has been widely used as a catalyst, metal polishing agent, three-way automotive catalytic converters for purification of exhaust gases, oxygen ion conductor in solid oxide fuel cells, oxidative coupling of methane and water-gas shift reaction, oxygen sensors, and so forth for long periods of time. Recently, CeO<sub>2</sub> nanoparticles has also emerged as a fascinating and lucrative material for environmental remediation application as photocatalyst for degradation of toxic pollutants. The key for most of the above mentioned applications of CeO<sub>2</sub> based materials is its extraordinary ability to release or uptake oxygen by shifting some Ce<sup>4+</sup> to Ce<sup>3+</sup> ions. Better catalytic performances of CeO<sub>2</sub> have been reported in the presence of Ce<sup>3+</sup> and oxygen vacancy defects, which are potentially potent surface sites for catalysis. The present work is undertaken on multigram synthesis of high content of Ce<sup>3+</sup>, high surface area and high quality mesoporous pure CeO<sub>2</sub> as well as Sm<sup>3+</sup>, and Eu<sup>3+</sup> doped CeO<sub>2</sub> using cheaper metal inorganic precursor. The XRD results showed that even as-prepared material has cubic fluorite structure of CeO<sub>2</sub> with no crystalline impurity phase. Thereby, confirming the ability of the present aqueous based synthetic approach to prepare mesoporous crystalline CeO<sub>2</sub> nanoparticles at a lower temperature of 100°C. All the nanopowder exhibited strong absorption in the UV region and good transmittance in the visible region. Sm<sup>3+</sup> and Eu<sup>3+</sup> doped CeO<sub>2</sub> nanopowder showed enhanced photoluminescence in the red and orange region. Mesoporous Sm<sup>3+</sup> doped CeO<sub>2</sub> sample could effectively photodegrade all types of cationic, anionic and nonionic dyes under natural sunlight irradiation. These high surface area mesoporous materials exhibited notable adsorption and effective removal of Cr(VI) from aqueous solutions at room temperature and without any adjustment of pH. Mesoporous Sm<sup>3+</sup> doped CeO<sub>2</sub> samples also exhibited excellent autocatalytical properties. The presence of increased surface hydroxyl group, mesoporosity, and surface defects have contributed towards an improved activity of mesoporous CeO<sub>2</sub>, which appears to be potential candidates for optical, environmental and biomedical applications.

**Keywords:** Ceria; Mesoporous; Optical Nanopowder; Photocatalyst.



# Contents

<b>Certificate of Examination</b>	<b>ii</b>
<b>Supervisors' Certificate</b>	<b>iii</b>
<b>Dedication</b>	<b>iv</b>
<b>Declaration of Originality</b>	<b>v</b>
<b>Acknowledgment</b>	<b>vi</b>
<b>Abstract</b>	<b>vii</b>
<b>List of Figures</b>	<b>xv</b>
<b>List of Tables</b>	<b>xxi</b>
<b>1 General Introduction</b>	<b>1-40</b>
1.1. Historical background	1
1.2. Cerium Dioxide (CeO <sub>2</sub> ): Structure and Properties	3
1.2.1. Crystal structure of CeO <sub>2</sub>	3
1.2.2. Defect structure of CeO <sub>2</sub>	4
1.2.2.1. Intrinsic defect	5
1.2.2.2. Extrinsic defects (disorder) in CeO <sub>2</sub>	5
1.2.3. Oxygen storage capacity of CeO <sub>2</sub>	6
1.3. Modification of CeO <sub>2</sub>	7
1.4. Introduction of nanomaterials	10
1.5. Synthetic approaches to ceria based materials	13

1.6.	Porous materials and their classification	15
1.7.	Synthesis of mesoporous materials	15
1.7.1.	Soft-matter templating	17
1.7.2.	Hard templating methods	22
1.8.	Mesoporous CeO <sub>2</sub> and CeO <sub>2</sub> based materials	23
1.9.	Applications of ceria based materials	26
1.10.	Objectives of the thesis	28
	References	29
<b>2</b>	<b>Experimental Procedure and Measurements</b>	<b>41-62</b>
2.1	Synthetic Methodology	42
2.1.1	Synthesis of pure CeO <sub>2</sub>	44
2.1.2	Synthesis of Sm <sup>3+</sup> doped CeO <sub>2</sub>	45
2.1.2.1	Synthesis of Sm <sup>3+</sup> doped CeO <sub>2</sub> by using different surfactants via conventional refluxing route	45
2.1.2.2	Synthesis of Sm <sup>3+</sup> doped CeO <sub>2</sub> by using SDS via microwave refluxing	45
2.1.3	Synthesis of Eu <sup>3+</sup> doped CeO <sub>2</sub> by using SDS through conventional and microwave refluxing	46
2.2	Characterization and measurements	47
2.2.1	Simultaneous thermal analysis (TGA/DSC)	48
2.2.2	X-ray diffraction (XRD)	48
2.2.3	Brunauer, Emmett and Teller (B.E.T.) measurements	50
2.2.4	Fourier transform-Infra red spectroscopy (FTIR)	51
2.2.5	UV-visible diffuse reflectance spectroscopy (UV-vis DRS)	52
2.2.6	Photoluminescence spectroscopy (PL)	53
2.2.7	X-ray photoelectron spectroscopy (XPS)	54
2.2.8	Field emission scanning electron microscopy (FESEM)	55
2.2.9	High resolution transmission electron microscopy (HRTEM)	56
2.2.10	Temperature programmed reduction (TPR) and temperature programmed desorption (TPD)	57
2.3	Cr(VI) adsorption study	58

2.3.1	Effect of variable parameters	58
2.3.1.1	Effect of contact time	59
2.3.1.2	Effect of pH	59
2.3.1.3	Effect of amount of adsorbent	59
2.3.1.4	Effect of adsorbate concentration	59
2.3.1.5	Study of adsorption isotherms	59
2.3.1.6	Study of adsorption kinetics	61
	References	61
<b>3</b>	<b>High Surface Area Mesoporous Ceria Synthesized With and Without Surfactant</b>	<b>63-88</b>
3.1	Introduction	64
3.2.	Experimental and characterization	65
3.3.	Results and Discussion	65
3.3.1.	TG–DSC	65
3.3.1.1.	Effect of surfactant	65
3.3.1.2	Effect of Microwave refluxing	66
3.3.2	XRD	67
3.3.2.1.	Effect of surfactant	67
3.3.2.2.	Effect of calcination temperature	68
3.3.2.3.	Effect of microwave reflux method	70
3.3.3	BET surface area	71
3.3.3.1	Effect of calcination temperature	71
3.3.3.2	Effect of microwave reflux methods	73
3.3.4.	FTIR spectra	74
3.3.5.	FESEM Micrograph	75
3.3.6.	TEM, HRTEM Micrograph & SAED Pattern	76
3.3.7.	UV–vis absorption spectra	78
3.3.7.1.	Effect of surfactant and calcination temperature	78
3.3.7.2	Effect of Microwave heating	80
3.3.8	Photoluminescence (PL) spectra	80
3.3.8.1.	Effect of surfactant	80

3.3.8.2.	Effect of calcination temperature	81
3.3.8.3.	Fluorescent microscopy images	82
3.3.9.	XPS Spectra	83
3.3.10.	NH <sub>3</sub> -TPD profiles	84
3.3.11.	TPR profiles	85
3.4.	Conclusions	86
	References	86
<b>4</b>	<b>High Surface Area Sm<sup>3+</sup> Doped Mesoporous CeO<sub>2</sub> Nanocrystals</b>	<b>89-133</b>
4.1	Introduction	90
4.2.	Synthesis and characterization of Sm <sup>3+</sup> doped CeO <sub>2</sub> nanocrystals	91
4.3.	Results and discussion	91
4.3.1	TG-DSC analysis of Sm <sup>3+</sup> doped CeO <sub>2</sub>	91
4.3.1.1	Effect of dopant concentration	91
4.3.1.2	Influence of conventional and microwave refluxing	95
4.3.1.3	Influence of anionic, cationic and nonionic surfactant	96
4.3.2	X-ray diffraction pattern of Sm <sup>3+</sup> doped CeO <sub>2</sub>	97
4.3.2.1	Effect of dopant concentrations	97
4.3.2.2	Effect of calcination temperatures	99
4.3.2.3	Effect of refluxing method	101
4.3.2.4	Effect of surfactants	102
4.3.3	N <sub>2</sub> sorption isotherm of Sm <sup>3+</sup> doped CeO <sub>2</sub>	103
4.3.3.1	Effect of dopant concentration	103
4.3.3.2	Effect of various calcination temperature	105
4.3.3.3	Influence of reflux methods	106
4.3.3.4	Effect of various surfactant	108
4.3.4	FTIR analysis	109
4.3.5	Microstructure analysis	112
4.3.5.1	FESEM images, EDAX analysis and elemental mapping	112
4.3.5.2	TEM & HRTEM images	115
4.3.6	UV-vis DRS studies	118
4.3.7.	PL analysis	121

4.3.7.1.	PL emission spectra	121
4.3.7.2.	PL excitation spectra	123
4.3.7.3.	Fluorescent microscopy images	125
4.3.8	XPS analysis	126
4.3.9	H <sub>2</sub> -TPR analysis	128
4.3.10	NH <sub>3</sub> -TPD analysis	130
4.4	Conclusion	131
	References	131
<b>5</b>	<b>Characterization of High Surface Area Eu<sup>3+</sup> Doped CeO<sub>2</sub> Nanopowders</b>	<b>134-169</b>
5.1	Introduction	135
5.2	Synthesis and characterization of Eu <sup>3+</sup> doped CeO <sub>2</sub> materials	136
5.3	Results and discussion	136
5.3.1	TG-DSC profiles of as-prepared Eu <sup>3+</sup> doped CeO <sub>2</sub> powders	136
5.3.1.1	Effect of dopant concentration	136
5.3.1.2	Effect of microwave refluxing	138
5.3.2.	XRD patterns of Eu <sup>3+</sup> doped CeO <sub>2</sub> nanopowders	140
5.3.2.1.	Effect of dopant concentrations	140
5.3.2.2.	Effect of calcination temperature	141
5.3.2.3.	Effect of microwave refluxing	143
5.3.3.	N <sub>2</sub> -sorption analysis	145
5.3.3.1.	Effect of dopant concentration	145
5.3.3.2.	Effect of calcination temperatures	146
5.3.3.3	Effect of microwave refluxing	147
5.3.4.	FTIR analysis	148
5.3.5.	Microstructure analysis	149
5.3.5.1.	FESEM images, EDAX analysis and elemental mapping	149
5.3.5.2.	TEM and HRTEM images	152
5.3.6.	UV-Vis diffuse reflectance spectroscopic studies	155
5.3.6.1.	Effect of dopant concentration	155
5.3.6.2	Effect of calcination temperatures	156
5.3.6.3.	Eu <sup>3+</sup> doped CeO <sub>2</sub> obtained via microwave refluxing	157

5.3.7.	PL analysis	159
5.3.7.1.	Effect of calcination temperature	159
5.3.7.2.	Effect of dopant concentration	160
5.3.7.3.	Fluorescent microscopy images	162
5.3.8.	XPS analysis	162
5.3.9.	H <sub>2</sub> -TPR analysis	165
5.3.10.	NH <sub>3</sub> -TPD analysis	166
5.4.	Conclusion	166
	References	167
<b>6</b>	<b>Applications of Pure and Doped CeO<sub>2</sub> Nanopowders for Environmental Remediation</b>	<b>170-205</b>
6.1	Effective adsorption of hazardous Cr(VI) ions in aqueous environment	171
6.1.1.	Introduction	171
6.1.2	Experimental condition of Cr(VI) adsorption	173
6.1.3.	Result and Discussion	174
6.1.3.1.	Effect of various adsorbent	174
6.1.3.2.	Effect of contact time	175
6.1.3.3.	Effect of pH	176
6.1.3.4.	Effect of adsorbent dose	177
6.1.3.5.	Effect of initial concentration	178
6.1.3.6.	Maximum adsorption capacity	178
6.1.3.7.	Adsorption isotherm study	179
6.1.3.7.1.	Langmuir isotherm	179
6.1.3.8.1.	Freundlich isotherm	180
6.1.3.8.	Adsorption kinetics	180
6.1.3.8.1.	The pseudo first-order equation	180
6.1.3.8.2.	The pseudo second-order equation	181
6.1.4.	Conclusion	182
6.2.	Evaluation of Photo degradation of Acid Orange 7 under natural sunlight	182

6.2.1.	Introduction	182
6.2.2.	Experimental details	185
6.2.3.	Result and discussion	186
6.2.3.1.	Effect of various photocatalysts	186
6.2.3.2	Effect of catalyst dosage	187
6.2.3.3	Effect of pH of the medium	188
6.2.3.4.	Effect of calcination temperature	188
6.2.3.5.	Effect of irradiation time	190
6.2.3.6.	FT-IR study on dye before and after photodegradation	191
6.2.3.7.	Active species to attack dye molecule	192
6.2.4.	Conclusion	196
6.3.	Autocatalytic activity	196
6.3.1.	Introduction	196
6.3.2.	Evaluation of autocatalytic behavior	197
6.3.3	Toxicity analysis	197
6.3.4.	Results and discussion	197
6.3.4.1.	Autocatalytic properties	197
6.3.4.2.	Effect of type of dopant	199
6.3.4.3	Effect of dopant concentration	200
6.3.4.4.	Cytotoxicity test	202
6.4.	Conclusion	202
	References	203
<b>7</b>	<b>Summary, Conclusion and Future Scope of the Work</b>	<b>206-210</b>
7.1	Summary and Conclusion	206
7.2	New achievement and implication	209
7.3	Future Scope of the Work	210

# List of Figures

<b>Fig No.</b>	<b>Title</b>	<b>Page No.</b>
<b>Fig. 1.1</b>	The crystal structure of CeO <sub>2</sub> : (a) unit cell as a <i>ccp</i> array of cerium atoms. The <i>ccp</i> layers are parallel to the [111] planes of the f.c.c. unit cell, (b) and (c) the same structure redrawn as a primitive cubic array of oxygens. [Adapted from ref. 93].	3
<b>Fig. 1.2</b>	The Lycurgus cup appears (a) green in reflected light, and (b) red in transmitted light and this cup is preserved in the British museum in London.	10
<b>Fig. 1.3</b>	Different types of surfactant structures (adopted from ref. 263).	20
<b>Fig. 1.4</b>	Schematic representation of the different types of silica-surfactant interfaces (adapted from ref. 252).	21
<b>Fig. 2.1</b>	Surfactants used in the synthesis of mesoporous CeO <sub>2</sub> or doped CeO <sub>2</sub> .	42
<b>Fig. 2.2</b>	Schematic flow chart illustrating various steps involved for the synthesis of pure CeO <sub>2</sub> .	43
<b>Fig. 2.3</b>	Schematic flow chart of various steps involved for the synthesis of Sm <sup>3+</sup> or Eu <sup>3+</sup> doped CeO <sub>2</sub> .	46
<b>Fig. 2.4</b>	Photograph of Rigaku Ultima-IV diffractometer.	49
<b>Fig. 2.5</b>	Photograph of Quantachrome Autosorb-1 apparatus.	51
<b>Fig. 2.6</b>	Schematic diagram showing transitions giving rise to absorption and fluorescence emission spectra.	54
<b>Fig. 2.7</b>	Photograph of Nova Nano SEM 450.	55
<b>Fig. 2.8</b>	Photograph of JEOL-JEM 2100 TEM.	56
<b>Fig. 3.1</b>	TG-DSC curves of (A) 100CSDSeasp and (B) 100Ceasp.	66
<b>Fig. 3.2</b>	TG-DSC curves of 100CeSDSMWasp.	67
<b>Fig. 3.3</b>	XRD patterns of the (a) 100Ceasp (b) 100CeSDSasp.	68
<b>Fig. 3.4</b>	XRD patterns of (a) 100CeSDSasp, and the samples calcined at (b) 500°C, (c) 650°C, (d) 800°C, and (e) 1000°C.	69
<b>Fig. 3.5</b>	XRD patterns of the (a) 100CeSDSMWasp and calcined at (b) 500°C (c) 650°C and (c) 800°C.	70
<b>Fig. 3.6</b>	(A) N <sub>2</sub> adsorption–desorption isotherms (B) BJH pore size distribution curves of the (a) 100Ceasp and the samples calcined at (b) 500°C, (c) 650°C, and (c) 800°C.	72
<b>Fig. 3.7</b>	(A) N <sub>2</sub> adsorption–desorption isotherms and (B) BJH pore size distribution of 100CeSDS samples (a) as prepared, calcined at (b) 500°C, (c) 650°C, and (c) 800°C.	73



<b>Fig. 3.8</b>	(A) N <sub>2</sub> adsorption–desorption isotherms and (B) BJH pore size distribution of 100CeSDSMW (a) as prepared samples, calcined at (b) 500°C and (c) 650°C.	73
<b>Fig. 3.9</b>	FTIR spectra of the (a) 100Ceasp and (b) 100ce500.	74
<b>Fig. 3.10</b>	FTIR spectra of the (a) pure SDS, (b) 100CeSDSasp and calcined at (c) 500°C (d) 650°C for 2 h.	75
<b>Fig. 3.11</b>	FESEM micrographs of (a) 100Ce500 and (b) 100CeSdS500°C.	76
<b>Fig. 3.12</b>	(a) TEM image, (b) HRTEM image, (c) Lattice fringes and corresponding (d) SAED pattern of 100Ce500°C.	76
<b>Fig. 3.13</b>	(a) TEM image, (b) HRTEM image, (c) Lattice fringes and corresponding (d) SAED pattern of 100CeSDS500°C.	77
<b>Fig. 3.14</b>	UV-vis spectra of (a) 100Ce500 and (b) 100CeSDS500.	78
<b>Fig. 3.15</b>	UV-visible spectra of the (a) 100CeSDSasp and calcined at (b)500°C, (c) 650°C, (d) 800°C and (e)1000°C.	79
<b>Fig. 3.16</b>	UV-visible spectra of the (a) 100CeSDSMWasp and calcined at (b) 500°C (c) 650°C and (c) 800°C.	80
<b>Fig. 3.17</b>	PL spectra of (a) 100Ce500 and (b) 100CeSDS500 samples excited at 335 nm.	81
<b>Fig. 3.18</b>	PL spectra of (a) 100CeSDSasp, and the samples calcined at (b) 500°C, (c) 650°C, (c) 800°C, and (d) 1000°C.	82
<b>Fig. 3.19</b>	(a-c) Fluorescent microscope images of 100CeSDS1000, excited at wavelengths of (a) 350 nm, (b) 405 nm, and (c) 532 nm.	82
<b>Fig. 3.20</b>	Ce 3d XPS spectra of (a) 100CeSDS500 and (b) 100Ce500.	83
<b>Fig. 3.21</b>	O 1s core level photoemission spectra from (a)100CeSDS500°C and (b)100Ce500°C.	84
<b>Fig. 3.22</b>	(A) TPD and (B) TPR profiles of pure CeO <sub>2</sub> synthesized (a) 100Ce500°C, (b) 100CeSDS500°C.	85
<b>Fig. 4.1</b>	TG-DSC curves of (a) 0.5, (b) 1, (c) 2, and (d) 5 mol% Sm <sup>3+</sup> doped as-synthesized CeO <sub>2</sub> samples.	93
<b>Fig. 4.2</b>	TG-DSC curves of (a) 10 and (b) 20 mol% Sm <sup>3+</sup> doped as-synthesized CeO <sub>2</sub> samples.	93
<b>Fig. 4.3</b>	(A) DSC and (b) TG curves of (B) 0.5, (b) 1.0, (c) 2.0, (d) 5.0, (e) 10 and (f) 20 mol% Sm <sup>3+</sup> doped as-prepared CeO <sub>2</sub> samples.	94
<b>Fig. 4.4</b>	(A) DSC and (B) TG curves of 1SmCeSDSasp prepared via (a) without refluxing, (b) normal refluxing, and (c) microwave refluxing method.	96
<b>Fig. 4.5</b>	(A) DSC and (B) TG curves of as-prepared 1SmCeSDSasp sample, prepared using different surfactants of (a) SDS, (b) DDA, and (c) PEG.	97

<b>Fig. 4.6</b>	XRD patterns of as-prepared (a) 0.5, (b) 1.0, (c) 2.0, (d) 5.0, (e) 10 and (f) 20 mol% Sm <sup>3+</sup> doped CeO <sub>2</sub> nanopowders.	98
<b>Fig. 4.7</b>	XRD patterns of Sm <sup>3+</sup> doped CeO <sub>2</sub> (a) as-prepared precursor and calcined at (b) 500°C, (c) 650°C and (d) 800°C for 2 h.	100
<b>Fig. 4.8</b>	XRD patterns of the as-prepared 1 mol% Sm <sup>3+</sup> doped CeO <sub>2</sub> powders synthesized via (a) without refluxing, (b) normal refluxing, and (c) microwave refluxing method.	102
<b>Fig. 4.9</b>	XRD patterns of the as-prepared 1 mol% Sm <sup>3+</sup> doped CeO <sub>2</sub> synthesized using (a) SDS, (b) DDA, and (c) PEG by conventional refluxing method.	103
<b>Fig. 4.10</b>	(A) BET N <sub>2</sub> adsorption–desorption isotherm and the (B) BJH pore size distributions of (a) 0.5, (b) 1.0, (c) 2.0, (d) 5.0, (e) 10 and (f) 20 mol% Sm <sup>3+</sup> doped CeO <sub>2</sub> powders and calcined at 500°C.	104
<b>Fig. 4.11</b>	(A) BET N <sub>2</sub> adsorption–desorption isotherms and the (B) BJH pore size distributions of 1 mol% Sm <sup>3+</sup> doped CeO <sub>2</sub> (a) as-prepared, and the samples calcined at (b) 500°C, (c) 650°C, and (d) 800°C for 2 h.	105
<b>Fig. 4.12</b>	(A) N <sub>2</sub> adsorption–desorption isotherms and (B) BJH pore size distribution of the samples prepared via (a) without refluxing, (b) normal refluxing, and (c) microwave refluxing method and calcined at 500°C.	107
<b>Fig. 4.13</b>	(A) N <sub>2</sub> adsorption–desorption isotherms (B) BJH pore size distribution of the as-prepared 1 mol% Sm <sup>3+</sup> doped CeO <sub>2</sub> synthesized via (a) SDS, (b) DDA, and (c) PEG by conventional refluxing method.	108
<b>Fig. 4.14</b>	FTIR spectra of 1 mol% Sm <sup>3+</sup> doped CeO <sub>2</sub> powders, (a) as-prepared, and the samples calcined at (b) 500°C, and (c) 650°C for 2 h, synthesized using SDS as surfactant.	109
<b>Fig. 4.15</b>	Expanded FTIR spectra of 1 mol% Sm <sup>3+</sup> doped as-prepared CeO <sub>2</sub> .	110
<b>Fig. 4.16</b>	FTIR spectra of 1 mol% Sm <sup>3+</sup> doped CeO <sub>2</sub> nanopowders, (a) as-prepared, and the samples calcined at (b) 500°C, and (c) 650°C for 2 h, synthesized using DDA as surfactant.	111
<b>Fig. 4.17</b>	FTIR spectra of 1 mol% Sm <sup>3+</sup> doped CeO <sub>2</sub> nanopowders, (a) as-prepared, and the samples calcined at (b) 500°C, and (c) 650°C for 2 h, synthesized using PEG as surfactant.	111
<b>Fig. 4.18</b>	FESEM micrographs of (a) 0.5, (b) 1.0, (c) 2.0, and (d) 5 mol% Sm <sup>3+</sup> doped CeO <sub>2</sub> calcined at 500°C.	112
<b>Fig. 4.19</b>	EDS graphs of (a) 0.5, (b) 1.0, (c) 2.0, and (d) 5 mol% Sm <sup>3+</sup> doped CeO <sub>2</sub> calcined at 500°C.	113
<b>Fig. 4.20</b>	Elemental mapping of 1 mol% Sm <sup>3+</sup> doped CeO <sub>2</sub> , (a) overall elemental mapping, and of the (b) Ce, (c) Sm, and (d) O.	114
<b>Fig. 4.21</b>	FESEM micrographs of 1.0 mol% Sm <sup>3+</sup> doped CeO <sub>2</sub> synthesized through (a) conventional refluxing, and (b) microwave assisted refluxing, and calcined at 500°C.	114

<b>Fig. 4.22</b>	FESEM micrographs of 1 mol% Sm <sup>3+</sup> doped CeO <sub>2</sub> , (a) asp, and calcined at (b) 500°C (c) 650°C, and (d) 800°C.	115
<b>Fig. 4.23</b>	TEM images (right), and HRTEM images (left) of Sm <sup>3+</sup> doped CeO <sub>2</sub> powders (a) as-prepared precursor, and calcined at (b) and (c) 500°C, and (d) 650°C for 2 h. Selected part of (c) is enlarged and shown in the inset.	116
<b>Fig. 4.24</b>	TEM and HRTEM micrographs of 1 mol% Sm <sup>3+</sup> doped CeO <sub>2</sub> , calcined at 800°C.	117
<b>Fig. 4.25</b>	UV-vis diffuse reflectance spectra of Sm <sup>3+</sup> doped CeO <sub>2</sub> powders (a) as-prepared precursor and calcined at (b) 500°C (compared with that of pure CeO <sub>2</sub> in the inset), (c) 650°C, (d) 800°C, and (e) 1000°C for 2 h.	118
<b>Fig. 4.26</b>	Plot of the transformed Kubelka–Munk function versus light energy for Sm <sup>3+</sup> doped CeO <sub>2</sub> samples.	119
<b>Fig. 4.27</b>	UV-visible absorption spectra of (a) 0, (b) 0.5, (c) 1.0, (d) 2.0, (e) 5.0, (f) 10, and (g) 20 mol% Sm <sup>3+</sup> doped CeO <sub>2</sub> nanopowders calcined at 500°C.	120
<b>Fig. 4.28</b>	PL emission spectra of (a) 0.5, (b) 1.0, (c) 2.0, and (d) 5 mol% Sm <sup>3+</sup> doped CeO <sub>2</sub> nanopowders calcined at 500°C.	121
<b>Fig. 4.29</b>	PL emission spectra of Sm <sup>3+</sup> doped CeO <sub>2</sub> (a) as-prepared precursor, and the samples calcined at (b) 500°C, (c) 650°C, (d) 800°C, (e) 1000°C, and (f) 1300°C for 2 h.	122
<b>Fig. 4.30</b>	PL excitation spectra of Sm <sup>3+</sup> doped CeO <sub>2</sub> (a) as-prepared precursor, and calcined at (b) 500°C, (c) 650°C, (d) 800°C, (d) 1000°C, and (d) 1300°C for 2 h.	123
<b>Fig. 4.31</b>	PL excitation spectra of (a) 0.5, (b) 1.0, (c) 2.0, and (d) 10 mol% Sm <sup>3+</sup> doped CeO <sub>2</sub> nanopowders calcined at 500°C for 2 h.	124
<b>Fig. 4.32</b>	Energy transfer mechanism from CeO <sub>2</sub> host to Sm <sup>3+</sup> ions.	125
<b>Fig. 4.33</b>	Fluorescent microscope images of 1SmCeSDS1000 at excitation wavelengths (a) 350 nm, (b) 405 nm and (c) 532 nm.	125
<b>Fig. 4.34</b>	High-resolution XPS spectrum and the corresponding deconvolution components of Ce 3d from Sm <sup>3+</sup> doped CeO <sub>2</sub> calcined at 500°C.	126
<b>Fig. 4.35</b>	Sm 3d <sub>5/2</sub> XP spectrum of Sm <sup>3+</sup> doped CeO <sub>2</sub> calcined at 500°C.	127
<b>Fig. 4.36</b>	O 1s XP spectra of CeO <sub>2</sub> and Sm <sup>3+</sup> doped CeO <sub>2</sub> samples calcined at 500°C.	127
<b>Fig. 4.37</b>	H <sub>2</sub> consumption as a function of temperature for mesoporous CeO <sub>2</sub> and Sm <sup>3+</sup> doped CeO <sub>2</sub> calcined at 500°C.	129
<b>Fig. 4.38</b>	NH <sub>3</sub> –TPD profiles of the (a) CeO <sub>2</sub> and (b) Sm <sup>3+</sup> doped–CeO <sub>2</sub> calcined at 500°C.	130
<b>Fig. 5.1</b>	TG-DSC profiles of as-prepared (a) 0.5, (b) 1.0, (c) 2.0, and (d) 5 mol% Eu <sup>3+</sup> doped CeO <sub>2</sub> samples obtained via conventional refluxing.	137
<b>Fig. 5.2</b>	TG-DSC profiles of the as-prepared 1 mol% Eu <sup>3+</sup> doped CeO <sub>2</sub> sample, obtained via microwave refluxing method.	139

<b>Fig. 5.3</b>	Comparative (A) DSC and (B) TG profiles of the as-prepared 1 mol% $\text{Eu}^{3+}$ doped $\text{CeO}_2$ samples obtained via (a) conventional, and (b) microwave refluxing method.	139
<b>Fig. 5.4</b>	XRD patterns of (a) 0.5, (b) 1.0, (c) 2.0, and (d) 5 mol% $\text{Eu}^{3+}$ doped $\text{CeO}_2$ obtained via conventional refluxing method and calcined at $500^\circ\text{C}$ for 2 h.	141
<b>Fig. 5.5</b>	XRD patterns 1 mol% $\text{Eu}^{3+}$ doped $\text{CeO}_2$ obtained via conventional refluxing method (a) as-prepared, and calcined at (b) $500^\circ\text{C}$ , (c) $650^\circ\text{C}$ and (d) $800^\circ\text{C}$ for 2 h.	142
<b>Fig. 5.6</b>	XRD patterns of 1 mol% $\text{Eu}^{3+}$ doped $\text{CeO}_2$ obtained via microwave refluxing method (a) as-prepared, and the samples calcined at (b) $500^\circ\text{C}$ , and (c) $800^\circ\text{C}$ for 2 h.	143
<b>Fig. 5.7</b>	(A) $\text{N}_2$ -sorption isotherms, and (B) BJH pore size distribution curves of (a) 0.5, (b) 1.0, (c) 2.0, and (d) 5 mol% $\text{Eu}^{3+}$ doped $\text{CeO}_2$ obtained via conventional refluxing method and calcined at $500^\circ\text{C}$ for 2 h.	145
<b>Fig. 5.8</b>	(A) $\text{N}_2$ -sorption isotherms and the (B) BJH pore size distribution curves of 1 mol % $\text{Eu}^{3+}$ doped $\text{CeO}_2$ samples, (a) as-prepared and calcined powders at (b) $500^\circ\text{C}$ , (c) $650^\circ\text{C}$ , and (d) $800^\circ\text{C}$ for 2 h, obtained via conventional refluxing.	147
<b>Fig. 5.9</b>	(A) $\text{N}_2$ -sorption isotherms, and (B) BJH pore size distribution curves of (a) 1EuCeSDSMWasp, (b) 1EuCeSDSMWasp, and (c) 1EuCeSDSMWasp.	148
<b>Fig. 5.10</b>	FTIR spectra of 1 mol% $\text{Eu}^{3+}$ doped $\text{CeO}_2$ (a) as-prepared, and the samples calcined at (b) $500^\circ\text{C}$ , and (c) $650^\circ\text{C}$ .	149
<b>Fig. 5.11</b>	FESEM micrographs of 1 mol% $\text{Eu}^{3+}$ doped $\text{CeO}_2$ , (a) as-prepared, and the samples calcined at (b) $500^\circ\text{C}$ , (c) $650^\circ\text{C}$ , and (d) $800^\circ\text{C}$ .	150
<b>Fig. 5.12</b>	FESEM micrographs of (a) 0.5, (b) 1.0, (c) 2.0, and (d) 5 mol% $\text{Eu}^{3+}$ doped $\text{CeO}_2$ samples obtained via conventional refluxing and calcined at $500^\circ\text{C}$ .	151
<b>Fig. 5.13</b>	Elemental mapping of 1 mol% $\text{Eu}^{3+}$ doped $\text{CeO}_2$ samples, (a) overall elemental mapping, (b) Ce, (c) Eu, and (d) O.	151
<b>Fig. 5.14</b>	EDS of (a) 0.5, (b) 1.0, (c) 2.0, and (d) 5 mol% $\text{Eu}^{3+}$ doped $\text{CeO}_2$ calcined at $500^\circ\text{C}$ .	152
<b>Fig. 5.15</b>	(a) TEM, (b) HRTEM images, (c) lattice fringes, and corresponding (d) SAED pattern of 1EuCeSDS $500^\circ\text{C}$ .	153
<b>Fig. 5.16</b>	HRTEM images and lattice fringes of (a) 0.5, (b) 1, (c) 2, and (d) 5 mol% $\text{Eu}^{3+}$ doped $\text{CeO}_2$ samples obtained via conventional refluxing and calcined at $500^\circ\text{C}$ .	154
<b>Fig. 5.17</b>	HRTEM images of 1EuCeSDS $650^\circ\text{C}$ at different magnifications.	155
<b>Fig. 5.18</b>	UV-vis absorbance spectra of (a) 0.5, (b) 1, (c) 2 and (d) 5 mol % $\text{Eu}^{3+}$ doped $\text{CeO}_2$ calcined at $500^\circ\text{C}$ for 2 h.	156
<b>Fig. 5.19</b>	UV-vis absorbance spectra of $\text{Eu}^{3+}$ doped $\text{CeO}_2$ powders obtained via conventional refluxing method, (a) as-prepared and calcined at (b) $500^\circ\text{C}$ (c) $650^\circ\text{C}$ , and (d) $800^\circ\text{C}$ for 2 h.	15

<b>Fig. 5.20</b>	UV-Vis absorbance spectra of 1 mol% Eu <sup>3+</sup> doped CeO <sub>2</sub> powders obtained via microwave refluxing method, (a) as-prepared and calcined at (b) 500°C, (c) 650°C, and (d) 800°C for 2 h.	158
<b>Fig. 5.21</b>	PL (A) emission and (B) excitation spectra of Eu <sup>3+</sup> doped CeO <sub>2</sub> obtained in conventional refluxing method, and calcined at (a) 500°, (b) 650°C, (c) 800°C, and (d) 1000°C for 2 h.	159
<b>Fig. 5.22</b>	PL (A) emission and (B) excitation spectra of (a) 0.5, (b) 1, (c) 2, and (d) 5 mol % Eu <sup>3+</sup> doped CeO <sub>2</sub> obtained via conventional refluxing method and calcined at 800°C for 2 h.	160
<b>Fig. 5.23</b>	Energy transfer mechanism from CeO <sub>2</sub> host to Eu <sup>3+</sup> ions.	161
<b>Fig. 5.24</b>	Fluorescent microscope images of 1 mol% Eu <sup>3+</sup> doped CeO <sub>2</sub> obtained via conventional refluxing method, and calcined at 800°C, excited at wavelengths of (a) 350 nm, (b) 405 nm, and (c) 532 nm.	162
<b>Fig. 5.25</b>	High resolution XPS spectrum of the Ce 3d core level regions for the 1 mol% Eu <sup>3+</sup> doped CeO <sub>2</sub> obtained via conventional refluxing method and calcined at 500°C for 2 h.	163
<b>Fig. 5.26</b>	High resolution XPS spectra of the (a) O1S and (b) Eu 3d core level regions for the 1 mol% Eu <sup>3+</sup> doped CeO <sub>2</sub> obtained via conventional refluxing and calcined at 500°C for 2 h.	164
<b>Fig. 5.27</b>	(A) H <sub>2</sub> consumption as a function of temperature, and (B) NH <sub>3</sub> -TPD profiles for (a) pure CeO <sub>2</sub> and (b)1 mol% Eu <sup>3+</sup> doped CeO <sub>2</sub> calcined at 500°C for 2 h.	166
<b>Fig. 6.1</b>	Time profile of Cr(VI) removal with 1SmCeSDSasp without adjustment of pH. The initial Cr(VI) concentration and the amount of adsorbent were 100 mgL <sup>-1</sup> and 10 gL <sup>-1</sup> , respectively. (b) Effect of pH (varied from 1.5 to 8) on the Cr(VI) adsorption by 1SmCeSDSasp (time = 60 min, initial Cr(VI) conc. = 100 mg L <sup>-1</sup> , and amount of 1SmCeSDSasp= 10 gL <sup>-1</sup> ).	175
<b>Fig. 6.2</b>	Effect of (a) adsorbent dose and (b) adsorbate concentration on % Cr(VI) adsorption by 1SmCeSDSasp (time: 60 min, initial Cr(VI) conc. 100 mgL <sup>-1</sup> , and without any further pH adjustment).	177
<b>Fig. 6.3</b>	Maximum adsorption capacity of 1SmCeSDSasp, variation with time (in h), initial Cr (VI) conc 100 mg L <sup>-1</sup> , amount of 1SmCeSDSasp 2 g L <sup>-1</sup> , at pH 2.	178
<b>Fig. 6.4</b>	(a) Langmuir and (b) Freundlich adsorption isotherms for Cr(VI) adsorption by 1SmCeSDSasp.	179
<b>Fig. 6.5</b>	Pseudo-first and (B) pseudo-second order kinetics for Cr(VI) adsorption by 1SmCeSDSasp.	181
<b>Fig. 6.6</b>	(a) Effect of 1SmCeSDSMW500 catalyst amount on UV–Vis spectra of AO7 (photodegradation % in the inset) (b) Effect of initial pH value on the photocatalytic degradation efficiency of AO7 in 10 h. during the decolorization process at solar irradiation time of 1 h. pH neutral.	187
<b>Fig. 6.7</b>	(a) Effect of calcination temperatures of 1SmCeSDSMW catalyst on UV–Vis spectra of AO7 (photodegradation % in the inset) during the	189

decolorization process at solar irradiation time of 1 h. pH neutral. (b) Evolution of the UV–vis spectra with irradiated time for the photocatalytic degradation of AO7 in aqueous solution in the presence of CeO<sub>2</sub>: Sm<sup>3+</sup> catalyst calcined at 500°C. pH neutral.

- Fig. 6.8** The photo of AO7 solutions in the presence of 1SmceSDSMW500 as catalyst under solar irradiation at different time intervals (h) as marked therein. 190
- Fig. 6.9** FT–IR spectra of AO7 (a) isolated, (b) adsorbed on catalyst, and after photodegradation at (c) 2 h, and (d) 6 h of irradiation. 191
- Fig. 6.10** Control experiments of photocatalytic degradation of AO7 with the addition of different radical scavengers: Isopropanol (scavenger for hydroxyl radicals), CrO<sub>3</sub> (scavenger for electrons), sodium oxalate (SOX, scavenger for holes), and benzoquinone (BQ, scavenger for superoxide radicals), over the optimum 1SmCeSDSMW500 under solar light irradiation for 6 h. 192
- Fig. 6.11** Proposed pathway for photocatalytic AO7 degradation. 194
- Fig. 6.12** Transmittance spectra showing autocatalytic behavior of (a) Sm<sup>3+</sup> doped CeO<sub>2</sub> calcined at 500°C. Photographs [in the inset of (c)] of the aqueous solution of the sample in absence and presence of H<sub>2</sub>O<sub>2</sub> showing characteristic reversible color changes. Transmittance spectra showing blue shift for the CeO<sub>2</sub> (blue line) and Sm<sup>3+</sup> doped CeO<sub>2</sub> samples (black: as-prepared; and red: calcined at 500°C) after addition of H<sub>2</sub>O<sub>2</sub> (b) 30 min, (c) 3 days, and (d) 30 min and 10 days (showing shift difference). 199
- Fig. 6.13** UV-visible transmittance spectra of (a) pure, Sm<sup>3+</sup> and Eu<sup>3+</sup> doped CeO<sub>2</sub> calcined at 500°C for 2 h, after 3 days of H<sub>2</sub>O<sub>2</sub> treatment, and (b) 0 to 10 mol% Sm<sup>3+</sup> doped CeO<sub>2</sub> calcined at 500°C for 2 h. 200
- Fig. 6.14** Cell viability by MTT assay of mesoporous CeO<sub>2</sub> and Sm<sup>3+</sup> doped CeO<sub>2</sub> calcined at 500°C after 1, 3 and 5 days incubation in MG-63 cell lines. 202

# List of Tables

<b>Table No.</b>	<b>Title</b>	<b>Page No.</b>
<b>Table 1.1</b>	Non-siliceous mesoporous oxides prepared by soft-templating methods (adopted from ref. 264)	16
<b>Table 1.2</b>	Non-siliceous mesoporous oxides prepared by hard-templating methods (Adopted from ref. 264)	17
<b>Table 1.3</b>	Mesostructured materials with different interactions between the surfactant and the inorganic framework.	22
<b>Table 2.1</b>	List of chemicals used in the synthesis of pure as well as Sm <sup>3+</sup> or Eu <sup>3+</sup> doped CeO <sub>2</sub> .	43
<b>Table 2.2</b>	Notations used in this thesis for pure, Sm <sup>3+</sup> or Eu <sup>3+</sup> doped CeO <sub>2</sub> samples.	47
<b>Table 3.1</b>	Crystallize size and lattice parameters of the as-prepared CeO <sub>2</sub> powders, (a) without, and (b) with surfactant.	67
<b>Table 3.2</b>	Crystallize size and lattice parameters of the 100CeSDSasp sample and calcined at different temperatures.	69
<b>Table 3.3</b>	Crystallize size and lattice parameters of as-prepared 100CeSDSMW samples and calcined at (b) 500°C (c) 650°C, and (c) 800°C.	71
<b>Table 3.4</b>	Surface area, pore diameter and total pore volume of 100Ce sample calcined at different temperatures.	72
<b>Table 3.5</b>	Surface area, pore diameter, and total pore volume of 100CeSDS samples calcined at different temperatures.	72
<b>Table 3.6</b>	Surface area, pore diameter, and total pore volume of 100CeSDSMWasp and the samples calcined at (b) 500°C and (c) 650°C.	74
<b>Table 3.7</b>	Band gap values of 100Ce, 100CeSDS and 100CeSDSMW samples calcined at different temperatures.	79
<b>Table 3.8</b>	TPD data of 100Ce500 and 100CeSDS500.	85
<b>Table 3.9</b>	Comparison of TPR data of 100Ce500 and 100CeSDS500 samples.	86
<b>Table 4.1</b>	Weight loss% observed in as-prepared Sm <sup>3+</sup> doped CeO <sub>2</sub> samples prepared through conventional refluxing method using SDS as surfactant.	94
<b>Table 4.2</b>	Weight loss % of Sm <sup>3+</sup> doped as-prepared CeO <sub>2</sub> samples prepared through without refluxing and microwave refluxing method.	94
<b>Table 4.3</b>	Weight loss % of Sm <sup>3+</sup> doped CeO <sub>2</sub> , synthesized using DDA and PEG assisted route by conventional refluxing method.	97
<b>Table 4.4</b>	Crystallite size and lattice parameters of Sm <sup>3+</sup> doped CeO <sub>2</sub> nanopowders.	99
<b>Table 4.5</b>	Crystallites size and lattice parameter values of Sm <sup>3+</sup> doped CeO <sub>2</sub> nanopowders calcined at different temperatures.	101

<b>Table 4.6</b>	Crystallites size and lattice parameter values of 1 mol% Sm <sup>3+</sup> doped CeO <sub>2</sub> powders synthesized via different routes.	102
<b>Table 4.7</b>	Crystallites size and lattice parameter values of 1 mol% Sm <sup>3+</sup> doped CeO <sub>2</sub> powders synthesized using different surfactants.	103
<b>Table 4.8</b>	Comparison of N <sub>2</sub> gas adsorption results for mesoporous Sm <sup>3+</sup> doped CeO <sub>2</sub> nanopowders calcined at different temperatures.	104
<b>Table 4.9</b>	N <sub>2</sub> gas adsorption results for mesoporous 1 mol% Sm <sup>3+</sup> doped CeO <sub>2</sub> nanopowders calcined at different temperatures.	106
<b>Table 4.10</b>	N <sub>2</sub> gas adsorption results for mesoporous 1 mol% Sm <sup>3+</sup> doped CeO <sub>2</sub> nanopowders calcined at different temperatures.	107
<b>Table 4.11</b>	N <sub>2</sub> gas adsorption results for mesoporous 1 mol% Sm <sup>3+</sup> doped CeO <sub>2</sub> nanopowders calcined at different temperatures.	108
<b>Table 5.1</b>	Weight loss % of Eu <sup>3+</sup> doped CeO <sub>2</sub> samples.	138
<b>Table 5.2</b>	Crystallite size, lattice parameters and lattice volumes of (a) 0.5, (b) 1.0, (c) 2.0, and (d) 5 mol% Eu <sup>3+</sup> doped CeO <sub>2</sub> samples obtained via conventional refluxing method and calcined at 500°C for 2 h.	141
<b>Table 5.3</b>	Crystallite size, lattice parameters and lattice volume of 1 mol% Eu <sup>3+</sup> doped CeO <sub>2</sub> samples obtained via conventional refluxing method.	143
<b>Table 5.4</b>	Crystallite size, lattice parameters and lattice volume of 1.0EuCeSDSMW, 1.0EuCeSDSMW500, and 1.0EuCeSDSMW800.	144
<b>Table 5.5</b>	BET surface area, pore volume, and pore size of Eu <sup>3+</sup> doped CeO <sub>2</sub> samples obtained via conventional refluxing and calcined at 500°C.	146
<b>Table 5.6</b>	BET surface area, pore volume, and pore diameter of 1 mol% Eu <sup>3+</sup> doped CeO <sub>2</sub> samples calcined at different temperatures.	147
<b>Table 5.7</b>	BET surface area, pore volume and pore diameter of 1 mol% Eu <sup>3+</sup> doped CeO <sub>2</sub> samples obtained microwave refluxing route.	148
<b>Table 5.8</b>	Bandgap energy of (a) 0.5, (b) 1, (c) 2 and (d) 5 mol % Eu <sup>3+</sup> doped CeO <sub>2</sub> obtained in conventional reflux method and calcined at 500°C for 2 h.	156
<b>Table 5.9</b>	Bandgap energy of Eu <sup>3+</sup> doped CeO <sub>2</sub> powders obtained in Conventional and Microwave refluxing method (a) as-prepared and calcined at (b) 500°C (c) 650°C and (d) 800°C for 2 h.	158
<b>Table 6.1</b>	Comparison of Cr(VI) uptake by different pure and doped CeO <sub>2</sub> nanopowders.	174
<b>Table 6.2</b>	Langmuir and Freundlich isotherm parameters for Cr(VI) adsorption by 1SmCeSDSasp.	180
<b>Table 6.3</b>	Kinetic parameters for pseudo-first order and pseudo-second order kinetic models.	182
<b>Table 6.4</b>	Comparison of photocatalytic degradation % of AO7 by different CeO <sub>2</sub> nanopowders during the decolorization process at solar irradiation time of 1 h. pH neutral.	186



## Chapter 1

# General Introduction

***Outline:** This chapter comprised a general introduction and thorough literature survey on cerium oxide and its composite oxides including structural, properties, synthesis strategies and potential applications. A short introduction of nanomaterials is also included. In addition an extensive discussion of synthesis and application of mesoporous materials has been discussed. Synthesis of mesoporous CeO<sub>2</sub> and CeO<sub>2</sub>-based oxides via templating method particularly, both the soft-templating and hard-templating methods are reviewed. Applications of mesoporous CeO<sub>2</sub> and CeO<sub>2</sub>-based oxides were also briefed with prominence to adsorption and removal of organic pollutants from aqueous solution. The main objectives of the present work are summarized towards the end of this chapter.*

### 1.1. Historical Background

Rare earth (RE) elements has been considered as an ‘industrial vitamin’ and a ‘treasury’ of new materials due to their wide applications in technical progress and the development of traditional industries along with information and biotechnology.<sup>1,2</sup> Because of the well shielded (by the filled 5s<sup>2</sup> and 5p<sup>6</sup> shells) and partially filled 4f shell, the chemistry of rare earth differs from main group elements and transition metals.<sup>1-3</sup> This shielding is mainly responsible for the unique catalytic, magnetic and electronic properties of the rare earth. In the last decade rare earth elements have attracted to accomplish new types of applications due to their unique features which are not possible with transition and main group metals.<sup>2,3</sup> The name ‘‘rare earth’’ is rather misleading since the lanthanides are neither ‘‘rare’’ nor ‘‘earth’’ like in properties.<sup>4</sup> The name rare earths referring to elements to the difficulty in obtaining the pure elements, and not to their relative abundances in the Earth's crust. Hence the name rare earth has origins as they are never found as free metals in the Earth's crust and pure minerals

of individual rare earths also do not exist. They are found as oxides which have proved to be particularly difficult to separate from each other, especially to 18<sup>th</sup> and 19<sup>th</sup> century chemists. All of the rare-earth elements are actually more abundant than silver, and some are more abundant than lead. Rather, the name “rare earth” connotes that these elements were isolated from uncommon minerals. Rather the term lanthanide, is the least confusing which means “to lie hidden” and it originates from the fact that lanthanum was first discovered “hidden” in a cerium containing mineral.<sup>4</sup> According to IUPAC rare earths are consist of a set of seventeen chemical elements, the fifteen lanthanides along with scandium and yttrium.<sup>5,6</sup> Cerium is the most abundant element among the rare earth family, which has crustal concentration (66.5 ppm) even more than that of copper (60 ppm) or tin (2.3 ppm).<sup>7,8</sup> It was discovered from cerite in 1803 by Jons Jakob Berzelius and Wilhelm Hisinger in Sweden, and Martin Heinrich Klaproth in Germany.<sup>9</sup> It was named after the dwarf planet Ceres, which was again named after the Roman goddess of agriculture (particularly the growth of cereals).<sup>10</sup> However, it was not until 1839–1843 that the Swede C.G. Mosander first separated these earths into their component oxides; thus ceria was resolved into the oxides of cerium and lanthanum and a mixed oxide ‘didymia’ (a mixture of the oxides of the metals from Pr through Gd).<sup>11</sup>

Cerium dioxide commonly known as “ceria (CeO<sub>2</sub>)”, has been extensively researched in chemistry, physics, material science, ceramic and biology has confirmed it unique and irreplaceable role since the 1980s, when it was first employed as an oxygen storage component of three way catalysts formulations,<sup>12-15</sup> due to its ability of rapidly switching its oxidation state under the reaction environment.<sup>16</sup> Latter the application of ceria-based materials in TWCs has been also reviewed by several authors.<sup>17-19</sup> Trovarelli and coworkers did a lot of work on the (redox) chemistry and catalysis of ceria-based materials.<sup>20,21</sup> CeO<sub>2</sub> because of its very interesting electrical properties is also consider as one of the most important electrolyte material in solid oxide fuel cells.<sup>22-30</sup> Understanding of CeO<sub>2</sub> from this point of view has enormously increased its technological important in the last decades and is considered as one of the essential rare earth oxides.

In this context it is necessary to look into a number of unique properties of CeO<sub>2</sub> such as high mechanical strength, oxygen ion conductivity, and oxygen storage capacity<sup>31-33</sup> strong absorption and photoluminescence in the UV-vis range,<sup>34-44</sup> high refractive index, good transmission in visible and infrared regions, strong adhesion, and high stability against

mechanical abrasion, chemical attack and high temperatures, high hardness,<sup>16,45-49</sup> high dielectric constant ( $\epsilon=26$ ) and wide-energy-gap ( $E_g = 5.5$  eV).<sup>50,51</sup> In addition to the above mentioned application there are significant examples where ceria bestowed with such unique properties have widely applied as low-temperature water–gas shift (WGS) reaction,<sup>33,52-59</sup> oxygen sensors,<sup>60-62</sup> oxygen permeation membrane systems,<sup>63-65</sup> solar cells,<sup>66</sup> high temperature ceramics,<sup>67</sup> glass polishing materials,<sup>31,39,68,69</sup> sunscreen materials,<sup>70,71</sup> UV-shielding materials,<sup>72-75</sup> hydrogen storage materials,<sup>76</sup> free radical scavenging activity,<sup>77,78</sup> antioxidant agent,<sup>79,80</sup> and luminescence.<sup>81,82</sup> Beside this major application they are also currently being used for the treatment of environmental pollutants for example remove organic and inorganic pollutants from water. It was reported by several authors that CeO<sub>2</sub> showed excellent removal capacities of Cr(VI) from aqueous solution.<sup>83-86</sup> The removal of organics pollutant such as acid orange 7 from waste water by CeO<sub>2</sub> has also been reported.<sup>87-90</sup> Motivated by both of their excellent properties and extensive applications, much attention has been directed to the controlled synthesis of CeO<sub>2</sub> materials.

## 1.2 Cerium Dioxide (CeO<sub>2</sub>): Structure and Properties

### 1.2.1. Crystal structure of CeO<sub>2</sub>

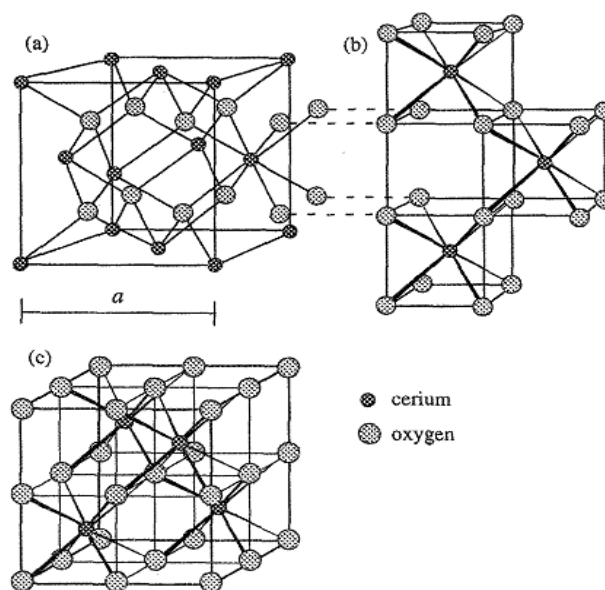


**Fig. 1.1.** The crystal structure of CeO<sub>2</sub>: (a) unit cell as a *ccp* array of cerium atoms. The *ccp* layers are parallel to the [111] planes of the f.c.c. unit cell, (b) and (c) the same structure redrawn as a primitive cubic array of oxygens. [Adapted from ref. 93].

CeO<sub>2</sub> is known to crystallize in the cubic fluorite crystal structure with space group Fm3m over the temperature range from room temperature to the melting point.<sup>91</sup> Figure 1.1 illustrates the structure of the CeO<sub>2</sub>, which consists of a face-centered cubic (f.c.c.) unit cell of cations with anions occupying the octahedral interstitial sites.<sup>91,92</sup> In this structure each cerium cation is coordinated by eight equivalent nearest-neighbor oxygen anions at the corner of a cube, while each oxygen anion is tetrahedrally coordinated by four nearest neighbor cerium cations.<sup>93</sup> This can also be seen as a cubic close-packed array of the metal atoms with oxygens stuffing all the tetrahedral gaps. Figure 1.1 also showed that the eight coordination sites are alternately empty and occupied by a cation which revealed that there are large amount of vacant octahedral gaps in the structure and this become a significant feature when movement of ions through the defect structure is considered. Even after losing considerable amount of oxygen, CeO<sub>2</sub> shows strong tendency to remain in the fluorite-structured lattice, which caused to an elevated number of oxygen vacancies to stabilize the structure.

### 1.2.2. Defect structure of CeO<sub>2</sub>

A perfect crystal is an idealization; there is no such thing in nature. Atom arrangements in real materials do not follow perfect crystalline patterns. There is also a fundamental physical reason why the crystal is imperfect.<sup>94</sup> Ceria in the cubic fluorite structure exhibits a few defects,<sup>91</sup> which influenced it many properties such as luminescence, conductivity, diffusion and many other applications. The crystal lattice defects can be classified by their dimension. The 0-dimensional defects alters the crystal pattern at a single point and affect isolated sites in the crystal structure, hence it's also called point defects. These types of defects are essentially collections of atoms in non-regular lattice positions (interstitials), vacant lattice sites, and occurrence of impurity atoms instead of host position. The 1-dimensional defects are termed dislocations. They are lines along which the crystal pattern is broken. The 2-dimensional defects are the external surface and the grain boundaries along which distinct crystallites are joined together. The 3-dimensional defects alter the crystal pattern over a finite volume and also include large voids or inclusions of second-phase particles. In general, there are two types of defects associated in CeO<sub>2</sub> lattice called intrinsic and extrinsic defects. Intrinsic defects is caused in a crystal due to thermal disorder or can be created by reaction between the solid and the surrounding atmosphere while extrinsic defects are formed by impurities incorporated in hosts during its synthesis, introduction of alliovalent dopants or by the oxidation-reduction process.<sup>93</sup>

### 1.2.2.1. Intrinsic defect

An intrinsic defect is formed if some of the lattice points in a crystal are unoccupied i.e. an atom is missing in the crystal and creating a vacancy, or when an atom occupies an interstitial position between the lattice point. Two most common types of intrinsic defects are observed in ionic materials, Frenkel and Schottky defects. Frenkel defect arise when an atom is displaced from its regular site to an interstitial site and creating a vacancy at the original site. However, it is very unlikely to form oxygen Frenkel defect. The other type of intrinsic defect is Schottky defect which are formed when oppositely charged ions leave their lattice sites and creating vacancies. In this case, vacancy defects must be formed in stoichiometric units, to maintain an overall neutral charge in the lattice. In general when the anion and cation differ significantly in size and the lattice polarization is pronounced leads to Frenkel disorder whereas similar sized anions and cations results in Schottky disorder. In close packed materials an interstitial ion can accommodate in the little lattice space available in the crystal hence Frenkel defect is not favored in these materials, whereas CeO<sub>2</sub> bearing open structure readily exhibit Frenkel defect by forming a defect pair. The three possible intrinsic disorders in stoichiometric CeO<sub>2</sub> can be expressed by using Kröger-Vink notation.<sup>95</sup>

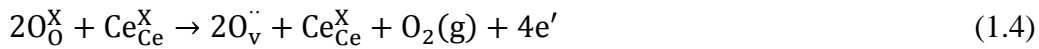


In ceria, the energies of anion Frenkel defects (2.81 eV) are lower than that of cation Frenkel defects (8.86 eV/per defect) and Schottky defects (3.33 eV). Hence, the most likely form of intrinsic disorder is anion Frenkel.

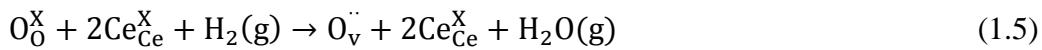
### 1.2.2.2. Extrinsic defects (disorder) in CeO<sub>2</sub>

Extrinsic defects appear in the compounds by impurities from oxidation or reduction of the lattices or by the introduction of aliovalent dopants if they are intentionally added to the material. Essentially, extrinsic disorder includes reaction with gaseous species from the environment that are constituents of the lattice and reaction with species from the environment that are not local to the lattice whereas intrinsic disorder includes only thermally activated defect processes there is no reaction with the environment. If the foreign atoms are added intentionally into the lattice, they are called solutes if they are not added intentionally

are called impurities. The type of the solute can be classified by two categories, a substitutional solute when it occupied in a lattice sites or interstitial solute when it fill in an interstitial site. Since the interstitial sites are relatively small, small atoms are often found in interstitial sites whereas larger atoms are usually substitutional. In ceria the extrinsic defects arises from the oxidation-reduction (redox) processes, which certainly produces nonstoichiometry in lattices. The reduction of ceria in oxygen deficient environment can be described by using so called “Kröger-Vink” notations.



While the process of reduction in the hydrogen rich environments may be represent as,



### 1.2.3. Oxygen storage capacity of CeO<sub>2</sub>

CeO<sub>2</sub> is considered as one of the most important components industrially because of its ability to undergo rapid redox cycles by releasing and storing oxygen,<sup>33,96</sup> consequently creating a high oxygen storage capacity.<sup>97</sup> Oxygen storage capacity (OSC) is defined as the ability of CeO<sub>2</sub> to release oxygen under reducing conditions and absorb oxygen under oxidizing conditions,<sup>98-100</sup> which leads to the comparative ease of oxygen vacancy formation in CeO<sub>2</sub>.<sup>101,102</sup> The formation of oxygen vacancy defects removing the oxygen from CeO<sub>2</sub> lattice, which induces the stoichiometry change from CeO<sub>2</sub> to CeO<sub>2-x</sub>.<sup>91</sup> In the nonstoichiometric ceria it is generally agreed that the oxygen vacancy formation leads to an increase of Ce<sup>3+</sup> fraction in order to compensate the electro-neutrality of the lattice.<sup>103,104</sup> In the fluorite structure of CeO<sub>2</sub> the oxygen atoms which are all in a plane, undergo rapid diffusion as a function of the number of oxygen vacancies<sup>92,105</sup> without changing its structural type.<sup>106</sup> Oxygen vacancies forming process can be described by the following defect reaction



where  $O_{\text{O}}^{\times}$ ,  $V_{\text{O}}^{\cdot\cdot}$  and  $e'$  are oxide ions in the lattice, doubly charged oxygen vacancies, and electrons in the conduction band made up of Ce 4f energy states, respectively.<sup>91</sup> The ability to undergo rapid exchange between the reduced and oxidized states enhances the process of the oxygen vacancy formation. More defects are formed on increasing the Ce<sup>3+</sup> concentration of total cerium.<sup>107</sup>

The remarkable oxygen storage capability of CeO<sub>2</sub> is the consequence of a unique and delicate balance between numerous factors such as structural (phase formation), kinetic (rate of redox of Ce) and textural (presence of surface cerium sites) factors.<sup>108</sup> To learn about the oxygen storage behavior of CeO<sub>2</sub>, it is therefore great important to understand the mechanism of oxygen vacancies formation in CeO<sub>2</sub>. The processes of oxygen vacancy formation involve the Mars-van Krevelen (MvK) mechanism<sup>109,110</sup> where the surface lattice oxygen may act as an oxidant and can be summarized as follows:

- A molecule at the surface accepts an oxygen atom from the ceria surface. A void (vacancy) is created in the surface.
- The vacancy migrates across the surface and eventually accepts an oxygen atom from another molecule. The vacancy becomes annihilated.

According to the mechanism the capability of the material to take up and release oxygen increases with increasing the number and mobility of oxygen vacancies. Hence any chemical modification which improving the number of structural disorder (oxygen vacancies) should provide a material with a higher oxygen storage capacity. The oxygen storage capacity of ceria can be modified by two ways. The first one is by promoting the ceria reduction,<sup>111</sup> and the second one is the doping of foreign metals with other transition or rare-earth elements into the ceria lattice.<sup>112</sup>

### 1.3. Modification of CeO<sub>2</sub>

Despite its wide applicability, pure CeO<sub>2</sub> is associated with some drawbacks like thermal sintering and deactivation of the redox properties, which strongly decreases the oxygen storage capacity and catalytic activity of CeO<sub>2</sub>.<sup>113-115</sup> Therefore, it is very necessary to improve the thermal properties of CeO<sub>2</sub> to avoid sintering and retention of its high surface area at high temperatures for various applications. Thermal stability of CeO<sub>2</sub> and doped CeO<sub>2</sub> was investigated in detail by Pijolat *et al.*<sup>116</sup> However, the drawbacks of pure CeO<sub>2</sub> have been eliminated by doping with different cations which significantly stabilize the CeO<sub>2</sub> against sintering and enhance the redox properties and chemical activity of pure CeO<sub>2</sub>. Ozawa *et al.* reported that among many different cations, the incorporation of Zr into the CeO<sub>2</sub> lattice is very effective in the inhibition of the sintering.<sup>117</sup> Recently the textural, structural, morphological and catalytic activity of nanosized CeO<sub>2</sub>-MO<sub>x</sub> (M = Mg<sup>2+</sup>, Al<sup>3+</sup>, and Si<sup>4+</sup>)

mixed oxides have been investigated.<sup>118</sup> They suggested that alumina could act as a very effective surface stabilizer and CeO<sub>2</sub>-Al<sub>2</sub>O<sub>3</sub> mixed oxides exhibited high surface area among these mixed oxides. CeO<sub>2</sub>-Al<sub>2</sub>O<sub>3</sub> mixed oxide also showed highest catalytic activity for CO oxidation which might be due to its excellent textural/structural properties, good homogeneity, and redox abilities.<sup>118</sup> Tian *et al.* observed that doping of Fe (or Co, Ni) in CeO<sub>2</sub> steep absorption peaks at lower energy ranging from 1.0 eV to 2.0 eV as compared with the undoped CeO<sub>2</sub>, which could be used for visible light absorption applications.<sup>119</sup> It is reported that OSC and redox properties of CeO<sub>2</sub> can be significantly improved by doping with transition metals.<sup>120-126</sup> Incorporation of transition metals in CeO<sub>2</sub> lattice also provide ultra-high thermal stability, which is necessary to meet the requirements of high-temperature catalytic reactions.<sup>127-128</sup> Ce<sub>1-x</sub>M<sub>x</sub>O<sub>2</sub> solid solution (M = Ti, Zr, and Hf) has been found to exhibit high catalytic activity for hydrogen reduction and ethanol reforming reactions, which make these nanomaterials efficient candidate for applications in catalysis and solid oxide fuel cells.<sup>129</sup> Kehoe *et al.* reported that the doping of CeO<sub>2</sub> with divalent noble metal ions lead to improved its reducibility and enhance the OSC.<sup>130</sup> Transition and rare earth metal cations such as Mn, Fe, Zr, Pr, La, and Sm were doped into the CeO<sub>2</sub> lattice. Very recently, transition-metals, like Cu, Co, Ni, Mn and Fe, were doped into CeO<sub>2</sub> microspheres by Zhou *et al.* which exhibited high catalytic activity and good recycling stability, as well as easy recovery.<sup>131</sup>

It has been observed that the ionic conductivity of pure CeO<sub>2</sub> is very low, incorporation of trivalent lanthanide into the CeO<sub>2</sub> lattice lead to the formation of oxygen vacancies through direct substitution of Ce<sup>4+</sup> by Ln<sup>3+</sup> as follows<sup>132-136</sup> which considerably improves its ionic conductivity.



In the past decade due to the high ionic conductivity, ceria-based mixed oxides with trivalent rare-earth such as La, Pr, Sm, Gd, Tb, and Er have been extensively studied as electrolytes in the field of catalysis and solid oxide fuel cells.<sup>33,137-139</sup> The catalytic activity and ionic conductivity of CeO<sub>2</sub> can be improved by doping with Gd<sub>2</sub>O<sub>3</sub>, Sm<sub>2</sub>O<sub>3</sub>, or La<sub>2</sub>O<sub>3</sub>,<sup>23, 140-144</sup> the increased ionic conductivity of Gd- and Sm-doped CeO<sub>2</sub> may be attributable due to the stabilization of the cubic fluorite structure with oxygen vacancies.<sup>140</sup>



Among the CeO<sub>2</sub> electrolytes Sm<sup>3+</sup> doped CeO<sub>2</sub> (SDC) at fixed doping levels show highest ionic conductivity<sup>23,145,146</sup> as well as the highest stability against reduction.<sup>23,147</sup> because Ce<sup>4+</sup> and Sm<sup>3+</sup> have similar ionic radii and electronegativity values, which also facilitated the formation of Ce–Sm–O solid solutions.<sup>148</sup> Therefore, it is proposed in some literatures that when the dopant ion has a radius closest to the critical radius, the doped CeO<sub>2</sub> will have the highest electrical conductivity.<sup>23,32,149</sup> Hence it is important to consider the ionic radius of dopant when selecting dopants to improve the OSC of any material. Sm<sup>3+</sup> is the best dopant for CeO<sub>2</sub> in this regard. Moreover, the ionic radius of the trivalent europium (0.1066 nm)<sup>150</sup> is also close to that of the Ce<sup>4+</sup> (0.097 nm), which make it a convenient dopant for ceria and allows it for an extensive solubility with the ceria lattice.<sup>151,152</sup> Additionally, the Eu<sup>3+</sup>/Eu<sup>2+</sup> redox pair has a potential of about 0.36 V, which is expected to promote the formation and stabilization of oxygen vacancies for low Eu<sup>3+</sup>/Ce atomic ratios.<sup>152</sup> This property resulted with high oxygen ion conductivity.<sup>153</sup>

Apart from this, photoluminescence is one of the most interesting features of the lanthanide ions. Since the 4f electrons of lanthanide ions are well shielded by the filled 5s<sup>2</sup>5p<sup>6</sup> sub-shells, the emission transitions yield line-like emission, which provide a high color purity of the emitted light.<sup>154</sup> The color of the emitted light depends on the lanthanide ion. For instance, Sm<sup>3+</sup> emit orange light, Eu<sup>3+</sup> red light, Tm<sup>3+</sup> blue light and Tb<sup>3+</sup> green light.<sup>155</sup> This feature makes rare earth doped oxide nanoparticles the best phosphor material in comparison with other inorganic metal oxide nanomaterials.<sup>155-157</sup> It was found that the undoped CeO<sub>2</sub> nanocrystals exhibits weak luminescence since Ce<sup>4+</sup> ions have no 4f electron, which could be remarkably enhanced by doping with rare earth ions required for imaging. CeO<sub>2</sub> can be advantageous of choosing as a one of the best luminescence host material for other rare earth ions due to its strong light absorption through O<sup>2-</sup>→Ce<sup>4+</sup> charge transfer band and subsequent energy transfer from host to the dopant. After the energy transfer is achieved from the CT state of CeO<sub>2</sub> to the doped rare-earth ions, the characteristic emissions of rare-earth ions are expected.<sup>158,159</sup> CeO<sub>2</sub> serve as one of the best host materials for Sm and Eu due to their comparable ionic radius as mentioned earlier. Sm<sup>3+</sup> doped CeO<sub>2</sub> nanoparticles are very important in developing new luminescence devices in orange and red regions.<sup>160</sup> The great interest of Eu<sup>3+</sup> luminescence is because of its major red emission. From which a wide spectrum of colors can be generated by appropriate mixing since it is one of the three primary

colors (namely, red, blue, and green). This strategy is in fact used for white light generation as well.<sup>161</sup> For this reason,  $\text{Eu}^{3+}$  has been thoroughly investigated as a luminescent activator in many host lattices.<sup>162,163</sup> Under such a hypothesis, many  $\text{CeO}_2:\text{RE}$  (RE= Sm, Eu) materials have already been investigated to exhibit excellent luminescent properties.<sup>151, 153, 159-161, 164-186</sup> Hence the incorporation of lanthanide ion in to the ceria lattice leads to extend its traditional applications to novel fields such as phosphors, bioimaging, and therapy, medical diagnosis, electroluminescence, optical markers and even laser materials, phosphors, fluorescent tubes, etc.

#### 1.4. Introduction of nanomaterials

Nanomaterials are such class of functional materials which having at least one dimension less than 100 nanometers.<sup>187</sup> Although nanotechnology is a new area of research, nanomaterials are known to be used for centuries. For example the Lycurgus cup a glass cup of 4<sup>th</sup> century AD,<sup>188</sup> represents one of the most outstanding example of the uses of nanomaterials in earlier days to dye the glass articles, which appears green in reflected light and red in transmitted light (**Fig. 1.2**). This effect is due to the presence of Au and Ag nanocrystals in the walls of the cup. This renewed interest in nanomaterials research started after the well-known lecture by the Nobel laureate Richard. P. Feynman in 1959.<sup>189</sup> He stated, “there is a plenty of room at the bottom” and indicated the vast potential of materials having small dimensions.



**Fig. 1.2.** The Lycurgus cup appears (a) green in reflected light, and (b) red in transmitted light and this cup is preserved in the British museum in London.

Nanomaterials can be classified into four different classes according to Siegel,<sup>190</sup> zero dimensional, one dimensional, two dimensional and three dimensional nanostructures.

**Zero dimensional (0-D):** These nanomaterials have nano-dimensions in all the three directions. Quantum dots are the perfect example of this kind of nanoparticles.

**One dimensional (1-D):** One dimension of the nanostructure will be outside the nanometer range. These include nanowires, nanorods, and nanotubes.

**Two dimensional (2-D):** In this type of nanomaterials, two dimensions are outside the nanometer range. Nano sheet, nano disk, nano flakes, ribbons and plates are few examples of this kind of materials.

**Three Dimensional (3-D):** All dimensions of these are outside the nano meter range. Materials in nanodimension exhibits exceptional properties which are caused by quantum mechanics, small grain sizes, large grain boundary environments, large surface area, interfacial volume fraction, high surface to volume ratio and other phenomena. Physical, chemical, optical, mechanical, electrical and magnetic properties of the nanomaterials are significantly different with respect to their bulk counterpart. As for example  $\text{Fe}_2\text{O}_3$ , maghemite; in it bulk form due to magnetic properties used in disc drives as a recording medium. However, in nanoparticulate form, these properties become “superparamagnetic”, and as a result has led to new applications in MRI. Optical properties may change also as mention above. An example of this is titanium dioxide in opaque in macroparticle form but transparent in nanoparticle form. Properties of the nanoparticles can be controlled by engineering the size, morphology and composition of the particles. Various effects which control the properties of nanostructured materials are discussed below:<sup>191</sup>

1. **Size effects:** Size effects result if the crystallite size of the microstructure becomes comparable with the critical length scales of physical phenomena (e.g. the mean free paths of electrons or phonons, a coherency length, a screening length, etc.) which modify the mechanical and optical properties.
2. **Change of the dimensionality of the system:** If two or one dimension of the building blocks of a nanostructured material which possess thin needle-shaped or flat two dimensional crystallites are comparable with the length scale of a physical

phenomenon. Then it becomes a two- or one-dimensional system with respect to this phenomenon.

3. **Changes of the atomic structure:** Atomic structures changes if a high density of incoherent interfaces or other lattice defects such as dislocations, vacancies, etc. are incorporated. As a consequence a defect associate solid differs structurally from a defect-free solid with the same chemical composition.
4. **Alloying of components:** Large surface energy in small particles facilitates alloying or mixing even in immiscible solids.
5. **Temperature effects:** The microstructures of nanostructured materials are seem to be affected by one or both of the following two types of processes.
  - i. **Grain growth:** Grain growth in nanostructured materials is primarily driven by the excess energy stored in the grain or interphase boundaries. Grain growth studies of various nanostructured materials have been performed by using DSC, X-ray diffraction, TEM, and Raman spectroscopy. For reducing the grain growth several approaches have been proposed such as to slow down the growth kinetics by reducing the driving force (the grain boundary free energy) or the grain boundary mobility.
  - ii. **Temperature-induced variations of the atomic structure:** Materials with nanometer-sized microstructures may be classified according to their free energy into equilibrium nanostructured materials and nanostructured materials far away from thermodynamic equilibrium. Properties altered by grain size include lowered thermal conductivity, increased hardness, and even low temperature ductility in some ceramics.

Nanocrystalline materials are characterized by their small crystallite size in the range of 2-20 nm, which are separated by their high angle grain or interface boundaries and, consequently, by their large volume fraction of disordered region of grain boundaries. In so small particles, usually defined as nanoparticles, 60-20 % of the total atoms from the surface of the particles. The fraction of the surface atoms ( $\phi$ ) is a strong function of size and morphology of the particle. Siegel performed a systematic analysis of  $\phi$  as a function of average particle diameter  $\langle D \rangle$  with different thickness for grain boundary. According to the special surface and  $\sigma$  the

surface energy density, the surface atoms in an isolated particle of size of a nanometer scale in general assume

1. A lower atomic density,
2. A lower coordination number,
3. A lower symmetry, and
4. An enhanced interatomic distance than those for the core atoms.

#### ❖ **Important characteristics and applications of nanomaterials**

Nanomaterials are of particular interest in recent year because at this scale unique optical, magnetic, electrical, and other properties emerge. As for example<sup>192</sup>

- (i) Nanostructured materials are more ductile at elevated temperatures as compared to the coarse-grained materials.
- (ii) The shape and size of nanomaterials are important parameters to control the properties of nanostructured materials. In recent year a great research interest have been devoted to develop nanowire, nanotube, nanodisc etc. to meet the desired characteristics and hence applications.
- (iii) Nanosized metallic powders have been used for the production of dense parts and porous coatings. Cold welding properties combined with the ductility make them suitable for metal-metal bonding especially in the electronic industry.
- (iv) Nanostructured semiconductors are known to show various non-linear optical properties which may lead to special properties.
- (v) Very small particles have special atomic structures with discrete electronic states, which give rise to special properties in addition to the superparamagnetism behavior.
- (vi) Nanostructured metal oxide can be served as heterogeneous catalysts which offer substantial advantages concerning activity, selectivity and lifetime in chemical transformations and electrocatalysis (fuel cells).

Nanomaterials offers an extremely broad range of potential applications such as catalysts, sensors, semiconductor devices with a wide band gap-energy, insulators of enhanced band gap, tunable lasers of enhanced power, permanent magnets, information storage systems, magnetic toner in xerography, ferrofluids, contrast agents in magnetic resonance imaging, magneto optic or magneto resistance devices so on.

### 1.5. Synthetic approaches to ceria based materials

An essential aspect of the preparation of ceria and ceria based oxides is the high purity of the phase, high surface area, narrow particle size, and the good chemical homogeneity. A wide variety of processes have been developed to synthesize these materials by both conventional and non-conventional way. In general, ceria-based oxides are fabricated by the decomposition of cerium (III and/or IV) inorganic salts, such as hydroxide, nitrate, halides, sulfates, carbonates, formates, oxalates, acetates, and citrates.<sup>193,194</sup> A number of synthesis methods can be used to prepare CeO<sub>2</sub> nanomaterials, such as precipitation method,<sup>195-204</sup> sol-gel method,<sup>205-207</sup> hydrothermal or solvothermal method,<sup>208-211</sup> surfactant-assisted method,<sup>212-214</sup> electrochemical deposition,<sup>215-219</sup> and so on. Each method has its own merit and demerit to fabricate the nanopowder with respect to phase purity, uniform morphology desirable composition and tunable surfaces. However, from the view point of industrial production of process needs to be economically feasible and should not be more complex. In this context, the chemical precipitation is a simple and easily-operable method, which involves low cost, high yield, good reproducibility and simple apparatus hence highly suitable for industrial application. In chemical precipitation method the formation of ceria nanopowder is carried out by applying alkali solution (NH<sub>4</sub>OH, NaOH and (NH<sub>2</sub>)<sub>2</sub>-H<sub>2</sub>O) or oxalic acid<sup>193, 220-222</sup> into the aqueous solution of inorganic cerium salt (Ce(NO<sub>3</sub>)<sub>3</sub>, CeCl<sub>3</sub>, CeSO<sub>4</sub>, and (NH<sub>4</sub>)<sub>2</sub>Ce(NO<sub>3</sub>)<sub>6</sub>) followed by the calcination of precipitates hydroxide or oxalate gel. This method can produce high quality nano-size powders and influence the morphology of the product by an appropriate monitoring of some parameters, like the concentration of the aqueous solution, the pH value of the medium, the nature of the precipitating agent, the reaction temperature and the aging time.<sup>195-204,223</sup> The use of surfactant-assisted routes has also gained lot of attention recently for the synthesis of ceria and ceria based oxides with high specific surface area and defined porosity.

In this study, a surfactant mediated chemical precipitation technique has been adopted for the preparation of ultrafine, monocrystalline, high surface area ceria and ceria based mixed oxide by using ceric ammonium nitrate as inorganic precursors followed by conventional refluxing method. A comparison with the microwave reflux method is also reported. The potential advantages of microwave reflux over conventional reflux method are rapid heating,

penetrating radiation which leads to high-efficiency and very rapid formation of nanoparticles with narrow size distribution, more uniform microstructure, and slight agglomeration.

In particular nanoporous materials have attracted intense attention because many of the major applications in various fields such as adsorption, catalysis, separation, sensors and energy storage are closely related to the pore structure. This class of materials offer uniform pore size distributions, ordered pore networks, high surface areas, excellent permeability, and better material stability. Many methods have been reported for the preparation of nanoporous materials with precisely controllable pore structure. The most common methods are template-based ones, including soft and hard template methods by using organic surfactants or solid templates, respectively. However, it is still remain a challenge to develop nanoporous materials with well-defined pore sizes, large surface areas for industrial, scientific, and domestic applications.

### **1.6. Porous materials and their classification**

Porous compounds or porous materials possess both the solid network matrix and continuous ordered pores or voids as their name implies. The pores of the material can be filled with liquid or gases. Porous structure could be described by means of various parameters among which pore shape and pore size are most important. When the orders of the pore or voids are of  $\approx 1-100$  nm, it's called nanoporous materials. Generally, porous materials can be classified into two types, when the pores connect to the outside of the materials it is called open pore, whereas closed pores are isolated from the outside. According to IUPAC convention, with respect to the pore size they can be further classified into three classes; (i) microporous, having pore size less than 2 nm, (ii) macroporous, having pore size greater than 50 nm, and (iii) mesoporous having pore size in between micropore and macropore i.e. typically between 2 and 50 nm.<sup>224,225</sup> In comparison with microporous and macroporous materials, mesoporous materials are of specific interest owing to their many unique characteristics such as high stability, surface areas, tunable porosity, alternative pore shape, approximate pore diameters and large pore volumes,<sup>226-234</sup> which make them a prominent candidates for wide variety of applications in the field of adsorbents, catalysts, ion-exchangers, etc.<sup>235-244</sup>

### 1.7. Synthesis of mesoporous materials

Since the scientists of Mobil oil corporation (USA) first reported a novel family of ordered mesoporous silica materials MCM41 in 1992,<sup>245</sup> significant attentions has been devoted to the synthesis of mesoporous materials. They employed cetyltrimethylammonium bromide, as a structure-directing agent for the synthesis of MCM 41 through supramolecular templating pathways. This materials exhibits very large surface area ( $>1000 \text{ m}^2/\text{g}$ ) and ordered mesopores which endow them with potential applications in the field of catalysis and adsorption. Their discovery not only developed a novel family of mesoporous materials but also provide a detailed synthesis strategy for the formation of mesopore. A major problem of these mesoporous siliceous materials are their chemical inertness, low mechanical strength, does not possess redox properties which make them inactive in electrochemistry and catalysis.<sup>246</sup> On the other hand in contrast to silica-based mesoporous materials nonsiliceous transition mesoporous materials exhibit many interesting properties due to their d-shell electrons, ordered pore networks, variable oxidation states and internal surfaces with redox properties.<sup>246</sup> These characters, therefore, pave the way for valuable application in catalysis, adsorption, energy conversion and storage, sensing, etc.<sup>247-253</sup> Thus the fabrication of ordered mesoporous nonsiliceous materials received tremendous interest in last decade. Among the mesoporous non-siliceous materials, mesoporous metal oxides have attracted substantial interest because of their broad functional properties and their potential industrial applications.

**Table 1.1** Non-siliceous mesoporous oxides prepared by soft-templating methods (adopted from ref. 264).

Product	Template	Structure	Pore size (nm)	Surface area ( $\text{m}^2 \text{g}^{-1}$ )	Ref.
$\text{Al}_2\text{O}_3$	SDS		0.8-6.0	112-810	254
$\text{TiO}_2$	Dodecyl sulphate	p6mm	2.7	128	255
$\text{CeO}_2$	P123	Disorder	3.5	86–150	257, 258
$\text{Eu}_2\text{O}_3$	KLE	Im3m	10–13		259
$\text{Gd}_2\text{O}_3$	SDS	p6mm	2.5–3.0	287	260
$\text{Sm}_2\text{O}_3$	Hexadecyl amine	Ia3d	2.4	122	261
$\text{Tb}_2\text{O}_3$	SDS	p6mm	2.5–3.0	348	260



Numerous methodologies have been developed to construct mesoporous materials. The concept of templating provided a simple, reliable and the most obvious approach for the direct and spontaneous formation of ordered mesoporous structures. The templating methodology has been considered the principal synthetic route for this class of materials and successfully applied to a diverse range of inorganic compositions. The use of template molecules to synthesize ordered mesoporous materials have attracted great interest in the last few decades. A Template is briefly defined as a material that can help to generate or design porosity in the matrix and act as structure directing agent (SDA).<sup>262,263</sup> The template induced route can be classified into two types. The first one is termed as soft template route or the cooperative self-assembly of inorganic precursors and amphiphilic surfactants. Surfactants and the block co-polymer are commonly used as “soft” templates. A large variety of metal oxides including lanthanides have been synthesized through Soft-templating methods are summarized in Table 1.1.<sup>264</sup> The second route for mesoporous oxide synthesis is hard templating or nanocasting method. Silica microsphere, polystyrene beads are commonly used as hard templates to create porosity within the matrix.<sup>263</sup> In this nanocasting approach pore system of the template is replicated as a “negative image”. This synthesis strategy is suitable for a wide variety of materials which cannot be obtained by soft-templating processes. It was widely used to prepare many interesting metal oxides, summarized in Table 1.2.<sup>264</sup> Both the templating methods are discussed here elaborately.

**Table 1.2.** Non-siliceous mesoporous oxides prepared by hard-templating methods (Adopted from ref. 264).

Product	Template	Structure	Pore size (nm)	Pore volume (cm <sup>3</sup> g <sup>-1</sup> )	Surface area (m <sup>2</sup> g <sup>-1</sup> )	Ref.
Al <sub>2</sub> O <sub>3</sub>	CMK-8	Ia3d	6.9	0.81	303	265
TiO <sub>2</sub>	SBA-15	p6mm	2.7	0.30	258	266
ZrO <sub>2</sub>	SBA-15	p6mm	2.9, 27	0.57	220	267
CeO <sub>2</sub>	SBA-15	p6mm	3.3–3.8	0.23–0.37	101–164	268

### 1.7.1. Soft-matter templating

Soft templates such as supramolecular self-assemblies offer innovative strategies for the preparation of mesoporous materials. Typically, in soft-templating route the supramolecular templates molecule initially formed a self-assembly in the synthesis media, the inorganic precursors then arrange themselves in regular fashion around the self-assembly to generate well-ordered inorganic-organic composite solid this method usually include three steps,<sup>263</sup> first, the formation surfactant self-assembly, second is the organization of inorganic precursor around this surfactant self-assembly, and third is the subsequent removal of the organic template to create the mesostructured materials. The formation process basically involve two different mechanism,<sup>238,239,244,269,270</sup> either by cooperative self-assembly (CSA) mechanism, which involved a simultaneous aggregation of self-assembled template molecule along with pre added inorganic species or by true liquid crystal template (TLCT) mechanism, in which the concentration of the surfactant is so high that under the prevailing conditions (temperature, pH) a lyotropic liquid-crystalline phase is formed in the absences of the inorganic precursor materials. However, to generate well developed mesopores it is essential to remove the template from this inorganic–organic nanocomposite. Sintering in aerobic atmosphere is the most widely used method applied to remove the organic template completely. But this methods leads to loss of porosity for air sensitive materials. This problem was overcome by using solvent extraction method, which very effectively eliminate the surfactant without disturbing the structure. Generally, solvents like tetra hydro furan, ethanol, dilute hydrochloride acid, ammonium acetate or ethylene diammine are used for this purpose.<sup>271,272</sup>

Over the past decade a rich variety of templates have been employed for the synthesis of mesostructured materials, which helps to create porosity in the matrix and acts as structure directing agent (SDA). Surfactants, dendrimer, and block copolymers are commonly employed as organic templates to obtain mesoporous materials via soft templating method. Surfactants are amphiphilic molecule composed of chemically bonded non polar hydrophobic ‘tail’ and a polar hydrophilic ‘head’ group. Surfactant, also called surface-active agent as because these molecules disrupts the cohesive energy at the surface and thus reduce the surface tension. When the concentration of the amphiphilic molecule reaching the critical micelle concentration (CMC) form aggregates called micelles.<sup>273</sup> Normal micelle in aqueous

solution arranges themselves such a way that the hydrophilic “head” of the surfactant remains in contact with surrounding solvent whereas the hydrophobic “tail” stays away from the solvent. In non-polar solvent amphiphilic molecules behave distinctly and form inverse micelles. In such cases hydrocarbon tails are oriented outwards the solvent, while the polar heads groups pointing toward the interior of the aggregate. The structure or geometry of the micelle are generally spherical, but the size and shape of the surfactant micelle may varies of different patterns such as cylindrical, lamellar, bilayer and so on<sup>274</sup> (as Shown in Fig. 1.3) depending upon the various factors like nature of template molecule, surfactant concentration, temperature, pH and ionic strength of the reaction media temperature. Hence, this amphiphiles molecule controls both the size and shape of the mesoporous materials.

Since the "tail" of most surfactants molecules are fairly similar, most commonly, they are classified according to their polar head groups. Depending upon their polar head group surfactant molecule can be classified into four types.

- (a) **Cationic:** If the head group of the surfactant molecule bears a positive charge it is called cationic surfactant. A large portion of cationic surfactant is belong to the amine salts and alkyl quaternary ammonium salts. The common examples are cetyltrimethylammonium bromide, dodecyl amine, N-dodecyl pyridinium chloride cetylpyridinium chloride etc. They are dissociated in water into an amphiphilic cation and an anion most often like halide.
- (b) **Anionic:** Anionic surfactants contain negatively charged head group and dissociates in water into an amphiphilic anion, and a cation. The anionic functional groups at their head are belong to sulfate, sulfonate, carboxylates, and phosphate. Few common examples are sodium dodecyl sulphate (SDS), sodium dodecyl benzene sulphonate etc.
- (c) **Nonionic:** The head group of nonionic surfactant possesses no charge hence they does not ionize in water. Many long chain alcohols exhibit this type of properties such as fatty alcohols, cetyl alcohol, stearyl alcohol, and cetostearyl alcohol. Common examples of non-ionic surfactants are pluronic P123, F127 etc.
- (d) **Zwitterion:** When the single surfactant molecule head group contains both anionic and cationic charge it is called zwitterion. Usually they behaves as cationic at low pH and anionic at high pH. However, there are also some zwitterion surfactants which are

insensitive towards pH. Few commonly used these type of surfactants are betaines, sulphobetaines, natural substances such as amino acids and phospholipids etc.

The formation of the mesostructured material is mainly governed by electrostatic interactions between the surfactant headgroup and inorganic precursor shown in Fig. 1.4.<sup>252</sup> An essential condition for this method is that a cationic surfactants are used as the SDA to ensure inclusion of the structure director in the negatively charged inorganic species, and vice versa. Three types of probable interactions will take place at the organic-inorganic interface i) ionic interactions, ii) hydrogen bonding and, iii) covalent bonds which are strongly dependent on reaction conditions, especially pH.<sup>275</sup>

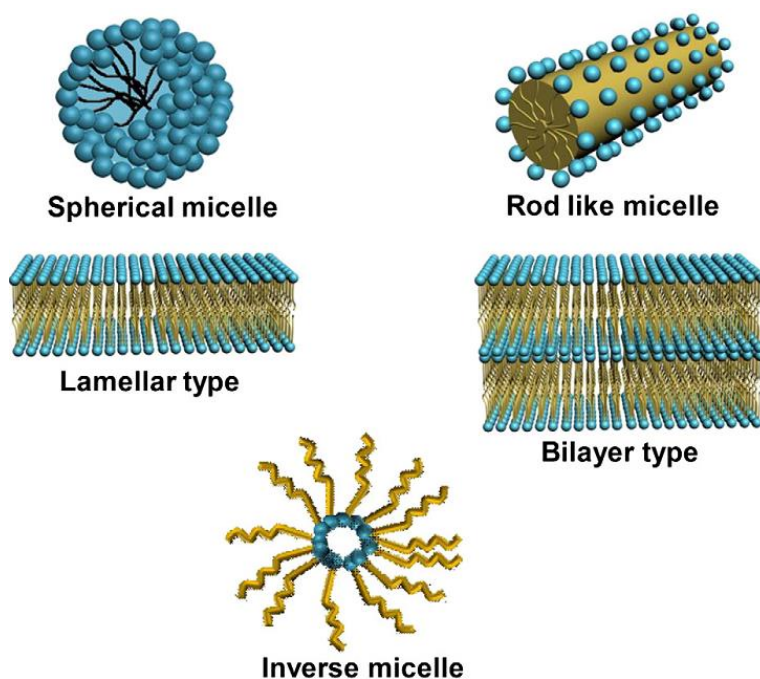


**Fig. 1.3.** Different types of surfactant structures (adopted from ref. 263).

These interactions mechanism are well documented by Huo *et al.*<sup>247,276</sup> They suggest six different synthesis pathways in their “charge matching” model schematized in Fig. 1.4, which are  $S^+I^-$ ,  $S^-I^+$ ,  $S^+X^-I^+$ ,  $S^-M^+I^-$ ,  $S^0I^0$  and  $N^0I^0$  where S is the surfactant, I is the inorganic precursors and X is the counter ion, M is the metal cation,  $S^0$  is the neutral amine, and  $N^0$  is non-ionic template present in the synthesis media. Among this six synthesis pathways  $S^+I^-$ ,  $S^-I^+$ , has been consider as direct synthesis route whereas two other routes,  $S^+X^-I^+$ ,  $S^-M^+I^-$  considered to be indirect. According to Huo *et al.* under basic conditions cationic surfactants are used as the SDA with the anionic inorganic species and the synthetic pathway is denoted

by  $S^+I^-$ . Conversely under acidic conditions the preparation can also take place with the interaction of anionic surfactant ( $S^-$ ) and positive charge bearing inorganic species via  $S^-I^+$  approach. When the inorganic precursors and surfactant molecule possess the similar charge a mediator ion  $X^-$  or  $M^+$  must be added opposite charge to that of the surfactant head group as charge compensating species to ensure the interaction between the organic and inorganic species. Meanwhile the non-ionic surfactant can also be used as templates for the attractive interactions with metal precursor through hydrogen bonding or covalent bonding and giving birth to the neutral path. Table 1.3 gives various examples of mesostructured inorganic materials obtained following the above mentioned paths.

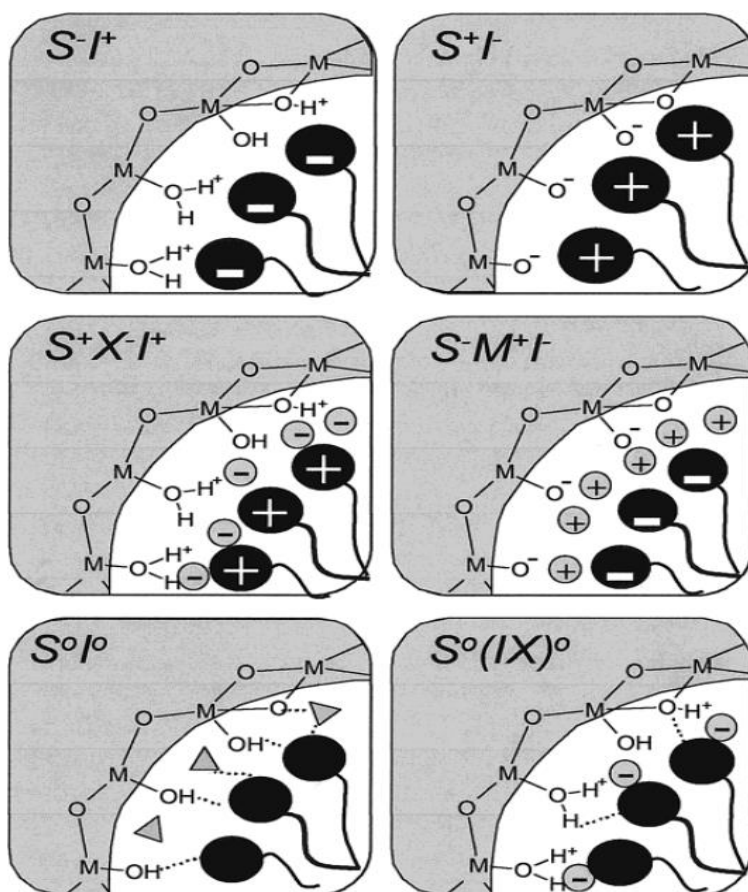


**Fig. 1.4.** Schematic representation of the different types of silica-surfactant interfaces (adapted from ref. 252).

**Table 1.3.** Mesostructured materials with different interactions between the surfactant and the inorganic framework.

Surfactant type	Interaction pathway	Interaction type	Examples	Ref.
Cationic $S^+$	Electrostatic interaction	$S^+I^-$	Tungsten oxide	276, 277
		$S^+XI^-$	Titanium oxide	278
Anionic $S^-$	Electrostatic interaction	$SI^+$	Lead oxide	276
		$S^-M^+I^-$	Zinc oxide	276
Neutral $S^0/N^0$	H-bonding	$S^0I^0$	Zirconium oxide	279
		$N^0I^0$	Silica MSU-X	280

However, the preparation of porous crystals with larger pores was the keen requirement for industrial necessities. Hence control of the pore size of resulting materials is a vital issue as it is directly linked to their applications. The formation of pore and its size mainly depend on shape of the surfactant micelle. Hence by changing the lengths of hydrophobic chains of the surfactant it could be possible to control the pore size.<sup>281</sup> Various strategies are available for controlling the shape and size of the pore with this core idea in mind by changing the size and volume of micelles. In general increasing the tail length of surfactant leads to increase in pore size.<sup>282</sup> The use of nonpolar organic swelling agents such as aromatic hydrocarbons, long-chain amines, or alkanes with cationic surfactant can enlarge the pore size up to ~10 nm. The pore size can be also enhanced by using the larger surfactant such as block copolymer. Mixture of surfactants with different chain lengths can also be used to tune finely pore size.

Due to several advantages soft-template approaches have been widely exploited to obtain tailored mesostructured materials. The most obvious advantage of this method are the relatively simple and effective synthesis approach, low production cost, mild experimental conditions, straightforward implementation and the capability of synthesize different materials with various morphologies.<sup>283,284</sup> However despite its numerous advantage also have some disadvantages.<sup>283,285</sup> The main disadvantages are difficult to control the hydrolysis and polymerization of the transition metal ion, the obtained product possesses amorphous or semi-crystalline walls and poor thermal stability, It's difficult to maintain good dispersity and controlled the particle size and shell thickness over broad range. The large scale production is

also difficult by this route as it need a large amount of surfactant. Furthermore it's also quite difficult to remove the complete template molecule.

### 1.7.2. Hard templating methods

In hard templating methods a porous solid like silica, zeolites, polystyrene beads, Porous alumina membranes and polymer latex colloids are used as the template instead of surfactant. Hard templating method, are also known as exotemplating or nanocasting involve filling of the inorganic precursor inside the pores system of template molecule as a negative image and in the and finally removal of the template by leaching with HF or NaOH solution or by high temperature to create resultant materials. Hard template method have several advantages<sup>283, 286</sup> such as easy tunability of pore sizes and pore wall, the replication process is easy to scale up, synthesis using mesoporous silica templates result good thermal stability mesoporous metal oxides compound even at relatively high temperatures.<sup>283</sup> The desired mesostructures can be produced by choosing appropriate templates which make this route suitable for synthesis of a wide variety of materials.<sup>264</sup> On the other hand this synthesis strategy is associated with few drawbacks also.<sup>283</sup> In a hard templating process complete filling of the silica template is very difficult as there occurred some interactions between the silica template and metal ion precursor, through hydrogen bonding, Coulombic interactions, coordinating interaction, or van der Waals.<sup>283, 287, 288</sup> This synthetic method is highly expensive, complicated and unfit able for large scale industrial production as it involve multiple preparation procedures. Moreover, the template removal processes is tedious and often destroys or disorder the formed nanostructures as it involves the use of strong acids, bases, or high-temperature calcination.

## 1.8. Mesoporous CeO<sub>2</sub> and CeO<sub>2</sub> based materials

Among these mesoporous materials mesoporous ceria (CeO<sub>2</sub>), is of particular interest because of their unique structural and thermal properties, such as high surface area, uniform pore size distribution, special interfaces, and well-defined pore topology along with high oxygen storage capacity and facile Ce<sup>3+</sup>↔Ce<sup>4+</sup> redox cycle. The high surface area is helpful for the high metal dispersion, and the pore channels help in the adsorption and desorption of reactants and increase the effectiveness of the contact between adsorbent and adsorbate. Thus, CeO<sub>2</sub> mesoporous spheres with narrow pore distributions, high surface areas, well-defined

morphologies, and rigid frameworks should have great advantages in confined-space and environmental catalysis. Hence much effort have been directed for the construction of CeO<sub>2</sub> mesoporous materials, the most common approach is the use of hard or soft sacrificial templates. In addition the formation of CeO<sub>2</sub> mesostructured without using any surfactant or template has been also reported.

Terribile *et al.*<sup>289</sup> first time reported the synthesis of high surface area mesoporous ceria by a surfactant assisted route employing cetyltrimethylammonium bromide (C16), myristyltrimethylammonium bromide (C14), or octadecyltrimethylammonium bromide (C18) as cationic surfactant and CeCl<sub>3</sub>·7H<sub>2</sub>O as inorganic precursors. They noticed that surfactant assisted route not only enhance the surface area but also allow the upper temperature limit to be raised to 900°C. Xu *et al.*<sup>290</sup> prepared a new mesoporous ceria catalyst with high surface area of (109-182 m<sup>2</sup>g<sup>-1</sup>) and tunable pore sizes of 5.1–5.4 nm through a soft-templating method using cerium nitrate as a precursor and cetyltrimethylammonium bromide as a template. Pavasupree *et al.*<sup>291</sup> elucidate the formation of mesoporous CeO<sub>2</sub> nanopowder by a modified sol–gel method using laurylamine hydrochloride (LAHC) as surfactant and Ce(O(CH<sub>2</sub>)<sub>3</sub>CH<sub>3</sub>)<sub>4</sub> as inorganic precursors. The BET surface area and the pore volume of the obtained nanopowder were found to be 73 m<sup>2</sup> g<sup>-1</sup> and 0.113 cm<sup>3</sup> g<sup>-1</sup>, respectively. Mesoporous CeO<sub>2</sub> with high surface area was prepared by Yuejnan *et al.*<sup>292</sup> using CTAB as surfactant, Ce(NO<sub>3</sub>)<sub>3</sub> as the precursors and NaOH as the precipitating agent. It was found that the obtained nano CeO<sub>2</sub> after calcination at 400 °c resulted in high-surface 200 m<sup>2</sup> g<sup>-1</sup> and showed good thermal stability. Flowerlike CeO<sub>2</sub> microspheres obtained via the glucose/acrylic acid system exhibits high surface area, large pore volume and narrow pore size distribution of 211 m<sup>2</sup>g<sup>-1</sup>, 0.32 cm<sup>3</sup>g<sup>-1</sup> and 3 nm, respectively. Liang *et al.*<sup>293</sup> have developed an effective method for the fabrication of monodisperse CeO<sub>2</sub> mesoporous spheres using simple inorganic salt Ce(NO<sub>3</sub>)<sub>3</sub>·6H<sub>2</sub>O and organic acids C<sub>2</sub>H<sub>5</sub>COOH as structure-directing agents without any other complex surfactants. These mesoporous CeO<sub>2</sub> spheres have high specific surface area of 216 m<sup>2</sup>g<sup>-1</sup>, which exhibits no significant change under different annealing temperatures revealing the good thermal stability. Mesoporous CeO<sub>2</sub> was prepared by Perkas *et al.*<sup>294</sup> via sonochemical method using sodium dodecyl sulfate (SDS) as a surfactant, Ce(NO<sub>3</sub>)<sub>3</sub>·9H<sub>2</sub>O as the cerium source, and urea as a precipitating agent. Spherical mesoporous CeO<sub>2</sub> nanoparticles of different shape have been synthesized by Ho *et al.*<sup>295</sup> via a simple solution route using



ethylene glycol and poly vinylpyrrolidone as surfactant. Liang *et al.*<sup>296</sup> synthesized both pure and homogeneous La/Ce mixed oxides over a wide range of La:Ce-ratios by a reverse microemulsion method using poly(ethylene glycol)-block-poly(propylene glycol)-block-poly(ethylene glycol) as surfactant. Resulting materials exhibits well-defined nanostructure and high surface areas of  $110 \text{ m}^2\text{g}^{-1}$  calcined at  $450^\circ\text{C}$ . Yuan *et al.*<sup>297</sup> successfully developed a surfactant-assisted hydrothermal route for the preparation of mesoporous cerium oxides nanorods  $\text{CeCl}_3 \cdot 7\text{H}_2\text{O}$  as cerium oxide precursor and cetyltrimethylammonium bromide (CTMABr) as surfactant. It was found that the surfactant concentration significantly influence the final cerium oxide structures and surface area. Mesoporous nanoscale ceria have been prepared by Zagaynov *et al.*<sup>298</sup> via sol-gel method using cerium (III) nitrate or acetylacetonate as cerium source dimethyloctylamine as surfactant or hydrolyzing agent and acetylacetone as a chelating ligand. Ni *et al.*<sup>299</sup> synthesized mesoporous  $\text{CeO}_2$  particles using cerium acetate hydrate as inorganic precursors and Pluronic P123 or F127 tri-block copolymer as soft template.

Mesoporous ceria with high surface area of  $224.7 \text{ m}^2\text{g}^{-1}$  and ordered structure was synthesized by Deprasertkul *et al.*<sup>300</sup> using MCM-48 as hard template via nanocasting method. Roggenbuck *et al.*<sup>301</sup> synthesized mesoporous  $\text{CeO}_2$  by nanocasting method using CMK-3 carbon as a structure matrix. The obtained products exhibit high specific surface area of  $148 \text{ m}^2 \text{ g}^{-1}$  and uniform pores with a diameter of ca. 5 nm. Laha *et al.*<sup>302</sup> reported the synthesis of highly ordered and thermally stable mesoporous cerium oxides by using mesoporous silica templates. The thermal stability of the mesoporous  $\text{CeO}_2$  samples was also investigated and it was found that the mesostructure does not collapse even at  $700^\circ\text{C}$ .

La or Pr-doped flower-like mesoporous  $\text{CeO}_2$  were prepared by Li *et al.*<sup>303</sup> by hydrothermally with the aid of glucose and acrylic acid. They have also showed that La or Pr-doped mesoporous  $\text{CeO}_2$  showed higher catalytic activities for methane combustion than the pure  $\text{CeO}_2$ . Changlin *et al.*<sup>304</sup> synthesized mesoporous ceria-zirconia solid solution by using different surfactants such as pluronic triblock copolymer P123, Brij 56 and cetyltrimethylammonium bromide (CTAB) as templates and the as-synthesized sample was calcined at  $500^\circ\text{C}$  for 4 h. The ceria- zirconia solid solution obtained in Brij56 assisted route showed highest surface area of  $99 \text{ m}^2 \text{ g}^{-1}$  and pore volume  $0.17 \text{ cm}^3 \text{ g}^{-1}$ . After calcinations at  $1000^\circ\text{C}$  for 4 h, the BET surface area and the pore volume decrease to  $14 \text{ m}^2\text{g}^{-1}$  and  $0.06 \text{ cm}^3\text{g}^{-1}$ , respectively. Hao *et al.*<sup>305</sup> successfully synthesized  $\text{Fe}^{3+}$  doped mesoporous  $\text{CeO}_2$  with

several compositions using  $\text{Ce}(\text{NO}_3)_3 \cdot 6\text{H}_2\text{O}$  and  $\text{Fe}(\text{NO}_3)_3 \cdot 9\text{H}_2\text{O}$  as raw materials and triblock copolymer P123 as the template. They have also find out the photocatalytic activities of the prepared samples by the decomposition of rhodamine B. The mesoporous 15% Ce–Fe–O catalyst exhibit highest surface area of  $146.6 \text{ m}^2 \text{ g}^{-1}$  and showed higher photocatalytic activity. Zhang *et al.*<sup>306</sup> synthesized a series of transition-metal-doped (Cu, Co, Ni, and Mn) hierarchically mesoporous  $\text{CeO}_2$  nanoparticles through a colloidal crystal template strategy.

Kamimura *et al.*<sup>307</sup> demonstrate the simple template-free synthesis of mesoporous ceria with a high surface area up to  $200 \text{ m}^2 \text{ g}^{-1}$  based on the sol-gel method. Lu *et al.*<sup>308</sup> synthesized mesoporous  $\text{CeO}_2$  without a template by the direct hydrothermal method using NaOH and  $\text{NH}_4\text{OH}$  solution. Li *et al.*<sup>309</sup> provided a novel strategy to prepare mesoporous nanorod like ceria with high surface area of  $121 \text{ m}^2 \text{ g}^{-1}$  by microwave-assisted hydrolysis of  $\text{Ce}(\text{NO}_3)_3 \cdot 6\text{H}_2\text{O}$  in presence of urea. Mesoporous  $\text{CeO}_2$  with hierarchical nanoarchitectures was synthesized by Zhang *et al.*<sup>310</sup> via a precursor method with different amino acids as crystallization modifiers. Hierarchically mesoporous  $\text{CeO}_2$  nanoparticles were prepared by Zhang *et al.*<sup>311</sup> through a facile solvothermal strategy which involve the preparation of the  $\text{Ce}(\text{HCOO})_3$  nanoparticles, and then transformation from  $\text{Ce}(\text{HCOO})_3$  to  $\text{CeO}_2$ . The obtained product exhibited very high surface area of  $147.6 \text{ m}^2 \text{ g}^{-1}$  and outstanding catalytic activities for CO oxidation. Chen *et al.*<sup>312</sup> successfully synthesized hollow mesoporous  $\text{CeO}_2$  via a solid-liquid interfacial reaction between the  $\text{Ce}_2(\text{SO}_4)_3$  precursor and NaOH in ethanol at room temperature. Neither additional surfactant molecules nor calcination was employed during the whole preparation process. However until now, limited reports are available on the direct template-assisted synthesis of  $\text{CeO}_2$  mesostructures, especially with narrow pore distributions, rigid frameworks, and well-defined morphologies. Therefore, it is highly desirable to produce mesoporous powder of  $\text{CeO}_2$  materials, which exhibits high surface area, and crystalline framework, using an efficient, simple and economic method to meet the growing demand of various applications.

### 1.9. Applications of ceria based materials

Since the beginning of the 1940's cerium oxide ( $\text{CeO}_2$ ) was used significantly as an efficient polishing agent by the glass industry.<sup>313,314</sup> A huge amounts of the yearly production of  $\text{CeO}_2$  is consumed for this purpose. The utilization of  $\text{CeO}_2$ , as a vital component in three-

way catalysts (TWC) constitutes its economically and technologically most important application due to its high oxygen storage and release capacity.<sup>315-317</sup> A significant amount of cerium oxide is consumed annually for the preparation of three way catalyst to remove pollutants from vehicle (auto-exhaust) emissions. CeO<sub>2</sub>-based oxides can be also used as a promoter for the low temperature water-gas shift reaction.<sup>52</sup> Another potential application of CeO<sub>2</sub>-based materials is as electrolytes in solid oxide fuel cells (SOFC). Because of its redox property, it can store and release oxygen under lean (oxygen rich) and rich fuel conditions, respectively. Popular electrolyte use in solid oxide fuel cell are yttria stabilized zirconia (YSZ) and scandia stabilized zirconia, but they have some limitation as they can work only at high temperature and also exhibits insufficient electro catalytic activity for oxygen reduction and poor ionic conductivity at intermediate temperature. The main features of CeO<sub>2</sub> containing SOFC are low operating temperature, higher ionic conductivity, chemical inertness, high crystalline-phase and chemical purity.<sup>318</sup> Its potential redox chemistry, rapid redox cycle between Ce<sup>3+</sup> ↔ Ce<sup>4+</sup> and the existence of both Lewis acid and base sites on surface make this oxide suitable as a catalyst for many chemical reactions. Further, due to weak Lewis acid and stronger Lewis base property CeO<sub>2</sub> can be used in various organic synthesis. Pure ceria is widely used in several organic reactions, such as the dehydration of alcohols, the alkylation of aromatic compounds, ketone formation, and aldolization, and in redox reactions.<sup>319</sup>

In addition to these major applications, CeO<sub>2</sub>-based systems are also considered as one of the most promising materials for environmental remediation application such as sorbents for removal of hazardous anions and photocatalyst for the degradation of the organic dyes. Cerium oxide is assumed to be one of the most outstanding adsorbents for removing hazardous anions as because of its very low solubility in acid media and it did not elute during the removal of hazardous ion.<sup>320</sup> Recently, ceria nanoparticles exhibited excellent adsorption capacity for the removal of arsenic<sup>321,322</sup> and chromium(VI) in aqueous solutions.<sup>323, 324</sup> Ceria supported on carbon nanotubes was reported to have good arsenate<sup>325</sup> and chromium<sup>326</sup> adsorption capacity from aqueous solution due to their high surface area, excellent electron transfer ability, small size, and easy surface-modification. Zhong *et al.* observed that 3D flower-like ceria micro/nanocomposites exhibits outstanding As(V) and Cr(VI) removal

capacity from water.<sup>84</sup> There are significant examples where cerium oxide had shown a high adsorption capacity for various anions, such as fluoride,<sup>327</sup> arsenic,<sup>326, 84</sup> and bichromate.<sup>323,324</sup>

Further CeO<sub>2</sub> nanomaterials have also potential applications in the field of photocatalysis. For example, Tang *et al.*<sup>328</sup> demonstrated that CeO<sub>2</sub> nanotubes exhibited a markedly enhanced photocatalytic activity toward the degradation of aromatic benzene. The photocatalytic degradation of dyes has been explored extensively by several research groups [ref]. Both CeO<sub>2</sub> and Fe<sup>3+</sup> doped CeO<sub>2</sub> exhibit an excellent photocatalytic performance for degradation of acid orange 7 (AO7) in the presence of H<sub>2</sub>O<sub>2</sub>.<sup>87,329</sup> Co-doped ceria nanorods<sup>330</sup> and Cu<sub>2</sub>O/CeO<sub>2</sub> composite<sup>331</sup> showed stronger photocatalytic activity towards AO7 degradation under UV and visible light illumination, respectively. Several reports suggested that ceria nanospheres are promising absorbents for the effective removal of heavy metal ions such as Cr(VI) and organic dye such as RhB from wastewater.<sup>85</sup> Chaudhary *et al.* reported that ceria nanocrystals exhibit excellent autocatalytic behavior and photo-decomposition ability for methylene blue under sunlight.<sup>332</sup> Autocatalytic behavior of the CeO<sub>2</sub> nanoparticles were further studied by various authors.<sup>333,334</sup> Because of their autocatalytic property and excellent biocompatibility CeO<sub>2</sub> nanoparticles can be used as antioxidant in many biomedical applications such as retinal degeneration, oxidative stress, inflammation and prevention from radiation damage.<sup>333, 335-340</sup>

Apart from this, one of the most interesting features of the lanthanide ions is their photoluminescence because of their line-like emission which leads to high color purity of the emitted light.<sup>154</sup> Since Ce<sup>4+</sup> ions have no 4f electron it can be a promising luminescence host material for other rare earth ions such as Eu, Sm, and Er, because of strong light absorption through charge transfer (CT) transition O<sup>2-</sup>→Ce<sup>4+</sup>.<sup>164</sup> Samarium doped CeO<sub>2</sub> nanoparticles are very important in developing new luminescence devices in orange and red regions.<sup>160</sup> Hence the lanthanide dopant imparts luminescence property to the CeO<sub>2</sub> host, extending the traditional applications of these materials to novel fields such as phosphors, bio imaging, and therapy.<sup>341</sup> CeO<sub>2</sub> is also considered an ideal component for sunscreen materials as it exhibits excellent ultraviolet radiation absorption properties.<sup>34</sup> Therefore, it is highly desirable to synthesize CeO<sub>2</sub> nanoparticles with the mixed valence state (Ce<sup>3+</sup> and Ce<sup>4+</sup>) for multifunctional applications.

### 1.10. Objectives of the thesis

Literature survey reveals that ceria and ceria-based oxides have been extensively investigated due to their varieties of applications including catalysis, solid oxide fuel cells, and environmental remediation etc. Rare earth doped CeO<sub>2</sub>, which impart luminescence property in the CeO<sub>2</sub> host extending its application for nanophosphors, bio imaging etc. The key for most of the above mentioned applications of CeO<sub>2</sub> based materials is its extraordinary ability to release or uptake oxygen by shifting some Ce<sup>4+</sup> to Ce<sup>3+</sup> ions.<sup>1,7,8</sup> Better catalytic performances of CeO<sub>2</sub> have been reported in the presence of Ce<sup>3+</sup> and oxygen vacancy defects, which are potentially potent surface sites for catalysis.<sup>6-9</sup> Therefore, it is highly desirable to synthesize multifunctional CeO<sub>2</sub> nanoparticles with the mixed valence state (Ce<sup>3+</sup> and Ce<sup>4+</sup>). Physicochemical properties and catalytic activities of CeO<sub>2</sub> can be improved by introducing lanthanide ions, which modifies the surface defects.<sup>7,16,17</sup> The concentration of single electron defects of Ce<sup>3+</sup> ions and oxygen vacancies can be remarkably enhanced after doping with Sm or Eu for charge compensation due to the Sm<sup>3+</sup> /Eu<sup>3+</sup> → Ce<sup>4+</sup> substitutions.<sup>18</sup> Motivated by the unique properties and varieties of applications of ceria-based materials, the present research work on synthesis of mesoporous CeO<sub>2</sub> as well as Sm<sup>3+</sup> or Eu<sup>3+</sup> doped CeO<sub>2</sub> has been taken-up with an especial emphasis of their structural characterization, photoluminescence properties and their novel applications. This involves series of experiments and measurements followed by a systematic analysis as follows:

- To explore simple chemical route using cheaper metal inorganic precursor to derive a high surface area mesoporous CeO<sub>2</sub> by using inorganic metal precursor and a surfactant.
- Effect of introduction of surfactants to the synthesis systems on the thermal, structural, optical properties, mesoporosity, and surface area of mesoporous pure CeO<sub>2</sub>.
- Development of thermally stable high surface area CeO<sub>2</sub> in mesoporous structure with Sm<sub>2</sub>O<sub>3</sub> and Eu<sub>2</sub>O<sub>3</sub> as additives in selected compositions via the surfactant-assisted route.
- Thermal analysis of pure and doped as-prepared precursors.
- Analysis of surface area, pore size, pore volume and morphology in inorganic-template hybrids, and with microstructure, BET, FESEM and HRTEM studies.
- Photoluminescence study of the doped CeO<sub>2</sub> at selected temperatures.
- Effects of the various amounts of Sm<sub>2</sub>O<sub>3</sub> and Eu<sub>2</sub>O<sub>3</sub> additives in the CeO<sub>2</sub> host lattice.

- Complete characterization of structure, microstructure, and spectroscopic analysis of selected specimens, with an emphasis on their applications.
- Investigation of applications of selected samples in heavy metal Cr(VI) adsorption and autocatalytic activity.
- Photocatalytic degradation of organic dyes (AO7, methylene blue, and rhodamine B) in aqueous system under natural solar light irradiation.

## References

1. Z. Hu, S. Haneklaus, G. Sparovek and E. Schnug, *Commun. Soil Sci. Plant. Anal.*, 2006, 37, 1381.
2. C. Bouzigues, T. Gacoin and A. Alexandrou, *Acs Nano.*, 2011, 5, 8488.
3. C. Xu and X. Qu, *NPG Asia Materials*, 2014, 6,e90; doi:10.1038/am.2013.88.
4. A. S. Weber, A. M. Grady and R. T. Koodali, *Catal. Sci. Technol.*, 2012, 2, 683.
5. W. H. Wells and V. L. Wells, *Patty's Toxicology*, John Wiley & Sons, Inc., 2001.
6. K. A. Gschneidner and B. Evans, *Van Nostrand's Encyclopedia of Chemistry*, John Wiley & Sons, Inc., 2005.
7. T. J. Ahrens, *Global Earth Physics: a Handbook of Physical Constants*, American Geophysical Union, Washington, DC, 1995.
8. D. Lide, *CRC Handbook of Chemistry and Physics*, CRC Publishing Co., Boca Raton, FL, 88th edn, 2007.
9. J. Emsley, *The Elements*, Oxford University Press, Oxford, 1989.
10. G. Houtzager, *Geillustreerde Griekse Mythologie Encyclopedie*, Rebo productions b.v., Lisse, 2003.
11. S. A. Cotton, *Lanthanide and Actinide Chemistry* John Wiley & Sons Ltd, 2006.
12. J. C. Summers and S. A. Ausen, *J. Catal.*, 1979, 58, 131.
13. G. Kim, *Ind. Eng. Chem. Prod. Res. Dev.*, 1982, 21, 267.
14. H. S. Gandhi, A. G. Piken, M. Shelef, and R. G. Delosh, *SAE Paper*, 1976, 760201, 55.
15. P. Fornasiero and A. Trovarelli, *Catal. Today*, 2015, 253, 1.
16. A. Trovarelli, C. de Leitenburg, M. Boaro and G. Dolcetti, *Catal. Today*, 1999, 50, 353.
17. J. Kaspar and P. Fornasiero, *J. Solid State Chem.*, 2003, 171, 19.
18. J. Kaspar, P. Fornasiero and M. Graziani, *Catal. Today*, 1999, 50, 285.
19. M. Boaro, M. Vicario, C. de Leitenburg, G. Dolcetti and A. Trovarelli, *Catal. Today*, 2003, 77, 407.
20. E. Aneggi, M. Boaro, C. de Leitenburg, G. Dolcetti and A. Trovarelli, *J. Alloys Compd.*, 2006, 408–412, 1096.
21. E. Aneggi, C. de Leitenburg, G. Dolcetti and A. Trovarelli, *Catal. Today*, 2006, 114, 40.
22. M. Godickemeier and L. J. Gauckler, *J. Electrochem. Soc.*, 1998, 145, 414.
23. K. Eguchi, T. Setoguchi, T. Inoue, and H. Arai, *Solid State Ionics*, 1992, 52, 165.
24. V. Esposito and E. Traversa, *J. Am. Ceram. Soc.*, 2008, 91, 1037.
25. B. C. H. Steele, *J. Power Sources*, 1994, 49, 1.
26. B. C. H. Steele, *Solid State Ionics*, 2000, 129, 95.
27. S. D. Park, J. M. Vohs and R. J. Gorte. *Nature*, 2000, 404, 265.
28. Y. P. Fu and C.H. Lin, *J. Alloy Compd.*, 2005, 389, 165.
29. D. Y. Chung and E. H. Lee, *J. Alloy Compd.*, 2004, 374, 69.

30. R. A. Rocha and E. N. S. Muccillo, *Br. Ceram. Trans.*, 2003, 102, 216.
31. X. Feng, D. C. Sayle, Z. L. Wang, M. S. Paras, B. Santora, A. C. Sutorik, T. X. T. Sayle, Y. Yang, Y. Ding, X. Wang and Y. S. Her, *Science*, 2006, 312, 1504.
32. H. Inaba and H. Tagawa, *Solid State Ion*, 1996, 83, 1.
33. A. Trovarelli, *Catal. Rev. Eng.*, 1996, 38, 439.
34. S. Yabe and T. Sato, *J. Solid State Chem.*, 2003, 171, 7.
35. S. Tsunekawa, T. Fukuda, and A. Kasuya, *J. Appl. Phys.*, 2000, 87, 1318.
36. A. Ahniyaz, Y. Sakamoto and L. Bergstrom, *Cryst. Growth Des.*, 2008, 8, 1799.
37. M. K. Devaraju, S. Yin, and T. Sato, *ACS Appl. Mater. Interfaces*, 2009, 1, 2694.
38. C. W. Sun, H. Li, H. R. Zhang, Z. X. Wang and L. Q. Chen, *Nanotechnology*, 2005, 16, 1454.
39. T. Morimoto, H. Tomonaga and A. Mitani, *Thin Solid Films*, 1999, 351, 61.
40. R. X. Li, S. Yabe, M. Yamashita, S. Momose, S. Yoshida, S. Yin and T. Sato, *Solid State Ionics*, 2002, 151, 235.
41. N. M. Bahadur, F. Kurayama, T. Furusawa, M. Sato, I. A. Siddiquey, M. M. Hossain and N. Suzuki, *J. Nanopart. Res.*, 2013, 15, 1390
42. S. Tsunekawa, R. Sahara, Y. Kawazoe and A. Kasuya, *Mater. Trans. JIM*, 2000, 41, 1104.
43. T. Masui, K. Fujiwara, K. I. Machida and G. Y. Adachi, *Chem. Mater.*, 1997, 9, 2197.
44. E. K. Goharshadi, S. Samiee, and P. Nancarrow, *J. Colloid Interface Sci.*, 2011, 356, 473.
45. D. Barreca, G. Bruno, A. Gasparotto, M. Losurdo, and E. Tondello, *Mater. Sci. Eng. C*, 2003, 23, 1013.
46. F. Zhang, S. W. Chan, J. E. Spanier, E. Apak, Q. Jin, R. D. Robinson and I.P. Herman, *Appl. Phys. Lett.*, 2002, 80, 127.
47. R. Suresh, V. Ponnuswamy and R. Mariappan, *Appl. Surf. Sci.*, 2013, 273, 457.
48. Krishnan, T. S. Sreeremya and S. Ghosh, *Cryst. Eng Comm.*, 2015, 17, 7094.
49. R. N. Blumenth, F. S. Brugner and J. E. Garnier, *J. Electrochem. Soc.*, 1973, 120, 1230.
50. M. F. G. Sanchez, A. Ortiz, G. Santana, M. Bizarro, J. Pena, F. C. Gandarilla, M. A. A. Frutis and J. C. Alonso, *J. Am. Ceram. Soc.*, 2010, 93, 155.
51. G. Wang, Q. Mu, T. Chen and Y. Wang, *J. Alloy Compd.*, 2010, 493, 202.
52. Q. Fu, A. Weber and M. Flytzani-Stephanopoulo, *Catal. Letters*, 2001, 77, 87.
53. Q. Fu, H. Saltsburg and M. Flytzani-Stephanopoulo, *Science*, 2003, 301, 935.
54. S. Carretin, P. Concepcion, A. Corma, J.M.L. Nieto and V.F. Puentes, *Angew. Chem. Int. Ed.*, 2004, 43, 2538.
55. R. K. Pati, I. C. Lee, S. C. Hou, O. Akhuemonkhan, K. J. Gaskell, Q. Wang, A. I. Frenkel,; D. Chu, L. G. S. Riba and S. H. Ehrman, *ACS Appl. Mater. Interfaces*, 2009, 1, 2624.
56. H. He, H. Dai and C. T. Au, *Catal. Today*, 2004, 90, 245.
57. G. Jacobs, S. Khalid, P. M. Patterson, D. E. Sparks and B. H. Davis, *Appl. Catal. A Gen.*, 2004, 268, 255.
58. P. Panagiotopoulou, J. Papavasiliou, G. Avgouropoulos, T. Ioannides and D.I. Kondarides, *Chem. Eng. J.*, 2007, 134, 16.
59. Q. Yu, W. Chen, Y. Li, M. Jin and Z. Suo. *Catal. Today*, 2010, 158, 324.
60. H. J. Beie and A. Gnorich, *Sens. Sensors Actuators B Chem.*, 1991, 4, 393.
61. P. Jasinski, T. Suzuki and H. U. Anderson, *Sensors Actuators B Chem.*, 2003, 95, 73.

62. N. Izu, T. Itoh, M. Nishibori, I. Matsubara and W. Shin, *Sensors Actuators B Chem.*, 2012, 171, 350.
63. M. Stoukides, *Catal. Rev. Eng.*, 2000, 42, 1.
64. X. Yin, L. Hong and Z. L. Liu, *J. Memb. Sci.*, 2006, 268, 2.
65. F. Larachi, J. Pierre, A. Adnot and A. Bernis, *Appl. Surf. Sci.*, 2002, 195, 236.
66. A. Corma, P. Atienzar, H. Garcia and J. Y. C. Ching, *Nat. Mater.*, 2004, 3, 394.
67. K. Eguchi, *J. Alloys Compd.*, 1997, 250, 486.
68. S. Armini, J. D. Messemaker, C. M. Whelan, M. Moinpour and K. Maex, *J. Electrochem. Soc.*, 2008, 155, 653.
69. D. G. Shchukin and R. A. Carus, *Chem. Mater.*, 2004, 16, 2287.
70. W. Wenwei, L. Shushu, L. Sen, X. Feng, and W. Xuehan, *Rare Metals*, 2010, 29, 149.
71. T. Masut, M. Yamamoto, T. Sakata, H. Mori and G. Adachi, *J. Mater. Chem.*, 2000, 10, 353.
72. S. Yabe, M. Yamashita, S. Momose, K. Tahira and T. Sato, *Int. J. Inorg. Mater.*, 2001, 3, 1003.
73. N. Imanaka, T. Masui, H. Hirai and G. Adachi, *Chem. Mater.*, 2003, 15, 2289.
74. Y. W. Zhang, R. Si, C. S. Liao and C. H. Yan, *J. Phys. Chem. B*, 2003, 107, 10159.
75. W. D. W. Duan, A. J. Xie, Y. H. Shen, X. F. Wang, F. Wang, Y. Zhang and J. L. Li, *Ind. Eng. Chem. Res.*, 2011, 50, 4441.
76. K. Sohlberg, S. T. Pantelides and S. F. Penneycook, *J. Am. Chem. Soc.*, 2001, 123, 6609.
77. I. Celardo, J. Z. Pedersen, E. Traversa and L. Ghibelli, *Nanoscale*, 2011, 3, 1411.
78. S. Babu, A. Velez, K. Wozniak, J. Szydlowska and S. Seal, *Chem. Phys. Lett.*, 2007, 442, 405.
79. A. Karakoti, S. Singh, J. Dowding, S. Seal and W. Self, *Chem. Soc. Rev.*, 2010, 39, 4422.
80. A. Asati, S. Santra, C. Kaittanis and J. M. Perez, *ACS Nano*, 2010, 9, 5321.
81. J. Guzman, S. Carrettin and A. Corma, *J. Am. Chem. Soc.*, 2005, 127, 3286.
82. P. Bera, A. Gayen, M. S. Hegde, N. P. Lalla, L. Spadaro, F. Frusteri and F. Arena, *J. Phys. Chem. B.*, 2003, 107, 6122.
83. H. Xiao, Z. Ai and L. Zhang, *J. Phys. Chem. C*, 2009, 113, 16625.
84. L. S. Zhong, J. S. Hu, A. M. Cao, Q. Liu, W. G. Song, and L. J. Wan, *Chem. Mater.*, 2007, 19, 1648.
85. J. Li, A. Kalam, A. S. A. Shihri, Q. Su, G. Zhong and G. Du, *Mater. Chem. Phys.*, 2011, 130, 1066.
86. A. Y. Cao, Z. M. Cui, C. Q. Chen, W. G. Song and W. Cai, *J. Phys. Chem. C*, 2010, 114, 9865.
87. F. Chen, X. Shen, Y. Wang and J. Zhang, *Appl. Catal. B Environ.*, 2012, 121–122, 223.
88. P. Ji, B. Tian, F. Chen and J. Zhang, *Environ. Technol.*, 2012, 33, 467.
89. P. Ji, J. Zhang, F. Chen and M. Anpo, *J. Phys. Chem. C*, 2008, 112, 17809.
90. P. Ji, J. Zhang, F. Chen and M. Anpo, *Appl. Catal. B Environ.*, 2009, 85, 148.
91. B. Sun, H. Liab and L. Chen, *Energy Environ. Sci.*, 2012, 5, 8475.
92. B. Zhang, X. Du, L. Shia and R. Gao, *Dalton Trans.*, 2012, 41, 14455.
93. A. Trovarelli, *Catalytic Science Series*, 2002, 2, 15.
94. J. W. Morris, M. Jin and A. M. Minor, *Mater. Sci. Eng. A*, 2007, 462, 412.
95. F.A. Kröger, *Chemistry of Imperfect Crystals*, North-Holland, Amsterdam, 1964, 194.
96. C. Zhang, A. Michaelides, D. A. King and S. J. Jenkins, *Phys. Rev. B - Condens. Matter Mater. Phys.*, 2009, 79, 1.



97. C. T. Campbell and C. H. F. Peden, *Science*, 2005, 309, 713.
98. P. R. L. Keating, D. O. Scanlon, B. J. Morgan, N. M. Galea and G. W. Watson *J. Phys. Chem. C.*, 2012, 116, 2443.
99. M.A. Henderson, C.L. Perkins, M. H. Engelhard, S. Thevuthasan, and C.H.F. Peden, *Surf. Sci.*, 2003, 526, 1.
100. D. A. Andersson, S. I. Simak, N. V. Skorodumova, I. A. Abrikosov and B. A. Johansson, *Appl. Phys. Lett.*, 2007, 90, 031909.
101. B. B. Lavik, I. Kosacki, H. L. Tuller, Y. M. Chiang and J. Y. Ying, *J. Electroceram.*, 1997, 1, 7.
102. M. Nolan, J. E. Fearon and G. W. Watson, *Solid State Ionics*, 2006, 177, 3069.
103. N. J. Lawrence, J. R. Brewer, L. Wang, T. Wu, J. Wells-Kingsbury, M. M. Ihrig, G. Wang, Y. Soo, W. Mei and C. L. Cheung, *Nano Lett.*, 2011, 11, 2666.
104. P. L. Land, *J. Phys. Chem. Solids*, 1973, 34, 1839.
105. B. Esch, S. Fabris, L. Zhou, T. Montini, C. Africh, P. Fornasiero, G. Comelli and R. Rosei, *Science*, 2005, 309, 752.
106. T.G. Kuznetsova and V.A. Sadykov, ISSN 0023-1584, *Kinetics and Catalysis*, 2008, 49, 840.
107. X. Liu, K. Zhou, L. Wang, B. Wang and Y. Li, *J. Am. Chem. Soc.*, 2009, 131, 3140.
108. A. Trovarelli, M. Boaro, E. Rocchini, C. de Leitenburg and G. Dolcetti, *J. Alloy Compd.*, 2001, 323–324, 584.
109. R. K. Grasselli and J. D. Burrington, *Adv. Catal.*, 30, 133 1981.
110. J. Kullgren, 2012, Uppsala. ISBN 978-91-554-8271-8.
111. P. Fornasiero, R. Di Monte, G. Ranga Rao, J. Kaspar, S. Meriani, A. Trovarelli and M. Graziani, *J. Catal.*, 1995, 151, 168.
112. B. K. Cho, *J. Catal.*, 1991, 131, 74.
113. T. Bunluesin, R. J. Gorte and G. W. Graham, *Appl. Catal. B Environ.*, 1997, 14, 105.
114. E. Mamontov, T. Egami, R. Brezny, M. Koranne and S. Tyagi, *J. Phys. Chem. B*, 2000, 104, 11110.
115. J. Mikulova, S. Rossignol, J. J. Barbier, D. Duprez and C. Kappenstein, *Catal. Today*, 2007, 124, 185.
116. M. Pijolat, M. Prin, M. Soustelle, O. Touret, and P. Nortier, *J. Chem. Soc. Faraday Trans.*, 1995, 91, 3941.
117. M. Ozawa, M. Kimura, H. Sobukawa, and K. Yokota, *Toyota Tech. Rev.*, 1992, 27, 43.
118. Q. Yu, X. Wu, C. Tang, L. Qi, B. Liu, F. Gao, K. Sun, L. Dong and Y. Chen, *J. Colloid Interface Sci.*, 2011, 354, 341.
119. D. Tiana, C. Zeng, Y. Fu, H. Wang, H. Luo, C. Xiang, Y. Wei, K. Li and X. Zhu, *Solid State Commun.*, 2016, 231-232, 68.
120. Y. Zuo, L. Li, X. Huang and G. Li, *Catal. Sci. Technol.*, 2014, 4, 3368.
121. P. Singh and M. S. Hegde, *J. Solid State Chem.*, 2008, 181, 3248.
122. K. Li, Q. Fu and M. Flytzani-Slephanopoulos, *Appl. Catal. B Environ.*, 2000, 27, 179.
123. B. Murugan, A. V. Ramaswamy, D. Srinivas, C. S. Gopinath and V. Ramaswamy, *Chem. Mater.*, 2005, 17, 3983.
124. X. Liu, Y. Zuo, L. Li, X. Huang and G. Li, *RSC Adv.*, 2014, 4, 6397.
125. Y. Zuo, X. Huang, L. Li and G. Li, *J. Mater. Chem. A*, 2013, 1, 374.
126. Y. Zuo, L. Li, X. Huang and G. Li, *Catal. Sci. Technol.*, 2014, 4, 402.

127. S. V. Manorama, N. Izu, W. Shin, I. Matsubara and N. Murayama, *Sensors Actuators B Chem.*, 2003, 89, 299.
128. A. S. Reddy, C. Y. Chen, C. C. Chen, S. H. Chien, C. J. Lin, K. H. Lin, C. L. Chen and S. C. Chang, *J. Mol. Catal. A Chem.*, 2010, 318, 60.
129. W. T. Chen, K. B. Chen, M. F. Wang, S. F. Weng, C. S. Lee and M. C. Lin, *Chem. Commun.*, 2010, 46, 3286.
130. A. B. Kehoe, D. O. Scanlon and G. W. Watson, *Chem. Mater.*, 2011, 23, 4464.
131. L. Zhou, X. Li, Z. Yao, Z. Chen, M. Hong, R. Zhu, Y. Liang and J. Zhao, DOI: 10.1038/srep23900.
132. D. Horlait, L. Claparede, N. Clavier, S. Szenknect, N. Dacheux, J. Ravoux, and R. Podor, *Inorg. Chem.*, 2011, 50, 7150.
133. L. Minervini, M. O. Zacate and R. W. Grimes, *Solid State Ionics*, 1999, 116, 339.
134. X. Guo and R. Waser, *Prog. Mater. Sci.*, 2006, 51, 151.
135. Y. Ikuma, E. Shimada and N. Okamura, *J. Am. Ceram. Soc.*, 2005, 88, 419.
136. S. J. Hong and A. V. Virkar, *J. Am. Ceram. Soc.*, 1995, 78, 433.
137. B. C. H. Steele and A. Heinzl, *Nature*, 2001, 414, 345.
138. Z. X. Song, W. Liu, H. Nishiguchi, A. Takami, K. Nagaoka and Y. Takita, *Appl. Catal. A Gen.*, 2007, 329, 86.
139. K. Krishna, A. B. Lopez, M. Makkee and J. Moulijn, *Appl. Catal. B Environ.*, 2007, 75, 201.
140. B. Hayashi, R. Sagawa, H. Inaba and K. Kawamura, *Solid State Ionics*, 2000, 131, 281.
141. M. O'Connell and M.A. Morris, *Catal. Today*, 2000, 59, 387.
142. E. R. Cabrera, A. Atkinson and D. Chadwick, *Appl. Catal. B Environ.*, 2002, 36, 193.
143. E. S. Putna, J. M. Vohs, R. J. Gorte and G. W. Graham, *Catal. Lett.*, 1998, 54, 17.
144. C. K. Narula, K. L. Taylor, L. P. Haack, L. F. Allard, A. Datye, M. Y. Slnev, M. Shelef, R. W. McCabe, W. Chun and G. W. Graham, *Mater. Res. Soc. Symp. Proc.*, 1998, 497, 15.
145. G. B. Balazs and R. S. Glass, *Solid State Ionics*, 1995, 76, 155.
146. K. Yamashita, K. V. Ramanujachary, and M. Greenblatt, *Solid State Ionics*, 1995, 81, 53.
147. B. Yahiro, Y. Egushi, K. Egushi and H. Arai, *J. Appl. Electrochem.*, 1988, 18, 527.
148. B. Kuntaiah, P. Sudarsanam, B. M. Redd and A. Vinu, *RSC Adv.*, 2013, 3, 7953.
149. H. Yahiro, K. Eguchi, and H. Arai, *Solid State Ionics*, 1989, 36, 71.
150. R. D. Shannon, *Acta Crystallogr., Sect. A: Cryst. Phys., Diffr., Theor. Gen. Cryst.*, 1976, 32, 751.
151. C. Tiseanu, V. I. Parvulescu, M. Boutonnet, B. Cojocaru, P. A. Primus, C. M. Teodorescu, C. Solans and M. S. Dominguez, *Phys. Chem. Chem. Phys.*, 2011, 13, 17135.
152. A. V. Thorat, T. Ghoshal, P. Carolan, J. D. Holmes and M. A. Morris, *J. Phys. Chem. C*, 2014, 118, 10700.
153. H. Yokokawa, T. Horita, N. Sakai, K. Yamaji, M. E. Brito, Y. P. Xiong and H. Kishimoto, *Solid State Ionics*, 2006, 177, 1705.
154. A. Binnemans, *Chem. Rev.*, 2009, 109, 4283.
155. Z. Wang, Z. Quan and J. Lin., *Inorg. Chem.*, 2007, 46, 5237.
156. G. K. Das and T. T. Y. Tan. *J. Phys. Chem. C*, 2008, 112, 11211.
157. B. Wang, J. L. Liu, Y. X. Zhang, W. Hou, X. L. Wu and S. K. Xu, *Mater. Lett.*, 2009, 63, 325.
158. J. Wu, S. Shi, X. Wang, J. Li, R. Zong and W. Chen, *J. Mater. Chem. C*, 2014, 2, 2786.
159. S. Fujihara and M. Oikawa, *J. Appl. Phys.*, 2004, 95, 8002.

160. E. C. C Souza, H. F. Brito and E. N. S. Muccillo, *J. Alloys. Compd.*, 2010, 491, 460.
161. R. H. Krishna, B. M. Nagabhushana, H. Nagabhushana, N. S. Murthy, S. C. Sharma, C. Shivakumara and R. P. S. Chakradhar, *J. Phys. Chem. C*, 2013, 117, 1915.
162. B. Gu, Q. Liu, S. P. Mao, D. L. Mao and C. K. Chang, *Cryst. Growth Des.*, 2008, 8, 1422.
163. E. M. Goldys, K. D. Tomsia, D. Dosev, I. M. Kennedy, S. Yatsunenko and M. Godlewski, *J. Am. Chem. Soc.*, 2006, 128, 14498.
164. R. Srinivasan and A. Chandra Bose, *Mater. Lett.*, 2010, 64, 1954.
165. E. Kaneko, M. Hagiwara and S. Fujihara, *ECS J. Solid State Sci. Technol.*, 2014, 3, 109.
166. V. V. Ursaki, V. Lair, L. Zivkovic, M. Cassir, A. Ringuedé and O. Lupan, *Optical Mater.*, 2012, 34, 1897.
167. M. Balestrieri, S. Colis, M. Gallart, G. Schmerber, M. Ziegler, P. Gilliot and A. Dinia, *J. Mater. Chem. C*, 2015, 3, 7014.
168. M. K. Rath, S. K. Acharya, B.H. Kim, K. T. Lee and B. G. Ahn, *Mater. Lett.*, 2011, 65, 955.
169. Y. Yoshida and S. Fujihara, *Eur. J. Inorg. Chem.*, 2011, 1577.
170. M. Oikawa and S. Fujihara, *J. Eur. Ceram. Soc.*, 2005, 25, 2921.
171. W. Gao, J. Li, X. Zhou, Z. Zhang, Y. Ma and Y. Qu, *J. Mater. Chem. C*, 2014, 2, 8729.
172. Y. Sohn, *J. Am. Ceram. Soc.*, 2013, 96, 3747.
173. Z. L. Wang, Z. W. Quan and J. Lin, *Inorg. Chem.*, 2007, 46, 5237.
174. A. Kumar, S. Babu, A. S. Karakoti, A. Schulte and S. Seal, *Langmuir*, 2009, 25, 10998.
175. H. Guo and Y. Qiao, *Appl. Surf. Sci.*, 2008, 254, 1961.
176. S. Babu, A. Schulte and S. Seal, *Appl. Phys. Lett.*, 2008, 92, 123112.
177. J. Roh, S. H. Hwang and J. Jang, *Acs. Appl. Mater. Interfaces*, 2014, 6, 19825.
178. A. Sharma, M. Varshney, J. Park, T. K. Ha, K. H. Chae and H. J. Shin, *Phys. Chem. Chem. Phys.*, 2015, 17, 30065.
179. S. Shi, M. Hossu, R. Hall and W. Chen, *J. Mater. Chem.*, 2012, 22, 23461.
180. K. W. Chae, T. R. Park, C. I. Cheon, N. I. Cho and J. S. Kim, *J. Lumin.*, 2013, 136, 109.
181. D. Fang, M. Zhang, Z. Luo, T. Cao, Q. Wang, Z. Zhou, M. Jiang and C. Xiong, *Opt. Mater.*, 2014, 38, 1.
182. L. Li, H. K. Yang, B. K. Moon, Z. Fu, C. Guo, J. H. Jeong, S. S. Yi, K. Jang and H. S. Lee, *J. Phys. Chem. C*, 2009, 113, 610.
183. R. Srinivasan and A. C. Bose, *Functional Mater. Lett.*, 2011, 4, 13.
184. J. Kaur, D. Chandrakar, V. Dubey, Y. Parganiha, and N. S. Suryanarayana, *Opt. Spectros.*, 2015, 118, 742.
185. G. Vimal, K. P. Mani, P. R. Biju, C. Joseph, N. V. Unnikrishnan and M. A. Ittyachen, *Appl. Nanosci.*, 2015, 5, 837.
186. C. Tiseanu, V. I. Parvulescu, M. S. Dominguez and M. Boutonnet, *J. Appl. Phys.*, 2012, 112, 013521-013529.
187. C. Buzea, I. I. P. Blandino, and K. Robbie, "Nanomaterials and Nanoparticles: Sources and Toxicity", *Biointerphases*, 2007, 2, MR17 - MR172.
188. I. Freestone, N. Meeks, M. Sax and C. Higgitt, *Gold Bulletin*, 2007, 40, 270.
189. R. Feynman, *Caltech Eng. Sci.*, 1960, 23:5, 22.

190. R. W. Siegel, Nanostructured Materials, Materials Science Division, Argonne National Laboratory Argonne, Illinois 60439 U.S.A.
191. H. Gleiter, *Acta mater.*, 2000, 48, 1.
192. H. Hofmann, *Nanomater.*, 2009, 1, 8.
193. L. Eyring, The Binary Lanthanide Oxides: Synthesis and Identification, in synthesis of Lanthanide and Actinide compounds, eds. L. R. Morss and G. Meyer (Kluwer, Dordrecht, 1991), 187.
194. G. Adachi and N. Imanaka, *Chem. Rev.*, 1998, 98, 1479.
195. M. C. Cabus-Llaurado, Y. Cesteros, F. Medina, P. Salagre and J. E. Sueiras, *Micropor. Mesopor. Mater.*, 2007, 100, 167.
196. H. Y. Chang and H. I. Chen, *J. Cryst. Growth*, 2005, 283, 457.
197. H. I. Chen and H. Y. Chang, *Solid State Commun.*, 2005, 133, 593.
198. H. I. Chen and H. Y. Chang, *Ceram. Int.*, 2005, 31, 795.
199. B. L. Chen and I. W. Chen, *J. Am. Ceram. Soc.*, 1993, 76, 1577.
200. N. Du, H. Zhang, B. G. Chen, X. Y. Ma and D. R. Yang, *J. Phys. Chem. C*, 2007, 111, 12677.
201. J. G. Li, T. Ikegami, Y. Wang and T. Mori, *J. Am. Ceram. Soc.*, 2002, 85, 2376.
202. C. W. Sun, H. Li, Z. X. Wang, L. Q. Chen and X. J. Huang, *Chem. Lett.*, 2004, 33, 662.
203. M. Yamashita, K. Kameyama, S. Yabe, S. Yoshida, Y. Fujishiro, T. Kawai and T. Sato, *J. Mater. Sci.*, 2002, 37, 683.
204. X. D. Zhou, W. Huebner and H. U. Anderson, *Appl. Phys. Lett.*, 2002, 80, 3814.
205. T. Yu, B. Lim and Y. Xia, *Angew. Chem.*, 2010, 122, 4586.
206. R. Si, Y. W. Zhang, L. -P. You and C. H. Yan, *Angew. Chem., Int. Ed.*, 2005, 44, 3256.
207. C. Laberty-Robert, J. W. Long, E. M. Lucas, K. A. Pettigrew, R. M. Stroud, M. S. Doescher and D. R. Rolison, *Chem. Mater.*, 2006, 18, 50.
208. G. Li, K. Chao, H. Peng, K. Chen and Z. Zhang, *J. Phys. Chem. C*, 2008, 112, 16452.
209. B. Liu, M. G. Yao, B. B. Liu, Z. P. Li, R. Liu, Q. J. Li, D. M. Li, B. Zou, T. A. Cui, G. T. Zou, J. Liu and Z. Chen, *J. Phys. Chem. C*, 2011, 115, 4546.
210. C. Paun, O. V. Safonova, J. Szlachetko, P. M. Abdala, M. Nachtegaal, J. Sa, E. Kleymentov, A. Cervellino, F. Krumeich and J. A. van Bokhoven, *J. Phys. Chem. C*, 2012, 116, 7312.
211. C. N. R. Rao, H. S. S. Ramakrishna Matte, R. Voggu and A. Govindaraj, *Dalton Trans.*, 2012, 41, 5089.
212. H. Imagawa and S. Sun, *J. Phys. Chem. C*, 2012, 116, 2761.
213. N. Qiu, J. Zhang, Z. Wu, T. Hu and P. Liu, *Cryst. Growth Des.*, 2012, 12, 629.
214. S. Shen and X. Wang, *Chem. Commun.*, 2010, 46, 6891.
215. K. S. Choi, *Dalton Trans.*, 2008, 5432.
216. X. Lu, T. Zhai, H. Cui, J. Shi, S. Xie, Y. Huang, C. Liang and Y. Tong, *J. Mater. Chem.*, 2011, 21, 5569.
217. X. H. Lu, X. Huang, S. L. Xie, D. Z. Zheng, Z. Q. Liu, C. L. Liang and Y. X. Tong, *Langmuir*, 2010, 26, 7569.
218. Y. N. Ou, G. R. Li, J. H. Liang, Z. P. Feng and Y. X. Tong, *J. Phys. Chem. C*, 2010, 114, 13509.
219. D. E. Zhang, X. J. Zhang, X. M. Ni, J. M. Song and H. G. Zheng, *Chem. Phys. Chem.*, 2006, 7, 2468.
220. C. D. Leitenburg, A. Trovarelli and J. Kaspar, *J. Catal.*, 1997, 166, 98.

221. N. Audebrand, J. P. Auffredic and D. Louer, *Chem. Mater.*, 2000, 12, 1791.
222. S. Nakane, T. Tachi, M. Yoshinaka, K. Hirota and O. Yamaguchi, *J. Am. Ceram. Soc.*, 1997, 80, 3221.
223. S. Yin, Y. Minamidate, S. Tonouchi, T. Goto, Q. Dong, H. Yamane and T. Sato, *RSC Adv.*, 2012, 2, 5976.
224. J. Rouquerol, D. Avnir, C. W. Fairbridge, D. H. Everett, J. M. Haynes, N. Pernicone, J. D. F. Ramsay, K. S. W. Sing and K. K. Unger, *Pure Appl. Chem.*, 1994, 66, 1739.
225. C. H. Tung, L. Z. Wu, Z. Y. Yuan and N. Su, *J. Am. Chem. Soc.*, 1998, 120, 11594.
226. K. S. W. Sing, D. H. Everett, R. H. W. Haul, L. Moscou, R. A. Pierotti, J. Rouquerol and T. Siemieniowska, *Pure Appl. Chem.*, 1985, 57, 603.
227. M. B. Park, Y. Lee, A. M. Zhang, F. S. Xiao, C. P. Nicholas, G. J. Lewis and S. B. Hong, *J. Am. Chem. Soc.*, 2013, 135, 2248.
228. T. E. Gier, X. Bu, P. Feng and G. D. Stucky, *Nature*, 1998, 395, 154.
229. X. Bu, P. Feng and G. D. Stucky, *Chem. Mater.*, 1999, 11, 3423.
230. T. D. Tang, L. Zhang, W. Q. Fu, Y. L. Ma, J. Xu, J. Jiang, G. Y. Fang and F. S. Xiao, *J. Am. Chem. Soc.*, 2013, 135, 11437.
231. N. Pal and A. Bhaumik, *RSC Adv.*, 2015, 5, 24363.
232. D. Zhao, Q. Huo, J. Feng, B. F. Chmelka and G. D. Stucky, *J. Am. Chem. Soc.*, 1998, 120, 6024.
233. S. Che, Z. Liu, T. Ohsuna, K. Sakamoto, O. Terasaki and T. Tatsumi, *Nature*, 2004, 429, 281.
234. Y. P. Zhu, T. Z. Ren and Z. Y. Yuan, *New J. Chem.*, 2014, 38, 1905.
235. M. E. Davis and R. F. Lobo, *Chem Mater.*, 1992, 4, 756.
236. G. A. Ozin, *Adv. Mater.*, 1992, 4, 612.
237. N. K. Mal, A. Bhaumik, R. Kumar and A. V. Ramaswamy, *Catal. Lett.*, 1995, 33, 387.
238. A. Corma, *Chem. Rev.*, 1997, 97, 2373.
239. J. Y. Ying, C. P. Mehnert and M. S. Wong, *Angew. Chem., Int. Ed.*, 1999, 38, 56.
240. F. Schuth, *Chem. Mater.*, 2001, 13, 3184.
241. M. E. Davis, *Nature*, 2002, 417, 813.
242. M. Hartmann, *Chem. Mater.*, 2005, 17, 4577.
243. B. G. Bruce, B. Scrosati and J. M. Tarascon, *Angew. Chem. Int. Ed.*, 2008, 47, 2930.
244. W. Li and D. Y. Zhao, *Chem. Commun.*, 2013, 49, 943.
245. C. T. Kresge, M. E. Leonowicz, W. J. Roth, J. C. Vartuli and J. S. Beck, *Nature.*, 1992, 359, 710.
246. Y. Ren, Z. Ma and P. G. Bruce, *J. Mater. Chem.*, 2012, 22, 15121.
247. B. S. Huo, D. I. Margolese, U. Ciesla, P. Y. Feng, T. E. Gier, P. Sieger, R. Leon, P. M. Petroff, F. Schuth and G. D. Stucky, *Nature*, 1994, 368, 317.
248. D. M. Antonelli and J. Y. Ying, *Curr. Opin. Colloid Interf. Sci.*, 1996, 1, 523.
249. D. M. Antonelli, A. Nakahira and J. Y. Ying, *Inorg. Chem.*, 1996, 35, 3126.
250. A. Sayari and P. Liu, *Micropor. Mater.*, 1997, 12, 149.
251. U. Ciesla and F. Schuth, *Micropor. Mesopor. Mater.*, 1999, 27, 131.
252. G. J. D. Soler-illia, C. Sanchez, B. Lebeau and J. Patarin, *Chem. Rev.*, 2002, 102, 4093.
253. D. E. De Vos, M. Dams, B. F. Sels and P. A. Jacobs, *Chem. Rev.*, 2002, 102, 3615.

254. B. Valange, J. L. Guth, F. Kolenda, S. Lacombe and Z. Gabelica, *Micropor. Mesopor. Mater.*, 2000, 35–36, 597.
255. V. Luca, J. N. Watson, M. Ruschena and R. B. Knott, *Chem. Mater.*, 2006, 18, 1156.
256. X. Yang, F. C. Jentoft, R. E. Jentoft, F. Girgsdies and T. Ressler, *Catal. Lett.*, 2002, 81, 25.
257. M. Lundberg, B. Skarman, F. Cesar and L. R. Wallenberg, *Micropor. Mesopor. Mater.*, 2002, 54, 97.
258. M. Lundberg, B. Skarman and L. R. Wallenberg, *Microporous Mesoporous Mater.*, 2004, 69, 187.
259. Y. Castro, B. Julian, C. Boissie`re, B. Viana, H. Amenitsch, D. Grosso and C. Sanchez, *Nanotech.*, 2007, 18, 055705.
260. M. Yada, H. Kitamura, A. Ichinose, M. Machida and T. Kijima, *Angew. Chem., Int. Ed.*, 1999, 38, 3506.
261. D. M. Lyons, L. P. Harman and M. A. Morris, *J. Mater. Chem.*, 2004, 14, 1976.
262. C. F. Cheng, Z. Luan and J. Klinowski, *Langmuir*, 1995, 11, 2815.
263. N. Pal and A. Bhaumik, *Adv. Colloid Interface Sci.*, 2013, 189–190, 21.
264. D. Gu and F. Schuth, *Chem. Soc. Rev.*, 2014, 43, 313.
265. B. Haffer, C. Weinberger and M. Tiemann, *Eur. J. Inorg. Chem.*, 2012, 3283.
266. C. S. Kim, H. I. Lee, J. K. Shon, J. Y. Hur, M. S. Kang, S. S. Park, S. S. Kong, J. A. Yu, M. Seo, D. Li, S. S. Thakur and J. M. Kim, *Chem. Lett.*, 2008, 140.
267. B. Liu and R. T. Baker, *J. Mater. Chem.*, 2008, 18, 5200.
268. Y. G. Wang, Y. Q. Wang, J. W. Ren, Y. Mi, F. Y. Zhang, C. L. Li, X. H. Liu, Y. Guo, Y. L. Guo and G. Z. Lu, *J. Solid State Chem.*, 2010, 183, 277
269. Y. F. Shi, Y. Wan and D. Y. Zhao, *Chem. Soc. Rev.*, 2011, 40, 3854.
270. K. Zimny, C. Carteret, M. J. Stebe and J. L. Blin, *J Phys Chem. C*, 2011, 115, 8684.
271. G. S. Prado and C. Airoidi, *J. Mater. Chem.*, 2002, 12, 3823.
272. A. Knoefel, M. Lutecki, C. Martin, M. Mertens, V. Hornebecq and P. L. Llewellyn, *Microporous Mesoporous Mater.*, 2010, 128, 26.
273. M. J. Rosen, *Surfactants and interfacial phenomena*, A John Wiley & Sons, Inc., Publication, 3rd edition, 2004.
274. R. M. M. Britoand and W. L. C. Vaz, *Anal. Biochem.*, 1986, 152, 250.
275. D. Bradshaw, S. E. Hankari and L. L. Spagnolo, *Chem. Soc. Rev.*, 2014, 43, 5431.
276. Q. Huo, D. I. Margolese, U. Ciesla, D. G. Demuth, P. Feng, T. E. Gier, P. Sieger, A. Firouzi, B. F. Chmelka, F. Schuth, and G. D. Stucky, *Chem. Mater.*, 1994, 6, 1176.
277. A. Sayari, *Stud. Surf. Sci. Catal.*, 1996, 102,1.
278. G. J. A. A. Soler-Illia, A. Louis and C. Sanchez, *Chem. Mater.*, 2002, 14, 750.
279. Y. Chena, S. K. Lunsford, Y. Song, H. Ju, P. Falaras, V. likodimos, A. G. Kontos, and D. D. Dionysiou, *Chem. Eng. J.*, 2011, 170, 518.
280. S. A. Bagshaw, E. Prouzet, and T. J. Pinnavaia, *Science*, 1995, 269, 1242.
281. Y. P. Zhu, Z. Y. Yuan, *Mesoporous Organic-Inorganic Non-Siliceous Hybrid Materials*, Springer Heidelberg New York Dordrecht London, 2015.
282. A. Sayari, Y. Yang, M. Kruk, and M. Jaroniec, *J. Phys. Chem. B*, 1999, 103, 3651.
283. Y. Ren, Z. Ma and P. G. Bruce, *Chem. Soc. Rev.*, 2012, 41, 4909.
284. Y. Liu, J. Goebler and Y. Yin, *Chem. Soc. Rev.*, 2013, 42, 2610

285. Z. Yang, Y. Zhang and Z. Schnepf, *J. Mater. Chem. A*, 2015, 3, 1408.
286. S. A. Ghom, C. Zamani, T. Andreu, M. Epifani and J. R. Morante, *Appl. Catal. B Environ.*, 2011, 108–109, 32.
287. E. Rossinyol, J. Arbiol, F. Peiro, A. Cornet, J. R. Morante, B. Tian, T. Bo and D. Zhao, *Sensors and Actuators B Chem.*, 2005, 109, 57.
288. H. F. Yang and D. Y. Zhao, *J. Mater. Chem.*, 2005, 15, 1217.
289. D. Terribile, A. Trovarelli, C. D. Leitenburg and G. Dolcetti, *Chem. Mater.*, 1997, 9, 2676.
290. J. Xu, K. Z. Long, F. Wu, B. Xue, Y. X. Li and Y. Cao, *Appl. Catal. A Gen.*, 2014 484,
291. S. Pavasupreea, Y. Suzukia, S. P. Art and S. Yoshikawa, *Ceramics International*, 2005, 31, 959.
292. W. Yuejnan, M. Jingnieng, L. Mengfei and H. Mai, *Journal of Rare Earths*, 2007, 25, 58.
293. X. Liang, J. Xiao, B. Chen and Y. Li, *Inorg. Chem.*, 2010, 49, 8188.
294. N. Perkas, H. Rotter, L. Vradman, M. V. Landau, and A. Gedanken, *Langmuir*, 2006, 22, 7072.
295. C. Ho, J. C. Yu, T. Kwong, A. C. Mak and S. Lai, *Chem. Mater.*, 2005, 17, 4514.
296. S. Liang, E. Broitman, Y. Wang, A. Cao and G. Veser, *J. Mater. Sci.*, 2011, 46, 2928.
297. Z. Y. Yuan, V. Idakiev, A. Vantomme, T. Tabakova, T. Z. Ren and B. L. Su, *Catal. Today*, 2008, 131, 203.
298. I. V. Zagaynov and A. K. Buryak, *J. Sol-Gel Sci. Technol.*, 2015, 74, 103.
299. C. Ni, X. Li, Z. Chen, H. Y. H. Li, X. Jia, I. Shah, J. Q. Xiao, *Microporous Mesoporous Mater.*, 2008, 115, 247.
300. C. Deeprasertkul, R. Longloilert, T. Chaisuwan and S. Wongkasemjit, *Mater. Lett.*, 2014, 130, 218.
301. J. Roggenbuck, H. Schafer, T. Tsoncheva, C. Minchev, J. Hanss and M. Tiemann, *Microporous Mesoporous Mater.*, 2007, 101, 335.
302. S. C. Laha and R. Ryoo, *Chem. Commun.*, 2003, 2138.
303. H. Li, G. Lu, Y. Wang, Y. Guo and Y. Guo, *Catal. Commun.*, 2010, 11, 946.
304. L. Changlin, G. Xin, W. Yanqin, W. Yaojun, W. Yangang, L. Xiaohui and L. Guanzhong, *Journal of Rare Earths*, 2009, 27, 211.
305. S. Hao, J. Hou, P. Aprea and T. Lv, *Ind. Eng. Chem. Res.*, 2014, 53, 14617.
306. J. Zhang, J. Guo, W. Liu, S. Wang, A. Xie, X. Liu, J. Wang and Y. Yang, *Eur. J. Inorg. Chem.*, 2015, 969.
307. Y. Kamimura, M. Shimomura and A. Endo, *J. Colloid Interface Sci.*, 2014, 436, 52.
308. B. Lu, Z. Li and K. Kawamoto, *Mater. Res. Bullet.*, 2013, 48, 2504.
309. Y. Li, Q. Sun, M. Kong, W. Shi, J. Huang, J. Tang and X. Zhao, *J. Phys. Chem. C*, 2011, 115, 14050.
310. G. Zhang, Z. Shen, M. Liu, C. Guo, P. Sun, Z. Yuan, B. Li, D. Ding and T. Chen, *J. Phys. Chem. B*, 2006, 110, 25782.
311. J. Zhang, H. Yang, S. Wang, W. Liu, X. Liu, J. Guo and Y. Yang, *Cryst. Eng. Comm*, 2014, 16, 8777.
312. G. Chen, Q. Xu, Y. Wang, G. Songa and W. Fan, *J. Mater. Chem. A*, 2015, 3, 7022.
313. B. D. Kosynkin, A. A. Arzgatkina, E. N. Ivanov, M. G. Chtoutsa, A. I. Grabko, A.V. Kardapolov and N. A. Sysina, *J. Alloys Compd.*, 2000, 303-304, 421.
314. T. C. Schutt, *Ceram. Bull.*, 1972, 51, 155.
315. S. Bernal, G. Blanco, J. J. Calvino, J. A. P. Omil and J. M. Pintado, *J. Alloys Compd.*, 2006, 408–412, 496.
316. J. Kaspar, P. Fornasiero and N. Hickey, *Catal. Today*, 2003, 77, 419.
317. R. Di Monte and J. Kaspar, *Top. Catal.*, 2004, 28, 47.

318. B. Sun and W. Liu, *J. Power Sources*, 2012, 217, 114.
  319. L. Vivier and D. Duprez, *Chem. Sus. Chem.*, 2010, 3, 654.
  320. M.F. Ahmed (Ed.), *Technologies for arsenic removal from drinking water*, Bangladesh University of Engineering and Technology, Dhaka, Bangladesh, 2001, 251.
  321. R. H. Li, Q. Li, S. Gao and J. K. Shang, *Chem. Eng. J.*, 2012, 185, 127.
  322. Q. Z. Feng, Z. Y. Zhang, Y. H. Ma, X. He, Y. L. Zhao and Z. F. Chai, *Nanoscale Res. Lett.*, 2012, 7, 1.
  323. S. Recillas, J. Colon, E. Casals, E. Gonzalez, V. Puentes, A. Sanchez and X. Font, *J. Haz. Mater.*, 2010, 184, 425.
  324. J. Suna, C. Wang, L. Zenga, P. Xua, X. Yanga, J. Chena, X. Xinga, Q. Jinb and R. Yua, *Mater. Res. Bullet.*, 2016, 75, 110.
  325. B. Peng, Z. Luan, J. Ding, Z. Di, Y. Li and B. Tian, *Mater. Lett.*, 2005, 59, 399.
  326. Z. C. Di, J. Ding, X. J. Peng, Y. H. Li, Z. K. Luan and J. Liang, *Chemosphere*, 2006, 62, 861
  327. A. M. Raichur and M. J. Basu, *Sep. Purif. Technol.*, 2001, 24, 121.
  328. Z. Tang, Y. Zhang and Y. Xu, *RSC Adv.*, 2011, 1, 1772.
  329. B. Cai, F. Chen, X. Shen, L. Chen and J. Zhang, *Appl. Catal. B Environ.*, 101, 160.
  330. N. S. Arul, D. Mangalaraj, P. C. Chen, N. Ponpandian, P. Meena and Y. Masuda, *J. Sol-Gel. Sci. Technol.*, 2012, 64, 515.
  331. S. Hu, F. Zhou, L. Wang and J. Zhang, *Catal. Comm.*, 2011, 12, 794.
  332. B. S. Chaudhary, S. Panigrahi, S. Nayak, B. Satpati, S. Bhattacharjee and N. Kulkarni, *J. Mater. Chem.*, 2010, 20, 2381.
  333. M. Das, S. Patil, N. Bhargava, J. F. Kang, L. M. Riedel, S. Seal and J. J. Hickman, *Biomaterials.*, 2007, 28, 1918.
  334. S. Kar, C. Patel and S. Santra, *J. Phys. Chem. C*, 2009, 113, 4862.
  335. A. Asati, S. Santra, C. Kaittanis, S. Nath and J. M. Perez, *Angew. Chem., Int. Ed.*, 2009, 48, 2308.
  336. R. W. Tarnuzzer, J. Colon, S. Patil and S. Seal, *Nano Lett.*, 2005, 5, 2573.
  337. J. M. Perez, A. Asati, S. Nath and C. Kaittanis, *Small*, 2008, 4, 552.
  338. D. Schubert, R. Dargusch, J. Raitano and S. W. Chan, *Biochem. Biophys. Res. Commun.*, 2006, 342, 86.
  339. S. S. Lee, H. G. Zhu, E. Q. Contreras, A. Prakash, H. L. Puppala and V. L. Colvin, *Chem. Mater.*, 2012, 24, 424.
  340. J. P. Chen, S. Patil, S. Seal and J. F. McGinnis, *Nat. Nanotechnol.*, 2006, 1, 142.
  341. S. Babu, J. H. Cho, J. M. Dowding, E. Heckert, C. Komanski, S. Das, J. Colon, C. H. Baker, M. Bass, W. T. Self and S. Seal, *Chem. Commun.*, 2010, 46, 6915.
-



## Chapter 2

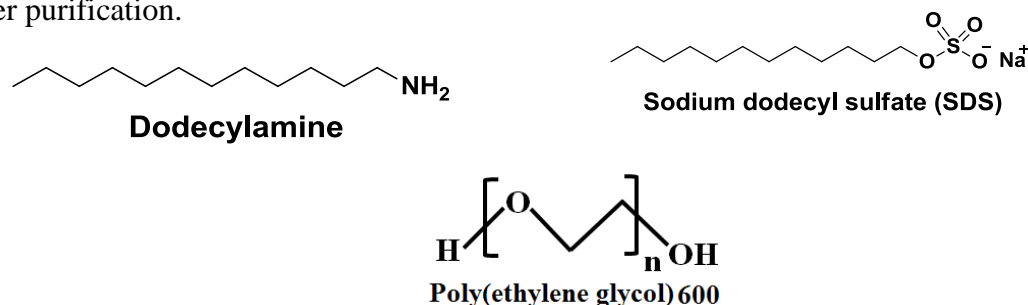
# Materials Synthesis and Characterization

**Outline:** *This chapter deals with a discussion of the synthetic methodology developed and adopted for the synthesis of pure as well as samarium ( $\text{Sm}^{3+}$ ) and europium ( $\text{Eu}^{3+}$ ) doped ceria ( $\text{CeO}_2$ ), and their characterization by various sophisticated instrumental techniques employed in the present study. Thermogravimetric analysis/differential scanning calorimetry (TGA/DSC), X-ray diffraction (XRD), BET  $\text{N}_2$  gas sorption, Fourier transform-infra red spectroscopy (FTIR), UV-visible diffuse reflectance spectroscopy (UV-vis DRS), photoluminescence (PL), Raman spectroscopy, X-ray photoelectron spectroscopy (XPS), electron paramagnetic resonance (EPR), field emission scanning electron microscopy (FESEM), high resolution transmission electron microscopy (HRTEM), temperature programmed reduction (TPR) and temperature programmed desorption (TPD) were used to understand the structural, optical and other typical properties of the synthesized pure and doped  $\text{CeO}_2$  powders. Finally, the adsorption and removal of Cr(VI), and photodegradation of dyes under direct sunlight by the high surface area mesostructured pure and  $\text{Sm}^{3+}$  modified mesoporous  $\text{CeO}_2$  samples have been investigated.*

## 2.1. Synthetic Methodology

In order to obtain high quality nano-sized CeO<sub>2</sub> particles in terms of their particle size, uniformity, purity, homogeneity, morphology, specific surface area and crystallinity etc., many methods have been developed and explored such as homogeneous precipitation techniques with different precipitating agents and additives, co-precipitation, combustion method, microemulsion, hydrothermal, spray pyrolysis, solid-state reactions, sol-gel, electrochemical methods, micelle route, surfactant assisted synthesis, microwave-assisted synthesis etc<sup>1-12</sup>. Each method has its own merits and demerits. Compared to the above mentioned methods, precipitation is one of the most utilized and economically feasible method for the large-scale production of nano-sized CeO<sub>2</sub> particles due to the cheaper salt precursors, simple operation and mild adjustable reaction conditions, which satisfy a variety of purposes.

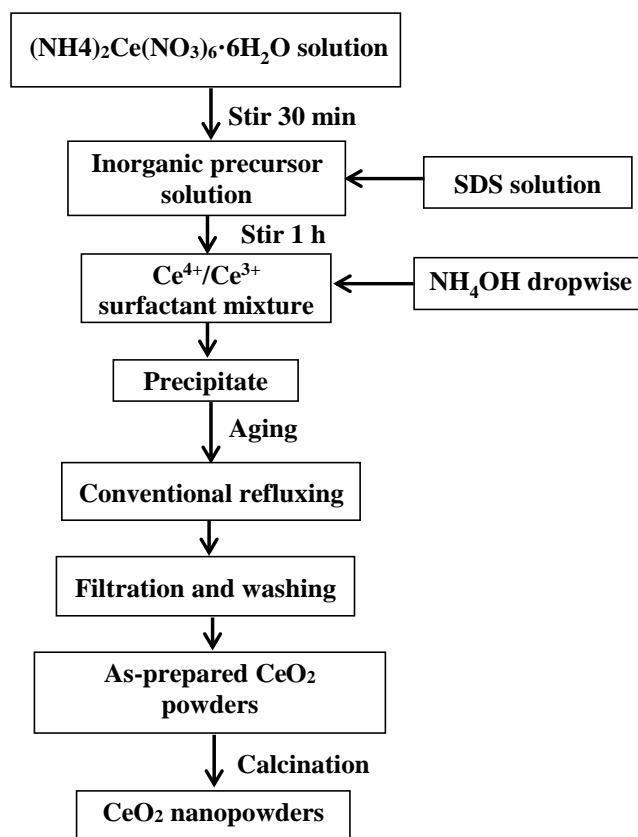
In this present work, a facile aqueous solution-based surfactant assisted route has been adopted for the synthesis of pure as well as Sm<sup>3+</sup> (0.5, 1, 2, 5, 10 and 20 mol%) and Eu<sup>3+</sup> (0.5, 1, 2 and 5 mol%) doped CeO<sub>2</sub>. The synthetic procedure adopted here is versatile, simple and cost-effective. The metal inorganic precursors were used for the synthesis of materials are cheaper and readily available. Surfactant acts as the template or pore directing agents. Chemical formulas of the surfactants used during synthesis in the present work are given in **Fig. 2.1**. The materials were synthesized using metal inorganic precursors by a homogeneous precipitation route and subjected to further hydrolysis via both conventional and microwave reflux method. The chemicals used for the synthesis purpose are given in **Table 2.1**. All chemicals are commercially available with 99.9 % purity and were used as received without further purification.



**Fig. 2.1.** Surfactants used in the synthesis of mesoporous CeO<sub>2</sub> or doped CeO<sub>2</sub>.

**Table 2.1.** List of chemicals used in the synthesis of pure as well as  $\text{Sm}^{3+}$  or  $\text{Eu}^{3+}$  doped  $\text{CeO}_2$ .

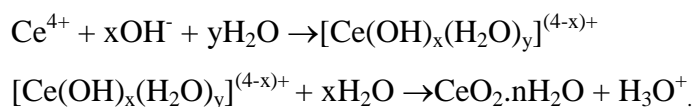
Chemicals	Formula	Manufacturer
Ceric ammonium nitrate	$(\text{NH}_4)_2\text{Ce}(\text{NO}_3)_6 \cdot 6\text{H}_2\text{O}$	Merck, India
Samarium oxide	$\text{Sm}_2\text{O}_3$	CDH, India
Europium oxide	$\text{Eu}_2\text{O}_3$	SD fine, India
Dodecylamine, DDA	$\text{C}_{12}\text{H}_{25}\text{NH}_2$	Merck, Germany
Sodium dodecyl sulfate, SDS	$(\text{C}_{12}\text{H}_{25}\text{SO}_4\text{Na})$	Merck, India
Polyethelene glycol	$\text{C}_{16}\text{H}_{33}(\text{OCH}_2\text{CH}_2)_{10}\text{OH}$	Sigma-Aldrich
Isopropanol	$(\text{CH}_3)_2\text{CHOH}$	Merck, India
Ethanol	$\text{C}_2\text{H}_5\text{OH}$	Merck, Germany
Ammonium hydroxide (25%)	$\text{NH}_4\text{OH}$	Merck, India
Nitric acid	$\text{HNO}_3$	Merck, India

**Fig. 2.2.** Schematic flow chart illustrating various steps involved for the synthesis of pure  $\text{CeO}_2$ .

### 2.1.1. Synthesis of pure CeO<sub>2</sub>

Pure CeO<sub>2</sub> was prepared by adopting a surfactant mediated co-precipitation method using (NH<sub>4</sub>)<sub>2</sub>Ce(NO<sub>3</sub>)<sub>6</sub>.6H<sub>2</sub>O as an inorganic precursor and sodium dodecyl sulfate (SDS) as a surfactant. Initially, 0.5 M (NH<sub>4</sub>)<sub>2</sub>Ce(NO<sub>3</sub>)<sub>6</sub>.6H<sub>2</sub>O solution was prepared by dissolving requisite amount of it in deionized water then a clear solution of 18 wt.% sodium dodecyl sulphate (SDS) was prepared in water-isopropanol (molar ratio 3 : 1). After that these two solutions were mixed with vigorous stirring for 2 h. Upon complete mixing, 30% NH<sub>4</sub>OH was added drop wise to get the precipitate (till the pH becomes 9). The resulting precipitate was kept for 2 days at room temperature for aging. It was then filtered by using Whatman filter paper and washed with distilled water several times and with absolute ethanol 2-3 times to remove excess surfactant and other impurities. Then it was dispersed in a certain volume of water and conventionally refluxed for 24 h. The final precipitate was washed with distilled water and ethanol and then dried in a water bath to obtain the as-prepared powder (denoted at 100CeSDSasp). The as-prepared powder was calcined in air atmosphere at selected temperatures, ranging from 500°C to 1000°C for 2 h.

For comparison purpose, pure CeO<sub>2</sub> without any surfactant was also prepared. The schematic flow chart of various steps involved for the synthesis of pure CeO<sub>2</sub> is given in Fig. 2.2 and the notation used for both the samples prepared by surfactants free and surfactant assisted route are tabulated in Table 2.2. Under basic conditions at room temperature the reaction of ceric ammonium nitrate with ammonia produce a gelatinous precipitation of hydrous cerium oxide. Ce<sup>4+</sup> ions produce from ceric ammonium nitrate precursors undergo strong hydration due to their lower basicity and higher charge which combines with water molecules or OH<sup>-</sup> form complexes in the form of [Ce(OH)<sub>x</sub>(H<sub>2</sub>O)<sub>y</sub>]<sup>(4-x)+</sup>, where (x + y) is the coordination number of Ce<sup>4+</sup>. In an aqueous solution further polymerization and precipitation of these hydroxides leading to the formation of hydrous oxide and then to the oxide as H<sub>2</sub>O, being a polar molecule, tends to take protons away from coordinated hydroxide. Probable reaction steps can be described as represented below<sup>13-16</sup>



## 2.1.2. Synthesis of Sm<sup>3+</sup> doped CeO<sub>2</sub>

### 2.1.2.1. Synthesis of Sm<sup>3+</sup> doped CeO<sub>2</sub> by using different surfactants via conventional refluxing route

For the synthesis of Sm<sup>3+</sup> doped CeO<sub>2</sub>, the similar preparative method as described above for pure CeO<sub>2</sub> was used. To understand the effect of surfactants on the properties of CeO<sub>2</sub>, a representative composition of 1 mol% Sm<sup>3+</sup> doped CeO<sub>2</sub> was prepared using (NH<sub>4</sub>)<sub>2</sub>Ce(NO<sub>3</sub>)<sub>6</sub>·6H<sub>2</sub>O and Sm<sub>2</sub>O<sub>3</sub> as inorganic precursors, dilute aqueous ammonia solution as the precipitating agent and dodecyl amine (DDA), sodium dodecyl sulphate (SDS), or poly ethylene glycol (PEG) as a surfactant. Initially, a clear surfactant solution (18 wt.%) of SDS, DDA, or PEG was prepared separately by dissolving it in water-isopropanol (1:3) at room temperature with stirring for 1 h. Samarium nitrate was prepared by dissolving the requisite amount of Sm<sub>2</sub>O<sub>3</sub> in the minimum volume of concentrated nitric acid. Samarium nitrate was then dissolved separately in distilled water. After that this solution was mixed with 0.5 M (NH<sub>4</sub>)<sub>2</sub>Ce(NO<sub>3</sub>)<sub>6</sub>·6H<sub>2</sub>O solution and stirred for 30 min. The surfactant solution was added dropwise to the mixture solution containing the inorganic salts under vigorous stirring conditions. Under magnetic stirring, an NH<sub>4</sub>OH solution (30 vol.%) was added dropwise to the above solution to obtain a precipitate at a pH of 9. After ageing, the precipitate was filtered, washed with water and ethanol for several times. Subsequently, it was dispersed in a certain volume of water and was subjected to conventional refluxing for 24 h. Finally, the precipitate was filtered, washed with distilled H<sub>2</sub>O and ethanol several times and dried. The as-prepared powder was grinded in an agate mortar to avoid agglomeration of particles and then calcined at various temperatures in air for 2 h.

### 2.1.2.2. Synthesis of Sm<sup>3+</sup> doped CeO<sub>2</sub> by using SDS via microwave refluxing

Sm<sup>3+</sup> doped CeO<sub>2</sub> (CeO<sub>2</sub>:Sm<sup>3+</sup>) by varying Sm<sup>3+</sup> concentrations (0.5, 1, 2, 5, 10 and 20 mol%) were synthesized using SDS as surfactant by the same procedure as described above except the precipitates were treated with microwave refluxing instead of conventional refluxing. Under magnetic stirring, an NH<sub>4</sub>OH solution (30 vol%) was added dropwise to the mixture solution of surfactant and salts to obtain a precipitate at a pH of 9. The mixture was aged at room temperature and then washed with water. Then it was dispersed in a certain volume of water and divided in to three parts of equal volume, one part directly filtered and

washed, and rest two parts were subjected to conventional and microwave refluxing (National, 2450 MHz, 300 W) for 24 h, and for 30 min at 90°C, respectively. Finally, the precipitate was filtered, washed with distilled water and ethanol several times and dried at 80°C. The as-prepared sample was then calcined at higher temperatures in air for 2 h.

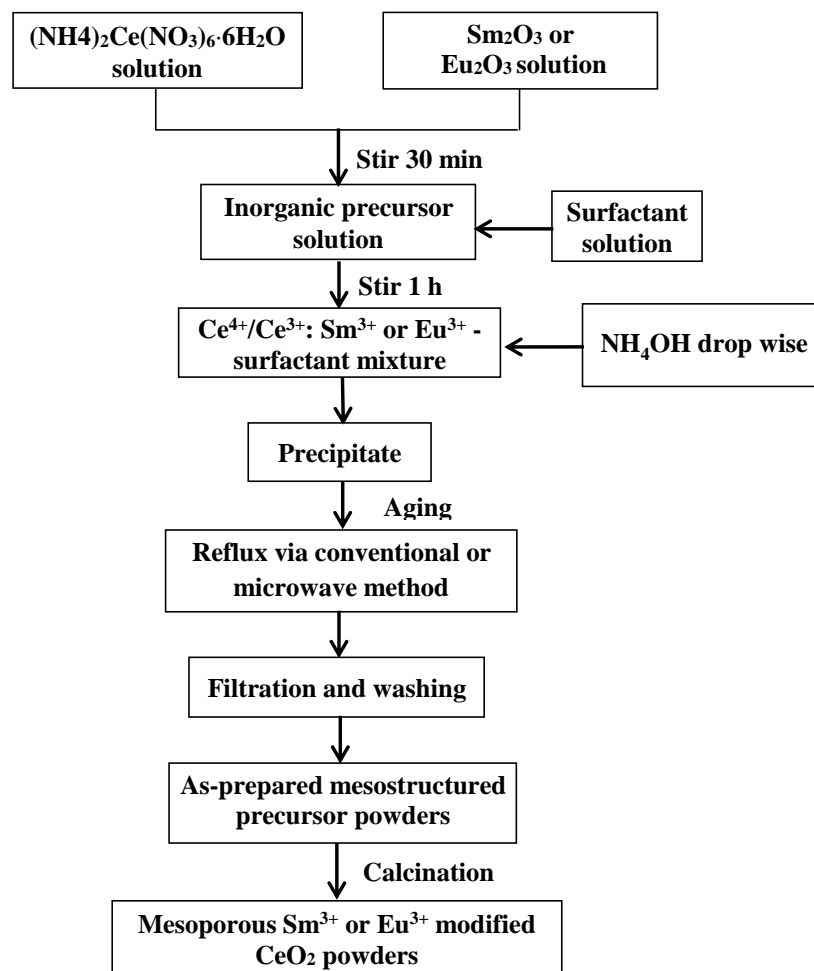


**Fig. 2.3.** Schematic flow chart of various steps involved for the synthesis of  $\text{Sm}^{3+}$  or  $\text{Eu}^{3+}$  doped  $\text{CeO}_2$ .

### 2.1.3. Synthesis of $\text{Eu}^{3+}$ doped $\text{CeO}_2$ by using SDS through conventional and microwave refluxing

Similar procedures were followed as described above for the synthesis of  $\text{Sm}^{3+}$  doped  $\text{CeO}_2$  at varying  $\text{Eu}^{3+}$  concentrations (0.5, 1, 2 and 5 mol%) using SDS as surfactant, except that  $\text{Eu}_2\text{O}_3$  was dissolved in the minimum volume of concentrated nitric acid and added to the

clear solution of  $(\text{NH}_4)_2\text{Ce}(\text{NO}_3)_6 \cdot 6\text{H}_2\text{O}$ . The flow chart of various steps involved for the synthesis of  $\text{Eu}^{3+}$  doped  $\text{CeO}_2$  is given in **Fig. 2.3**. Notations assigned for the as-prepared and calcined samples at various temperatures are listed in **Table 2.2**.

**Table 2.2.** Notations used in this thesis for pure,  $\text{Sm}^{3+}$  or  $\text{Eu}^{3+}$  doped  $\text{CeO}_2$  samples.

<b>Samples</b>	<b>Designation</b>	<b>Designation for as-prepared samples</b>	<b>Designation for calcined samples (say at <math>x^\circ\text{C}</math>)</b>
Pure $\text{CeO}_2$ prepared without SDS followed by conventional refluxing.	100Ce	100Ceasp	100Cex
Pure $\text{CeO}_2$ prepared with SDS followed by conventional refluxing.	100CeSDS	100CeSDSasp	100CeSDSx
$n$ mol% $\text{Sm}^{3+}$ doped $\text{CeO}_2$ prepared with SDS followed by conventional refluxing.	nSmCeSDS	nSmCeSDSasp	nSmCeSDSx
$n$ mol% $\text{Sm}^{3+}$ doped $\text{CeO}_2$ prepared with DDA followed by conventional refluxing.	nSmCeDDA	nSmCeDDAasp	nSmCeDDAx
$n$ mol% $\text{Sm}^{3+}$ doped $\text{CeO}_2$ prepared with PEG followed by conventional refluxing.	nSmCePEG	nSmCePEGasp	nSmCePEGx
$n$ mol% $\text{Sm}^{3+}$ doped $\text{CeO}_2$ prepared with SDS followed by microwave refluxing	nSmCeSDSMW	nSmCeSDSMWasp	nSmCeSDSMWx
$n$ mol% $\text{Sm}^{3+}$ doped $\text{CeO}_2$ prepared with SDS followed by microwave refluxing	nSmCeSDSNR	nSmCeSDSNRasp	nSmCeSDSNRx
$n$ mol% $\text{Eu}^{3+}$ doped $\text{CeO}_2$ prepared with SDS followed by conventional refluxing	nEuCeSDS	nEuCeSDSasp	nEuCeSDSx
$n$ mol% $\text{Eu}^{3+}$ doped $\text{CeO}_2$ prepared with SDS followed by microwave refluxing	nEuCeSDSMW	nEuCeSDSMWasp	nEuCeSDSMWx

## 2.2. Characterization and measurements

A brief description of various characterization techniques employed in the present study to understand the complete structural, optical and spectroscopic properties of the synthesized materials, such as thermogravimetric analysis/differential scanning calorimetry (TGA/DSC), X-ray diffraction (XRD), BET-BJH-surface area and pore size analysis, Fourier transform-infra red spectroscopy (FTIR), UV-visible diffuse reflectance spectroscopy (UV-vis DRS), X-ray photoelectron spectroscopy (XPS), field emission scanning electron microscopy (FESEM), high resolution transmission electron microscopy (HRTEM), temperature programmed reduction (TPR) and temperature programmed desorption (TPD) are discussed in this section.

### 2.2.1. Simultaneous thermal analysis (TGA/DSC)

Simultaneous thermal analysis (STA) allows the simultaneous measurement of both thermogravimetric (TGA) and differential scanning calorimetry (DSC) of a sample in a single instrument.<sup>17</sup> The crucible containing the sample and an empty reference crucible are heated at constant heat flow as a function of time or temperature and maintained at nearly the same temperature throughout the experiment.<sup>18</sup> The reference sample should possess a well-defined heat capacity over the scanned temperatures.<sup>18</sup> As the difference in the amount of heat required to increase the temperature of a sample and reference are measured as a function of temperature,<sup>19</sup> it provides information in details about the change of material property with the change of temperature.

The basic principle of this technique is that during the phase transitions of the sample more or less heat will flow to the sample holder than to the reference to maintain both at the same temperature.<sup>15</sup> Therefore, heat must flow in or out to the sample depends on whether the process is endothermic or exothermic. Both the shape and size of the peaks provide information about the nature of the sample. Generally, the sharp endothermic peak arises due to the change in crystallinity or fusion process where as the broad endotherm revealed dehydration or decomposition reaction. In general endothermic peaks arise due to the physical changes and exothermic peaks arise due to the chemical reaction.<sup>20</sup> Thermogravimetric analysis (TGA) is a technique in which the weight loss of a specimen in an environment (air or in an inert atmosphere, such as He/Ar) arises due to physical transition or chemical reaction, recorded as a function of time or temperature during heating or cooling at a controlled rate. A remarkable % of mass loss indicates the presence of volatile fraction in the substance. Thermal behavior of the synthesized nanopowders were studied using Netzsch, Germany (DSC/TGA), which was performed by continuous heating from 30°C to 1000°C at the heating rates of 10°C/min under air atmosphere using  $\alpha$ -Al<sub>2</sub>O<sub>3</sub> as a reference material.

### 2.2.2. X-ray diffraction (XRD)

X-ray diffraction (XRD) is an extremely important technique to determine the information about the crystal structure of all crystalline materials. Subsequently the technique of X-ray diffraction also provides information about the crystallite size, lattice parameter, chemical composition, state of ordering etc. X-rays are electromagnetic radiation of exactly



the same nature as light but of very much shorter wavelength and X-rays used in diffraction have wavelengths lying approximately in the range of 0.5-2.5 Å. According to Bragg's law the X-ray radiation of wavelength  $\lambda$  (in Å) at the incident angle  $\theta$  diffracted from two scattering planes which are separated by the distance  $d$  (in Å) is describe by equation:

$$n\lambda = 2d \sin\theta \quad (2.1)$$

Where  $n$  is the order of diffraction.



**Fig. 2.4.** Photograph of Rigaku Ultima-IV diffractometer.

The crystallite size of the nanopowder can be calculated by using Scherer's equation, from X-ray line broadening.

$$d = \frac{0.89\lambda}{\beta_c \cos\theta} \quad (2.2)$$

Where  $d$  is the crystallite size,  $\lambda$  is the wavelength of the X-rays,  $\theta$  is the diffraction angle and  $\beta_c$  is the instrumental corrected full width at half maximum corresponding to the diffraction peak.<sup>21</sup> The full width at half maximum ( $\beta_c$ ) corresponding to the diffraction peak was corrected by the relation:

$$\beta = \sqrt{(\beta_m^2 - \beta_i^2)} \quad (2.3)$$

Where  $\beta_m$  and  $\beta_i$  are the measured and instrumental full width at half maximum of the peaks, respectively. Powder X-ray diffraction data were recorded using Rigaku Ultima-IV (shown in Fig. 2.4) using  $\text{CuK}_\alpha$  radiation. The samples were scanned in  $2\theta$  ranges from 20 to 80° with the step size of 0.05° and scan rate of 4°/min.

### 2.2.3. Brunauer, Emmett and Teller (B.E.T.) measurements

Determination of the surface area of the nanosize particles is of paramount importance in the field of nanotechnology. The most extensively used technique for this purpose is B.E.T. isotherm.<sup>22</sup> As the various type of experimental adsorption isotherm is not to be explainable by Langmuir monolayer adsorption theory, Braunauer, Emmett and Teller developed a theory of multilayer adsorption which is known as B.E.T. theory. This theory based on following assumptions:<sup>23</sup>

- (a) Adsorption involves the formation of multilayer rather than monolayer,
- (b) Adsorption at one site does not affect the adsorption of neighboring site,
- (c) There is a dynamic equilibrium between the successive layer, and
- (d) Langmuir theory is adopted for the formation of single complexes.

On the basis of above postulates they derived the following equation:

$$\frac{1}{v[(P_0/P)-1]} = \frac{c-1}{v_m c} \left( \frac{P}{P_0} \right) + \frac{1}{v_m c} \quad (2.4),$$

which is called B.E.T. equation.

where P and P<sub>0</sub> are the equilibrium and the saturation pressure of adsorbates at the temperature of adsorption, v is the adsorbed gas quantity (for example, in volume units), and v<sub>m</sub> is the monolayer adsorbed gas quantity. The BET constant c, is expressed by:

$$c = \exp\left(\frac{E_1 - E_L}{RT}\right) \quad (2.5)$$

where E<sub>1</sub> is the heat of adsorption for the first layer, and E<sub>L</sub> is that for the second and higher layers and is equal to the heat of liquefaction.

Equation (2.4) is an adsorption isotherm and can be plotted as a straight line with  $\frac{1}{v[(P_0/P)-1]}$  on the y-axis and  $\frac{P}{P_0}$  on the x-axis. This plot is called a BET plot. The linear relationship of this equation is maintained only in the range of  $0.05 < \frac{P}{P_0} < 0.35$ . The value of the slope A and the y-intercept I of the line are used to calculate the monolayer adsorbed gas quantity v<sub>m</sub> and the BET constant c. The following equations can be used:

$$v_m = \frac{1}{A+I} \quad (2.6)$$

$$c = 1 + \frac{A}{I} \quad (2.7)$$

A total surface area  $S_{\text{total}}$  and a specific surface area  $S$  are evaluated by the following equations:

$$S_{\text{BET,total}} = \frac{v_m N s}{V} \quad (2.8)$$

$$S_{\text{BET}} = \frac{S_{\text{BET,total}}}{a} \quad (2.9)$$

where  $N$  is Avogadro's number,  $s$  is adsorption cross section,  $V$  is molar volume of adsorbent gas, and  $a$  is the molar weight of adsorbed species.



**Fig. 2.5.** Photograph of Quantachrome Autosorb-1 apparatus.

The textural properties of the sample were investigated by nitrogen sorption analysis. The nitrogen sorption isotherms and the corresponding pore size distribution were obtained at 77 K on a Quantachrome Autosorb-1 apparatus (shown in Fig. 2.5) after degassing the samples at 200°C for 3 h. The surface area, total pore volume and pore diameter of the samples were also calculated.

#### **2.2.4. Fourier transform-Infra red spectroscopy (FTIR)**

Fourier transform-infra red spectroscopy (FTIR) is a spectroscopic technique to study the interactions between matter and various frequencies of electromagnetic radiation in the infrared region of the electromagnetic spectrum.<sup>24</sup> In this spectral region molecules are excited to higher vibrational state by coupling of the electromagnetic waves with the molecular vibrations. The probability of a particular FTIR frequency being absorbed depends on the actual interaction between this frequency and the molecule. A vibrational mode in a

molecule to be “IR active”, it must be associated with changes in the dipole. A permanent dipole is not necessary, as the rule requires only a change in dipole moment.<sup>25</sup> FTIR spectroscopy is therefore a very powerful technique which provides fingerprint information on the chemical composition of the sample.

The essential equations for a Fourier-transformation relating the intensity falling on the detector,  $I(\delta)$ , to the spectral power density at a particular wavenumber,  $\bar{\nu}$ , given by  $B(\bar{\nu})$ , are as follows:  $\int_0^{+\infty} B(\nu) \cos(2\pi\nu)$

$$I = \int_0^{+\infty} B(\bar{\nu}) \cos(2\pi\nu \bar{\delta}) d\nu \quad (2.10)$$

which is one half of a cosine Fourier-transform pair, with the other being:

$$I = \int_{-\infty}^{+\infty} B(\bar{\nu}) \cos(2\pi\nu \bar{\delta}) d\nu \quad (2.11)$$

These two equations are interconvertible and are known as a Fourier-transform pair. The first shows the variation in power density as a function of the difference in pathlength, which is an interference pattern. The second shows the variation in intensity as a function of wavenumber. Each can be converted into the other by the mathematical method of Fourier-transformation. FTIR studies were carried on the prepared powders dispersed in analytical grade KBr using Perkin-Elmer IR spectrophotometer with a resolution of  $4 \text{ cm}^{-1}$ , in the range of  $400\text{-}4000 \text{ cm}^{-1}$ . The sample preparation was done by properly mixing about 0.1 g of the powder sample with KBr (sample: KBr = 1:4). This mixture was finely grounded and then it was placed between two evacuable die under pressure for 3-4 minutes to form a transparent pellet. These transparent pellets were used for the analysis. The FTIR spectrums are recorded in the spectral range of  $4000\text{-}400 \text{ cm}^{-1}$  with a Perkin Elmer FTIR spectrometer. FT-IR spectra of  $\text{CeO}_2$  powders in KBr pellets were recorded on a Perkin Elmer spectrum RX in the range of  $400\text{-}4000 \text{ cm}^{-1}$ .

### 2.2.5. UV-visible diffuse reflectance spectroscopy (UV-vis DRS)

UV-visible spectroscopy is the most useful optical techniques refer to absorption spectroscopy or reflectance spectroscopy in the ultraviolet-visible spectral region i.e. 200-800 nm. In the case of ultraviolet visible spectroscopy, electrons get excited from its ground state to higher energy state due to absorption of the electromagnetic radiations.<sup>26</sup> The energy of the

absorbed electromagnetic radiation is equal to the energy difference between the ground state and excited states.<sup>24</sup> Generally, the most favored transition is from the highest occupied molecular orbital (HOMO) to lowest unoccupied molecular orbital (LUMO). UV-Vis spectroscopy are used to measure both in a quantitative way to determine concentrations of an absorbing species in solution, and band gap of the semiconductor by using the Beer-Lambert law and Kubelka-Monk plot, respectively.

The expression of Beer-Lambert law is

$$A = \log \frac{I_0}{I} = \epsilon cL \quad (2.12)$$

where A is the absorbance, in absorbance units (a.u.),  $I_0$  is the intensity of the incident light at a given wavelength, I is the transmitted intensity, L the path length through the sample, and c the concentration of the absorbing species and  $\epsilon$  is the molar absorptivity or extinction coefficient. For the evaluation of band gap energy of the nanopowder the reflectance data was converted to the absorption coefficient  $F(R_\infty)$  values according to the Kubelka–Munk equation<sup>27-29</sup> i.e.

$$F(R_\infty) = \frac{(1-R_\infty)^2}{2R_\infty} \quad (2.13)$$

Where  $F(R_\infty)$  is equivalent to the absorption coefficient. band gap of the nanopowder were calculated by plotting  $[F(R_\infty) hv]^{1/2}$  vs.  $hv$ . UV-visible (UV-vis) diffuse reflectance spectra of the nanopowder were measured using a Shimadzu spectrometer (UV-2450) using  $BaSO_4$  as a blank.

### 2.2.6. Photoluminescence spectroscopy (PL)

Although photoluminescence (PL) spectroscopy is very similar to that of UV-visible absorption spectroscopy but they have two basic differences (i) in PL spectroscopy transition involved from a higher energy level or state to a lower energy level which is the reverse process of UV-visible absorption spectroscopy, and (ii) PL spectroscopy is a zero background experiment whereas UV-visible absorption spectroscopy is non zero background experiment.<sup>30</sup> Therefore, PL measurement is more sensitive than UV-visible absorption spectroscopy and widely used for the detection of optoelectronic properties of the nanopowder, which provide valuable information about the quality of surface, impurity levels, gauge alloy disorder and interface roughness. A typical PL spectrum is just a plot of

the PL intensity as a function of wavelength for a fixed excitation wavelength. Photoluminescence excitation (PLE) measurement is also very useful for materials with low transmission which are difficult to study via electronic absorption spectrum.

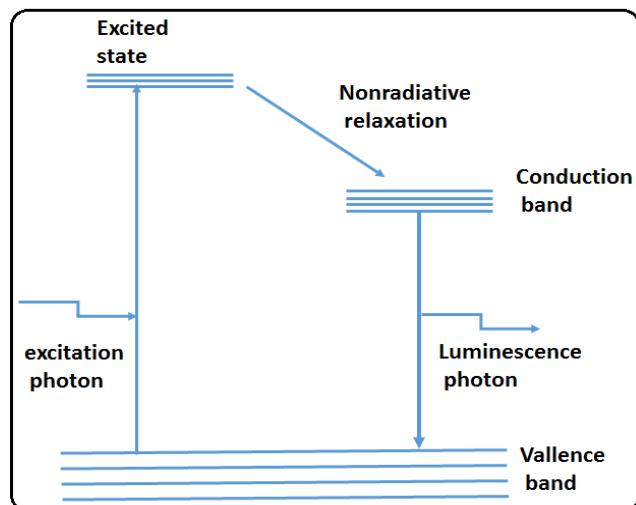


**Fig. 2.6.** Schematic diagram showing transitions giving rise to absorption and fluorescence emission spectra.

There has been a great interest in lanthanide luminescence due to their line-like emission arises from well shielded intraconfigurational f-f transitions, which leads to high color purity of the emitted light.<sup>31</sup> Basic principles of luminescence spectroscopy are shown in above Fig. 2.6. The emission and excitation spectra of the nanopowder were recorded using Jobin Yvon spectrofluorimeter (Fluoromax-4P) at room temperature.

### 2.2.7. X-ray photoelectron spectroscopy (XPS)

X-ray photoelectron spectroscopy (XPS) is a surface-sensitive quantitative spectroscopic technique, which can be used to analyze the specific element, surface composition, empirical formula, chemical environment and discriminate between different oxidation states of the sample under study.<sup>32</sup> In XPS material being analyzed is illuminated with a beam of X-rays (most commonly employed sources are  $MgK_{\alpha}$  radiation :  $h\nu = 1253.6$  eV and  $AlK_{\alpha}$  radiation :  $h\nu = 1486.6$  eV) in a high vacuum ( $P \sim 10^{-8}$  millibar) or ultra-high vacuum (UHV;  $P < 10^{-9}$  millibar) conditions leading to ionization and the emission of a core (inner shell) electron. As the core atomic orbital of each and every element is associated with a characteristic binding energy therefore the peaks at particular energies indicates the

presence of a specific element furthermore concentration of the element or its particular oxidation state can be calculated quantitatively from the relative area of the peak. Binding energy of the emitted electrons can be determined by using Ernest Rutherford equation:

$$E_{\text{binding}} = E_{\text{photon}} - (E_{\text{kinetic}} + \phi) \quad (2.14)$$

where  $E_{\text{binding}}$  is the binding energy (BE) of the electron,  $E_{\text{photon}}$  is the energy of the X-ray photons being used,  $E_{\text{kinetic}}$  is the kinetic energy of the electron as measured by the instrument and  $\phi$  is the work function dependent on both the spectrometer and the material.

X-ray photoelectron spectra were recorded by using a SPECS, Germany spectrometer, with an Al monochromator (1486.6 eV) and a MgK $_{\alpha}$  source (1253.6 eV) operating under a vacuum of  $2 \times 10^{-8}$  Torr. The deconvolution of the XPS spectra for the analysis of chemical composition of the prepared samples, were carried out using origin software.

### 2.2.8. Field emission scanning electron microscopy (FESEM)

The field emission scanning electron microscope (FESEM) is a type of electron microscope which provides topographical and elemental information at magnifications of 10x to 3,00,000x, by scanning the sample on surface or entire with a high-energy beam of electrons emitted from field emission gun.<sup>33</sup>

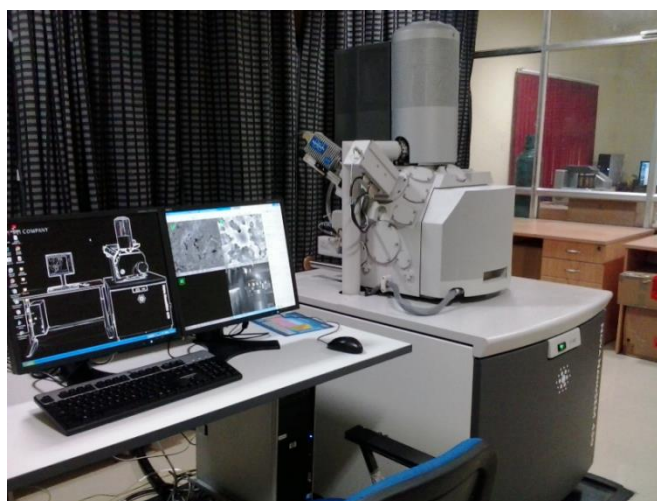


**Fig. 2.7.** Photograph of Nova Nano SEM 450.

Field emission SEM (FESEM) produces clearer and less electrostatically distorted images with better spatial resolution of 0.5 to 1 nm than scanning electron microscope (SEM)

and also minimized sample charging during analysis. In FESEM primary electrons liberated from a field emission source are subjected to narrow scan beam to interact with the specimen as a result secondary electrons are emitted from each spot on the object which combined with back scattered electron produces an electronic signal that finally transformed to a video scan-image. In this study FESEM micrograph were carried out with a Nova Nano SEM 450 (shown in Fig. 2.7) equipped with an energy dispersive X-ray spectrometer (EDX). The samples were coated with gold by sputter coater before analysis.

### 2.2.9. High resolution transmission electron microscopy (HRTEM)

High resolution transmission electron microscopy (HRTEM) is a technique which allowing unique advantage for analyzing crystal structures, lattice imperfections, stacking faults, dislocations, crystallite size and grain boundaries to a variety of materials on an atomic resolution scale.<sup>34,35</sup>



**Fig. 2.8.** Photograph of JEOL-JEM 2100 TEM.

The technique involved a direct interaction of energetic electrons with the sample and allowed both the transmitted and the scattered beams to create an interference image. Specimen preparation is consider very important factor in electron microscopy as the image quality is highly dependent on the thickness of solid phases. Thinner the specimen less than 50-100 nm provide better the resolution and better contrast due to sufficient transmittance. Specimen for HRTEM analysis prepared by disperse a few milligram of the powder in a few



milliliter of ethanol (EtOH) then subjected to ultrasonication for 30 min after that a drop of the suspension deposit it on a carbon coated copper grid and allowed it to keep in open atmosphere for few minute to evaporate liquid. The electron microscopic investigations of the nanopowder were carried on JEOL-JEM 2100 transmission electron microscope (shown in Fig. 2.8) operating at 200 kV.

#### **2.2.10. Temperature programmed reduction (TPR) and temperature programmed desorption (TPD)**

Temperature programmed reduction (TPR) is a widely used technique to study the reduction behaviour of catalysts and determines the number of reducible species present on the catalyst surface.<sup>36</sup> In TPR the specimen is exposed to a reductive gaseous stream ( $H_2$  or CO in an inert gas nitrogen or argon) in a well-defined temperature change, which is usually linear in time. Total amount of  $H_2$  or CO consumed by the specimen can be determined quantitatively by measuring the composition ( $H_2$  or CO content) of the reducing gas mixture at the outlet of the reactor, from which the degree of reduction can be calculated. Many authors suggest that the utility of temperature programmed reduction can be further enhanced by combining it with other techniques, such as temperature programmed desorption.<sup>37</sup> It is very useful to define the nature of the catalyst surface which may contain acidic or basic site, for this purpose the most often required experiments are TPD-measurements by using an acid ( $CO_2$  and  $SO_2$ ) or base gas (dry  $NH_3$ ). The TPR and TPD measurements were performed in an Auto Chem II (Micromeritics) Chemisorb 2750 TPD/TPR system. For TPR analysis, 140 mg of the nanopowder were pre-treated at  $120^\circ C$  in high pure helium gas (25cc/min) for 1 h, then cooled to room temp in helium. The TPR measurements were performed first by reducing the sample with 5%  $H_2/Ar$  with a flow rate 25 cc/min, from room temperature to  $850^\circ C$ . The temperature increased with a ramping rate of  $10^\circ C$ . For  $NH_3$ -TPD experiment, 200 mg of the sample was pre-treated at  $600^\circ C$  in 30 mL high pure helium flow for 10 min, then cooled down to  $120^\circ C$  in helium flow which was further subjected to  $NH_3$  adsorption/saturation by 10%  $NH_3$  in He gas@30mL/min for 30 min. Finally, the sample was exposed to flowing He ( $30\text{ mL min}^{-1}$ ) for 1 h at  $120^\circ C$  to remove physically bound ammonia from the surface. The desorption experiment was carried out from 120 to  $800^\circ C$  at a heating rate of  $10^\circ C\text{ min}^{-1}$ .

### 2.3. Cr(VI) adsorption study

Due to the large specific surface area, synthesized nanopowder are supposed to be an excellent sorbent for the removal of poisonous pollutants or heavy metal ions from aqueous solution. In the present study, Cr(VI) adsorption capacities of the synthesized nanopowder were examined in details as a function of contact time, pH of the medium, amount of adsorbent and concentration of adsorbate. Experimental data were also analyzed to verify both the adsorption kinetics and isotherms according to pseudo first-order and pseudo-second-order kinetic models and Langmuir and Freundlich isotherm models.

100 mg L<sup>-1</sup> of Cr(VI), stock solution was prepared by dissolving 0.2834 g of K<sub>2</sub>Cr<sub>2</sub>O<sub>7</sub> in 1000 mL of deionized water. Different Cr(VI) concentrations (20, 40, 60, and 80 mg L<sup>-1</sup>) were prepared by dilution of the stock K<sub>2</sub>Cr<sub>2</sub>O<sub>7</sub> standard solution with deionized water. The experiments were carried out in 100 mL borosil beaker by stirring 0.1 g of nanopowders with 10 mL of the aqueous Cr(VI) solution of desired concentration at room temperature (25°C), and without the further pH adjustment. Adsorption isotherm study was carried out with different initial concentrations of Cr(VI) from 20 to 100 mg L<sup>-1</sup>. The initial pH of Cr(VI) solution was 5. The amount of Cr(VI) adsorbed per unit mass of the adsorbent was evaluated by using the mass balance equation:

$$q_t = (C_0 - C_t)V/W \quad (2.15)$$

Where  $q_t$  (mg g<sup>-1</sup>) is the amount adsorbed per gram of adsorbent at time  $t$  (min),  $C_0$  is the initial concentration of Cr(VI) in the solution (mg L<sup>-1</sup>),  $C_t$  is the concentration of Cr(VI) at time  $t$  of adsorption (mg L<sup>-1</sup>),  $W$  is the mass of the adsorbent used (g), and  $V$ (L) is the initial volume of the Cr(VI) solution. The Cr(VI) concentration in the supernatant was determined by monitoring the absorbance at 352.5 nm on a Shimadzu ultraviolet-visible-2450 spectrophotometer.<sup>38</sup> The percentage of adsorption can be calculated by using the equation:

$$\text{Adsorption (\%)} = \left( \frac{C_i - C_f}{C_i} \right) \times 100, \quad (2.16)$$

where  $C_i$  and  $C_f$  represent the initial and final Cr(VI) ion concentration (mg L<sup>-1</sup>) in solution.

#### 2.3.1. Effect of variable parameters

The effect of various parameters on the percentage of Cr adsorption was evaluated as explained below:

### ***2.3.1.1. Effect of contact time***

Contact time between the adsorbate and adsorbent is of great importance in adsorption as it depends on the nature of the system used. The effect of contact time was studied by adding 0.1 g of nanopowder into 10 mL of Cr(VI) solution and stirred for a period ranging from 5 min to 3 h at room temperature without any further adjustment of pH i.e. at initial pH of 5.

### ***2.3.1.2. Effect of pH***

The pH of the aqueous solution is a significant controlling factor in adsorption mechanism. Desired pH value for maximum removal efficiency was optimized by adding 0.1 g of nanopowder in 10 mL of Cr(VI) solution ( $100 \text{ mg L}^{-1}$ ) at different pH values from 1 to 13 with constant stirring for fixed contact time of 1 h. The pH of the solution was adjusted by adding dilute solutions of  $\text{NH}_4\text{OH}$  or  $\text{HNO}_3$ .

### ***2.3.1.3. Effect of amount of adsorbent***

The amount of adsorbent dosage also play key role on adsorption. In order to study the effect of adsorbent dose on chromium removal, different amount of adsorbent was added into 10 mL of Cr(VI) solution at pH 5 with constant stirring of fixed contact time of 1h.

### ***2.3.1.4. Effect of adsorbate concentration***

Adsorption processes of the metal ion strongly depend upon the initial concentration. For this investigation Cr(VI) adsorption study was carried out by adding 0.1g of nanopowder into varying concentrations of Cr(VI) solution ( $20 \text{ mg L}^{-1}$  to  $100 \text{ mg L}^{-1}$ ) at pH 5 with constant stirring of fixed contact time of 1h.

### ***2.3.1.5. Study of adsorption isotherms***

Adsorption isotherm described the interactive behaviour between the adsorbate and adsorbents which are very important for investigating the adsorption mechanisms. Chromium adsorption behaviour of the nanopowder were described by fitting the isotherms data to the Freundlich and Langmuir adsorption models. These two isotherms provide information about the total amount of adsorbent needed to adsorb a required amount of adsorbate from solution.

### (a) Langmuir adsorption isotherm

Langmuir adsorption isotherm<sup>39</sup> is based on the assumption that adsorbed layer will be monolayer coverage of the adsorbate on the adsorbent surface and all sorption sites are identical and energetically equivalent. The Langmuir isotherm model is utilized to calculate the maximum adsorption capacity, in terms of amount of the Cr(VI) ion adsorbed per unit weight of the nanopowder. The linear forms of the Langmuir isotherm can be mathematically represented by the equation:

$$\frac{C_e}{q_e} = \frac{1}{q_m b} + \frac{C_e}{q_m} \quad (2.17)$$

Where  $q_e$  is the amount adsorbed ( $\text{mg g}^{-1}$ ) at equilibrium,  $q_m$  is the maximum adsorption capacity ( $\text{mg g}^{-1}$ ),  $C_e$  is the equilibrium concentration of the adsorbate ( $\text{mg L}^{-1}$ ), and  $b$  ( $\text{L mg}^{-1}$ ) is the Langmuir constant. The maximum adsorption capacity,  $q_m$  and the constant  $b$  can be obtained from the slope and intercept of the plot of  $C_e/q_e$  against  $C_e$ . The nature of the Langmuir isotherm can be expressed in terms of a dimensionless constant separation factor,  $R_L$  which is defined as:

$$R_L = \frac{1}{1 + bC_o} \quad (2.18)$$

where  $b$  and  $C_o$  are Langmuir constant and initial Cr(VI) concentration ( $\text{mg L}^{-1}$ ).<sup>40</sup> The  $R_L$  values indicate the shape of the isotherms. Adsorption would be irreversible when  $R_L = 0$ , favorable when  $0 < R_L < 1$ , linear when  $R_L = 1$  and unfavorable when  $R_L > 1$ .<sup>41</sup>

### (b) Freundlich isotherm

The Freundlich isotherm<sup>42</sup> is another useful model based on multilayer adsorption with the assumption that adsorbent consists of a heterogeneous surface sites, which provides an empirical relationship between the sorption capacity and the equilibrium concentration of the adsorbent. The linearized form of this isotherm can be expressed as

$$\log q_e = \log K_F + \frac{1}{n} \log C_e \quad (2.19)$$

where  $C_e$  is the equilibrium concentration of the metal ion in  $\text{mg L}^{-1}$ ,  $q_e$  is the amount of chromium(VI) adsorbed at equilibrium in  $\text{mg g}^{-1}$ , and  $K_F$  and  $n$  are the Freundlich constants,

which indicate the adsorption capacity and the adsorption intensity, respectively. The values of  $K_F$  and  $n$  can be determined from the slope and intercept of the logarithmic plot of  $q_e$  vs  $C_e$ .

### 2.3.1.6. Study of adsorption kinetics

Several kinetic models have been developed<sup>43</sup> to describe the mechanism of heavy metal ion removal, among which two most commonly used models are pseudo-first-order and pseudo-second-order models. In order to understand the kinetics of Cr (VI) adsorption by the synthesized nanopowder, experimental data were modeled using Lagergren's pseudo-first-order and pseudo-second order kinetic equations.

## References

1. L. A. Bruce, M. Hoang, A. E. Hughes and T. W. Turney, *Appl. Catal. A Gen.*, 1996, 134, 351.
2. J. E. Spanier, R. D. Robinson, F. Zhang, S. W. Chan and I. P. Herman, *Phys. Rev. B Condens. Matter Mater. Phys.*, 2001, 64, 245407.
3. L. Madler, W. J. Stark and S. E. Pratsinis, *J. Mater. Res.*, 2002, 17, 1356.
4. Y. J. He, B. L. Yang and G. X. Cheng, *Mater. Lett.*, 2003, 57, 1880.
5. M. Hirano and E. Kato, *J. Am. Ceram. Soc.*, 1999, 82, 786.
6. J. L. M. Rupp, T. Drobek, A. Rossi and L. J. Gauckler, *Chem. Mater.*, 2007, 19, 1134.
7. X. H. Yu, F. Li, X. R. Ye, X. Q. Xin and Z. L. Xue, *J. Am. Ceram. Soc.*, 2000, 83, 964.
8. C. L. Robert, J. W. Long, E. M. Lucas, K. A. Pettigrew, R. M. Stround, M. S. Doescher and D. R. Rolison, *Chem. Mater.*, 2006, 18, 50.
9. Y. Zhou, R. J. Philips and J. A. Switzer, *J. Am. Ceram. Soc.*, 1995, 78, 981.
10. T. Masui, K. Fujiwara, K. I. Machida and G. Y. Adachi, *Chem. Mater.*, 1997, 9, 2197.
11. C. Ho, C. J. Yu, T. Kwong, A. C. Mak and S. Lai, *Chem. Mater.*, 2005, 17, 4514.
12. M. M. Natile, G. Boccaletti and A. Glisenti, *Chem. Mater.*, 2005, 17, 6272.
13. H. Wang, J. J. Zhu, J. M. Zhu, X. H. Liao, S. Xu, T. Ding and H. Y. Chen, *Phys. Chem. Chem. Phys.*, 2002, 4, 3794.
14. M. L. D. Santos, R. C. Lima, C. S. Riccardi, R. L. Tranquilin, P. R. Bueno, J. A. Varela and E. Longo, *Mater. Lett.*, 2008, 62, 4509.
15. M. Hirano and M. Inagaki, *J. Mater. Chem.*, 2000, 10, 473.
16. H. Yang, C. Huang, A. Tang, X. Zhang and W. Yang, *Mater. Res. Bullet.*, 2005, 40, 1690.
17. M. Guglielmi, G. Kickenbick and A. Martucci, *Sol-Gel Nanocomposites*, ed., Springer, New York, 3rd edn., 2014, pp. 102.
18. R. Daniel and J. Musil, *Novel Nanocomposite Coatings*, Taylor & Francis Group, USA, 2013, pp. 102.
19. V. K. Ahuliwala and A. Mishra, *Polymer Science: A Textbook*, Ane Books Pvt. Ltd., India, 2009, pp. 118.

20. G. R. Chatwal and S. K. Anand, *Instrumental Methods of Chemical Analysis*, Himalaya Publishing House, India, 5th ed., 2007, pp. 2.719.
21. B. D. Cullity and S. R. Stock, *Elements of X-Ray Diffraction*, Addison-Wesley Publishing Company, Inc., USA, 3rd ed., 1956, pp. 99.
22. S. Brunauer, P.H. Emmet and E. Teller, *J. Am. Chem. Soc.*, 60, 1938, 309.
23. D. N. Bajpai, *Advanced Physical Chemistry*, S. Chand and Company Ltd., India, 2nd ed., 2001, pp. 727.
24. D.L. Pavia, G.M. Lampman and G.S. Kriz, *Introduction to Spectroscopy*, Thomson Learning Inc., 3rd ed. USA, 2001, pp. 13.
25. P. Atkins and J. D. Paula, *Elements of physical chemistry*, W. H. Freeman, 5th ed., Oxford, 2009, pp. 459.
26. D. A. Skoog, F. J. Holler and R. S. Crouch, *Principles of instrumental analysis*, Thomson Brooks/Cole, Belmont, CA., 6th ed., 2007, pp. 169.
27. G. Kortum, *Reflectance Spectroscopy: Principles, Methods, Applications*, Springer, New York, 1969.
28. G. Burgeth and H. Kisch, *Coord. Chem. Rev.*, 230, 2002, 41.
29. E.L. Simmons, *Appl. Opt.*, 14, 1975, 1380.
30. J. Z. Zhang, *Optical Properties and Spectroscopy of Nanomaterials*, World Scientific Publishing Co. Pte. Ltd., USA, 2009, pp. 18.
31. K. Binnemans, *Chem. Rev.*, 2009, 109, 4283.
32. *X-Ray Photoelectron Spectroscopy*, ed. J. M. Wagner, Nova Science Publishers, Inc., New York, 2011, pp. 2.
33. J. M. Huggett and H. F. Shaw, *Clay Minerals*, 1997, 32, 197.
34. J. C. H. Spence, *High-Resolution Electron Microscopy*, Oxford U. Press, Oxford, 3rd ed., 2003.
35. *High-Resolution Transmission Electron Microscopy: and Associated Techniques*, ed. P. Buseck, J. Cowley and L. Eyring, Oxford U. Press, Oxford, 1988.
36. J. Lynch, *Physico-Chemical Analysis of Industrial Catalysts: A Practical Guide to Characterization*, Edittion Technip, Paris, 2001, pp. 26.
37. S. Subramanian, *Platinum Metals Rev.*, 36, 2, 1992, 98.
38. ASTM D 1687-92, *Chromium in Water, Test Method A*, 1996.
39. I. Langmuir, *J. Am. Chem. Soc.*, 40, 1918, 1361.
40. A. S. K. Kumar, S. Kalidhasan, V. Rajesh and N. Rajesh, *Ind. Eng. Chem. Res.*, 2012, 51, 58.
41. R. Zhang, B. Wang and H. Ma, *Desalination*. 2010, 255, 61.
42. H. M. F. Freundlich, *J. Phys. Chem.*, 1906, 57, 385.
43. H. Qiu, L. Lv, B. C. Pan, Q. Zhang, W. Zhang, and Q. Zhan, *J. Zhejiang Univ. Sci. A.*, 2009, 10, 716.

## Chapter 3

# High Surface Area Mesoporous Ceria Synthesized With and Without Surfactant

### Outline

*Surfactant assisted synthesis of pure CeO<sub>2</sub> materials remarkably control the structural and functional characteristics of the materials. A comparative study has been done to find out the role of a surfactant sodium dodecyl sulphate (SDS) on the structural, microstructural and optical properties of CeO<sub>2</sub>. The CeO<sub>2</sub> samples were characterized by TG–DSC, XRD, BET, XPS, Raman, EPR, UV, PL, HRTEM, TPR and TPD. Thermal analysis showed that the weight loss of as-prepared CeO<sub>2</sub> sample (100Ceasp) was much higher (16.85%) than the sample synthesized with surfactant (100CeSDSasp) (9.58%). XRD and thermal analyses showed that the surfactant has played important role in crystallization of cubic CeO<sub>2</sub> at a lower temperature. The 100CeSDSasp sample showed significantly better control over the reduction in the surface area that occurred during the heat treatments than the 100Ceasp sample. XPS and EPR analysis confirm the existence of mixed valence states (Ce<sup>3+</sup> and Ce<sup>4+</sup>) in the nanocrystals. Surfactant molecules also enhance both the UV absorption and PL intensity of CeO<sub>2</sub> nanoparticles. TPD profile illustrates the more acidity on the surface of the CeO<sub>2</sub> sample synthesized via surfactant assisted route, which is attributed to the presence of residual sulfate as sodium dodecyl sulphate. The smaller crystallite size of the CeO<sub>2</sub> nanopowder synthesized via surfactant free route with lower Ce–O symmetry leads to higher number of reactive surface oxygen sites and/or surface oxygen vacancy clusters in the sample. This study reveals that surfactant assisted synthesis approach is significantly a better strategy for the synthesis of crystalline CeO<sub>2</sub> nanopowder at lower temperature and showed better stability of surface property for the possibility of these materials to be used as better UV blockers, nanophosphor, adsorption for toxic metal, dye degradation and catalysis.*

### 3.1. Introduction

Due to various unique properties such as high refractive index, good transmission in visible and infrared regions, strong adhesion, and high stability against mechanical abrasion, chemical attack and high temperatures<sup>1</sup> CeO<sub>2</sub> with an extraordinary capacity to store and release oxygen with cubic fluorite structure,<sup>2</sup> is considered to be one of the most useful promising metal oxides for wide varieties of technological applications in automotive three way catalysts,<sup>3</sup> ultraviolet absorbers,<sup>4</sup> hydrogen storage materials,<sup>5</sup> oxygen sensors,<sup>6</sup> optical devices,<sup>7</sup> and polishing materials.<sup>8</sup> Potential uses of CeO<sub>2</sub> includes the removal of soot from diesel engine exhaust, for the removal of organics from wastewaters, as an additive for combustion processes, and in fuel cell technology.<sup>9,10</sup>

Now a days much interest is being focused on the preparation of transition metal oxides through templating pathways.<sup>11-13</sup> Few mesostructured materials showed a regular pore structure even after calcination<sup>14,15</sup> but often the pore structure collapses upon calcination.<sup>16</sup> The use of surfactants as liquid crystal templating agents is to create a regular three dimensional micellar array about which an inorganic precursor could form a framework gives a reliable method to produce structurally ordered, porous solids. The subsequent removal of surfactant in a controlled manner yields a material with an open framework with uniform pore dimensions. In many methods to synthesize nanoparticles, surfactants are employed as a stabilizer, capping agent and template, which can control the size, anisotropic growth and agglomeration. CTAB (cetyltrimethylammonium bromide) and SDS (sodium dodecyl sulphate) surfactants have been widely used as cationic and anionic surfactants, respectively, for synthesizing a large numbers of inorganic materials with controlled shape and size.<sup>17,18</sup> The addition of surfactant in precursor solution reduces the surface tension of the solution, facilitates nucleation, and controls the growth of the particle and hence resulting in smaller sized particles. Surfactant molecules are composed of a hydrophilic head and a hydrophobic tail which results in the formation of reverse micelles in the precursor solution. Surfactant assisted route is widely used to prepare nanocrystalline CeO<sub>2</sub>. Terribile *et al.* suggested that the cationic surfactant CTAB does not act as a true templating agent but as a surface area enhancer by incorporation into the hydrous oxide and lowering of the surface tension of water in the pores during drying.<sup>19</sup> Wang *et al.* synthesized stable and crystalline pure CeO<sub>2</sub> nanoparticles by using cationic surfactant CTAB.<sup>20</sup> Rhombic micro plates of CeO<sub>2</sub> was



synthesized using aqueous cerium nitrate solution in presence of urea and CTAB. BET surface area, and pore volume of the microplates were  $57 \text{ m}^2/\text{g}$ , and  $0.03 \text{ cm}^3/\text{g}$ , respectively.<sup>21</sup> Tabrizi *et al.* studied simultaneously the effects of process variables of pH, CTAB/metal molar ratio and calcination temperatures on the surface area of  $\text{CeO}_2$  nanopowders prepared by surfactant assisted precipitation method.<sup>22</sup> Brigante evaluated the effect of pH on the morphology and texture of  $\text{CeO}_2$  by using the cationic surfactant cetyltrimethylammonium tosylate (CTAT) as template. The surface area and pore volume of the synthesized material were  $33.52 \text{ m}^2/\text{g}$  and  $0.06 \text{ cm}^3/\text{g}$ , respectively.<sup>23</sup> Zhang *et al.* obtained 0.5–21 nm sized plates having thickness of 100–400 nm, and surface area of  $29.1 \text{ m}^2/\text{g}$  of rhombic  $\text{CeO}_2$  microplate using CTAB-urea at aqueous refluxing temperature.<sup>24</sup> However, limited publications are available on the influence of surfactant on size, morphology, and optical properties of  $\text{CeO}_2$  nanostructures. In this study,  $\text{CeO}_2$  nanoparticles have been synthesized with and without surfactant through a facile chemical route using aqueous solutions of inorganic precursors and surfactant. We have explored the use of sodium dodecyl sulphate as a surfactant for the synthesis of nanocrystalline  $\text{CeO}_2$ . The samples are characterized by several instrumental techniques such as TG–DSC, XRD, BET, XPS, Raman, EPR, UV, PL, HRTEM, TPR and TPD to find out the influence of surfactant molecules in the formation of  $\text{CeO}_2$  nanoparticles with controlled size and hence on the properties.

### 3.2. Experimental and characterization

Pure  $\text{CeO}_2$  with (100CeSDSasp) and without (100Ceasp) surfactant were synthesized using cheaper inorganic precursor of ceric ammonium nitrate as metal ion precursor and SDS as surfactant. The samples were prepared via both conventional and microwave refluxing methods and then characterized by different instrumental techniques (details are given in chapter-II).

### 3.3. Results and Discussion

#### 3.3.1. TG–DSC

##### 3.3.1.1. Effect of surfactant

TG–DSC curves of the as-prepared materials synthesized with and without surfactant are shown in Fig. 3.1(A) and (B) respectively. An endothermic peak centered at 77 or  $98^\circ\text{C}$  was observed for the sample prepared with or without surfactant. This endothermic peak is

attributed to desorption of physisorbed water from the as-prepared sample. The more intense endothermic peak for the 100Ceasp sample as compared to that for the 100CeSDSasp indicates that the former contains more amorphous phase than the latter. The total weight loss for the 100Ceasp sample was found to be much higher (16.85%) than the surfactant assisted synthesized  $\text{CeO}_2$  (9.58%). The results indicate that the less structural water and amorphous phase is associated with the  $\text{CeO}_2$  nanoparticles synthesized via surfactant mediated route and maximum amount of surfactant was removed just by simple washing of the precursor with water and ethanol. So, it can be suggested that the 100Ceasp sample contains more  $\text{Ce}(\text{OH})_4$  and  $\text{CeO}_2 \cdot 2\text{H}_2\text{O}$ , while the 100CeSDSasp sample contains more  $\text{CeO}_2$ , and  $\text{CeO}_2 \cdot \text{H}_2\text{O}$ . Exothermic peaks centering around  $185^\circ\text{C}$  and  $400^\circ\text{C}$  for the surfactant-derived sample are attributed to the decomposition of the amorphous precursor and the residual surfactant present in the sample.

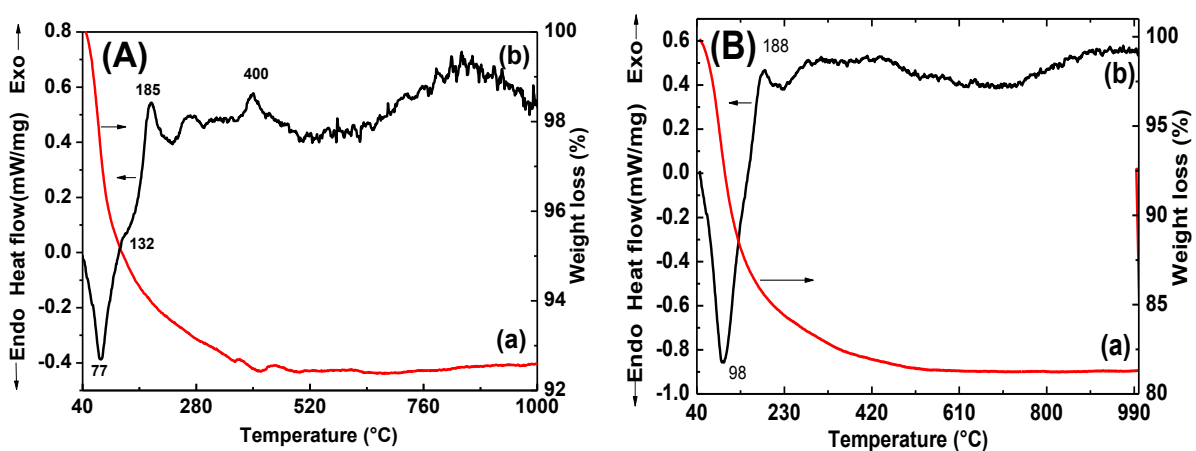


**Fig. 3.1** TG(a)-DSC(b) curves of (A) 100CeSDSasp and (B) 100Ceasp.

### 3.3.1.2. Effect of Microwave refluxing

It is quite interesting to note that the  $\text{CeO}_2$  sample synthesized via microwave refluxing exhibits higher total weight loss of 18.7 % and a very prominent exothermic peak (related to the decomposition of the precursor) centered at  $219^\circ\text{C}$  shown in Fig.3.2. The results infer that the sample synthesized via conventional refluxing method is quite advantageous over the microwave refluxing method to obtain crystalline and surfactant free  $\text{CeO}_2$  sample.

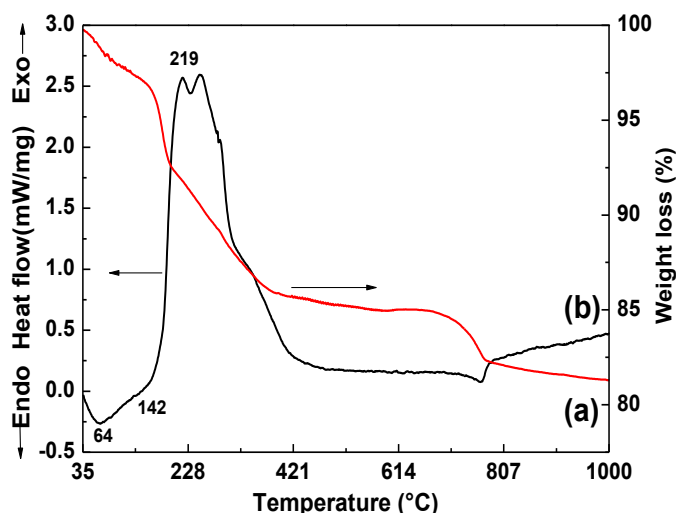


Fig. 3.2. TG(a)-DSC(b) curves of 100CeSDSMWasp.

### 3.3.2. XRD

#### 3.3.2.1. Effect of surfactant

Fig. 3.3 shows the X-ray diffraction patterns of the as-prepared nanopowders synthesized (a) without and (b) with surfactant. The broad and weak intensities of 100Ceasp powders indicate the formation of poorly crystalline  $\text{CeO}_2$  with amorphous phase. The XRD pattern of the 100CeSDSasp nanopowder show the formation of highly crystalline cubic  $\text{CeO}_2$  phase, which revealed the utility of sodium dodecyl sulphate as structure directing agent to impart better crystallinity even at lower temperature. The average crystallite sizes  $d$  of the as-prepared  $\text{CeO}_2$  samples were calculated from X-ray line by using Scherrer's equation (i.e.,  $d = \frac{0.89\lambda}{\beta \cos\theta}$ ) of the most intense peak (111), where  $d$  is the average crystallite size,  $\lambda$  is the wavelength of the X-rays,  $\theta$  is the diffraction angle, and  $\beta$  is the full width at half maxima of the peak. The lattice parameters of both the as-prepared samples were also determined and all are summarized in Table. 3.1.

**Table. 3.1.** Crystallize size and lattice parameters of the as-prepared  $\text{CeO}_2$  powders, (a) without, and (b) with surfactant.

Sample	Crystallite size (nm)	Lattice parameter (nm)
100CeSDSasp	8.43	0.5410
100Ceasp	3.39	0.5413

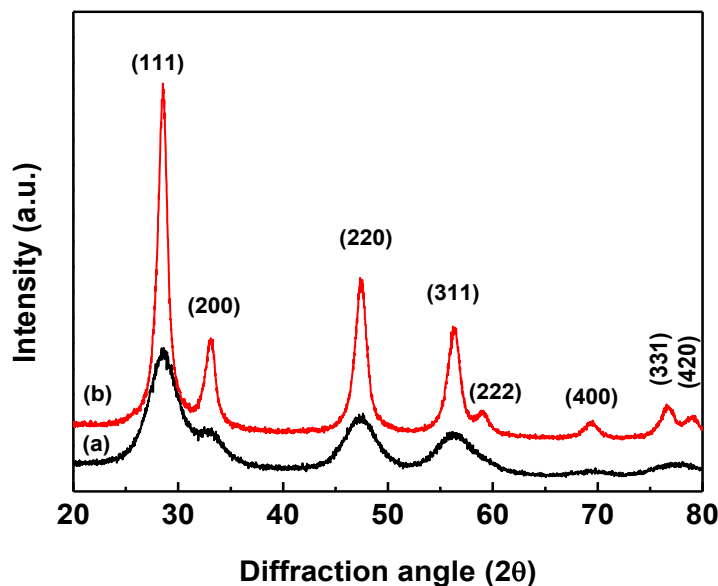


Fig. 3.3 XRD patterns of the (a) 100Ceasp (b) 100CeSDSasp.

### 3.3.2.2. Effect of calcination temperature

XRD patterns of the (a) 100CeSDSasp sample and calcined at various temperatures of (b) 500°C, (c) 650°C, (d) 800°C, and (e) 1000°C for 2 h are shown in Fig. 3.4. All are indexed to cubic fluorite structure and was in good agreement with literature data (JCPDS No.34-0394). Diffraction peaks characteristic of crystalline  $\text{Ce}_2\text{O}_3$  phase were not observed in the XRD pattern. Both crystallite size and lattice parameters of all the samples were calculated and summarized in Table 3.2. A consistent increase in crystallite size of  $\text{CeO}_2$  was observed with increasing the calcinations temperatures. Further, no diffraction peaks of any sample that could be attributed to cerium hydroxide were observed. Li *et al.* noted that the crystallite size of  $\text{CeO}_2$  shows an exponential dependence on the calcination temperature because the crystallite growth of  $\text{CeO}_2$  is controlled by diffusion.<sup>25</sup> These results reveal that the crystallite growth is very slow till 650°C temperatures. However, when the as-synthesised  $\text{CeO}_2$  powders were calcined at higher temperature of 800°C and 1000°C, the crystallite sizes of  $\text{CeO}_2$  rapidly increased. Continuous grain boundary networks are formed at higher calcination temperatures. These networks lead to the bridging of fine crystallites, thereby increasing the crystallite size. The results suggest that the pores existing in the interior of the  $\text{CeO}_2$  precursor powders are rapidly eliminated under these conditions.

**Table 3.2.** Crystallite size and lattice parameters of the 100CeSDSasp sample and calcined at different temperatures.

Sample	Crystallite size (nm)	Lattice parameter (nm)
100CeSDSasp	8.4	0.5410
100CeSDS500	8.2	0.5408
100CeSDS650	11.0	0.5409
10CeSDS800	26.2	0.5416
10CeSDS1000	53.9	0.5403

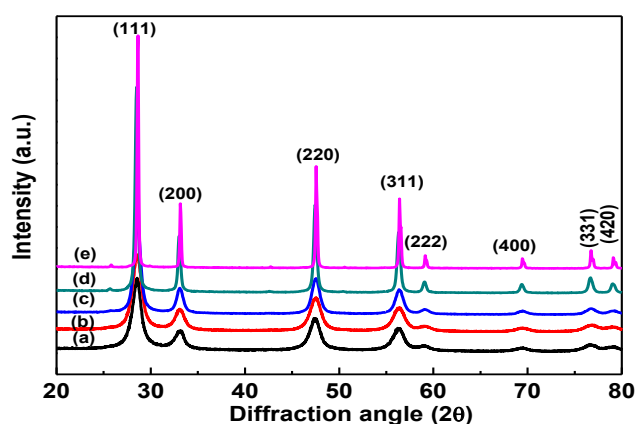


**Fig. 3.4** XRD patterns of (a) 100CeSDSasp, and the samples calcined at (b) 500°C, (c) 650°C, (d) 800°C, and (e) 1000°C.

The lattice parameter ( $a = 0.5413$  nm) of 100Ceasp was higher than that of 100CeSDSasp (0.5410 nm) but was close to 0.5415 nm of the bulk  $\text{CeO}_2$ . It gradually decreased as the calcination temperature increased. The lattice parameters of nanocrystalline  $\text{CeO}_2$  decreases with the increasing the particle size.  $\text{CeO}_2$  in the core is very close to that of bulk  $\text{CeO}_2$ . The  $\text{CeO}_2$  at surface tends to relax, as a result the lattice parameter of surface  $\text{CeO}_2$  increases locally. Our results are in good agreement with those of Leoni *et al.*, who reported that the lattice parameter of nanocrystalline  $\text{CeO}_2$  powders changes as a function of calcination temperatures.<sup>26</sup> In nanocrystalline particles or grains, the structure of the core is very close to that of bulk nanocrystalline  $\text{CeO}_2$  and the surface tends to relax. The lattice parameter, therefore, increases locally at the surface. In addition, it was found that the grain surface relaxation contributes to the line broadening, thus tending to reduce the measured value of dislocation density.<sup>27</sup>

### 3.3.2.3. Effect of microwave reflux method

The crystallinity of the as prepared nanopowder was confirmed by the XRD patterns. The diffraction peaks of the pure CeO<sub>2</sub> obtained in microwave assisted route as-prepared and calcined at various temperatures were identical to the CeO<sub>2</sub> obtained in conventional reflux method as shown in Fig. 3.5. Nanopowder annealed at higher temperature showed more intense and sharp diffraction peaks, which are due to the continuous growth of CeO<sub>2</sub> crystallites during calcination. The average crystallite sizes (D) were also calculated by using Scherrer's equation: are tabulated below in Table 3.3. As can be seen from Table 3.3, the crystallite size of 100CeSDSMW sample calcined at a particular temperature was higher as compared to that of the 100CeSDS samples prepared via conventional refluxing route. For example, the crystallite sizes were 26.2 and 39.8 nm for 100CeSDS800 and 100CeSDSMW800, respectively. The lattice parameter obtained in the both the process were found to be comparable.

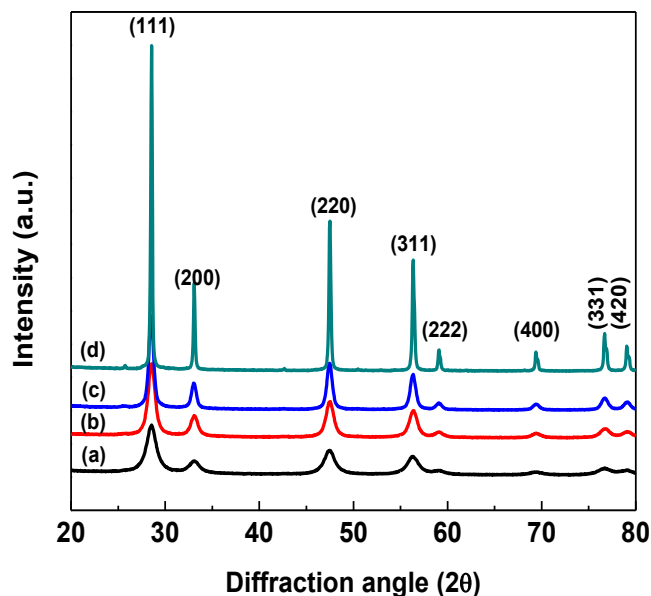


**Fig. 3.5.** XRD patterns of the (a) 100CeSDSMW as prepared and calcined at (b) 500°C (c) 650°C and (d) 800°C.

**Table. 3.3.** Crystallize size and lattice parameters of as-prepared 100CeSDSMW samples and calcined at (b) 500°C (c) 650°C, and (c) 800°C.

Sample	Crystallite size (nm)	Lattice parameter (nm)
100CeSDSMWasp	6.4	0.5413
100CeSDSMW500	8.9	0.5408
100CeSDSMW650	13	0.5416
10CeSDSMW800	39.8	0.5409

### 3.3.3. BET surface area

#### 3.3.3.1. Effect of calcination temperature

The nitrogen adsorption desorption isotherms of 100Ce and 100CeSDS samples calcined at different temperatures showed Type-IV isotherms, and are shown in Fig. 3.6 and Fig. 3.7, respectively. The BET surface area was estimated using adsorption data in a relative pressure range from 0.02 to 1.0. The specific surface areas of 100CeSDSasp (151 m<sup>2</sup>/g) is lower as compared to that of 100Ceasp (292 m<sup>2</sup>/g). This is due to the presence of higher content of amorphous cerium hydroxide in the as-prepared sample prepared without surfactant, as is also evident from the TG-DSC results. As the calcination temperature increases, the isotherms shift downward while the hysteresis loops at high relative pressure become smaller; these changes indicate a decrease in BET surface area. The surface areas of 100Ce500, 100Ce650 and 100Ce800 are 108, 39 and 24 m<sup>2</sup>/g, respectively. While the surface areas of 100CeSDS500, 100CeSDS650 and 100CeSDS800 are 115, 75, and 39 m<sup>2</sup>/g, respectively. The more rigorous decrease in the specific surface area with calcination temperatures for the samples synthesized without surfactant indicates that the surfactant plays a very important role in controlling particle size, particle growth, and surface area of CeO<sub>2</sub>. BET surface area and the pore volumes decreases while the average pore diameter increases with an increase of calcination temperature. This is due to the tendency of the nanoparticles to agglomerate intensively and collapsing of the pores at higher temperatures.<sup>21</sup> The pore size distributions of 100Ce and 100CeSDS samples calcined at different temperatures are shown in the Fig. 3.6(B) and 3.7(B), respectively. Table. 3.4 and 3.5 present the detailed results about the specific surface area, pore size, and pore volume of 100Ce and 100Cesds samples calcined at different temperatures.

**Table 3.4.** Surface area, pore diameter and total pore volume of 100Ce sample calcined at different temperatures.

Sample	Surface area (m <sup>2</sup> /g)	Pore diameter (nm)	Total pore volume (cm <sup>3</sup> /g)
asp	292	3	0.22
500°C	108	4	0.11
650°C	39	6	0.05
800°C	24	7	0.04

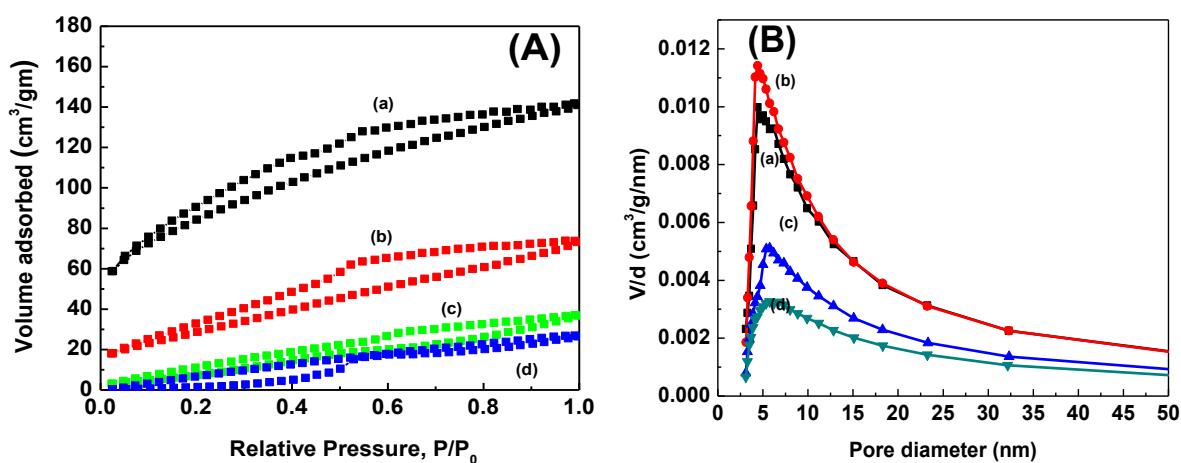


**Fig. 3.6.** (A) N<sub>2</sub> adsorption–desorption isotherms, and (B) BJH pore size distribution curves of the (a) 100Ceasp and the samples calcined at (b) 500°C, (c) 650°C, and (c) 800°C.

**Table 3.5.** Surface area, pore diameter, and total pore volume of 100CeSDS samples calcined at different temperatures.

Sample	Surface area (m <sup>2</sup> /g)	Pore diameter (nm)	Total pore volume (cm <sup>3</sup> /g)
asp	151	4.4	0.17
500°C	115	5.0	0.14
650°C	75	5.3	0.10
800°C	39	6.0	0.06



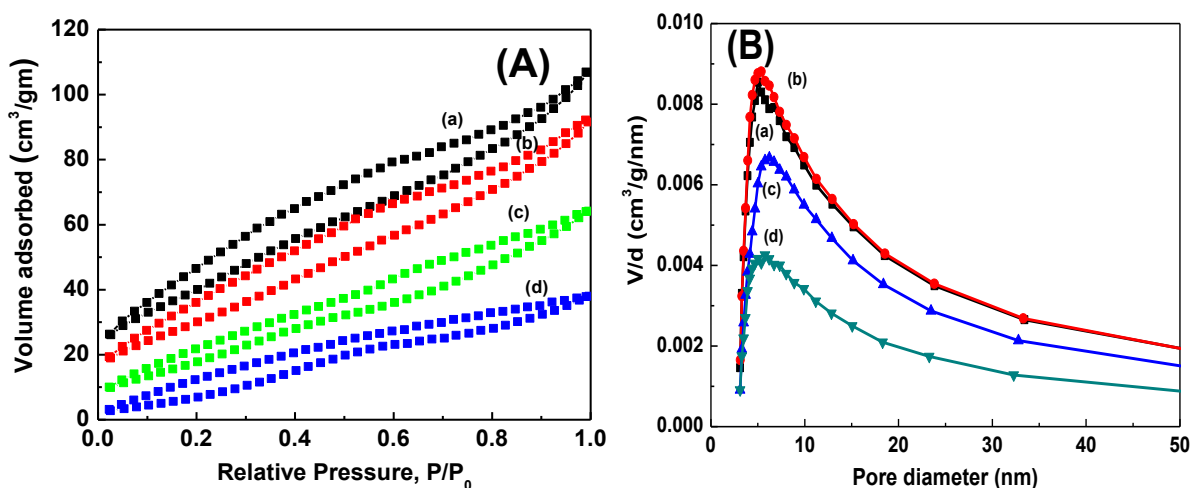


**Fig. 3.7.** (A) N<sub>2</sub> adsorption–desorption isotherms and (B) BJH pore size distribution of 100CeSDS samples (a) as prepared, calcined at (b) 500°C, (c) 650°C, and (c) 800°C.

### 3.3.3.2. Effect of microwave reflux methods

The nitrogen sorption isotherms of 100CeSDSMW samples calcined at different temperatures showing the Type-IV isotherms are shown in Fig. 3.8. The surface area and total pore volume of the 100CeSDSMW samples (as given in Table 3.6) calcined at a particular temperature are much lower as compared to those of the samples synthesized via microwave refluxing. This envisages that the conventional refluxing method is more advantageous in obtaining CeO<sub>2</sub> nanopowders with higher surface area and pore volume.

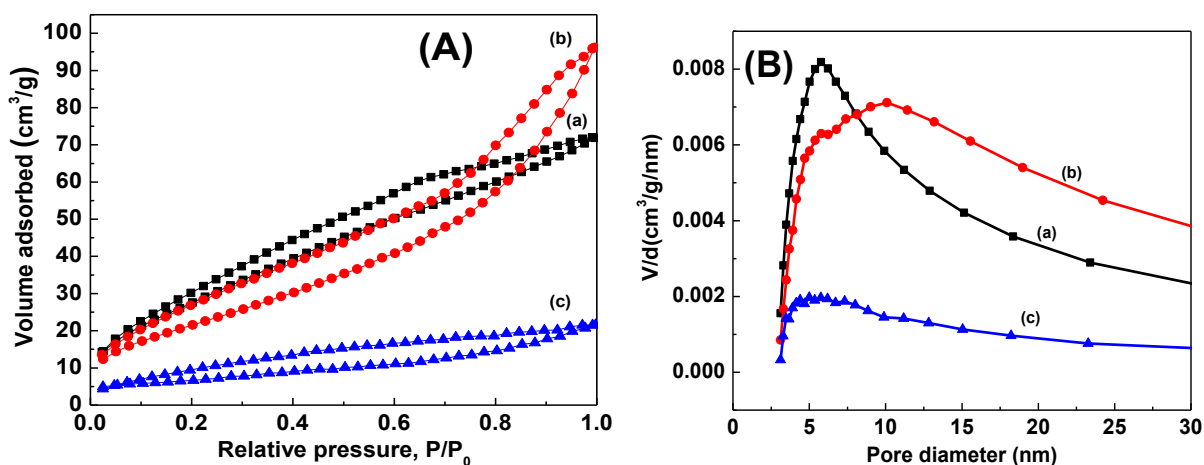


**Fig. 3.8.** (A) N<sub>2</sub> adsorption–desorption isotherms and (B) BJH pore size distribution of 100CeSDSMW (a) as prepared samples, calcined at (b) 500°C and (c) 650°C.

**Table 3.6.** Surface area, pore diameter, and total pore volume of 100CeSDSMWasp and the samples calcined at (b) 500°C and (c) 650°C.

Sample	Surface area (m <sup>2</sup> /g)	Pore diameter (nm)	Pore volume (cm <sup>3</sup> /g)
asp	109.7	4.0	0.11
500°C	82.4	7.2	0.15
650°C	24.1	5.5	0.03

### 3.3.4. FTIR spectra

Fig. 3.9 shows the FTIR spectra of the pure CeO<sub>2</sub> obtained in surfactant free route route asprepared and calcined at 500°C. Both the as-prepared and calcined samples show a broad absorption band in the range of 3330–3400 cm<sup>-1</sup> are attributed to the stretching vibration of O-H bond in the surfaced hydroxyl group.<sup>28</sup> The absorption band around 1615 cm<sup>-1</sup> could be assigned to the bending vibration of absorbed molecular water.<sup>29</sup> The bands centered at 1058 and 1332 cm<sup>-1</sup> are due to Ce–O–Ce vibration.<sup>30</sup> The bands observed at 946 cm<sup>-1</sup> may be due to the δ(Ce–O–Ce) mode.<sup>31</sup>

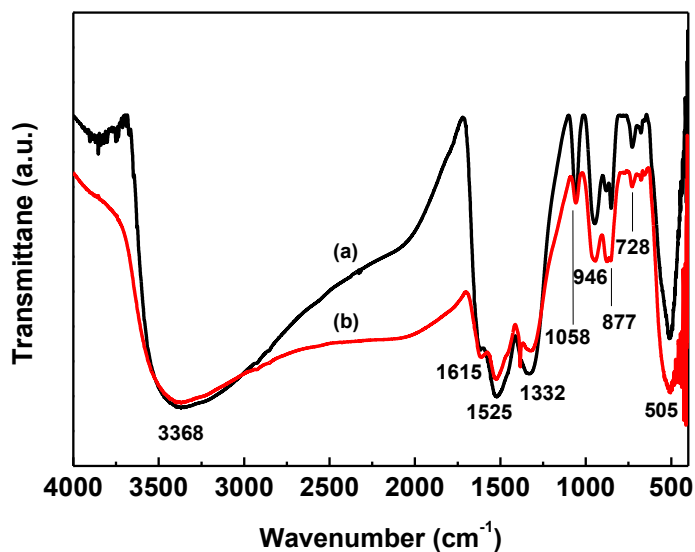


**Fig. 3.9.** FTIR spectra of the (a) 100Ceasp and (b) 100ce500°C.

Surface interaction between the inorganic precursors and the surfactant were studied by means of FTIR spectroscopy. Fig. 3.10, shows the FTIR spectra of the pure SDS and pure CeO<sub>2</sub> obtained in SDS assisted route as-prepared and calcined at various temperature. The

major bands of pure SDS can be divided into two regions, two absorption bands in the range of 2950–2850  $\text{cm}^{-1}$ , attributed to asymmetric and symmetric stretching of  $-\text{CH}_2$  groups<sup>32</sup> and another band at 1226  $\text{cm}^{-1}$ , attributed to main band of  $\text{OSO}_3$  group.<sup>32</sup> The intensity of the characteristic peak of the  $-\text{CH}_2$  group near 2924 and 2856  $\text{cm}^{-1}$  decreases while the sintering temperature raised upto 650°C. Peak appeared at 1467  $\text{cm}^{-1}$  attributed to the  $-\text{CH}_2$  deformation band.<sup>33</sup> In addition calcined sample did not showed any characteristics peaks of the  $\text{SO}_4^{2-}$  group which suggests that the residual surfactant molecule get remove completely after calcination. The bands around at 962  $\text{cm}^{-1}$  are postulated to be  $\delta(\text{Ce}-\text{O}-\text{Ce})$  mode.

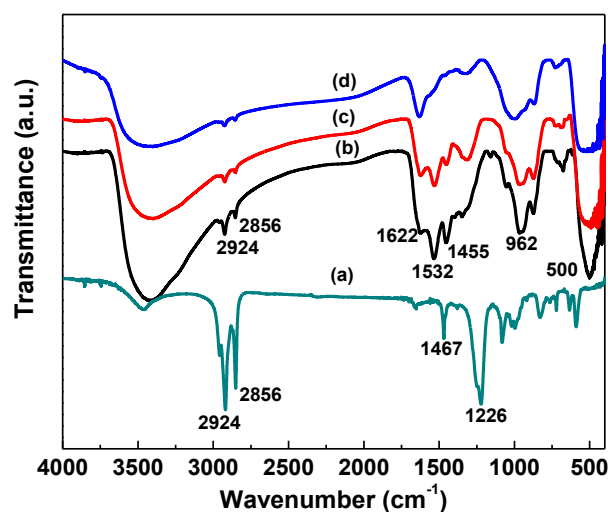


**Fig. 3.10.** FTIR spectra of the (a) pure SDS, (b) 100CeSDSasp and calcined at (c) 500°C (d) 650°C for 2 h.

### 3.3.5. FESEM Micrographs

The morphology of the pure  $\text{CeO}_2$  obtained in (a) surfactant free and (b) surfactant assisted route and calcined at 500°C for 2 h was analyzed by FESEM, and the results are shown in Fig. 3.11. It was found that the FESEM image of  $\text{CeO}_2$  nanoparticles obtained in surfactant free route exhibit an unclear shape whereas the  $\text{CeO}_2$  nanoparticles obtained in surfactant assisted route are close to spherical morphology. Nanopowder obtained in surfactant free route exhibits less agglomeration and composed with nearly monodispersed particles as compared to that of the nanopowder obtained in surfactant free route which revealed that surfactant molecule play a significant role in the synthesis process and provided agglomerated free spherical monodispersed nanoparticles.

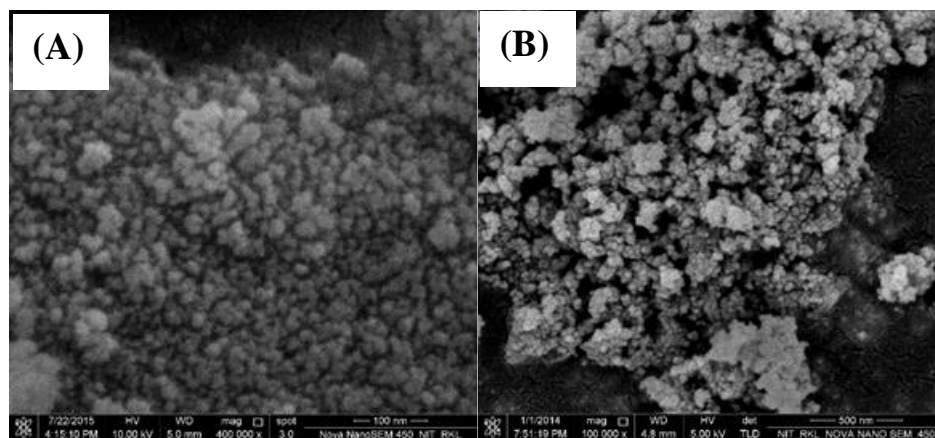
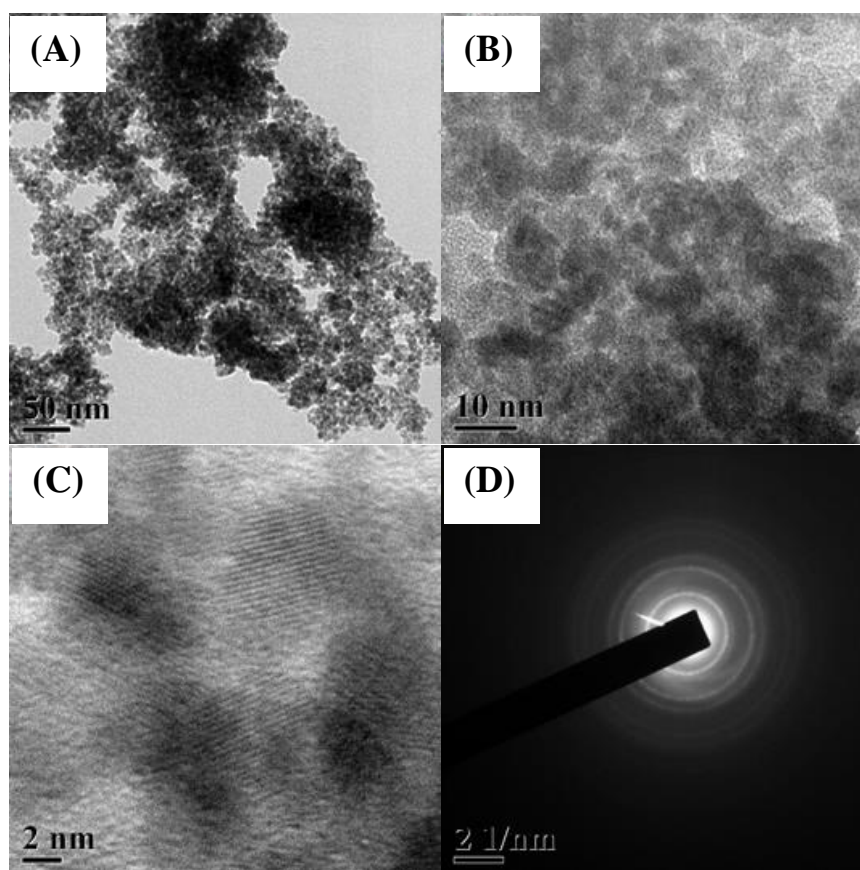


Fig. 3.11. FESEM micrographs of (A) 100Ce500 and (B) 100CeSdS500°C.

### 3.3.6. TEM, HRTEM Micrographs & SAED Pattern



**Fig. 3.12.** (A) TEM image, (B) HRTEM image, (C) Lattice fringes and corresponding (D) SAED pattern of 100Ce500°C.

The micro structure of the pure CeO<sub>2</sub> nanoparticles obtained in (a) surfactant free and (b) surfactant assisted route and calcined at 500°C for 2 h was further analyzed by HRTEM and the results are shown in Fig. 3.12 and Fig. 3.13 respectively. It can be seen that the morphology of pure CeO<sub>2</sub> obtained in surfactant assisted route becomes more prominent in shape and size as compared to that of the pure CeO<sub>2</sub> obtained in surfactant free route, which on further magnification at high resolution showed close to hexagonal morphology. Spotty SAED pattern of both the nanoparticles indicate the formation of pure crystalline phase with cubic fluorite structure. The lattice fringes was more clear in the HRTEM image of pure CeO<sub>2</sub> obtained in surfactant assisted route further confirmed it highly crystalline nature.

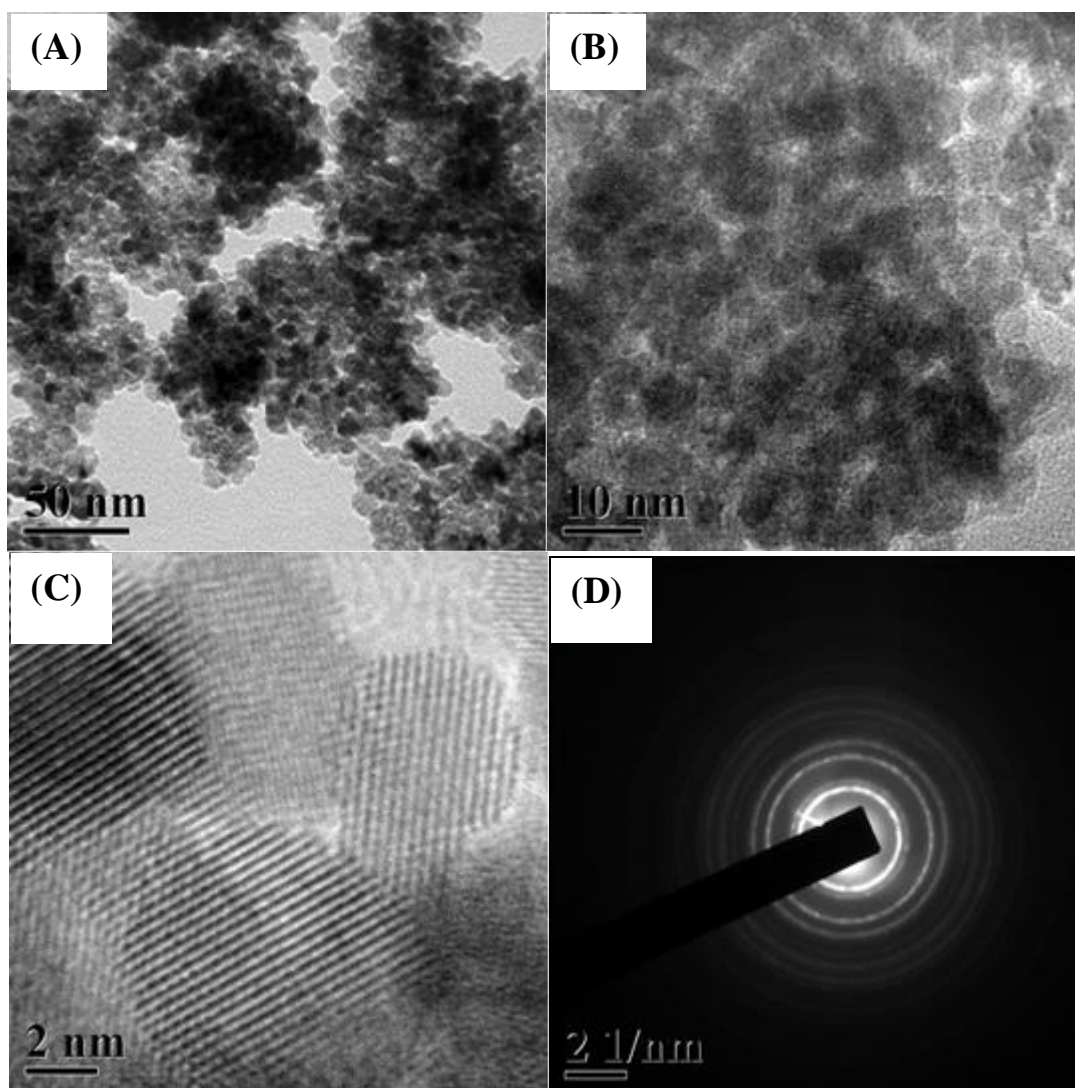


**Fig. 3.13.** (a) TEM image, (b) HRTEM image, (c) lattice fringes and corresponding (d) SAED pattern of 100CeSDS500°C.

### 3.3.7. UV-vis absorption spectra

#### 3.3.7.1. Effect of surfactant and calcination temperature

Fig. 3.14 compares the UV-vis absorption spectra of 100Ce500 and 100CeSDS500 samples. Both the samples exhibited excellent UV-absorption capacity and high transparency in the visible light region. The strong absorption may be due to the charge-transfer transition from  $O_2(2p)$  to the  $Ce^{4+}(4f)$  orbital in  $CeO_2$ .<sup>34</sup> It is quite interesting to note that the ultraviolet light adsorption edge of 100CeSDS500 nanopowder is blue shifted as compared to that of the 100Ce500 sample. The UV-visible absorption spectra of the pure  $CeO_2$  obtained in surfactant assisted route as prepared and calcined at various temperature are depicted in Fig. 3.15. All the nanoparticles showed a strong absorption in the UV region. The band gap values of the 100Ce and 100CeSDS samples calcined at different temperatures are compared in the Table 3.7. The band gap values of 100CeSDS nanopowder calcined at a particular temperature is much higher than that of the 100Ce nanopowder. The band gap values increases from 2.71 to 2.98 eV for the 100Ceasp and 100CeSDSasp nanopowders with crystallite size of 3.4 and 8.4 nm, respectively. The larger is the particle size of the semiconductor compound, the lower is the forbidden band energy.

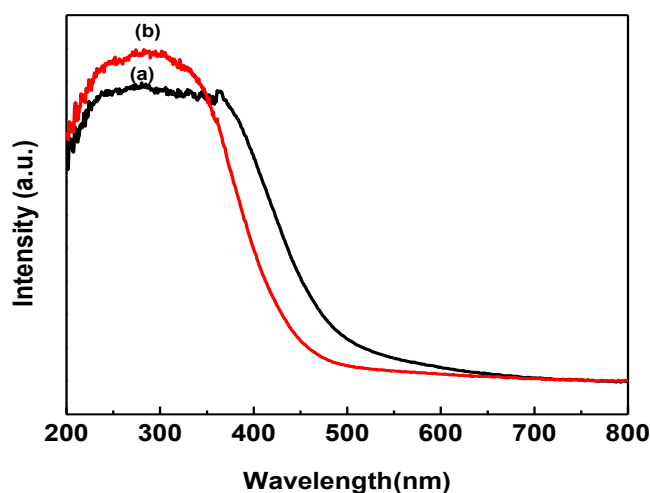


**Fig. 3.14.** UV-vis spectra of (a) 100Ce500 and (b) 100CeSDS500.

The optical properties of  $CeO_2$  are related to the particle size and the aggregation condition of the particles. The blue shift of the adsorption edge indicates the increase of the forbidden band energy. The quantity of photons reaching the core of a spherical particle depends on the particle size and the optical properties of  $CeO_2$  nanocrystals. The larger

particles are generally better light scatterer than smaller particles due to their smoother surface. On the smooth surface, the incident photons are scattered and lost mostly by reflection. The rougher surface formed by the smaller particles allows a greater number of scattered photons to penetrate into the particles. The band gap values of 100Ce and 100CeSDS nanoparticles decrease on calcination at 500°C with an increase in the crystallite size. This red shift with increasing the crystallite size at 500°C is not due to the quantum size effect. It has been reported that the presence of  $Ce^{3+}$  and oxygen vacancies in  $CeO_2$  sample induced a decrease in the band gap.<sup>35</sup> On calcination above 500°C, the amount of  $Ce^{3+}$  and oxygen vacancies decreases from the surface of  $CeO_2$ , and hence again a blue shift in the band gap is observed.

**Table 3.7.** Band gap values of 100Ce, 100CeSDS and 100CeSDSMW samples calcined at different temperatures.

Sample	Band gap	Sample	Band gap	Sample	Band gap
100Ceasp	2.71	100CeSDSasp	2.98	100CeSDSMWasp	2.68
100Ce500	2.52	100CeSDS500	2.83	100CeSDS500	2.58
100Ce650	2.55	100CeSDS650	2.92	100CeSDS650	2.56
10Ce800	2.58	10CeSDS800	2.93	10CeSDS800	2.93
10Ce1000	2.80	10CeSDS1000	3.1		

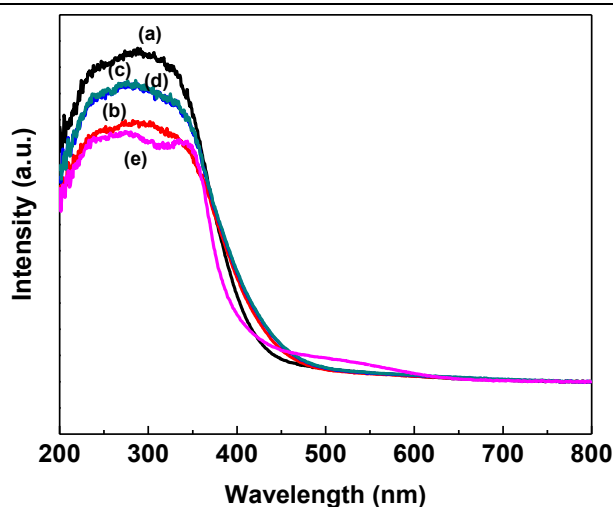


**Fig. 3.15.** UV-visible spectra of the (a) 100CeSDSasp and calcined at (b)500°C, (c) 650°C, (d) 800°C and (e)1000°C.

### 3.3.7.2. Effect of microwave heating.

Fig. 3.16 shows the absorption spectra of the pure CeO<sub>2</sub> nanoparticles obtained in microwave assisted route and calcined at various temperature. Several factor affect the value of the absorbance such as particles size, flaws or defects in grain structure and oxygen deficiency. Lower band gap value (E<sub>g</sub>) of pure CeO<sub>2</sub> obtained in microwave reflux route (2.68 eV) compared to conventional reflux route (2.98 eV) might be due to the presence of larger no of oxygen vacancy defects, which is in good agreement with the E<sub>g</sub> value determined in the literature.<sup>36,37</sup> From Table 3.7, it is seen that the band gap energy initially decreases from 2.68 to 2.56 eV with the increase in calcination temperature upto 650°C further increasing the calcination temperature to 800°C leads to the increase in band gap value 2.93 eV.

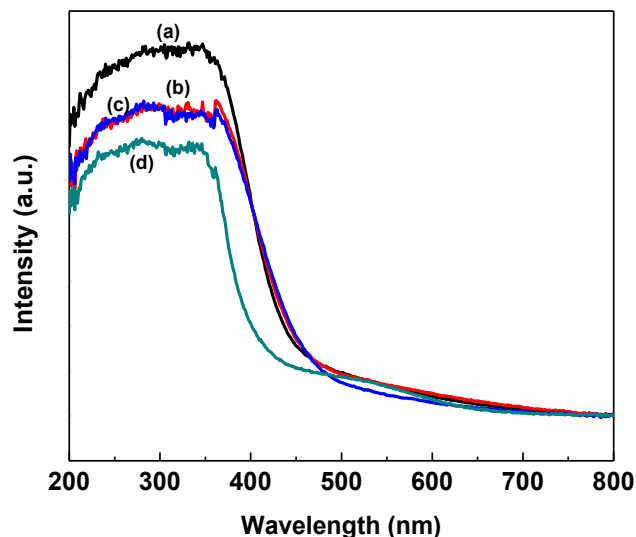


**Fig. 3.16.** UV-visible spectra of the (a) 100CeSDSMWasp and calcined at (b) 500°C (c) 650°C and (c) 800°C.

### 3.3.8. Photoluminescence (PL) spectra

#### 3.3.8.1. Effect of surfactant

Fig.3.17 shows the room temperature PL spectra of the pure CeO<sub>2</sub> obtained by both surfactant free and surfactant assisted route and calcined at 500°C with an excited wavelength of 335 nm. Although the spectra of both the samples are almost identical but the surfactant assisted route leads to the strong emission peak intensity. PL spectrum of the CeO<sub>2</sub> nanoparticles exhibits several strong emission bands in the blue-green region of visible range, i.e. a strong photoluminescence peak at 469 nm (2.64 eV) and three relative weak peaks at



452, 483, and 493 nm, respectively. The three emission peaks located at 370, 414, and 468 nm can be found from the rod-like CeO<sub>2</sub>,<sup>38</sup> while two peaks at 415 and 435 nm has been reported for the flowerlike CeO<sub>2</sub>.<sup>39</sup> A wide PL peak could be observed at 476 nm with a FWHM of 110 nm from CeO<sub>2</sub> thin film.<sup>40</sup> The blue-green emissions are attributed to surface defects in the CeO<sub>2</sub> nanoparticles.<sup>41</sup> The investigation showed that the emission bands ranging from 400 to 500 nm for CeO<sub>2</sub> sample are attributed to the hopping from different defect levels of the range from Ce 4f to O 2p band.<sup>38</sup> It is suggested that the strong emission of the CeO<sub>2</sub> nanoparticles at 469 nm is related to the abundant defects such as dislocations, which is helpful for fast oxygen transportation. Ce 4f level with a width of 1 eV is localized at the forbidden gap, which lies at 3 eV over the valence band (O2p). The defects energy levels between Ce4f and O2p are dependent on the temperature and density of defects in the crystal. At room temperature, electron transition mainly occurred from defects level to O2p level.<sup>42</sup>

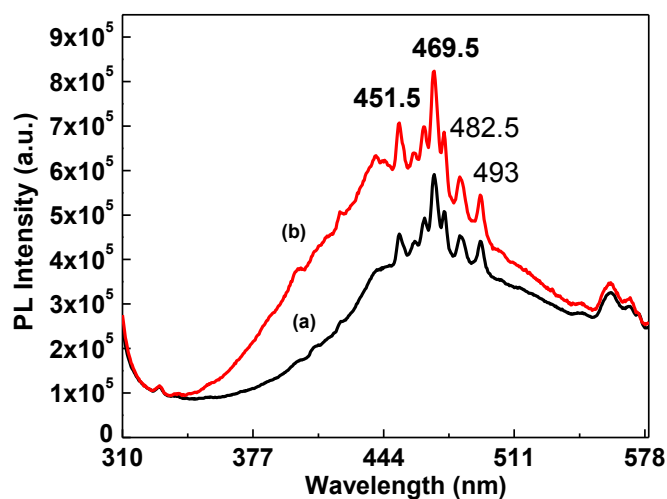


**Fig. 3.17.** PL spectra of (a) 100Ce500 and (b) 100CeSDS500 samples excited at 335 nm.

### 3.3.8.2. Effect of calcination temperature

The photoluminescence (PL) emission spectra of the pure CeO<sub>2</sub> obtained in surfactant assisted route as prepared and calcined at various temperatures are shown in Fig. 3.18. It was found that the all the samples exhibits a good strong blue band emission. In addition shapes of all the spectra are almost identical and mainly consist of multiple emission bands. The PL emission spectra mainly caused by the transition from 4f band of Ce<sup>3+</sup> to the 2p band of O. The broad emission band could be also the result of defects, including oxygen vacancies in the crystal with electronic energy levels below the 4f band.<sup>43</sup> It can be seen that the sample

calcined at 500°C exhibit highest PL emission intensity which might be due to the highest contain of surface  $\text{Ce}^{3+}$  ion as well as oxygen vacancy concentration.<sup>44,45</sup> Our results are in well agreement with the previous report for  $\text{CeO}_2$  in the literature.<sup>44,45</sup>

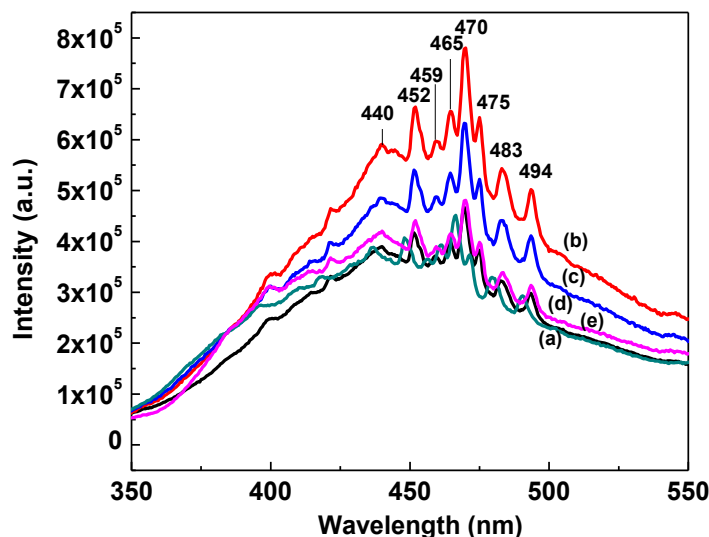


**Fig. 3.18.** PL spectra of (a) 100CeSDSasp, and the samples calcined at (b) 500°C, (c) 650°C, (c) 800°C, and (d) 1000°C.

### 3.3.8.3. Fluorescent microscopy images

Optical properties of the 100CeSDS100 were further investigated under a fluorescent microscope upon exciting at various wavelengths. The fluorescent microscopy images [Fig. 3.19a-c] of the sample exciting at three different wavelengths of 350, 405 and 532 nm exhibits distinct color emission upon excitation at different wavelength. So, the results indicate that the multicolored emissions from the 100CeSDS1000 can be achieved by exciting the material at different wavelengths.

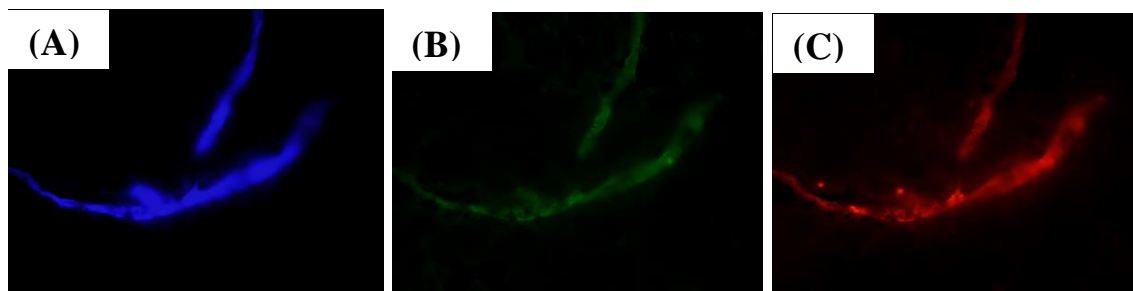


**Fig. 3.19 (A-C)** Fluorescent microscope images of 100CeSDS1000, excited at wavelengths of (A) 350 nm, (B) 405 nm, and (C) 532 nm.

### 3.3.9. XPS spectra

The Ce 3d core level spectra of the pure CeO<sub>2</sub> obtained in both the surfactant assisted route and the surfactant free route are shown in Fig. 3.20(a) and Fig. 3.20(b). The concentration of Ce<sup>3+</sup> in CeO<sub>2</sub> sample synthesized by both surfactant free and surfactant assisted method were determined by XPS curve fitting. In general, it is well accepted that 10 peaks appear for CeO<sub>2</sub> in the Ce3d XPS spectrum.<sup>46,47</sup> These spectra are fully consistent with those reported previously.<sup>48-50</sup> Among the deconvoluted Ce3d fine XPS spectrum shown in Fig. 3.20(a) and Fig. 3.20(b) u, u'', u''', v, v'' and v''' peaks were characterized by Ce<sup>4+</sup> ions, and the four peaks of u<sub>0</sub>, u', v<sub>0</sub>, and v' were characterized by Ce<sup>3+</sup> ions.<sup>51,52</sup> The percentage of Ce<sup>3+</sup> was calculated with these 10 peaks and using the equation given below,<sup>47</sup> which was found to be about 18.5% and 21.3% for surfactant free synthesized CeO<sub>2</sub> and surfactant mediated synthesized CeO<sub>2</sub> sample samples respectively.

$$\text{Ce}^{3+} = V_0 + V' + U_0 + U' \quad (3.1)$$

$$\text{Ce}^{4+} = V + V'' + V''' + U + U'' + U''' \quad (3.2)$$

$$\% \text{Ce}^{3+} = \frac{u_0 + u' + v_0 + v'}{u_0 + u' + u + u'' + u''' + v_0 + v' + v + v'' + v'''} \quad (3.3)$$

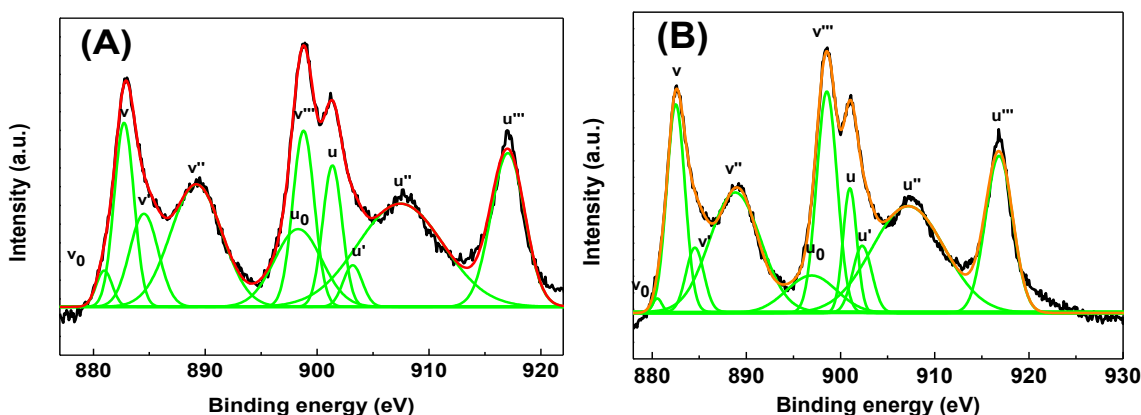


**Fig. 3.20.** Ce 3d XPS spectra of (a) 100CeSDS500 and (b) 100Ce500.

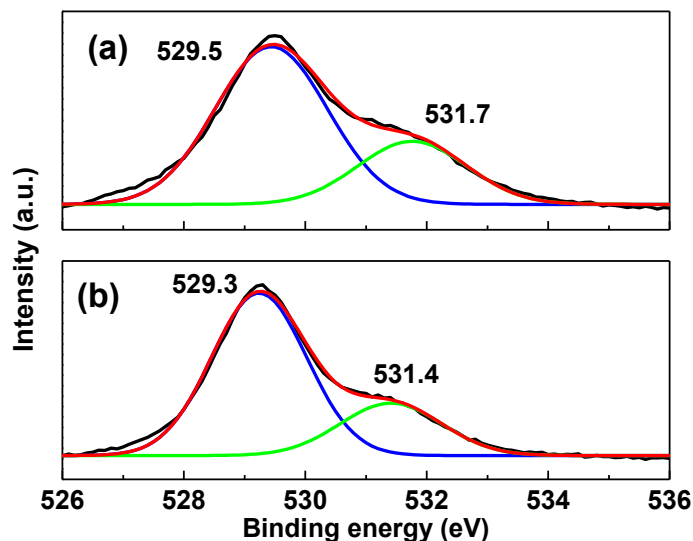


**Fig. 3.21.** O 1s core level photoemission spectra from (a) 100CeSDS500°C and (b) 100Ce500°C.

Fig. 3.21 shows the O 1s spectra of both pure CeO<sub>2</sub> obtained with and without surfactant and calcined at 500°C for 2 h. The low-BE component in the range of  $529.3 \pm 0.2$  eV could be assigned to oxidic species, whereas high-BE components ( $531.4 \pm 0.3$  eV) is ascribable to hydroxidic species and/or ambient moisture. This indicates that Ce<sup>4+</sup> ions is mainly located on the surface of cerium oxide nanoparticles which might have some additional contribution to the blue shift of cerium oxide nanoparticles, this might be due to the change of charge state from 3+ to 4+ which in turn increases the charge-transfer gap between O2p and Ce 4f bands according to PL results.

### 3.3.10. NH<sub>3</sub>-TPD profiles

NH<sub>3</sub>-TPD profiles of 100Ce500 and 100CeSDS500 are compared in Fig. 3.22(A), which provides clear information about the surface acidity properties. The strength of the sites retaining NH<sub>3</sub> below 300°C is characterized as weak acid sites and the retention of NH<sub>3</sub> above 300°C has been considered as strong acidic sites. The intense broad peak in the lower temperature range from 127°C to 327°C were found in both the nanopowders, which revealed the existence of higher number of moderate acidic sites as compared to strongest acid sites. The positions of the peaks are compared in Table 3.8. The strongest acid sites releasing NH<sub>3</sub> at temperatures as high as 658°C are Lewis-acidic in nature, while moderate acid sites

desorbing  $\text{NH}_3$  at lower temperatures are attributed as Brønsted acidic sites. The 100CeSDS500 shows both higher Lewis acidic and Brønsted acidic sites than the 100Ce500. The higher acidity on the surface of the 100CeSDS500 is attributed to the presence of residual sulfate originating from the sodium dodecyl sulphate used during the synthesis procedure, which remains even after calcination at  $500^\circ\text{C}$ .

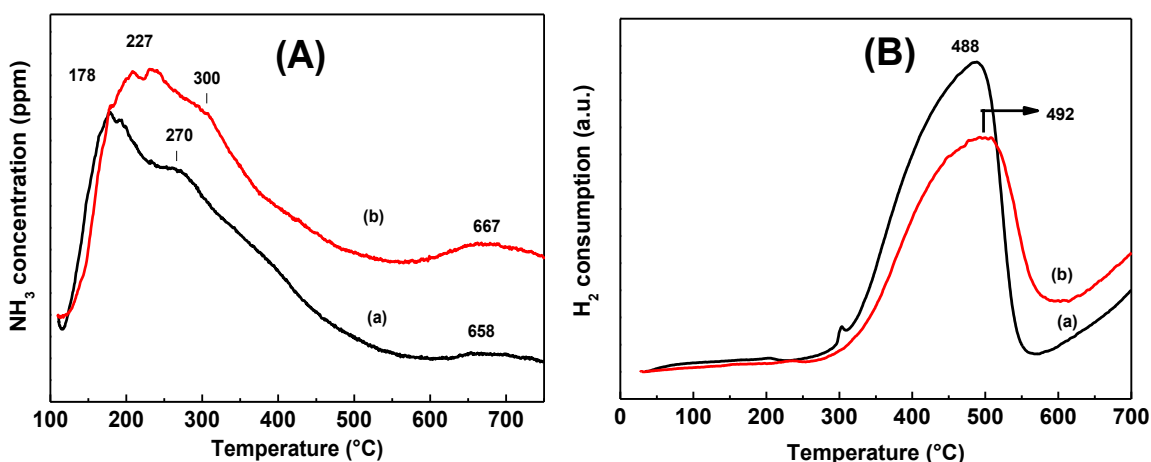


Fig. 3.22. (A) TPD and (B) TPR profiles of (a) 100Ce500, (b) 100CeSDS500.

Table 3.8. TPD data of 100Ce500 and 100CeSDS500.

Sample	No. of peaks	Temperature maximum ( $^\circ\text{C}$ )	Volume (mL/g STP)	Peak height
100Ce500	1	178	0.1830	0.0051
	2	658	0.2257	0.0040
100CeSDS500	1	227	0.8286	0.0058
	2	667	0.2426	0.0020

### 3.3.11. TPR profiles

Fig. 3.22(B) shows the TPR profiles of 100Ce500 and 100CeSDS500. The reduction of  $\text{CeO}_2$  taking place in the temperature range  $277\text{--}577^\circ\text{C}$  are characteristics of surface reduction processes. This may be due to the higher number of effective oxygen sites and/or oxygen vacancy clusters on the surface of  $\text{CeO}_2$ .<sup>53-55</sup> The hydrogen consumption is slightly higher in the lower temperature regions in case of 100Ce500 sample as compared to that of 100CeSDS500 are given in below Table 3.9. The smaller crystallite size of the  $\text{CeO}_2$

nanopowder synthesized via surfactant free route with lower Ce–O symmetry leads to higher number of reactive surface oxygen sites and/or surface oxygen vacancy clusters in the sample. Further, the surfactant associated with CeO<sub>2</sub> crystallite increases the reduction temperature of surface oxygen species from 488°C to 492°C by promoting the reduction process efficiently.

**Table 3.9.** Comparison of TPR data of 100Ce500 and 100CeSDS500 samples.

Sample	Temperature maximum (°C)	Volume (mL/g STP)	Peak height
100Ce500	488	19.49	0.108
100CeSDS500	492	14.42	0.068

### 3.4. Conclusions

Nanocrystalline CeO<sub>2</sub> particles with high surface area were synthesized through a facile wet chemical route using inorganic precursors of ceric ammonium nitrate, with and without SDS as surfactant. All samples have been studied by using TG–DSC, XRD, BET, XPS, UV, PL, HRTEM, TPR and TPD techniques. Surfactant promoted the formation of well crystalline cubic CeO<sub>2</sub> at a lower temperature of 100°C. A better control over the growth of the CeO<sub>2</sub> particles against calcination were observed in 100CeSDS sample than in the CeO<sub>2</sub> synthesized without surfactant. XPS analysis showed that the percentage of Ce<sup>3+</sup> was found to be 18.5 and 21.3% for 100Ce500 and 100CeSDS500 samples, respectively. Surfactant molecule also enhances the UV absorption, and surface acidity of CeO<sub>2</sub> nanoparticles. 100CeSDS500 showed a stronger blue PL emission centered at 469.5 nm with higher emission intensity compared to that of 100Ce500. HRTEM image of pure CeO<sub>2</sub> obtained in surfactant assisted route further confirmed its highly crystalline nature as compared to that of pure CeO<sub>2</sub> obtained in surfactant free route. NH<sub>3</sub>-TPD analysis revealed that surfactant assisted route imparts better surface acidity in the synthesized nanopowder.

### References

1. F. Zhang, S. W. Chan, J. E. Spanier, E. Apak, Q. Jin, R. D. Robinson and I. P. Herman, *Appl. Phys. Lett.*, 2002, 80, 127.
2. J. R. V. Garcia, L. B. Romero, R. Tu and T. Goto, *Thin Solid Films*, 2010, 519, 1.
3. M. Asadullah, K. Tomishige and K. Fujimoto, *Catal. Commun.*, 2001, 2, 63.

4. L. Qian, J. Zhu, W. Du and X. Qian, *Mater. Chem. Phys.*, 2009, 115, 835.
5. K. Sohlberg, S. T Pantelides and S. F Pennycook, *J. Am. Chem. Soc.*, 2001, 123, 6609.
6. P. Jasinski, T. Suzuki and H. U. Anderson, *Sens. Act. B.*, 2003, 95, 73.
7. F. Goubin, X. Rocquefelte, M. H. Whangbo, Y. Montardi, R. Brec and S. Jobic, *Chem. Mater.*, 2004, 16, 662.
8. D. G. Shchukin and R. A. Caruso, *Chem. Mater.*, 2004, 16, 2287.
9. A. Trovarelli, C. Leitenburg, M. Boaro and G. Dolcetti, *Catal. Today*, 1999, 50, 353.
10. Y. Li, Q. Fu and M. F. Stephanopoulos, *Appl. Catal. B: Environ.*, 2000, 27, 179.
11. C. T. Kresge, M. E. Leonowicz, W. J. Roth, J. C. Vartuli and J. S. Beck, *Nature*, 1992, 359, 710.
12. Q. Huo, D. I. Margolese, U. Ciesla, P. Feng, T. E. Gier, P. Sieger, R. Leon, P. M. Petroff, B. Schueth and G. D. Stucky, *Nature*, 1994, 368, 317.
13. P.T. Tanev and T.J. Pinnavaia, *Science*, 1995, 267, 865.
14. U. Ciesla, S. Schacht, G. D. Stucky, K. K. Unger and F. Schueth, *Angew. Chem. Int. Ed. Engl.*, 1996, 35, 541.
15. D. M. Antonelli and J. Y. Ying, *Angew. Chem. Int. Ed. Engl.*, 1996, 35, 426.
16. Q. Huo, D. I. Margolese, U. Ciesla, D. G. Demuth, P. Feng, T. E. Gier, P. Sieger, A. Firouzi, B. F. Chmelka, B. Schueth and G. D. Stucky, *Chem. Mater.*, 1994, 6, 1176.
17. S. Lv, C. Wang, T. Zhou, S. Jing, Y. Wu and C. Zhao, *J. Alloys. Compds.*, 2009, 477, 364.
18. R. Elansezhian, B. Ramamoorthy and P. K. Nair, *J. Mater. Process. Technol.*, 2009, 209, 233.
19. D. Terribile, A. Trovarelli, J. Llorca, C. de Leitenburg and G. Dolcetti, *J. Catal.*, 1998, 178, 299.
20. G. Wang, Q. Mu, T. Chen and Y. Wang, *J. Alloys Compd.*, 2010, 493, 202.
21. N. K. Renukaa, A. K. Praveen and C. U. Aniz, *Microporous Mesoporous Mater.*, 2013, 169, 35.
22. S. A. H. Tabrizi, *Appl. Surf. Sci.*, 2011, 257, 10595.
23. M. Brigante and P. C. Schulz, *Chem. Eng. J.*, 2012, 191, 563.
24. D. Zhang, L. Huang, J. Zhang and L. Shi, *J. Mater. Sci.*, 2008, 43, 5647.
25. J. G. Li, T. Ikegami, J. H. Lee and T. Mori, *Acta Mater.*, 2001, 49, 419.
26. M. Leoni, R. D Maggio, S. Polizzi and P Scardi, *J. Am. Ceram. Soc.*, 2004, 87, 1133.
27. P Scardi., *International Union of Crystallography Series*; Bunge, H.-J., Fiala, J, Snyder, R. L., Eds.; Oxford University Press: Oxford, U.K., 1999, 570.
28. J. Seo, J. W. Lee, J. Moon, W. Sigmund and U. Paik, *ACS Appl. Mater. Interfaces*, 2014, 6, 7388.
29. S. Soren, M. Besso and P. Parhi, *Ceramics International*, 2015, 41, 8114.
30. T. S. Sreeremya, K. M. Thulasi, A. Krishnan and S. Ghosh, *Ind. Eng. Chem. Res.*, 2012, 51, 318.
31. C. Binet, A. Badri and J. C. Lavalley, *J. Phys. Chem.*, 1994, 98, 6392.
32. T. Taniguchi, Y. Sonoda, M. Echikawa, Y. Watanabe, K.o Hatakeyama, S. Ida, M. Koinuma, and Y. Matsumoto, *ACS Appl. Mater. Interfaces*, 2012, 4, 1010.
33. P. W. Dunne, A. M. Carnerup, A. Węgrzyn, S. Witkowski, and R. I. Walton, *J. Phys. Chem. C*, 2012, 116, 13435.

34. Y. W. Zhang, R. Si, C. S. Liao, C. H. Yan, C. X. Xiao and Y. Kou, *J. Phys. Chem. B*, 2003, 107, 10159.
  35. P. Patsalas, S. Logothetidis, L. Sygellou and S. Kennou, *Phys. Rev. B*, 2003, 68, 035104.
  36. C. Aydin, M. S. Abd El-Sadek, K. Zheng, I. S. Yahia and F. Yakuphanoglu, *Opt. Laser Technol.*, 2013, 48, 447.
  37. A. E. Morales, E. S. Mora and U. Pal, *Rev. Mex. Fis.*, 2007, 53, 18.
  38. C. W. Sun, H. Li, H. R. Zhang, Z. X. Wang and L. Q. Chen, *Nanotechnology*, 2005, 16, 1454.
  39. C. W. Sun, H. Li and L. Q. Chen, *J. Phys. Chem. Solids.*, 2007, 68, 1785.
  40. C. L. Chai, S. Y. Yang, Z. K. Liu, M. Y. Liao and N. F. Chen, *Chin. Sci. Bull.*, 2003, 48, 1198.
  41. S. Phoka, P. Laokul, E. Swatsitang, V. Promarak, S. Seraphin and S. Maensiri, *Mater. Chem. Phys.*, 2009, 115, 423.
  42. C. G. Kim, *Appl. Phys. Lett.*, 2001, 79, 3047.
  43. A. H. Morshed, M. E. Moussa, S. M. Bedair, R. Leonard, S. X. Liu and N. E. Masry, *Appl. Phys. Lett.*, 1997, 70, 1647.
  44. S. Phokha, S. Pinitsoontorn, P. Chirawatkul, Y. Pooarporn and S. Maensiri, *Nanoscale Research Lett.*, 2012, 7, 425.
  45. K. K. Babitha, A. Sreedevi, K. P. Priyanka, B. Sabu and T. Varghese, *Indian J. of Pure & Appl. Phys.*, 2015, 53, 596.
  46. E. J. Preisler, O. J. Marsh, R. A. Beach, T. C. McGill and J. Vac. Sci. Tech. B, 2001, 19, 1611.
  47. J. Zhang, X. Ju, Z. Y. Wu, T. Liu, T. D. Hu, Y. N. Xie and Z. L. Zhang, *Chem. Mater.*, 2001, 13, 4192.
  48. S. Tsunekawa, T. Fukuda and A. Kasuya, *Surf. Sci.*, 2000, 457, 437.
  49. D. R. Mullins, S. H. Overbury and D. R. Huntley, *Surf. Sci.*, 1998, 409, 307.
  50. R. Vercaemst, D. Poelman, R. L. Van Meirhaeghe, L. Fiermans, W. H. Laflike and F. Cardon, *J. Lumin.*, 1995, 63, 19.
  51. S. Watanabe, X. L. Ma and C. S. Song, *J. Phys. Chem. C*, 2009, 113, 14249.
  52. A. Kumar, S. Babu, A.S. Karakoti, A. Schulte and S. Seal, *Langmuir*, 2009, 25, 10998.
  53. H. C. Yao and Y. F. Y. Yao, *J. Catal.*, 1984, 86, 254.
  54. M. F. L. Johnson and J. Mooi, *J. Catal.*, 1987, 103.
  55. L. A. Bruce, M. Hoang, A. E. Hughes and T. W. Turney, *Appl. Catal. A: Gen.*, 1996, 134, 351.
-



## Chapter 4

# High Surface Area $\text{Sm}^{3+}$ Doped Mesoporous $\text{CeO}_2$ Nanocrystals

### Outline

*This chapter deals with the intensive characterization of nanosized  $\text{Sm}^{3+}$  (0.5, 1, 2, 5, 10 and 20 mol%)-doped  $\text{CeO}_2$  (Ce-Sm) synthesized through a surfactant assisted wet chemical route using inorganic precursors of samarium oxide and ceric ammonium nitrate, and sodium dodecyl sulphate as surfactant. The synthesized nanopowders were investigated by various structural, optical and spectroscopic techniques such as TG-DSC, XRD, BET surface area, FESEM, HRTEM, UV-vis diffuse reflectance, PL,  $\text{H}_2$ -TPR, TPD and XPS techniques. For the purpose of comparison, the representative sample 1 mol%  $\text{Sm}^{3+}$  doped  $\text{CeO}_2$  were also synthesized by using cationic and non-ionic surfactants of DDA and PEG, respectively. In addition, the influence of microwave refluxing during synthesis on the structural and optical properties of the representative sample 1 mol%  $\text{Sm}^{3+}$  doped  $\text{CeO}_2$  nanopowders were also evaluated. The XRD results indicate that the calcined Ce-Sm and even as-prepared material have cubic fluorite structure of  $\text{CeO}_2$  with no crystalline impurity phase. XRD studies along with HRTEM results confirmed the formation of mesoporous nanocrystalline  $\text{CeO}_2$  at a lower temperature as low as  $100^\circ\text{C}$  and the crystallite size increases with increasing the calcination temperature. A detailed analysis revealed that  $\text{Sm}^{3+}$  doping in to  $\text{CeO}_2$  has increased the lattice volume, surface area, mesopore volume and engineered the surface defects. Further  $\text{Sm}^{3+}$  doping was found to cause unusual emissions with a dominant  ${}^4\text{G}_{5/2} \rightarrow {}^6\text{H}_{5/2}$  transition centered at 573 nm. Additionally, the luminescence intensities enhanced with increasing  $\text{Sm}^{3+}$  concentration from 0.5 mol% to 1 mol% with further increasing  $\text{Sm}^{3+}$  concentration leads to the decrease in luminescence intensities.*

#### 4.1. Introduction

Ceria ( $\text{CeO}_2$ ) nanoparticles especially doped with rare earths have attracted growing interest and opened many new possibilities for technological applications, such as adsorption, transportation/storage of fluids and gases, solar cell, solid oxide fuel cell, auto-motive exhaust promoter, catalysis, chemical sensor and phosphors.<sup>1-7</sup> Samaria ( $\text{Sm}_2\text{O}_3$ ) doped  $\text{CeO}_2$  nanoparticles is known for their unique properties such as high thermal and chemical stability, high ionic-electrical conductivity, high refractive index, large oxygen storage capacity, UV-shielding, and the quick and expedient mutation of the oxidation state of cerium between Ce(III) and Ce(IV).<sup>3,5,8-10</sup> Additionally,  $\text{CeO}_2$  is one of the best host materials for  $\text{Sm}^{3+}$  ions, and can serve as the high performance phosphor material to develop a wide range of nanotechnological optical devices, in comparison with other inorganic metal oxide nanomaterials.<sup>10-12</sup> Many of the studies have been focused on the preparation of nanostructured  $\text{Sm}^{3+}$  doped  $\text{CeO}_2$ .<sup>5,8,13-15</sup> But there are only a very limited numbers of publications available regarding the synthesis of mesoporous  $\text{CeO}_2$  based materials especially  $\text{Sm}_2\text{O}_3$  doped  $\text{CeO}_2$ .<sup>16,17</sup> Hao *et al.* synthesized  $\text{Fe}^{3+}$  doped mesoporous  $\text{CeO}_2$  using triblock copolymer P123 as the template and  $\text{Ce}(\text{NO}_3)_3 \cdot 6\text{H}_2\text{O}$  and  $\text{Fe}(\text{NO}_3)_3 \cdot 9\text{H}_2\text{O}$  as raw materials by means of a hydrothermal procedure.<sup>18</sup> To the best of our knowledge, there is no publication available regarding the synthesis of mesoporous  $\text{Sm}_2\text{O}_3$  doped  $\text{CeO}_2$  materials via surfactant templating route. Mesoporous  $\text{Ce}_{0.8}\text{Sm}_{0.2}\text{O}_{1.9}$  oxide with surface area in the range of 29 to 85  $\text{m}^2/\text{g}$  was prepared by a glycine-nitrate combustion process<sup>16</sup> or EDTA-citrate combined complexing sol-gel process<sup>17</sup> based on an in situ created nickel oxide as template after calcining at a higher temperature of 700°C. In common, hard-template methods suffer from the drawbacks such as tedious and complicated preparation and removal of the template after the synthesis and impurities further restrict the applications of the product. It is still a challenge to synthesize thermally stable mesoporous doped  $\text{CeO}_2$  with a high surface area as doping typically facilitates the sintering of  $\text{CeO}_2$  due to increased mobility of oxygen ion in the lattice.<sup>19</sup> Therefore, it is highly desirable to produce mesoporous powder of  $\text{Sm}^{3+}$  doped  $\text{CeO}_2$  materials, which exhibits high surface area, and crystalline framework, using an efficient, simple and economic method to meet the growing demand of various applications.

Recently, few studies have been reported concerning the photoluminescence (PL) properties of  $\text{CeO}_2$  doped with  $\text{Sm}^{3+}$  ion, mostly above as large as 5 mol%.<sup>12-15</sup> Luminescent

properties of nanocube and nanorod morphologies of  $\text{Sm}^{3+}$  doped  $\text{CeO}_2$  synthesized by hydrothermal treatments was reported.<sup>10</sup> A decrease in PL intensity was observed with increase in  $\text{Sm}^{3+}$  concentration (5 to 20 mol%) in  $\text{Sm}^{3+}$  doped  $\text{CeO}_2$ , synthesized by modified sol-gel route and then calcined at  $1000^\circ\text{C}$  for 4 h.<sup>15</sup> The present study report a simple surfactant route using cheaper aqueous solutions of inorganic precursors and surfactant for the synthesis of mesoporous and high surface area  $\text{Sm}^{3+}$  doped  $\text{CeO}_2$  powders, with crystalline cubic phase even at lower temperature of  $100^\circ\text{C}$ . This approach has a high yield and can produce ultrafine  $\text{CeO}_2$  powder in multigram-scale from the same batch. Only very few reports are available on PL properties of  $\text{Sm}^{3+}$  doped cubic  $\text{CeO}_2$  in mesoporous morphology and its as-prepared hybrid material with sodium dodecyl sulphate (SDS). In the present study, we report a simple surfactant assisted route using cheaper aqueous solutions of inorganic precursors and a surfactant for the synthesis of mesoporous and high surface area  $\text{Sm}^{3+}$  (0.5 to 20 mol%) doped  $\text{CeO}_2$  powders, with crystalline cubic phase even at lower temperatures of  $100^\circ\text{C}$ , and their enhanced PL properties.

## 4.2. Synthesis and characterization of $\text{Sm}^{3+}$ doped $\text{CeO}_2$ nanocrystals

The methodology for the synthesis of mesostructured as-synthesized precursor and  $\text{Sm}^{3+}$  doped  $\text{CeO}_2$  using surfactant is given in chapter-2. All the mesoporous 0.5 to 20 mol%  $\text{Sm}^{3+}$  doped  $\text{CeO}_2$  nanocrystals synthesized using different surfactants were yellowish white and non-agglomerated. The prepared samples were analyzed using different characterization techniques (details of the techniques are discussed in chapter 2) such as TG-DSC, XRD, FTIR,  $\text{N}_2$  sorption analysis, FESEM, HRTEM, UV-vis, PL, XPS,  $\text{H}_2$ -TPR and  $\text{NH}_3$ -TPD.

## 4.3. Results and discussion

### 4.3.1. TG-DSC analysis of $\text{Sm}^{3+}$ doped $\text{CeO}_2$

#### 4.3.1.1. Effect of dopant concentration

The thermal behavior of the as-synthesized nanopowders was studied by using TG–DSC technique in air atmosphere from 25 to  $1000^\circ\text{C}$  with a temperature ramp of  $10^\circ\text{C min}^{-1}$ . The TG-DSC curves of the as-synthesized  $\text{Sm}^{3+}$  doped  $\text{CeO}_2$  samples, prepared using SDS through conventional reflux method, at different molar ratios of  $\text{Sm}^{3+}$  (0.5 to 20 mol%) are shown in Figs. 4.1 and 4.2. Four steps of weight losses in the regions of AB, BC, CD and DE were observed in all samples over 25 to  $1000^\circ\text{C}$ . The % of mass loss obtained from TG

curves of the samples are summarized in Table 4.1. The DSC profile of all samples show two endothermic peaks, which appear around 50-70°C and 120-150°C in desorption of physisorbed water in the as-prepared sample. In this region (AB), the mass loss of the material was 2 to 4%. A prominent exothermic peak in DSC curve centering at 200-210°C along with several shoulder peaks attributed to the decomposition of the residual organic template. Shoulder peaks are due to the removal of sulphate of SDS molecules and the formation of crystalline cubic CeO<sub>2</sub> structure from the remaining amorphous cerium hydroxide, respectively. Another small shoulder peak at 260°C may be caused by the oxidation of Ce compound and the formation of CeO<sub>2</sub>.<sup>20</sup> This particular exotherms in the Fig. 4.1 and 4.2 were associated with a relatively less weight loss of ~ 7-13 % in the BC region, which further suggests that only a small amount of undecomposed precursor with surfactant is present in the as-prepared sample. Ramimoghadam *et al.* recorded the thermal degradation of pure SDS and observed a weight loss in the range of 160 to 380°C.<sup>21</sup> Zhang *et al.* also reported the weight loss of pure SDS in TG curve was found in the temperature range 190-350°C due to the decomposition of the alkyl chain.<sup>22</sup> No significant weight loss (0.2-1.5 %) was observed in the CD region. At the same time, it is noticed that the weight loss of 2-4 % occurred over reasonably higher temperatures from 690 to 1000°C in the DE region, which may be due to the removal of SO<sub>2</sub> adsorbed gases from bound dodecyl sulfate group that are adsorbed into the mesopores according to Dunne *et al.*<sup>23</sup> It should also be noted that no shift in the peak position of endothermic peaks as well as exothermic peaks was observed with increasing Sm<sup>3+</sup> content (shown Fig. 4.3a) but the intensity of the exothermic peak centered around 200°C become weaker with increasing Sm<sup>3+</sup> content up to 20 mol%, we anticipate that this peak might correspond to surfactant decomposition. Above 40 % weight loss were observed in Sm<sup>3+</sup>-doped CeO<sub>2</sub> nanowires.<sup>5</sup> A total mass loss of 17.29 % would occurs for decomposition of CeO(OH)<sub>2</sub>·H<sub>2</sub>O → CeO<sub>2</sub> + 2H<sub>2</sub>O or in Ce(OH)<sub>4</sub> anhydrite. A relatively low weight loss of total ~ 12 to 26 % over room temperature to 1000°C suggests that the sample consisted of a mixture of more CeO<sub>2</sub> than the undecomposed precursor of cerium oxyhydroxide/ hydroxide with surfactant.

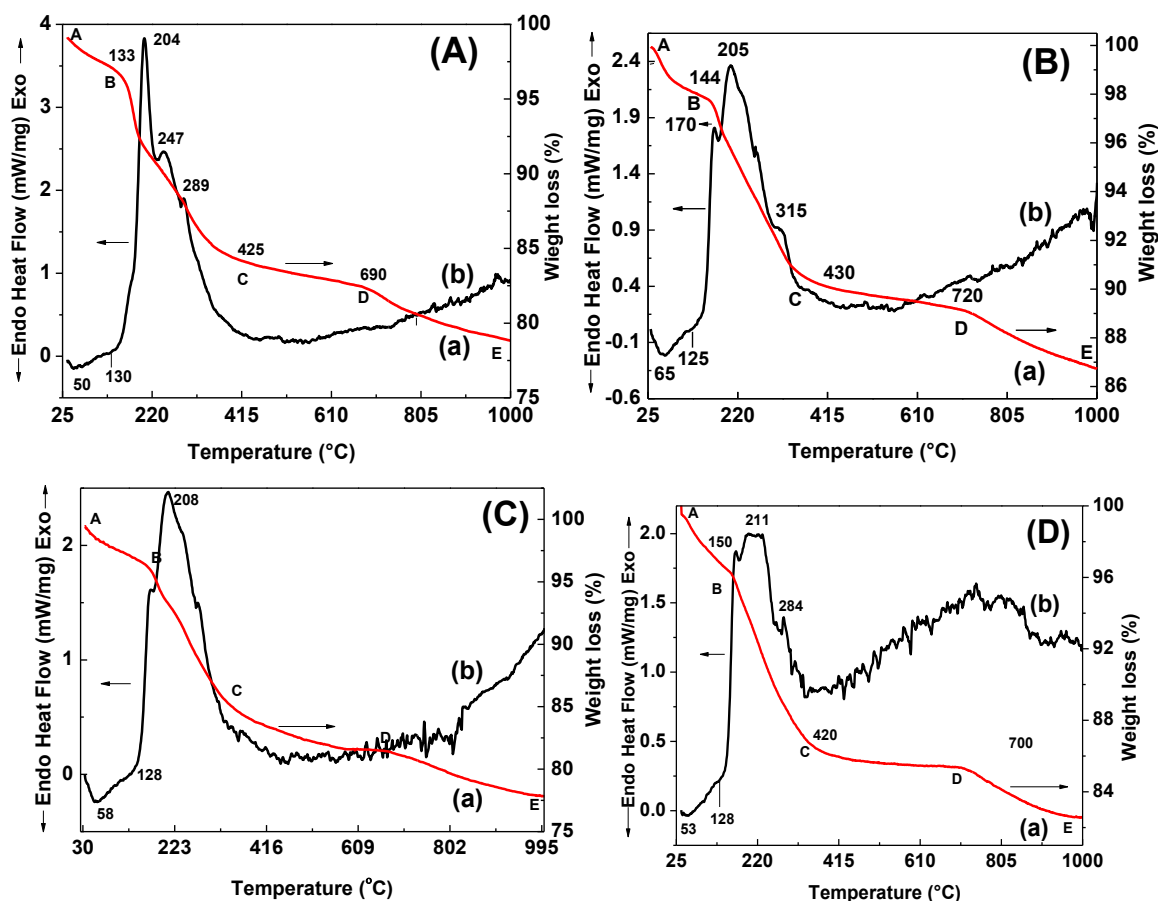


**Fig. 4.1.** (a) TG and (b) DSC curves of (A) 0.5, (B) 1, (C) 2, and (D) 5 mol% Sm<sup>3+</sup> doped as-synthesized CeO<sub>2</sub> samples.

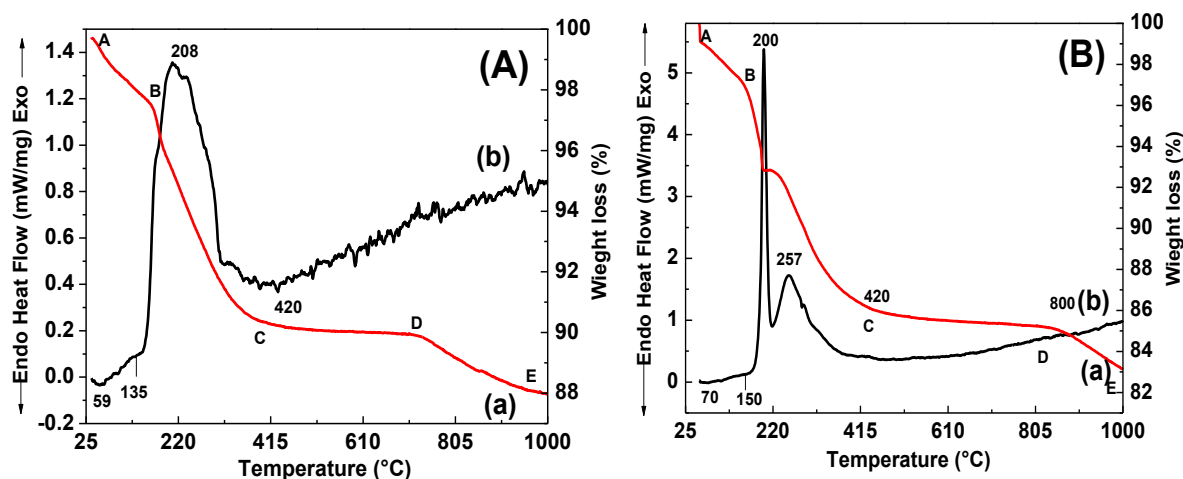


**Fig. 4.2.** (a) TG and (b) DSC curves of (A) 10 and (B) 20 mol% Sm<sup>3+</sup> doped as-synthesized CeO<sub>2</sub> samples.

**Table 4.1.** Weight loss% observed in as-prepared Sm<sup>3+</sup> doped CeO<sub>2</sub> samples prepared through conventional refluxing method using SDS as surfactant.

Samples	TG result			
	Region	Temperature range (°C)	Mass Loss (%)	Total mass loss (%)
0.5SmCeSDSasp	AB	30-140	3	21.2
	BC	140-425	13	
	CD	425-690	1.5	
	DE	690-1000	3.7	
1SmCeSDSasp	AB	30-140	2	13
	BC	140-430	8	
	CD	430-690	0.5	
	DE	690-1000	2.5	
2SmCeSDSasp	AB	30-150	2.7	26
	BC	140-420	13.2	
	CD	420-670	2.0	
	DE	670-1000	3.5	
5SmCeSDSasp	AB	30-150	3.6	17.5
	BC	150-420	10.4	
	CD	420-700	0.6	
	DE	690-1000	2.9	
10SmCeSDSasp	AB	30-150	2.4	12.1
	BC	150-420	7.4	
	CD	420-700	0.3	
	DE	700-1000	2.0	
20SmCeSDSasp	AB	30-150	3.0	17
	BC	150-440	11	
	CD	440-800	0.6	
	DE	800-1000	2.4	

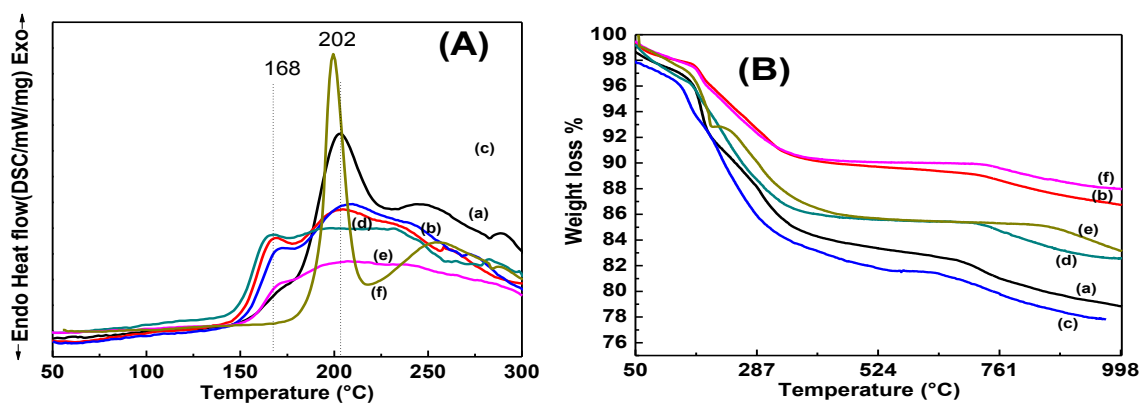


**Fig. 4.3.** (A) DSC and (B) TG curves of (a) 0.5, (b) 1.0, (c) 2.0, (d) 5.0, (e) 10, and (f) 20 mol% Sm<sup>3+</sup> doped as-prepared CeO<sub>2</sub> samples.

### 4.3.1.2. Influence of conventional and microwave refluxing

Fig. 4.4 show the DSC and TGA curves of the as-synthesized 1 mol% Sm<sup>3+</sup> doped CeO<sub>2</sub> prepared by using SDS as surfactant and followed by (a) without refluxing, (b) normal refluxing, and (c) with microwave refluxing method. A remarkably higher mass loss (28%) was observed (see Table 4.2) in the sample synthesized without refluxing as compared to that of the samples prepared via conventional (13%) and microwave refluxing (11%) method, suggesting that the as-prepared powder obtained through without refluxing method contain more amount of oxhydroxide precursors. Refluxing method play a significant role for the transformation of the amorphous portion Ce(OH)<sub>4</sub> to crystalline CeO<sub>2</sub>. DSC curve shows that both the prominent exothermic peak and shoulder peaks notably shifted towards lower temperatures in case of the sample obtained by refluxing method than that of the sample obtained without refluxing method. The result suggests that the refluxing method enhances the crystallization process. However, no change in the position of the exothermic peak of 1SmceSDSasp was observed when compared to that of 1SmCeSDSMWasp. But the shoulder peak become sharper and intensity become stronger in case of the latter sample. TG curve shows that above 700°C, apparent mass loss was ~ 4% in case of sample synthesized via without refluxing method as compared to the conventional (2.5%) and microwave refluxing (1.5%) method, may be attributed to it higher contain of SO<sub>2</sub>, which gradually decomposed at higher temperature.

**Table 4.2.** Weight loss % of Sm<sup>3+</sup> doped as-prepared CeO<sub>2</sub> samples prepared through without refluxing and microwave refluxing method.

Samples	TG result			
	Region	Temperature range (°C)	Mass loss (%)	Total mass loss (%)
1SmCeSDSNRasp	AB	30-150	4	28.7
	BC	150-400	18.5	
	CD	400-700	1.6	
	DE	700-1000	4.6	
1SmCeSDSMWasp	AB	30-147	5.4	10.8
	BC	147-400	5	
	CD	400-800	0.2	
	DE	800-1000	0.2	

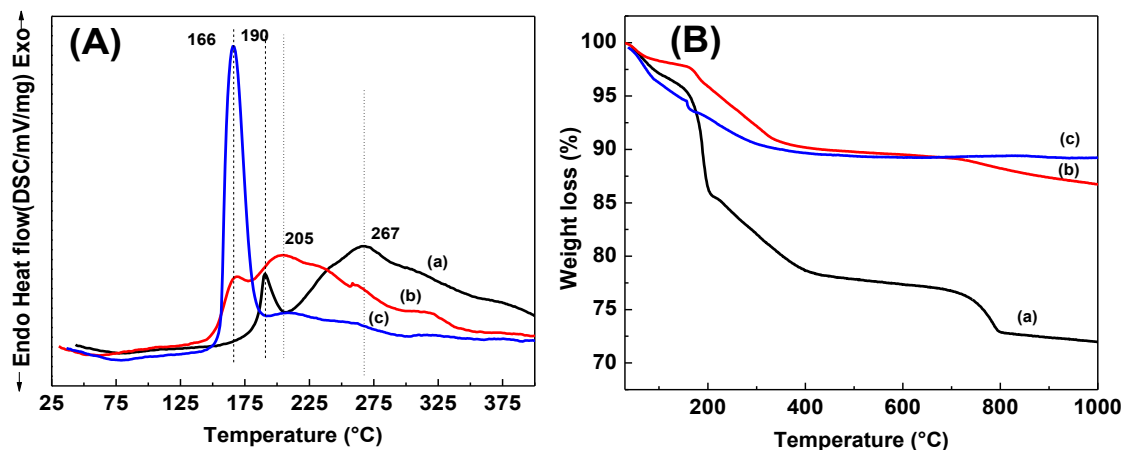


**Fig. 4.4.** (A) DSC and (B) TG curves of 1SmCeSDSasp prepared via (a) without refluxing, (b) normal refluxing, and (c) microwave refluxing method.

#### 4.3.1.3. Influence of anionic, cationic and nonionic surfactant

The comparative results of the thermal decomposition of as-synthesized precursors obtained upon varying the type of surfactant provided some informations on the interaction between the surfactant molecules and inorganic precursors. Fig. 4.5 show the TG and DSC curves of the as-synthesized 1 mol%  $\text{Sm}^{3+}$  doped  $\text{CeO}_2$  prepared by conventional refluxing method using DDA and PEG, respectively. In the TG curve, very low weight loss of 4% was observed for the nanopowder synthesized using nonionic surfactant PEG, while 8.4% and 13% were observed for the samples synthesized using DDA and SDS, respectively. The result indicates that the nonionic surfactant molecule has weaker interaction with the inorganic precursor molecule; hence a substantial amount of it can be removed just by simple washing. As can also be seen from the DSC curve (Fig. 4.5A), the temperature required for the degradation of PEG surfactant molecule was also centered at a comparatively lower temperature of 186°C. The anionic surfactant molecule SDS exhibit stronger interaction with the inorganic precursors and show greater mass loss of 13% as compared to that with the cationic surfactant molecule DDA, and showing a mass loss of 8.4% (Table 4.3). The peak corresponding to the surfactant degradation was also shifted to a higher temperature of 205°C for the sample synthesized using SDS. A remarkable weight loss above 700°C due to the removal of  $\text{SO}_2$  group was observed only in the sample prepared using SDS.



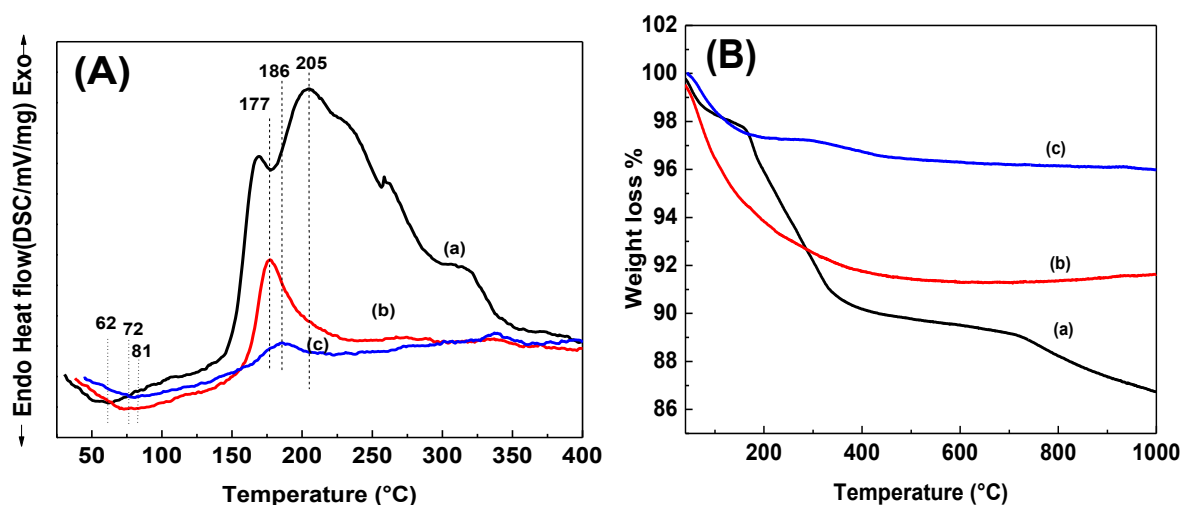


**Fig. 4.5.** (A) DSC and (B) TG curves of as-prepared 1SmCeSDSasp sample, prepared using different surfactants of (a) SDS, (b) DDA, and (c) PEG.

**Table 4.3.** Weight loss% of  $\text{Sm}^{3+}$  doped  $\text{CeO}_2$ , synthesized using DDA and PEG assisted route by conventional refluxing method.

Samples	TG results			
	Region	Temperature range (°C)	Mass loss (%)	Total mass loss (%)
1SmCeDDAasp	AB	30-170	5.6	8.4
	BC	170-800	3.2	
	CD	800-1000	-0.4	
1SmCePEGasp	AB	30-280	2.8	6.0
	BC	280-460	1.7	
	CD	460-930	0.4	
	DE	930-1000	0.1	

### 4.3.2. X-ray diffraction pattern of $\text{Sm}^{3+}$ doped $\text{CeO}_2$

#### 4.3.2.1. Effect of dopant concentrations

XRD patterns of the as-prepared 0.5, 1, 2, 5, 10 and 20 mol%  $\text{Sm}^{3+}$  doped  $\text{CeO}_2$  samples are shown in Fig. 4.6. The XRD patterns of all samples are similar corresponding to cubic fluorite structure of  $\text{CeO}_2$  and can be indexed to the (111), (200), (220), (311), (222), (400), (331) and (420) planes (JCPDS 34-0394). No additional diffraction peaks corresponding to the  $\text{Sm}_2\text{O}_3$  were observed indicating the formation of a single phase  $\text{CeO}_2$ – $\text{Sm}_2\text{O}_3$  solid solution.

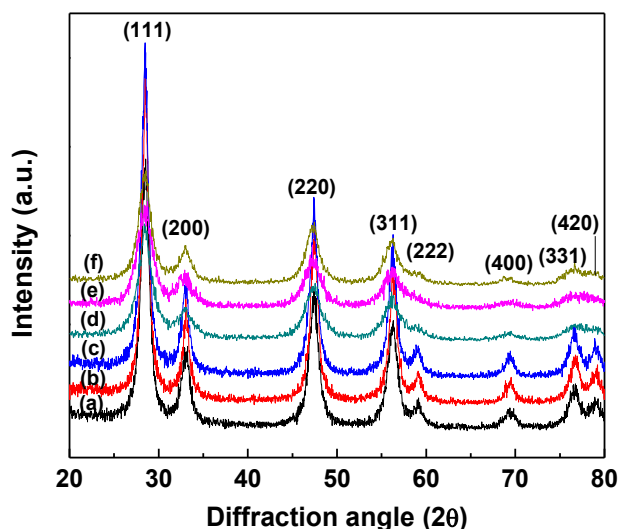


**Fig. 4.6.** XRD patterns of as-prepared (a) 0.5, (b) 1.0, (c) 2.0, (d) 5.0, (e) 10 and (f) 20 mol%  $\text{Sm}^{3+}$  doped  $\text{CeO}_2$  nanopowders.

The narrow and sharp diffraction peaks of all the as-synthesized samples imply the formation of a highly crystalline cubic phase through our developed synthetic route. It was observed that the XRD peaks of  $\text{Sm}^{3+}$  doped  $\text{CeO}_2$  shift to a lower  $2\theta$  value as dopant concentration increased from 0.5 to 20 mol%. The result suggests the effective insertion of  $\text{Sm}^{3+}$  dopant into the  $\text{CeO}_2$  host matrix, which is also well accordance with the previous study.<sup>24</sup> The crystallinity was increased as the  $\text{Sm}^{3+}$  content was increased up to 2 mol%. Further increase in the dopant concentration leads to the decrease in the phase crystallinity as was clear from the broadened diffraction peaks.

The average crystallite size and lattice parameter of all the samples were estimated from the X-ray line broadening of the most intense reflections (111) diffraction peak by using the Scherrer equation and tabulated in Table 4.4. The crystallite size of the doped  $\text{CeO}_2$  was found to be more as compared to that of the pure  $\text{CeO}_2$ . This indicates that an incorporation of the  $\text{Sm}^{3+}$  content even in a small amount up to 1 mol% improves the crystallinity of the sample. However, with a further increase in the  $\text{Sm}^{3+}$  content from 2.0 to 20% suppresses the crystallization of  $\text{CeO}_2$  and crystallite size drops from 9.5 to 5 nm. On increasing the dopant concentration from 1 to 2 mol%, the crystallite size remains almost the same. However, crystallite size decreased rapidly from 9.5 to 5.7 nm on increasing the  $\text{Sm}^{3+}$  content from 2 to 5 mol%. Our results are in good agreement with the previous reports showing that  $\text{CeO}_2$ -

based phase crystallinity is highly depending on the  $\text{Sm}^{3+}$  doping amount. Zivkovic *et al.* reported the similar observation that crystallization of electrodeposited  $\text{Sm}^{3+}$ -doped  $\text{CeO}_2$  thin film reduced beyond  $\text{Sm}^{3+}$  content greater than 1 mol%.<sup>25</sup>

**Table 4.4.** Crystallite size and lattice parameters of  $\text{Sm}^{3+}$  doped  $\text{CeO}_2$  nanopowders.

Sample	Crystallite size (nm)	Lattice parameter (nm)
0.5SmCeSDSasp	8.1	0.5423
1SmCeSDS5asp	9.6	0.5418
2SmCeSDSasp	9.5	0.5426
5SmCeSDSasp	5.8	0.5421
10SmCeSDSasp	4.9	0.5426
20SmCeSDSasp	6.1	0.5428

#### 4.3.2.2. Effect of calcination temperatures

Fig. 4.7 displays the XRD patterns of (a) as-prepared precursor powders of  $\text{Sm}^{3+}$ -doped  $\text{CeO}_2$  and the powders calcined at (b) 500°C, (c) 650°C, and (d) 800°C for 2 h. The well crystalline nature of the as-synthesized powders is evident from the X-ray reflections exhibited by the sample. The sample does not contain any appreciable amount of undecomposed precursor unlike previous reports nor need any further heat treatment at higher temperatures (typically above 400°C) for the synthesis of  $\text{CeO}_2$  nanoparticles from as-synthesized precursor.<sup>26-28</sup> Thereby, confirming the ability of the present aqueous based synthetic approach to prepare mesoporous (as was evident from HRTEM) crystalline  $\text{CeO}_2$  nanoparticles at a lower temperature of 100°C. XRD patterns in Fig. 4.7 reveal that the formation of single crystalline cubic-fluorite structure of  $\text{CeO}_2$  with the space group  $\text{Fm}\bar{3}\text{m}$  (JCPDS powder diffraction File No. 34-0394). All the peaks of the XRD pattern in 20-80° range of  $2\theta$ -value are indexed to (111), (200), (220), (311), (222), (400), (331) and (420) reflections. Mixed phases of fluorite-type  $\text{CeO}_2$  and NiO were observed in mesoporous  $\text{Ce}_{0.8}\text{Sm}_{0.2}\text{O}_{1.9}$  oxides with surface area in the range of 29 to 85  $\text{m}^2/\text{g}$ , prepared using nickel oxide as hard template after calcining at 700°C.<sup>17</sup> The corresponding peaks in  $\text{Sm}^{3+}$ -doped  $\text{CeO}_2$  samples become sharper and their intensity increases with increase in calcination temperatures due to the progressive growth of crystallites. The average crystallite sizes of as-prepared  $\text{Sm}^{3+}$ -doped  $\text{CeO}_2$  sample and the samples heated at 500°C, 650°C, and 800°C were

calculated using Scherrer's equation as 9.5, 9.7, 13.5 and 19.4 nm, respectively. An activated growth of crystallite size from 8.4 to 26.1 nm was observed on increasing the annealing temperature from 100 to 800°C in pure mesoporous CeO<sub>2</sub>. This signifies that the Sm<sup>3+</sup> doping in CeO<sub>2</sub> stabilizes the solid solution against the crystal growth during calcination. Sm<sup>3+</sup> doping also changes the surface energies of CeO<sub>2</sub>, which always play an important role in grain growth during thermal treatment. The (111) peak of Sm<sup>3+</sup>-doped CeO<sub>2</sub> sample calcined at 500°C shift towards lower 2θ values as compared to pure CeO<sub>2</sub>, which is attributed to the lattice expansion induced by Sm<sup>3+</sup> doping. The absence of any peak related to Sm<sub>2</sub>O<sub>3</sub> and shifting of peaks to lower 2θ values for the Sm<sup>3+</sup>-doped CeO<sub>2</sub> sample obviously reveal that Sm<sup>3+</sup> is incorporated into the CeO<sub>2</sub>.

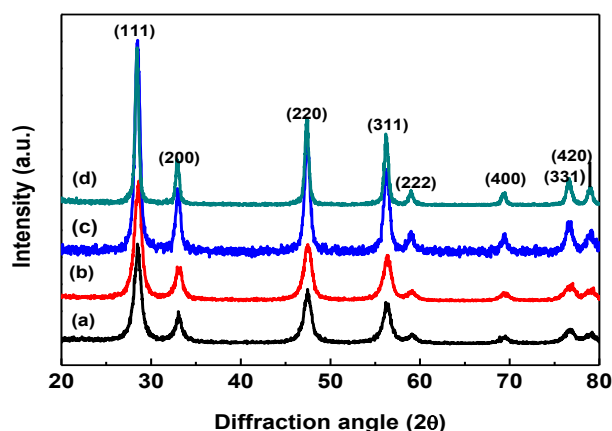


**Fig. 4.7.** XRD patterns of Sm<sup>3+</sup> doped CeO<sub>2</sub> (a) as-prepared precursor and calcined at (b) 500°C, (c) 650°C and (d) 800°C for 2 h.

In previous section it was found that the lattice parameter (*a*) values of the mesoporous Sm<sup>3+</sup> doped CeO<sub>2</sub> samples were higher when compared with that of mesoporous pure CeO<sub>2</sub> samples. This increase in the lattice parameter in Sm<sup>3+</sup> doped CeO<sub>2</sub> nanocrystallites can be attributed to the replacement of Ce<sup>4+</sup> (0.97°Å) with a larger size Sm<sup>3+</sup> (1.08°Å) without changing the cubic fluorite CeO<sub>2</sub> structure.<sup>29</sup> We also observed that the lattice parameter of pure mesoporous CeO<sub>2</sub> (*a* = 0.5410 nm) is very close to the bulk CeO<sub>2</sub> (*a* = 0.5411 nm). This increase in the lattice parameter can be attributed to the creation of Ce<sup>3+</sup> ions, which possess a larger ionic radius (1.14°Å) than the Ce<sup>4+</sup> ions. In order to balance the charge compensation, Sm<sup>3+</sup> additives and Ce<sup>3+</sup> create oxygen vacancies in the CeO<sub>2</sub> lattice, causing further lattice expansion.<sup>29,30</sup>

**Table 4.5.** Crystallites size and lattice parameter values of Sm<sup>3+</sup> doped CeO<sub>2</sub> nanopowders calcined at different temperatures.

Sample	Crystallite size (nm)	Lattice parameter (nm)
1SmCeSDSasp	9.6	0.5418
1SmCeSDS500	9.7	0.5410
1SmCeSDS650	13.5	0.5422
1SmCeSDS800	19.4	0.5433

Surprisingly, a decrease in lattice volume value to 0.5410 nm was observed when the sample was calcined at 500°C (see Table 4.5). This lattice contraction observed in the mesoporous structure may be due to the strains imposed by the pore wall structure. Interestingly, the lattice parameter value was increased to 0.5421 or 0.5433 nm on further increase in the calcination temperature to 650°C or 800°C due to the gradual increase in the crystallite size and collapsing of pores. Huang *et al.* observed a linear increase in lattice parameters on increasing the calcination temperatures from room temperature to 1000°C in Ce<sub>0.83</sub>Sm<sub>0.17</sub>O<sub>1.915</sub> solid solution synthesized by the hydrothermal method.<sup>31</sup> So, the lattice expansion observed here on mesoporous Sm<sup>3+</sup>-doped CeO<sub>2</sub> materials is resulting from the complex effects of substitution and mesoporosity.

#### 4.3.2.3. Effect of refluxing method

Fig. 4.8 shows XRD patterns of the as-synthesized 1 mol% Sm<sup>3+</sup> doped CeO<sub>2</sub> powders obtained using SDS as surfactant via (a) without refluxing, (b) conventional refluxing, and (c) microwave refluxing method. The as-synthesized samples obtained via normal refluxing showed better crystallinity and larger crystallite size of 9.6 nm. The crystallite sizes were 8.3 and 8.1 nm for the samples obtained via without refluxing and microwave refluxing method, respectively. The calculated values of average crystallite size and lattice parameters from the XRD are summarized in Table 4.6. The lattice parameters of the 1SmCeSDSasp are larger than those of 1SmCeSDSNRasp but smaller than those of 1SmCeSDSMWasp.

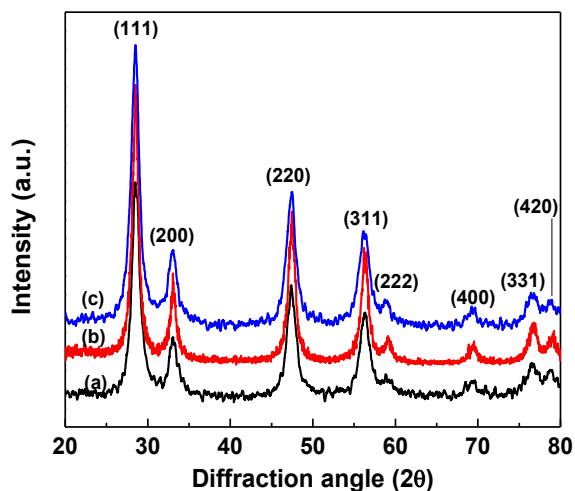


**Fig. 4.8.** XRD patterns of the as-prepared 1 mol%  $\text{Sm}^{3+}$  doped  $\text{CeO}_2$  powders synthesized via (a) without refluxing, (b) normal refluxing, and (c) microwave refluxing method.

**Table. 4.6.** Crystallites size and lattice parameter values of 1 mol%  $\text{Sm}^{3+}$  doped  $\text{CeO}_2$  powders synthesized via different routes.

Sample	Crystallite size (nm)	Lattice parameter (nm)
1SmCeSDSNRasp	8.25	0.5407
1SmCeSDS5asp	9.62	0.5418
1SmCeSDS5MWasp	8.05	0.5422

#### 4.3.2.4. Effect of surfactants

X-ray diffraction analysis of the representative as-prepared 1 mol%  $\text{Sm}^{3+}$  doped  $\text{CeO}_2$  sample obtained by conventional refluxing method using three different surfactants of (a) SDS, (b) DDA and (c) PEG were employed to get the informations about the influence of surfactants on the phase formation and crystalline size of the materials and shown in Fig. 4.9. We observed a lattice contraction (see Table 4.7) of cubic phase in the sample synthesized using SDS, than the samples synthesized using the DDA and PEG surfactants. The crystallite sizes were 9.6, 7.7, and 10.1 nm for the samples synthesized using SDS, DDA, and PEG, respectively. The lattice contraction observed in the mesoporous structure is a result of strains imposed by the pore wall structure. The addition of surfactants could significantly regulate the size of the crystallites of  $\text{Sm}^{3+}$  doped  $\text{CeO}_2$  samples.

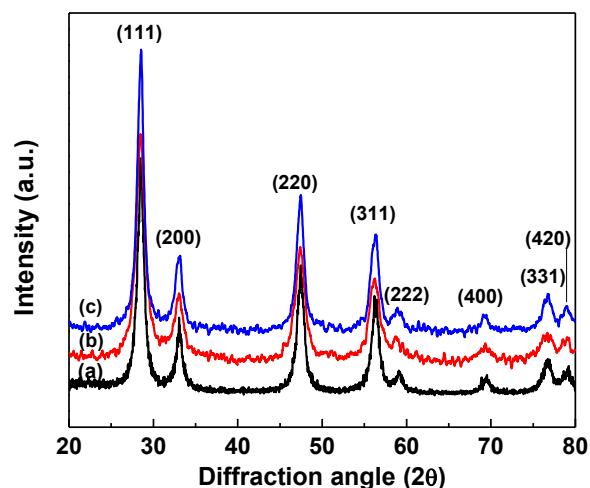


**Fig. 4.9.** XRD patterns of the as-prepared 1 mol%  $\text{Sm}^{3+}$  doped  $\text{CeO}_2$  synthesized using (a) SDS, (b) DDA, and (c) PEG by conventional refluxing method.

**Table. 4.7.** Crystallites size and lattice parameter values of 1 mol%  $\text{Sm}^{3+}$  doped  $\text{CeO}_2$  powders synthesized using different surfactants.

Sample	Crystallite size (nm)	Lattice parameter (nm)
1SmCeSDSasp	9.6	0.5418
1SmCeDDAasp	7.7	0.5422
1SmCePEGasp	10.1	0.5422

### 4.3.3. $\text{N}_2$ sorption isotherm of $\text{Sm}^{3+}$ doped $\text{CeO}_2$

#### 4.3.3.1. Effect of dopant concentration

To understand the textural characteristics of 0.5, 1, 2, 5, 10, and 20 mol %  $\text{Sm}^{3+}$  doped  $\text{CeO}_2$  nanopowders synthesized using SDS via conventional refluxing method and calcined at  $500^\circ\text{C}$  are subjected to nitrogen sorption measurements and the obtained isotherms are shown in Fig. 4.10. All the calcined samples irrespective of dopant concentrations exhibit a type-IV isotherm with a mixed hysteresis loop in the relative pressure ( $p/p_0$ ) range of 0.0–1.0, which are relevant to the characteristic of porous materials.<sup>32</sup> Hysteresis loop appeared at a relatively high pressure range of 0.4 to 0.8 could be related to the existence of mesostructures, whereas the hysteresis loop observed even at higher relative pressures in the range 0.8–1.0 are originated from the substantial inter-particle pores.<sup>33</sup> However, the hysteresis loops are not

identical for all the samples implying that the porosity system is different in the samples. It should also be noted that the adsorption-desorption isotherms do not coincide in the low relative pressure region. The presence of organic impurity in the form of networks leads to larger desorption pore volume than the adsorption pore volume even in the low relative pressure region.<sup>34-36</sup> Textural properties of the samples such as BET surface area, pore diameter, and pore volume of all the samples are summarized in Table. 4.8. The specific surface area increases with increasing the dopant concentration and the results are in good agreement with the previous reports for  $\text{Sm}^{3+}$  doped  $\text{CeO}_2$ .<sup>37,2</sup>

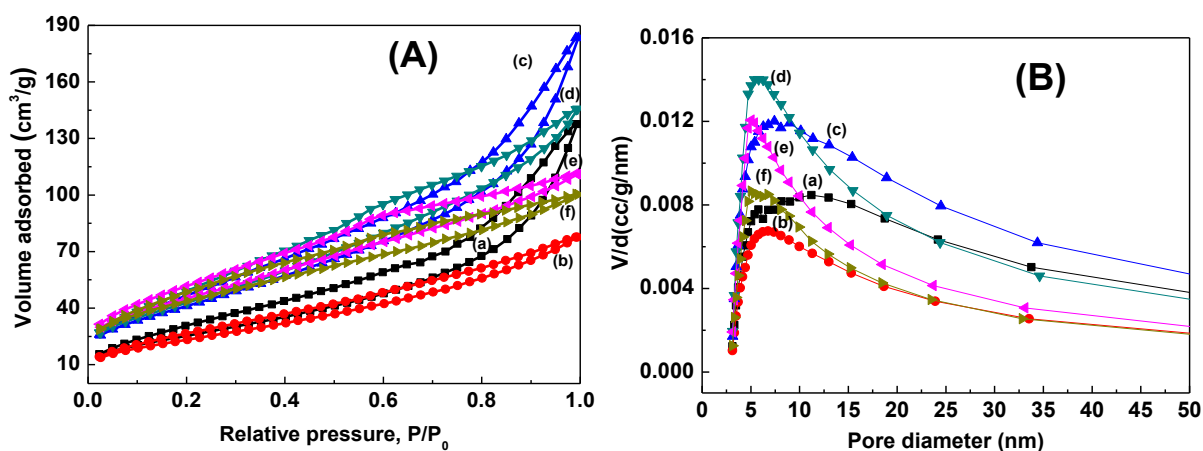


**Fig. 4.10.** (A) BET  $\text{N}_2$  adsorption-desorption isotherms and the (B) BJH pore size distributions of (a) 0.5, (b) 1.0, (c) 2.0, (d) 5.0, (e) 10 and (f) 20 mol%  $\text{Sm}^{3+}$  doped  $\text{CeO}_2$  powders and calcined at  $500^\circ\text{C}$ .

**Table 4.8.** Comparison of  $\text{N}_2$  gas adsorption results for mesoporous  $\text{Sm}^{3+}$  doped  $\text{CeO}_2$  nanopowders calcined at different temperatures.

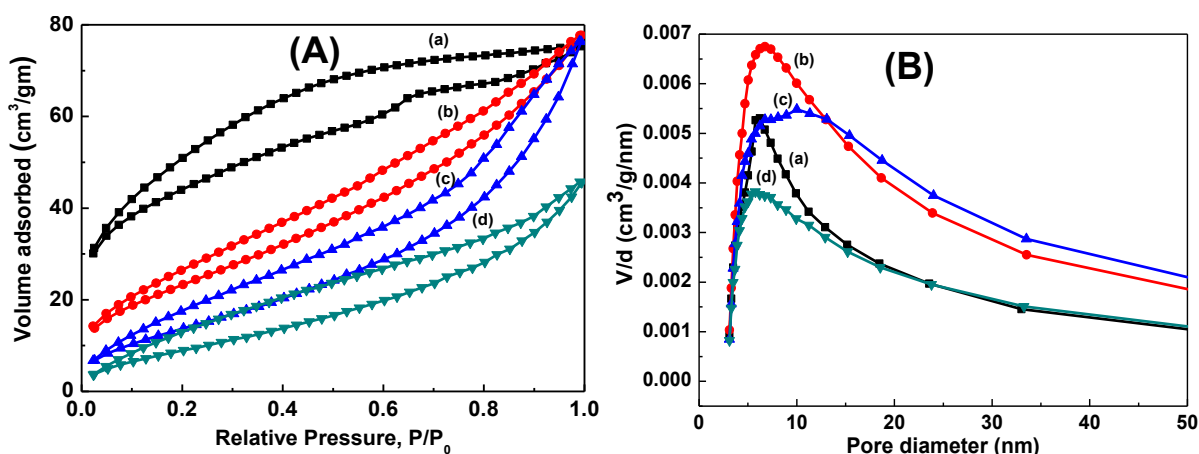
Sample	Surface area ( $\text{m}^2/\text{g}$ )	Pore volume ( $\text{cc/g}$ )	Average pore diameter (nm)
0.5SmCeSDS500	97	0.2128	8.8
1.0SmCeSDS500	138	0.1560	4.5
2.0SmCeSDS500	155	0.2838	7.3
5.0SmCeSDS500	161	0.2255	5.6
10SmCeSDS500	164	0.1718	4.2
20SmCeSDS500	158	0.1551	3.9



Fig. 4.10B shows the corresponding pore size distribution of the samples. All the nanopowders showed an irregular unimodal pore size distributions over 1 to 50 nm range indicating the presence of pore network of different sizes.

#### 4.3.3.2. Effect of various calcination temperature

$N_2$  adsorption–desorption isotherm measurements were performed to further study the porous structure of the 1 mol%  $Sm^{3+}$  doped  $CeO_2$  powders calcined at different temperatures. Fig. 4.11 shows the nitrogen sorption isotherms and the corresponding pore size distribution (in the inset) of  $Sm^{3+}$  doped  $CeO_2$  (a) as-prepared and heated at (b) 500°C, (c) 650°C, and (d) 800°C. The isotherms can be attributed to the type-IV behaviour, which is characteristic of capillary condensation in mesopores. Besides the mesopores,  $Sm^{3+}$  doped  $CeO_2$  samples showed interparticle porosity, which was evidenced by the adsorption at high relative pressures ( $>0.8$ ). The as-prepared 1 mol%  $Sm^{3+}$  doped  $CeO_2$  sample has a higher specific surface area of  $185\text{ m}^2/\text{g}$ , which decreased slightly to  $138\text{ m}^2/\text{g}^{-1}$  after calcination at 500°C. The increase in pore volume ( $0.1560\text{ cm}^3/\text{g}^{-1}$ ) in the template-free mesostructured sample calcined at 500°C when compared with that of  $0.1171\text{ cm}^3/\text{g}^{-1}$  in as-prepared sample, was due to the formation of pores after removal of remaining template in the as-prepared material.



**Fig. 4.11.** (A) BET  $N_2$  adsorption–desorption isotherms, and the (B) BJH pore size distributions of 1 mol%  $Sm^{3+}$  doped  $CeO_2$  (a) as-prepared, and the samples calcined at (b) 500°C, (c) 650°C, and (d) 800°C for 2 h.

This relatively lower surface area in the sample when calcined at 500°C is because of the increased materials density and aggregation of particles induced by the thermal treatment of the mesoporous  $CeO_2$  framework and possibly it arises from the partial loss of structural order

as also evident from the broader BJH pore size distribution (see Fig. 4.11B) with larger average pore size of 8.2 nm. Similarly, a reduced surface area was observed in mesostructured zirconia modified by 2 mol% ceria upon calcination at higher temperatures.<sup>38</sup> The sample calcined at 650°C or 800°C exhibited BET surface area of 75 m<sup>2</sup>g<sup>-1</sup> or 45 m<sup>2</sup>g<sup>-1</sup>, and total pore volume of 0.1253 cm<sup>3</sup>g<sup>-1</sup> or 0.0706 cm<sup>3</sup>g<sup>-1</sup>. The determined values of BET surface area ( $S_{\text{BET}}$ ), average pore size ( $D_{\text{A}}$ ), and total pore volume ( $V_{\text{total}}$ ) are summarized in Table 4.9. Mesoporous CeO<sub>2</sub> and Fe<sup>3+</sup> doped CeO<sub>2</sub> with surface areas 109 to 147 m<sup>2</sup>/g were synthesized by means of a hydrothermal procedure operating at 100°C.<sup>18</sup> It is well known fact that the CeO<sub>2</sub> suffers from a lack of thermomechanical stability that reduces its active surface area at higher temperatures by coarsening and sintering processes, which represents a severe limitation for its implementation in high-temperature devices. A very low weight loss (as observed from TG analysis) during thermal treatment of the as-prepared mesoporous material leads to less shrinkage, which in turn plays important role in preventing grain growth and retaining the mesoporosity up to higher temperature and thus resulting high surface area material. So, the present synthetic route using SDS as surfactant is beneficial to obtain high surface area materials up to higher temperature. These mesoporous materials having small pores and high surface area are expected to show high activity in adsorption and catalysis even at higher temperatures.

**Table 4.9.** N<sub>2</sub> gas adsorption results for mesoporous 1 mol% Sm<sup>3+</sup> doped CeO<sub>2</sub> nanopowders calcined at different temperatures.

Sample	Surface area (m <sup>2</sup> /g)	Pore volume (cc/g)	Average pore diameter (nm)
1.0SmCeSDSasp	184	0.1171	2.5
1.0SmCeSDS500	138	0.1560	4.5
1.0SmCeSDS650	59	0.1253	8.4
1.0SmCeSDS800	38	0.07055	7.4

#### 4.3.3.3. Influence of reflux methods

The N<sub>2</sub> sorption isotherms (Fig. 4.12) of the 1 mol% Sm<sup>3+</sup> doped CeO<sub>2</sub> sample calcined at 500°C prepared using SDS and via without refluxing, conventional refluxing, and microwave refluxing methods were analyzed in order to understand the influence of refluxing

method. Fig. 4.12B displays the corresponding BJH pore size distributions. Table 4.10 summarizes the textural properties obtained from their respective physisorption analysis. It was observed that the nanopowders obtained via both the conventional and microwave refluxing method have almost equal surface areas of 138 and 137  $\text{m}^2\text{g}^{-1}$  with corresponding pore volumes of 0.156 and 0.163  $\text{cm}^3\text{g}^{-1}$ , respectively. The values are much higher than the surface area 46  $\text{m}^2\text{g}^{-1}$  and pore volume 0.131  $\text{cm}^3\text{g}^{-1}$  of the nanopowder obtained via without refluxing method. The results are implying that the refluxing method facilitating the formation of higher fraction of multimodal mesopores. While the nanopowders obtained via conventional and microwave refluxing methods have conterminous textural porosity. The lower surface area of the nanopowders synthesized via without refluxing method most probably is due to the presence of larger pore size and lower pore volume in the sample.

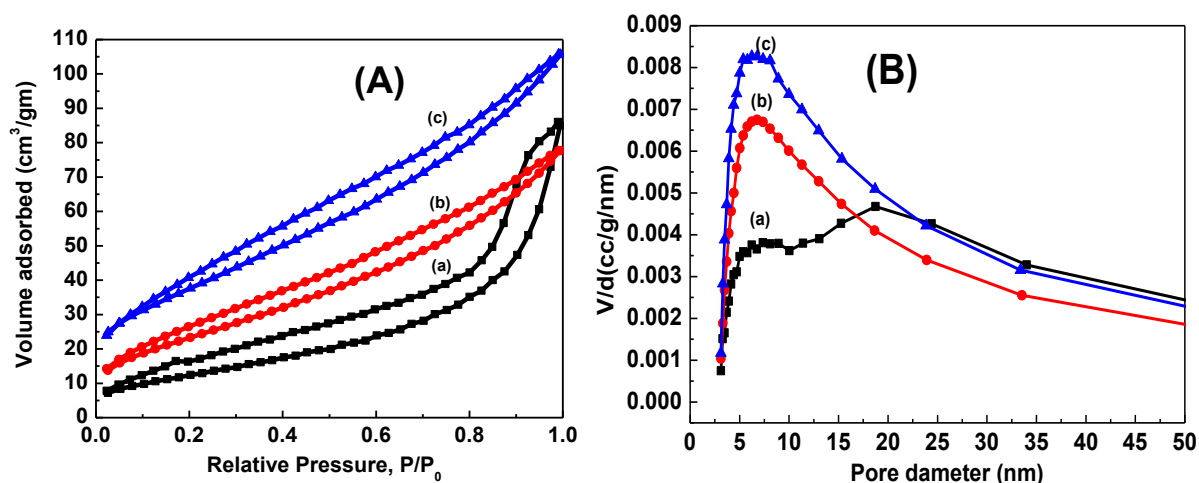


**Fig. 4.12.** (A)  $\text{N}_2$  adsorption–desorption isotherms and (B) BJH pore size distribution of the sample prepared via (a) without refluxing, (b) normal refluxing, and (c) microwave refluxing method and calcined at  $500^\circ\text{C}$ .

**Table 4.10.**  $\text{N}_2$  gas adsorption results for mesoporous 1 mol%  $\text{Sm}^{3+}$  doped  $\text{CeO}_2$  nanopowders calcined at different temperatures.

Samples calcined at $500^\circ\text{C}$	Surface area ( $\text{m}^2/\text{g}$ )	Average pore diameter (nm)	Total pore volume (cc/g)
No reflux	46	11.4	0.1315
Normal reflux	138	4.5	0.1560
Microwave reflux	137	4.8	0.1634

## 4.3.3.4. Effect of various surfactant

Fig. 4.13 represents the N<sub>2</sub> adsorption-desorption isotherms of the 1 mol% Sm<sup>3+</sup> doped CeO<sub>2</sub> synthesized using SDS, DDA and PEG as surfactants by conventional refluxing method and calcined at 500°C. Table 4.11 summarizes the surface areas, pore volume and pore diameter of the samples. It can be seen from the table that the surfactant plays significant role on their respective isotherm and pore size distribution curve indicating different textural properties.

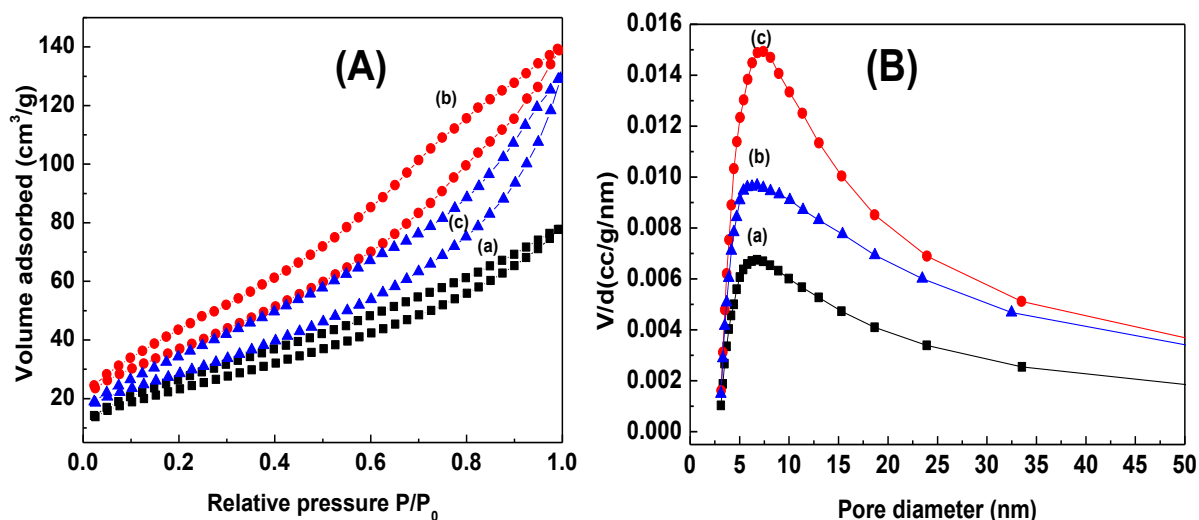


**Fig. 4.13.** (A) N<sub>2</sub> adsorption–desorption isotherms, and (B) BJH pore size distribution of the as-prepared 1 mol% Sm<sup>3+</sup> doped CeO<sub>2</sub> synthesized via (a) SDS, (b) DDA, and (c) PEG by conventional refluxing method.

**Table 4.11.** N<sub>2</sub> gas adsorption results for mesoporous 1 mol% Sm<sup>3+</sup> doped CeO<sub>2</sub> nanopowders calcined at different temperatures.

Sample calcined at 500°C	Surface area (m <sup>2</sup> /g)	Average pore diameter (nm)	Total pore volume (cc/g)
1SmCeSDS	138	4.53	0.16
1SmCe DDA	139	6.20	0.21
1SmCe PEG	106	7.55	0.20

There is no significant difference in surface area of the calcined nanopowder obtained in SDS and DDA assisted route both show almost same surface area of 138 and 139 m<sup>2</sup> g<sup>-1</sup>,

respectively, whereas the calcined sample obtained via PEG assisted route showed a lower surface area of  $106 \text{ m}^2 \text{ g}^{-1}$ . The discrepancy in surface area might be associated with the different types of interaction between the surfactant molecule and inorganic precursors which led to introduce different amount of carbon in the porous skeleton, and thus formed different amount of mesopores after calcination in air.

#### 4.3.4. FTIR analysis

Surface interaction between synthesized nanopowder and surfactant were studied using FTIR spectroscopy. FTIR spectra of the pure SDS and 1 mol%  $\text{Sm}^{3+}$  doped  $\text{CeO}_2$  (a) as-prepared and calcined at different temperatures (b)  $500^\circ\text{C}$  and (c)  $650^\circ\text{C}$  are shown in Fig. 4.14. The broad band at  $\sim 3100 \text{ cm}^{-1}$  and a sharp band around  $1615 \text{ cm}^{-1}$  can be attributed to the stretching and bending modes of the surface hydroxyl group.<sup>39</sup> Two typical absorption bands at  $2918$  and  $2850 \text{ cm}^{-1}$  are due to the symmetrical and unsymmetrical  $\text{CH}_2$  stretching modes of the alkyl chain of the template.<sup>40</sup> Peaks at  $1468 \text{ cm}^{-1}$  can be assigned to the C–H deformation vibration in SDS. Dunne *et al.* observed this band at  $1466 \text{ cm}^{-1}$ . Another band at  $1250$  and  $1220 \text{ cm}^{-1}$ , have been allocated to the sulfonic acid (head group).<sup>23</sup> The broad band at  $1370 \text{ cm}^{-1}$  can be assigned to the deformation vibration of Ce–OH. It has been found that after calcination at  $500^\circ\text{C}$ , all the characteristic peaks of SDS are almost disappeared indicating the complete decomposition of SDS molecules attached to the inorganic framework.

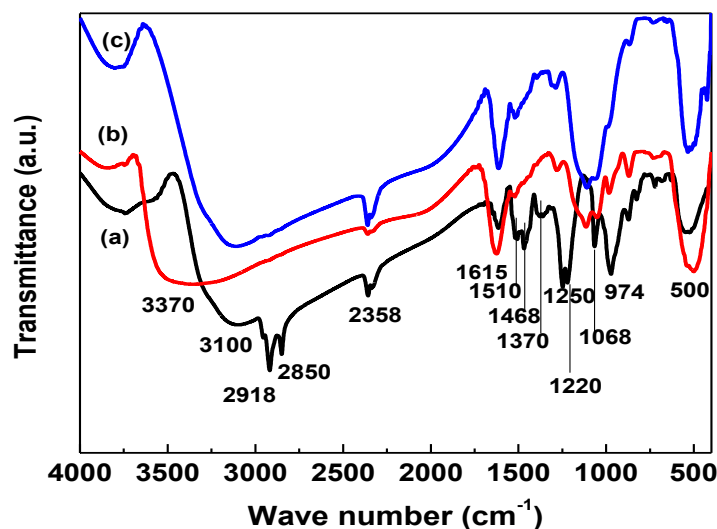


**Fig. 4.14.** FTIR spectra of 1 mol%  $\text{Sm}^{3+}$  doped  $\text{CeO}_2$  powders, (a) as-prepared, and the samples calcined at (b)  $500^\circ\text{C}$ , and (c)  $650^\circ\text{C}$  for 2 h, synthesized using SDS as surfactant.

Although the characteristic peak of Ce–OH deformation vibration centered at  $1370\text{ cm}^{-1}$  is disappeared after calcination but the characteristic stretching and bending vibrations of –OH still existed with decreased intensity at  $3100$  and  $1615\text{ cm}^{-1}$ , respectively, arises from chemisorbed  $\text{H}_2\text{O}$  molecule in the mesoporous network. This provides evidence for the presence of surface adsorbed water in the porous calcined sample. Weak peak at  $2358\text{ cm}^{-1}$  can be assigned to  $\text{CO}_2$  from air, confined in the pores of the samples. The peak at  $1068\text{ cm}^{-1}$  in the as-prepared sample indicates the formation of Ce–O–Ce, networks.<sup>41,42</sup> Absorption bands below  $1000\text{ cm}^{-1}$  correspond to Ce–O stretching vibrations.<sup>39</sup> The higher frequency region between  $1370$  and  $1058\text{ cm}^{-1}$  is due to the absorption of cerium-oxygen groups having a larger double bond character.

The type of surface hydroxyl groups was also estimated by broadening the FTIR spectra of as-prepared 1 mol%  $\text{Sm}^{3+}$  doped  $\text{CeO}_2$  in the range of  $3800$ – $3650\text{ cm}^{-1}$  as shown in Fig 4.15. According to the literature the surface hydroxyl group could be classified into three sections. The peaks appeared in the region  $3770$ – $3750\text{ cm}^{-1}$  are due to the terminal hydroxyl group, whereas peaks centered in the range  $3750$ – $3720\text{ cm}^{-1}$  can be attributed to the bi-bridge hydroxyl group and the peak obtained in the range  $3680$  to  $3660\text{ cm}^{-1}$  are assigned to tri-bridge hydroxyl group.<sup>43,44</sup>

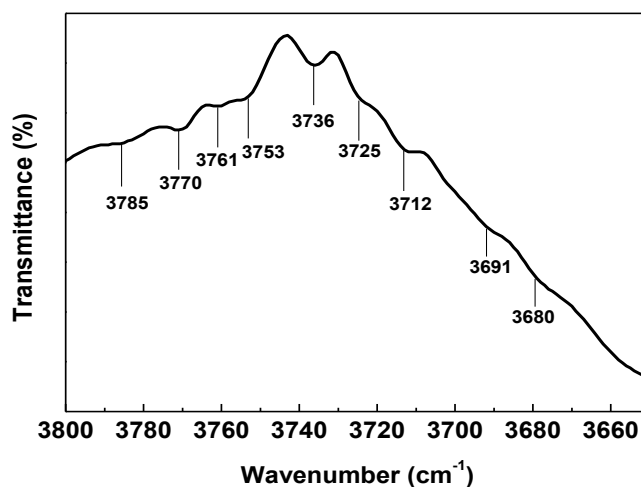


**Fig. 4.15.** Expanded FTIR spectra of 1 mol%  $\text{Sm}^{3+}$  doped as-prepared  $\text{CeO}_2$ .

1.0 mol %  $\text{Sm}^{3+}$  doped  $\text{CeO}_2$  synthesized using DDA and PEG surfactants are shown in Fig 4.16 and 4.17, respectively. The as-prepared sample synthesized using DDA showed a characteristic peak of N–H bending of the amine group at  $1532\text{ cm}^{-1}$ . The peak centered at

3410  $\text{cm}^{-1}$ , 1630  $\text{cm}^{-1}$  and 1356  $\text{cm}^{-1}$  corresponds to the  $-\text{OH}$  stretching,  $-\text{OH}$  bending and Ce-OH deformation vibration, respectively. On calcination at 500 $^{\circ}\text{C}$ , the peaks intensity of  $-\text{NH}_2$  group at 1532  $\text{cm}^{-1}$  as well as the symmetrical and unsymmetrical  $\text{CH}_2$  stretching modes centered at 2925 and 2856  $\text{cm}^{-1}$  were diminished. Similarly, the decrease in peaks intensity with increasing calcination temperatures related to the surfactant were also observed in the nanopowder synthesized using PEG assisted route.

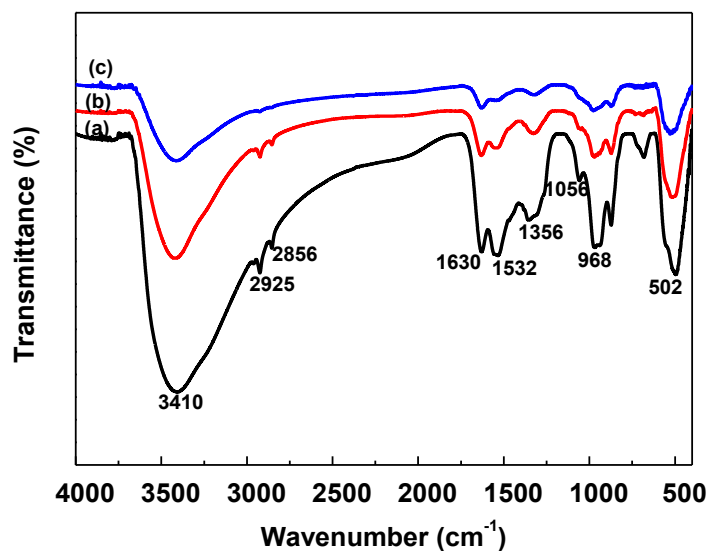


**Fig. 4.16.** FTIR spectra of 1 mol%  $\text{Sm}^{3+}$  doped  $\text{CeO}_2$  nanopowders, (a) as-prepared, and the samples calcined at (b) 500 $^{\circ}\text{C}$ , and (c) 650 $^{\circ}\text{C}$  for 2 h, synthesized using DDA as surfactant.

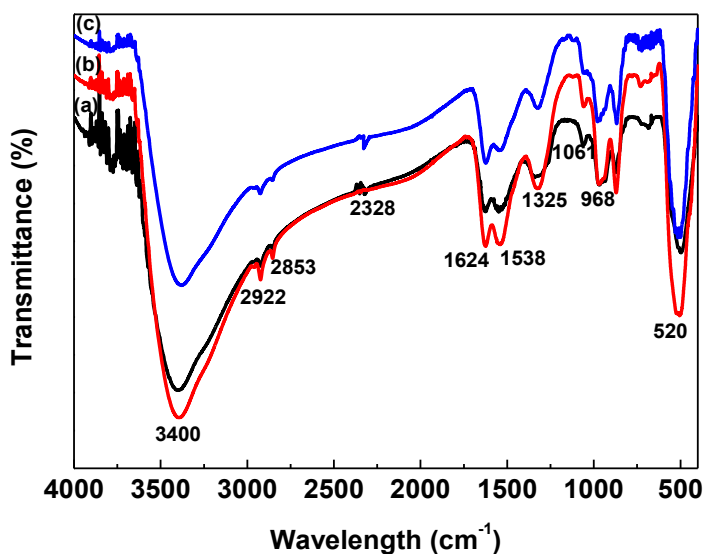


**Fig. 4.17.** FTIR spectra of 1 mol%  $\text{Sm}^{3+}$  doped  $\text{CeO}_2$  nanopowders, (a) as-prepared, and the samples calcined at (b) 500 $^{\circ}\text{C}$ , and (c) 650 $^{\circ}\text{C}$  for 2 h, synthesized using PEG as surfactant.

### 4.3.5. Microstructure analysis

#### 4.3.5.1. FESEM images, EDAX analysis and elemental mapping

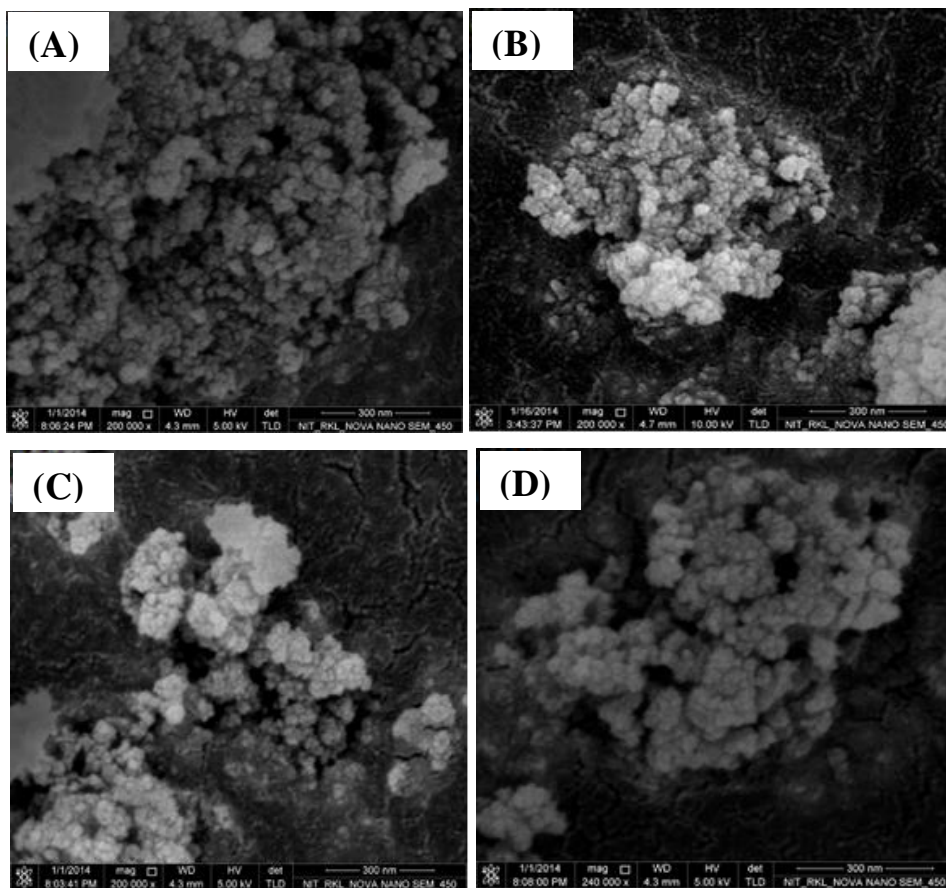


**Fig. 4.18.** FESEM micrographs of (A) 0.5, (B) 1.0, (C) 2.0, and (D) 5 mol% Sm<sup>3+</sup> doped CeO<sub>2</sub> calcined at 500°C.

The surface morphology of the Sm<sup>3+</sup> doped CeO<sub>2</sub> nanoparticles calcined at 500°C for 2 h were analyzed by using FESEM and are shown in Fig. 4.18. The average particle sizes were 10 to 20 nm, which reasonably matches with the crystallite size calculated from the XRD analysis using the Scherrer formula. The surface morphology of the nanopowders did not change much with increasing the dopant concentration from 0.5 to 5%. EDS spectra for the (a) 0.5, (b) 1.0, (c) 2.0, and (d) 5 mol% Sm<sup>3+</sup> doped CeO<sub>2</sub> calcined at 500°C is given in Fig. 4.19. From the EDX spectra of Sm<sup>3+</sup> doped CeO<sub>2</sub> samples, the expected peaks of Ce were observed at ~ 0.9, 4.9, 5.3 and 6.0 keV and Sm peaks at ~ 1.1 and 5.6 keV. For 1 mol% Sm<sup>3+</sup> doped CeO<sub>2</sub>, the final incorporation of Sm was 1.22 at.% into the CeO<sub>2</sub>. The homogeneous distribution of Sm<sub>2</sub>O<sub>3</sub> over the surface of CeO<sub>2</sub> was further confirmed by EDS elemental mapping analysis. The EDS spectrum shows the signatures of constituent elements. The EDS



mapping profile for the elements Ce (red color), Sm (green color) and O (blue color) were scanned in the 1 mol%  $\text{Sm}^{3+}$  doped  $\text{CeO}_2$  nanopowder and are shown in Fig. 4.20. The mappings of independent elements of Ce, Sm and O are shown in Fig. 4.20 (b–d) and the mapping display a clear homogeneous distribution of elements in the  $\text{CeO}_2$  matrix.

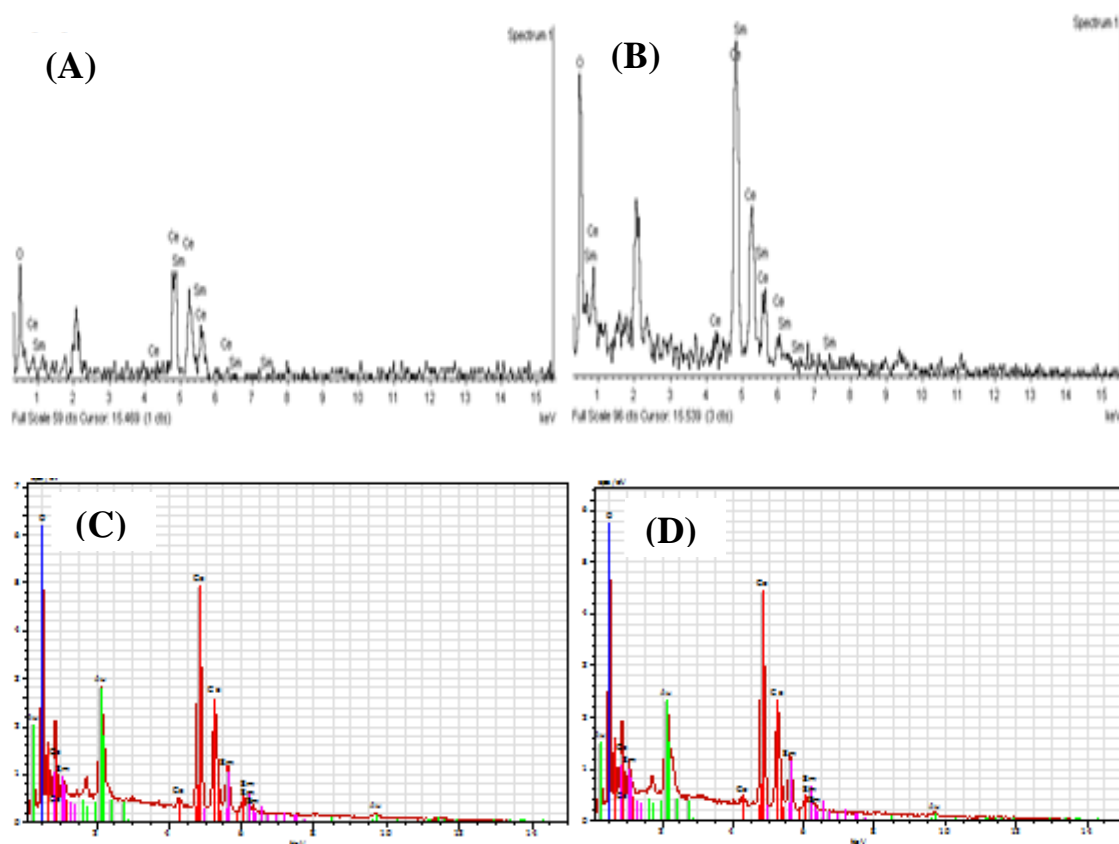


**Fig. 4.19.** EDS graphs of (A) 0.5, (B) 1.0, (C) 2.0, and (D) 5 mol%  $\text{Sm}^{3+}$  doped  $\text{CeO}_2$  calcined at  $500^\circ\text{C}$ .

It can be seen from Fig. 4.21, the microstructure of 1 mol%  $\text{Sm}^{3+}$  doped  $\text{CeO}_2$  synthesized using microwave refluxing and calcined at  $500^\circ\text{C}$  showed higher degree of agglomeration than the sample synthesized using conventional refluxing. In addition, the influences of calcination temperatures on the morphology of  $\text{Sm}^{3+}$  doped  $\text{CeO}_2$  samples were also investigated by FESEM and shown in Fig. 4.22. The morphology of the as-prepared sample was irregular, and the particle size was randomly distributed. The calcined samples show less agglomeration. It is clearly observed that the morphology of the nanopowders do not undergo any remarkable change up to  $800^\circ\text{C}$ .

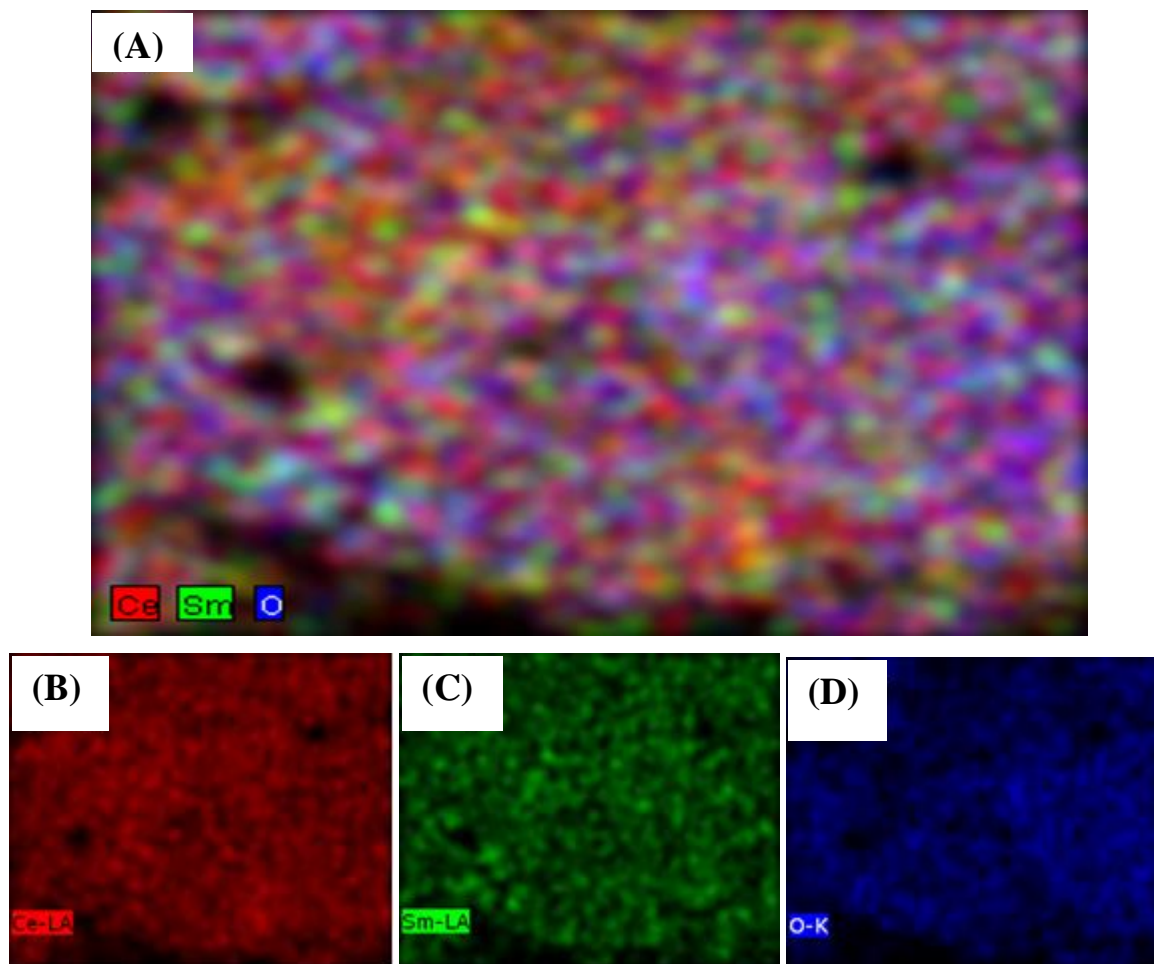


**Fig. 4.20.** Elemental mapping of 1 mol% Sm<sup>3+</sup> doped CeO<sub>2</sub>, (A) overall elemental mapping, and of the (B) Ce, (C) Sm, and (D) O.

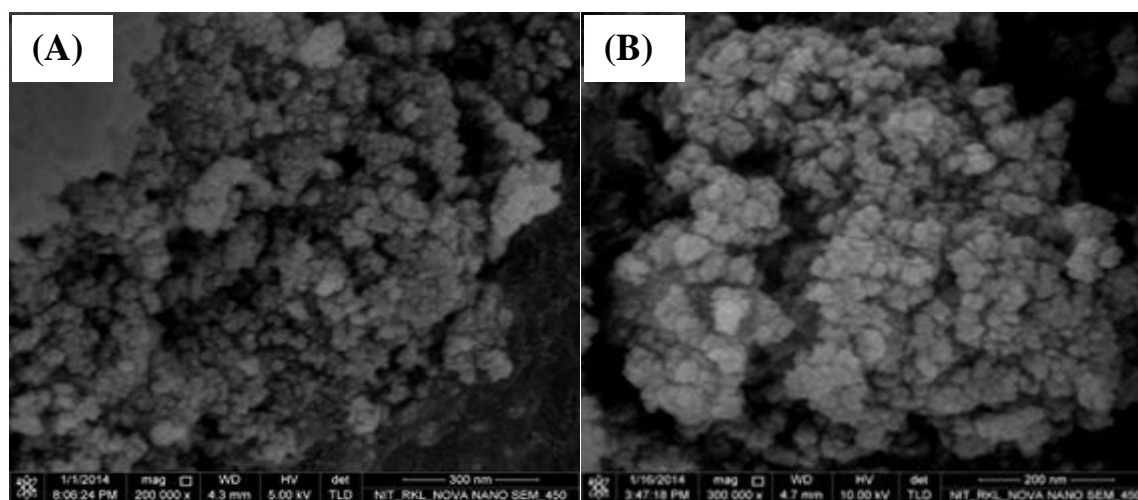


**Fig. 4.21.** FESEM micrographs of 1.0 mol% Sm<sup>3+</sup> doped CeO<sub>2</sub> synthesized through (A) conventional refluxing, and (B) microwave assisted refluxing, and calcined at 500°C.

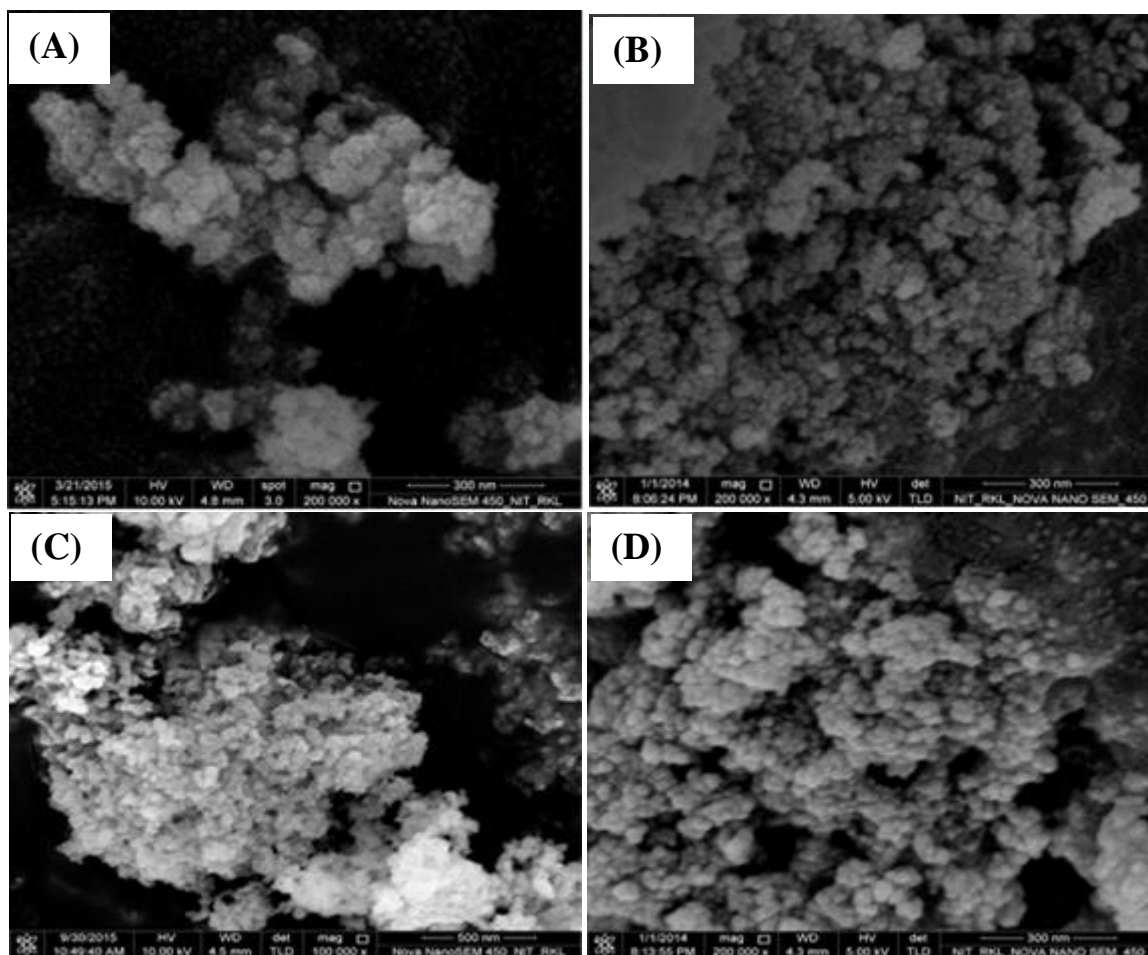


**Fig. 4.22.** FESEM micrographs of 1 mol%  $\text{Sm}^{3+}$  doped  $\text{CeO}_2$ , (A) asp, and calcined at (B) 500°C (C) 650°C, and (D) 800°C.

#### 4.3.5.2. TEM & HRTEM images

Fig. 4.23 shows the representative TEM-HRTEM micrographs of mesoporous structure in as-prepared and calcined samples of  $\text{Sm}^{3+}$  doped  $\text{CeO}_2$  powders. As can be seen from the Fig. 4.23a, the mesopore size is about 4-7 nm, and the particles have average diameter of 8 nm. The mesopores are surrounded by the  $\text{CeO}_2:\text{Sm}^{3+}$  crystallites. Part of the microstructure, especially at the upper corner part (marked by open arrow) of the Fig. 4.23a, appears disordered or even amorphous. The results indicate the presence of surfactant in the as-prepared sample as was also confirmed by FTIR study. The high resolution TEM image also confirms some micropores in between nanocrystals along with the mesopores. The nanocrystals show lattice fringes corresponding to the cubic  $\text{CeO}_2$  phase, which confirms that the pore walls are nanocrystalline.

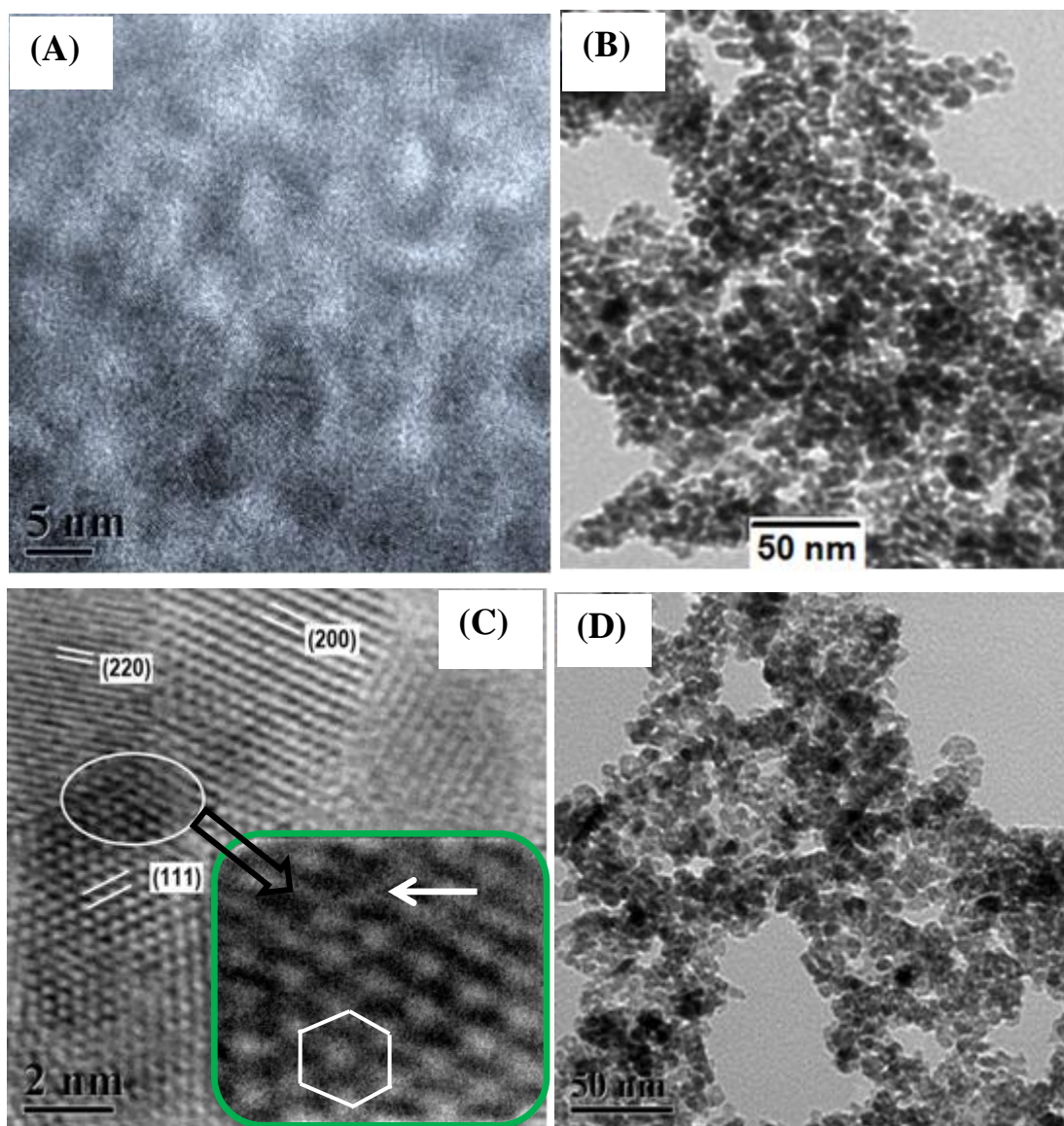


**Fig. 4.23.** TEM images (right), and HRTEM images (left) of  $\text{Sm}^{3+}$  doped  $\text{CeO}_2$  powders (A) as-prepared precursor, and calcined at (B) and (C)  $500^\circ\text{C}$ , and (D)  $650^\circ\text{C}$  for 2 h. Selected part of (C) is enlarged and shown in the inset.

After calcination at  $500^\circ\text{C}$ , the mesoporous structure almost remains unchanged (Fig. 4.23b). Average pore and particle diameters in the sample are in the range of 6-9 and 9-10 nm, respectively. The (111), (220), and (200) lattices of nanocrystalline  $\text{Sm}^{3+}$  doped  $\text{CeO}_2$  can be detected clearly by high resolution TEM image (Fig. 4.23c), giving proof of a high degree of crystallinity in mesoporous framework. A close check-up of Fig. 4.23c shows hexagonally arranged surface oxygen atoms. A missing atom (marked by arrow) surrounded by six atoms may be recognized as the surface oxygen vacancy as was observed by Torbrugge *et al.* by

atomic resolution dynamic force microscopy.<sup>45</sup> The free two electrons from the missing surface oxygen ion are captured by the two of the three  $\text{Ce}^{4+}$  ions of the second layer next to the vacancy, and transformed to  $\text{Ce}^{3+}$  ions.<sup>45</sup> Dark regions (see inset of Fig. 4.23c) might be line defects arising from multiple subsurface oxygen vacancies, which formed at the higher oxygen defect density.<sup>46</sup> According to the theoretical calculation, the association of two surface oxygen vacancies side by side on  $\text{CeO}_2$  (111) were energetically favored against two isolated surface oxygen vacancies by 0.52 eV.<sup>35</sup> It is noteworthy that the sample calcined at 650°C still exhibit mesoporous structure (see in Fig. 4.23d), confirming that the framework is stable. The higher crystallinity of the inorganic wall and grain growth during the calcination process resulted in a more disordered mesostructure. TEM-HRTEM in line with the XRD results further confirmed that high crystallinity was achieved during the synthesis of the mesoporous material.

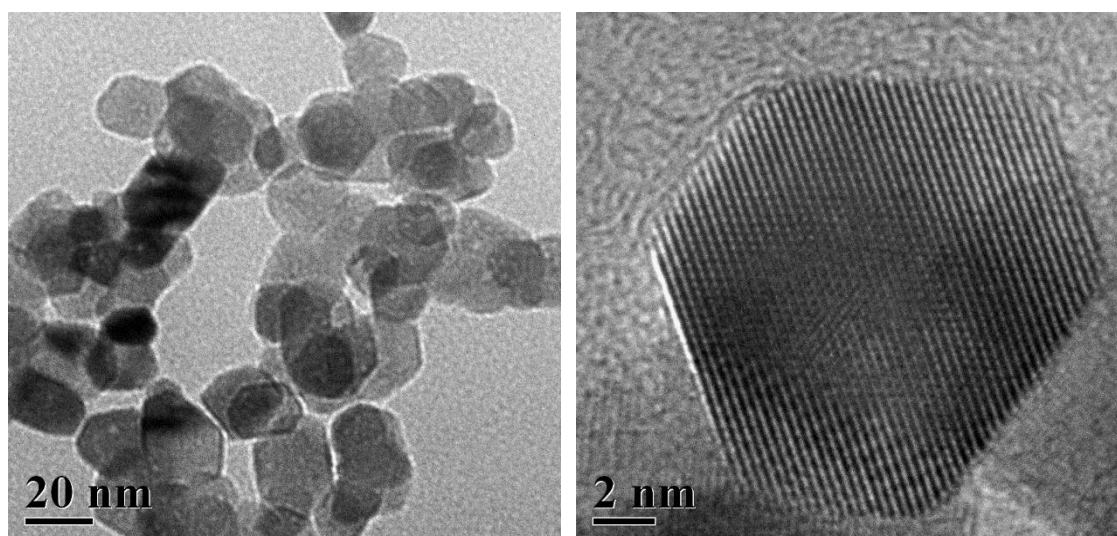


**Fig. 4.24.** TEM and HRTEM micrographs of 1 mol%  $\text{Sm}^{3+}$  doped  $\text{CeO}_2$ , calcined at 800°C

Fig. 4.24 show the representative TEM and HRTEM micrographs of the 1 mol%  $\text{Sm}^{3+}$  doped  $\text{CeO}_2$  calcined at 800°C. It can be noted from the figures that the particle size increased with an increase of the calcination temperature and exhibit clear hexagonal shaped particles. In addition the sample calcined at 800°C shows clearly visible lattice fringes [from (111) plane] due to a higher degree of crystallinity which are in good agreement with the XRD results. The particle sizes were in the range of 20 to 25 nm. A similar increase in particle size of the nanocrystalline Ce–Sm–oxide solid solution from ~ 7 to 25 nm was observed on increasing the calcination temperature from 500 to 800°C by Kuntaiah *et al.*<sup>47</sup>

## 4.3.6. UV-vis DRS studies

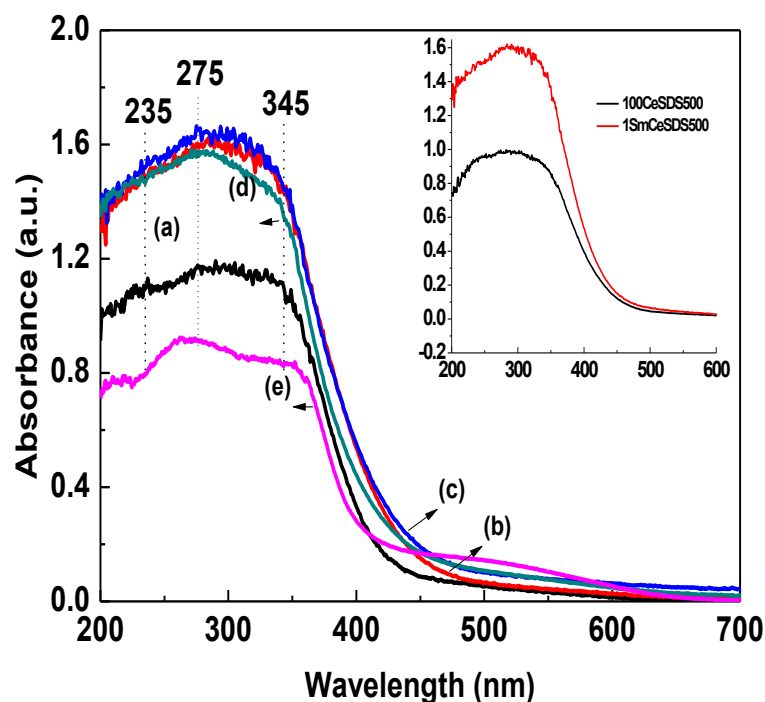


**Fig. 4.25.** UV-vis diffuse reflectance spectra of  $\text{Sm}^{3+}$  doped  $\text{CeO}_2$  powders (a) as-prepared precursor and calcined at (b)  $500^\circ\text{C}$  (compared with that of pure  $\text{CeO}_2$  in the inset), (c)  $650^\circ\text{C}$ , (d)  $800^\circ\text{C}$ , and (e)  $1000^\circ\text{C}$  for 2 h.

The well-known ultraviolet blocking material,  $\text{Sm}^{3+}$  doped  $\text{CeO}_2$  nanocrystals possesses strong absorption properties near the ultraviolet region. Spectra a-e of Fig. 4.25 compares the UV-vis diffuse reflectance spectra of  $\text{Sm}^{3+}$  doped  $\text{CeO}_2$  as-prepared, and heated at  $500^\circ\text{C}$ ,  $600^\circ\text{C}$ , and  $800^\circ\text{C}$ , respectively. A very careful observation revealed that all the samples exhibit three absorption maxima in the UV region, centered around 235, 275 and 345 nm, which correspond to charge-transfer transitions from  $\text{O}^{2-}$  (2p) to the  $\text{Ce}^{3+}$  (4f) and  $\text{O}^{2-}$  (2p) to the  $\text{Ce}^{4+}$  (4f) orbitals, and inter-band transitions, respectively, in agreement with previous reports.<sup>30</sup> As compared with the pure mesoporous  $\text{CeO}_2$ , doped  $\text{CeO}_2$  possess higher light absorption intensity and the adsorption edge also shifted toward the longer wavelength i.e., red shift (shown in the inset). The red shift of the absorption peaks of  $\text{Sm}^{3+}$  doped  $\text{CeO}_2$  indicates a narrowing of the bandgap.

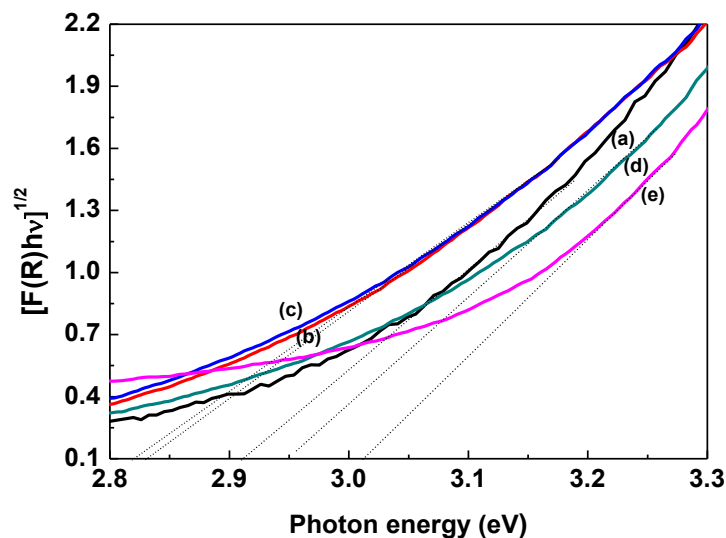


**Fig. 4.26.** Plot of the transformed Kubelka–Munk function versus light energy for  $\text{Sm}^{3+}$  doped  $\text{CeO}_2$  samples.

The spectra also show that the mesoporous  $\text{Sm}^{3+}$  doped  $\text{CeO}_2$  samples calcined at  $500^\circ\text{C}$  and  $600^\circ\text{C}$  possess higher light absorption intensity and a red shifted absorption edge compared to the as-prepared sample. The decrease in intensity of absorption bands probably due to the presence of surfactant molecules along with  $\text{CeO}_2$  in the as-prepared sample. The absorption edge of the  $\text{Sm}^{3+}$  doped  $\text{CeO}_2$  samples calcined  $\leq 800^\circ\text{C}$  exhibited a shift to shorter wavelength (blue shift). The corresponding transformed Kubelka–Munk functions  $[\text{F}(\text{R})\text{h}\nu]^{1/2}$  versus light energy ( $\text{h}\nu$ ) plot<sup>48</sup> for each of the samples are shown in Fig. 4.26. A straight line is drawn on the linear part of the curves, which on extrapolation on the X-axis gives the band gap ( $E_g$ ). According to the plots, the bandgap was estimated to be 2.91, 2.82, 2.83, and 2.95 eV for as-prepared  $\text{Sm}^{3+}$  doped  $\text{CeO}_2$  and calcined at 500, 650, and  $800^\circ\text{C}$ , respectively. Pure mesoporous  $\text{CeO}_2$  calcination at  $500^\circ\text{C}$  showed an estimated bandgap of 2.90 eV, which was smaller than that of bulk  $\text{CeO}_2$  powders (3.19 eV).

Many reports have revealed that quantum confinement effect contributes to the blue-shift of the absorption edge of the  $\text{CeO}_2$  due to the higher localization of energy bands with decreasing particle size.<sup>49</sup> So, the blue shift with increasing particle size in  $\text{Sm}^{3+}$  doped  $\text{CeO}_2$  upon calcination above  $500^\circ\text{C}$  is not due to quantum-size effect. The single  $4f^1$  electron in  $\text{Ce}^{3+}$  undergoes  $4f^1 \rightarrow 5d$  transition and gives absorption red shifted. Both the pure and doped  $\text{CeO}_2$  samples calcined at  $500^\circ\text{C}$  possess similar average sizes. Thus the decrease in the

fundamental gap  $E_g$  in  $\text{Sm}^{3+}$  doped  $\text{CeO}_2$  was mainly induced by the valence and oxygen vacancies state change.<sup>49</sup> Chen *et al.* observed that the content of  $\text{Ce}^{3+}$  and oxygen vacancies decreased with growth and oxidation of the nanoparticles (with grains of 10–20 nm) during annealing.<sup>50</sup> The results envisage that the  $\text{Sm}^{3+}$  doped  $\text{CeO}_2$  calcined at 500°C possesses highest  $\text{Ce}^{3+}$  content. The higher relative absorption intensity and the extended absorption tail in  $\text{Sm}^{3+}$  doped  $\text{CeO}_2$  also indicates that the  $\text{Sm}^{3+} \rightarrow \text{Ce}^{4+}$  substitution indeed facilitates the formation of  $\text{Ce}^{3+}$  and oxygen vacancy of the materials.

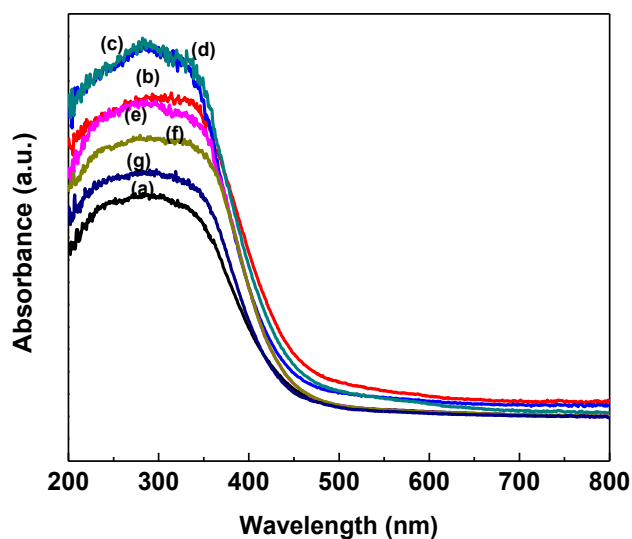


**Fig. 4.27.** UV-visible absorption spectra of (a) 0, (b) 0.5, (c) 1.0, (d) 2.0, (e) 5.0, (f) 10, and (g) 20 mol%  $\text{Sm}^{3+}$  doped  $\text{CeO}_2$  nanopowders calcined at 500°C.

The UV-vis diffuse reflectance spectra of pure  $\text{CeO}_2$  and 0.5, 1, 2, 5 and 10 mol%  $\text{Sm}^{3+}$  -doped  $\text{CeO}_2$  nanopowders are shown in Fig. 4.27. All the samples shows a strong absorption in the UV region (<400 nm) with a well-defined absorbance peak at around 255, 280, and 325 nm. The absorption edge of doped  $\text{CeO}_2$  is red-shifted as compared to that of the pure  $\text{CeO}_2$  and leads to the narrowing of the band-gap due to the introduction of energy levels in the interband gap. It is also observed that the absorption intensities in the UV light region were increased with increasing the doping concentration from 0 to 2 mol %. On further increase in the  $\text{Sm}^{3+}$  doping to 10 mol%, the absorption intensity again decreased which suggest that the  $\text{Sm}^{3+}$  doping in  $\text{CeO}_2$  has induced higher concentration of  $\text{Ce}^{3+}$  till 2 mol% doping. The intensity of ultraviolet absorption is a relative proportion with  $\text{Ce}^{3+}$  content, which will increase the oxygen vacancy concentration of Ce-based materials due to a charge compensation mechanism.<sup>51</sup>



### 4.3.7. PL (photo luminescence) analysis

#### 4.3.7.1. PL emission spectra

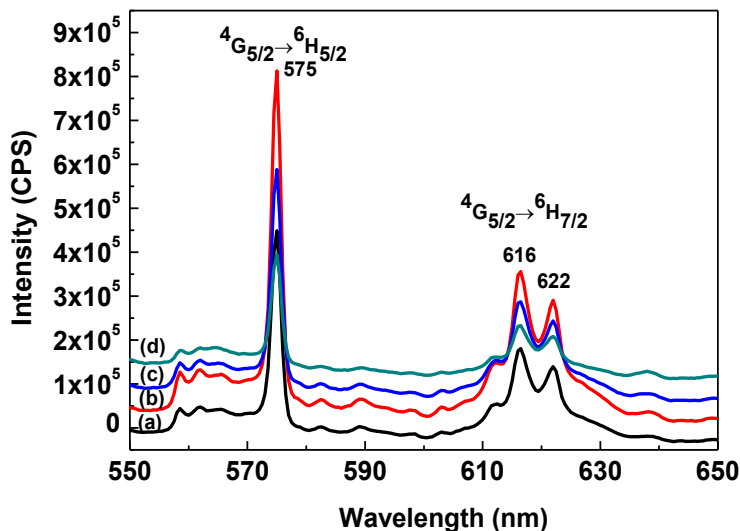


**Fig. 4.28.** PL emission spectra of (a) 0.5, (b) 1.0, (c) 2.0, and (d) 5 mol% Sm<sup>3+</sup> doped CeO<sub>2</sub> nanopowders calcined at 500°C.

Fig 4.28 shows the PL emission spectra of the 0.5, 1, 2, and 10 mol % Sm<sup>3+</sup> doped CeO<sub>2</sub> nanoparticles annealed at 500°C, recorded at excitation wavelength of 335 nm. The orange-red emission of the Sm<sup>3+</sup> doped CeO<sub>2</sub> can be attributed to the  ${}^4G_{5/2} \rightarrow {}^6H_{5/2}$ , (558.5, 561.5, 565.5, 575 and 582.5 nm) and  ${}^4G_{5/2} \rightarrow {}^6H_{7/2}$  transitions (607.5, 612, 616.5 and 622 nm). As both of the above magnetic dipole transitions follow the selection rule  $\Delta J=0$  and  $\Delta J=1$ , respectively, (where J is the total angular momentum), hence both are allowed for Sm<sup>3+</sup> in a site with inversion symmetry. According to the Kramer degeneracy, Sm<sup>3+</sup> ion with its odd 4f<sup>5</sup> electron configuration give the maximum number of Stark sublevels  $(2J+1)/2$ , i.e. three for the  ${}^6H_{5/2}$  manifold, and four for the  ${}^6H_{7/2}$  manifold.<sup>52</sup> It has been found that although the number of lines for  ${}^4G_{5/2} \rightarrow {}^6H_{7/2}$  transition (607.5 nm, 612 nm, 616.5 nm and 622 nm) is consistent with the stark splitting of the  ${}^6H_{7/2}$  manifold, but five lines are observed for the  ${}^4G_{5/2} \rightarrow {}^6H_{5/2}$  transition, instead of expected three lines which revealed that some samarium ions are situated in non-equivalent crystallographic sites. The strong emission line centered at 575 nm for the  ${}^4G_{5/2} \rightarrow {}^6H_{5/2}$  transition, and two emission lines centered at 616.5 and 622 nm for the  ${}^4G_{5/2} \rightarrow {}^6H_{7/2}$  transition is indicative of a predominant incorporation of the Sm<sup>3+</sup> ions into the Ce<sup>4+</sup> sites. Further it was also seen that the PL intensity increases with increasing the Sm<sup>3+</sup>

content from 0.5 to 1.0 mol %, indicative of the successful incorporation of  $\text{Sm}^{3+}$  into the  $\text{CeO}_2$  lattice. On further increase in the  $\text{Sm}^{3+}$  content in  $\text{CeO}_2$  resulted in a decrease in the PL intensity due to concentration quenching.

The effect of calcination temperatures on luminescence behavior has been investigated. Fig. 4.29 shows the photoluminescence spectra of the as-prepared 1.0 mol%  $\text{Sm}^{3+}$  doped  $\text{CeO}_2$  and calcined at 500°C, 650°C, 800°C, 1000°C and 1300°C temperature for 2 h. The PL spectra were measured for all the samples under the same experimental conditions at room temperature, using an excitation wavelength of 335 nm. PL results show that the nanopowders calcined at 500°C did not significantly enhance the emission intensity than the as-prepared powder. An increase in the calcination temperature leads to the continuous growth of crystallite size and also decrease the surface-to-volume ratio, as a result, the fluorescence quench centers (crystal defects) decrease, hence the PL intensity increases with increasing calcination temperature. There is good correlation between the observed luminescence behavior and the crystallite size extracted by using Debye sherrer equation. Calcination temperature also change the local symmetry of the crystal field around  $\text{Sm}^{3+}$  ion, induced more ordered structure. Again conglomeration of particles will decrease the PL intensity due to the decreases in cross section for absorption of light.<sup>53</sup> However the occurrence of the  $\text{Sm}^{3+}$  emissions indicates that  $\text{Sm}^{3+}$  was homogeneously doped in  $\text{CeO}_2$  without segregation as  $\text{Sm}_2\text{O}_3$  or other Sm-related compounds.

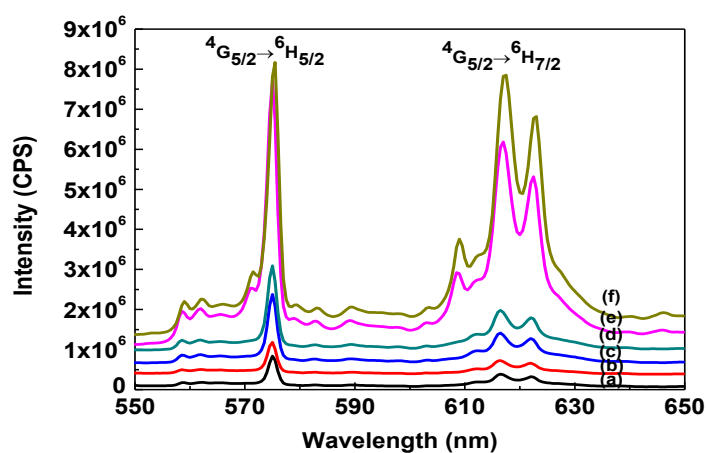


**Fig. 4.29.** PL emission spectra of  $\text{Sm}^{3+}$  doped  $\text{CeO}_2$  (a) as-prepared precursor, and the samples calcined at (b) 500°C, (c) 650°C, (d) 800°C, (e) 1000°C, and (f) 1300°C for 2 h.

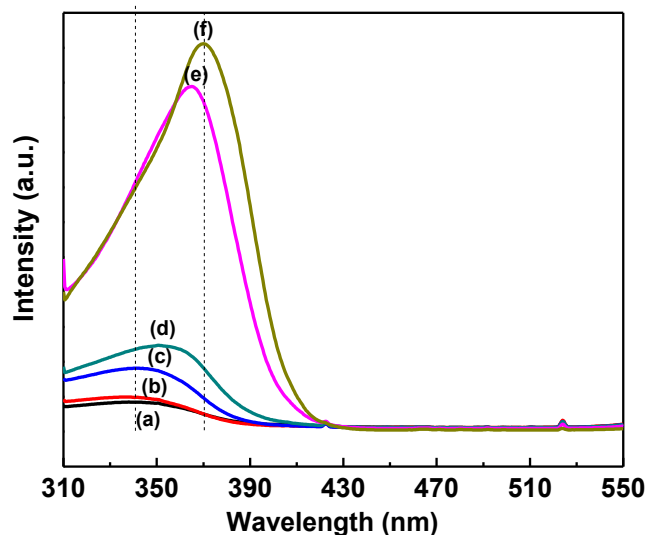


**Fig. 4.30.** PL excitation spectra of  $\text{Sm}^{3+}$  doped  $\text{CeO}_2$  (a) as-prepared precursor, and calcined at (b)  $500^\circ\text{C}$ , (c)  $650^\circ\text{C}$ , (d)  $800^\circ\text{C}$ , (d)  $1000^\circ\text{C}$ , and (d)  $1300^\circ\text{C}$  for 2 h.

#### 4.3.7.2. PL excitation spectra

Photoluminescence excitation spectra of 1 mol%  $\text{Sm}^{3+}$  doped  $\text{CeO}_2$  nanophosphors as a function of annealing temperatures are shown in Fig. 4.30. The excitation spectra were obtained by monitoring the strong single emission line at 575 nm for the  $^4\text{G}_{5/2} \rightarrow ^6\text{H}_{5/2}$  transition. The excitation spectrum consists of a broad band around 330–350 nm due to the charge transfer (CT) between the  $\text{O}^{2-}$  valence band and the  $\text{Ce}^{4+}$  conduction band and the subsequent energy transfer to  $\text{Sm}^{3+}$ . Additionally, we observe that the charge transfer band maxima of excitation spectra shifts toward the higher wavelength with an increase in the calcination temperatures. This indicates that the calcination changed the covalence between  $\text{O}^{2-}$  and  $\text{Sm}^{3+}$ . According to Ghosh *et al.* the CT energy position depends on the crystal field of ions surrounding  $\text{O}^{2-}$ , the strength of anion binding, the size of the cation site, and the coordination number.<sup>54</sup> Similar band shifts to higher wavelength upon calcination have been reported previously by many authors.<sup>55,14</sup> As the crystallite size of the particles increases with increasing the calcination temperatures, it leads to shortening the distance between the  $\text{O}^{2-}$  and  $\text{Eu}^{3+}$  ions as a result the intensity of the charge transfer band increases with the calcination temperature.<sup>56</sup> Hence the excitation spectra suggest that the synthesized materials are quite suitable to meet the demands of UV LEDs near-UV excitation range.

The excitation spectra of 0.5, 1, 2, and 10 mol%  $\text{Sm}^{3+}$  doped  $\text{CeO}_2$  nanopowders calcined at  $500^\circ\text{C}$  with monitoring at 575 nm emissions are illustrated in Fig. 4.31. All the nanopowders showed a broad and strong absorption band centered at 300 nm including few sharp lines in the longer wave length region. The broadband corresponds to  $\text{O}^{2-} \rightarrow \text{Ce}^{4+}$  charge transfer transitions whereas the sharp line at longer wavelength region (350–450 nm) attributed to the f–f transition.<sup>57</sup> The intensity of the excitation bands showed an initial increase as the  $\text{Sm}^{3+}$  doping concentration increases from 0.5 to 1 mol%. On increasing the dopant concentration, the absorbed energy gets quenched by the energy migration along  $\text{CeO}_2$  framework via exchange mechanism resulting in weak absorption peak. Hence, it can be concluded that the energy acquired by the host lattice upon excitation by UV light are able to transfer it to the  $\text{Sm}^{3+}$  and produces the red emission.

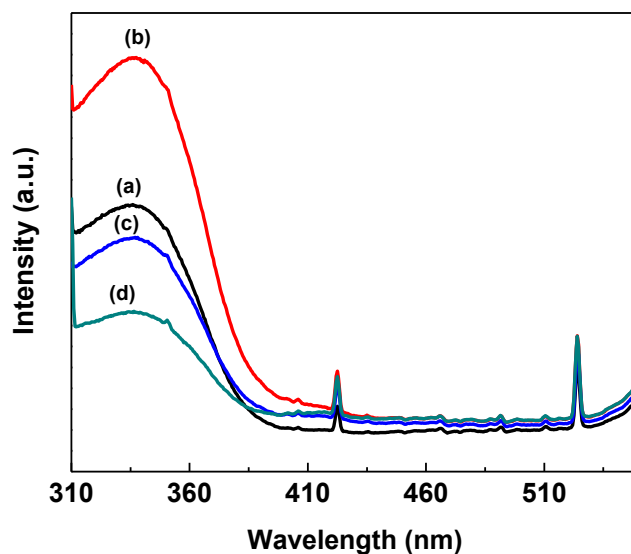


**Fig. 4.31.** PL excitation spectra of (a) 0.5, (b) 1.0, (c) 2.0, and (d) 10 mol%  $\text{Sm}^{3+}$  doped  $\text{CeO}_2$  nanopowders calcined at  $500^\circ\text{C}$  for 2 h.

A model has been proposed by us to explain the energy transfer in  $\text{Sm}^{3+}$  doped  $\text{CeO}_2$  system which involves relaxation to defect states on  $\text{CeO}_2$  before the energy is transferred to the  $\text{Sm}^{3+}$  ion. Fig. 4.32 represents the energy transfer mechanism involved in  $\text{Sm}^{3+}$  doped  $\text{CeO}_2$  system. Excitation by UV light above the bandgap of  $\text{Sm}^{3+}$ -doped  $\text{CeO}_2$  caused the excitation of the oxygen-vacancy-trapped electrons from the defect states present at the top of the VB of  $\text{CeO}_2$  to the defect states present in the lower part of the CB, subsequently the photo excited electrons migrate to the excited states of  $\text{Sm}^{3+}$ . Finally, the excited photo-electrons at the excited states of  $\text{Sm}^{3+}$  could transfer to the long-lived  $^4\text{G}_{5/2}$  of  $\text{Sm}^{3+}$  via

nonradiative relaxation, and then produce strong orange-red emissions via radiative relaxation. Many authors have proposed similar type of mechanism to interpret the PL of other  $\text{Sm}^{3+}$  doped systems.<sup>58-60</sup>

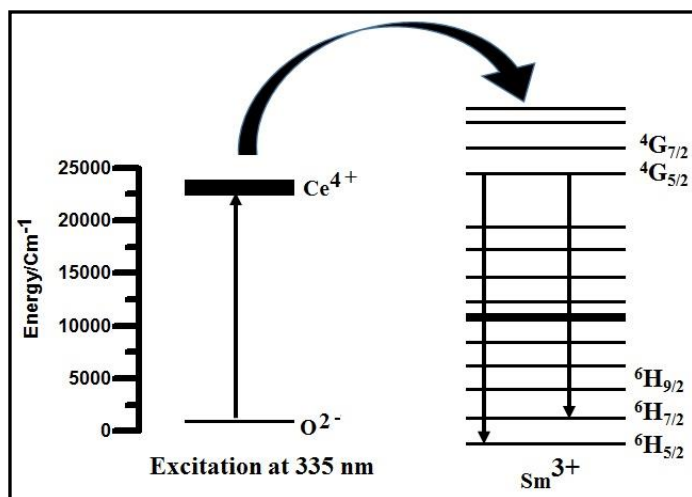


**Fig. 4.32.** Energy transfer mechanism from  $\text{CeO}_2$  host to  $\text{Sm}^{3+}$  ions.

#### 4.3.7.3. Fluorescent microscopy images

In addition to that it is also noteworthy that the representative sample of 1mol%  $\text{sm}^{3+}$  doped  $\text{CeO}_2$  calcined at  $1000^\circ\text{C}$  exhibit a number of distinct color emissions under a fluorescent microscope upon excitation at different wavelengths, (a) 350, (b) 405 and (c) 532 nm as shown in Fig. 4.33. Krishnan *et al.* also observed cerium oxide nanodots exhibiting a number of distinct color emissions.<sup>61</sup>

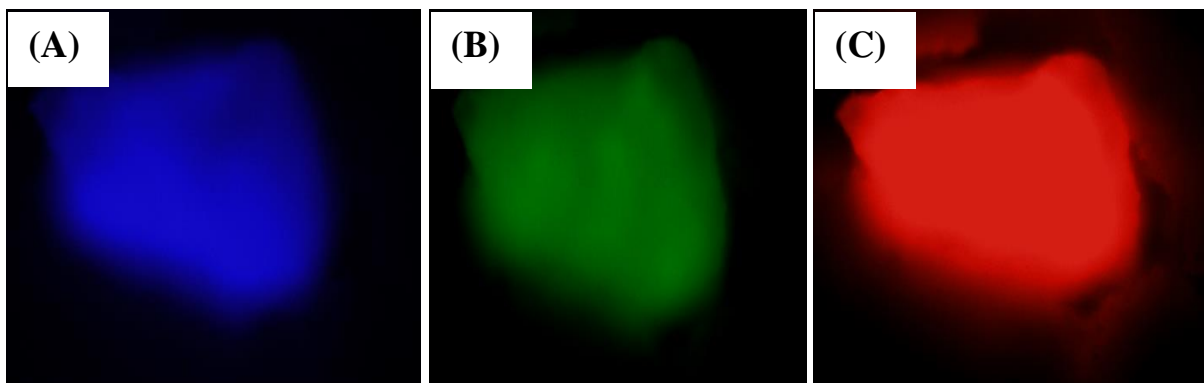


**Fig. 4. 33.** Fluorescent microscope images of 1SmCeSDS1000 at excitation wavelengths (A) 350 nm, (B) 405 nm and (C) 532 nm.

### 4.3.8. XPS analysis

X-ray photoelectron spectroscopy (XPS) study was performed to analyse the elemental composition and valence states of the  $\text{Sm}^{3+}$  doped  $\text{CeO}_2$  sample calcined at  $500^\circ\text{C}$ . A detailed survey of XPS spectra of the sample revealed the prominent presence of the peaks of Ce 3d, O 1s, Sm 4f and C1s. It is well accepted that if we take into account of spin-orbit coupling, the Ce 3d XPS spectrum can be resolved into ten peaks, which includes six structures from  $\text{Ce}^{4+}$  compound and four more when  $\text{Ce}^{3+}$  species are also present.<sup>29,30</sup> The series of peaks labelled with ‘u’ and ‘v’ are due to  $3d_{3/2}$  and  $3d_{5/2}$  spin-orbit states.<sup>29,30</sup> The high-resolution XPS spectrum in the region of 877-922 eV along with Gaussian fits is displayed in Fig. 4.34 to distinguish the  $\text{Ce}^{4+}$  and  $\text{Ce}^{3+}$  ionic states. The six peaks labelled v, v'', v''', u, u'', and u''' are characteristic peaks of  $\text{Ce}^{4+}$ , while the peaks labelled v<sub>0</sub>, v', u<sub>0</sub>, and u' are attributed to  $\text{Ce}^{3+}$ .<sup>30,62</sup> So, the XPS spectrum reveals the presence of a mixed valence state ( $\text{Ce}^{3+}$  and  $\text{Ce}^{4+}$ ) for the synthesized mesoporous  $\text{Sm}^{3+}$  doped  $\text{CeO}_2$  sample. The total concentrations of  $\text{Ce}^{3+}$  in the sample is calculated as the ratio of the sum of the integrated areas of all  $\text{Ce}^{3+}$  peaks to the total area of each peak in the spectrum.<sup>30,63,64</sup> The percentage of  $\text{Ce}^{3+}$  was calculated to be ~ 24.1% for  $\text{Sm}^{3+}$  doped  $\text{CeO}_2$  while decreased to ~ 21.3% in pure  $\text{CeO}_2$ . Similarly, 21%  $\text{Ce}^{3+}$  was present in the  $\text{Ce}_{0.95}\text{Sm}_{0.05}\text{O}_2$  sample with surface area  $95 \text{ m}^2\text{g}^{-1}$ , synthesized using aqueous ammonium carbonate complex of  $\text{Ce}^{4+}$  and  $\text{Sm}^{3+}$  under supercritical water condition.<sup>63</sup>

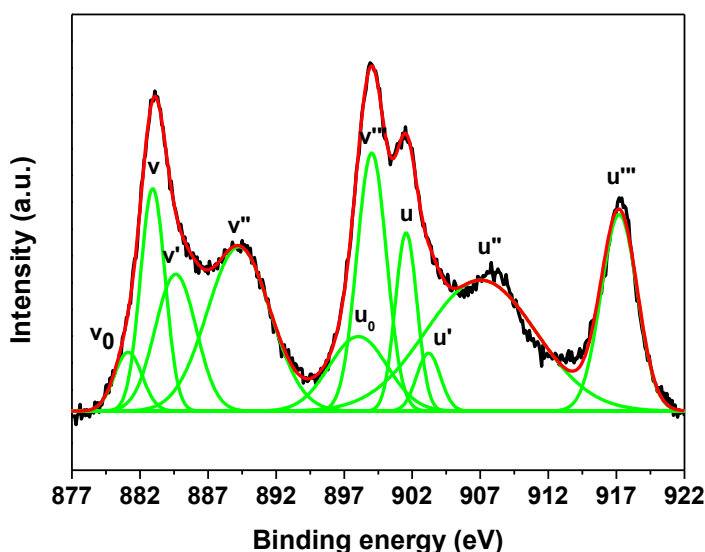


**Fig. 4.34.** High-resolution XPS spectrum and the corresponding deconvolution components of Ce 3d from  $\text{Sm}^{3+}$  doped  $\text{CeO}_2$  calcined at  $500^\circ\text{C}$ .

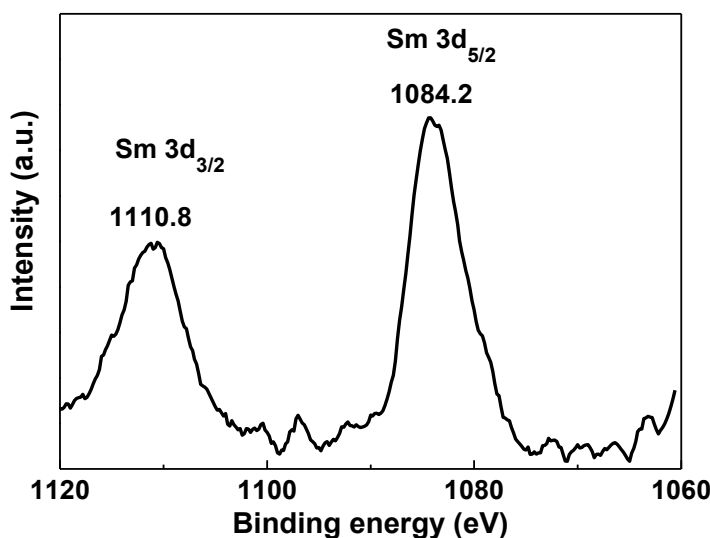


**Fig. 4.35.** Sm 3d<sub>5/2</sub> XP spectrum of Sm<sup>3+</sup> doped CeO<sub>2</sub> calcined at 500°C.

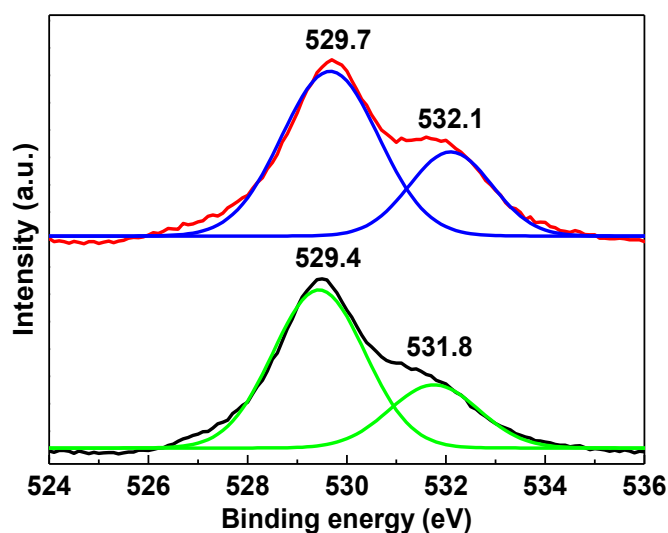


**Fig. 4.36.** O 1s XP spectra of CeO<sub>2</sub> and Sm<sup>3+</sup> doped CeO<sub>2</sub> samples calcined at 500°C.

Fig. 4.35 shows the Sm3d XP spectrum, which confirms the doping of Sm<sup>3+</sup> in CeO<sub>2</sub>. The core level Sm3d<sub>3/2</sub> and Sm3d<sub>5/2</sub> bands are observed at binding energies of 1110.8 and 1084.2 eV, respectively. Due to the low Sm doping concentration in the material, the peak intensity is weak. The high resolution O1s XP spectrum, which is composed of two components in the region 524-536 eV is shown in Fig. 4.36. The main peak at 529.7 eV can be assigned to O<sup>2-</sup> ions of Sm<sup>3+</sup> doped CeO<sub>2</sub> lattice oxygen and the shoulder peak at higher binding energy of 532.1 eV clearly shows the presence of adsorbed oxygen species of surface hydroxyl groups.<sup>29</sup> It is interesting to note that the peaks related to lattice oxygen and surface hydroxyl groups in pure mesoporous CeO<sub>2</sub> are shifted to lower BE values of 529.4 and 531.8 eV,

respectively. The result reveals that the incorporation of  $\text{Sm}^{3+}$  to the  $\text{CeO}_2$  sample significantly influenced the chemical environment of oxygen in the  $\text{Sm}^{3+}$  doped  $\text{CeO}_2$  sample. The intensity of the peak of surface hydroxyl group was significantly high although the samples were calcined at 500°C temperatures. It is important to notice that peak intensity for the surface hydroxyl group is higher in mesoporous  $\text{Sm}^{3+}$  doped  $\text{CeO}_2$  as compared to that of pure  $\text{CeO}_2$ , which may be attributed to its higher surface area and pore volume. The presence of  $\text{Ce}^{3+}$  ions in the  $\text{CeO}_2$  lattice is attributed to the oxygen vacancies in the nanocrystals. The results indicated that the present synthesis procedure is robust and capable of producing surface defect state engineered  $\text{CeO}_2$ .

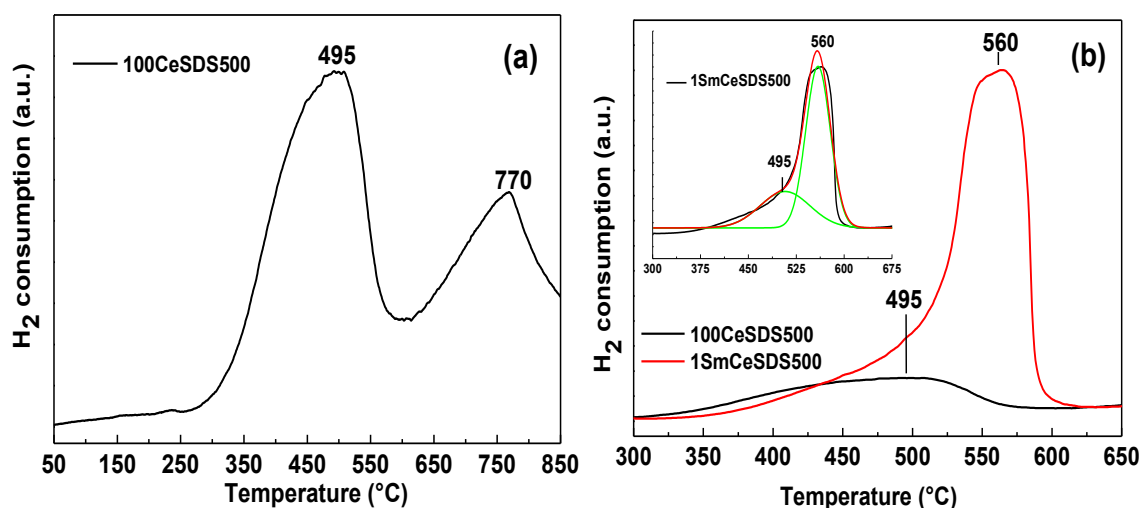
#### 4.3.9. $\text{H}_2$ -TPR analysis

Temperature programmed reduction by  $\text{H}_2$  ( $\text{H}_2$ -TPR) has been employed to ascertain the reduction behavior of pure  $\text{CeO}_2$  and  $\text{Sm}^{3+}$  doped  $\text{CeO}_2$  calcined at 500°C, and the respective profiles are shown in Fig. 4.37. It is generally accepted that the reduction of surface lattice oxygen, as it can contact directly with  $\text{H}_2$  (surface reduction), occurs first at lower temperature and then the reduction of the bulk oxygen occurs at relatively higher temperatures.<sup>65,66</sup> The TPR profile of pure  $\text{CeO}_2$  (Fig. 4.37a) displays two distinct peaks, where the low-temperature peak at 495°C is attributed to reduction of oxygen species present at surface and the high-temperature peak at 770°C is observed due to bulk reduction. The higher relative intensity of surface reduction peak than the bulk reduction peak inferred that the sample has a significant amount of reducible surface oxygen.

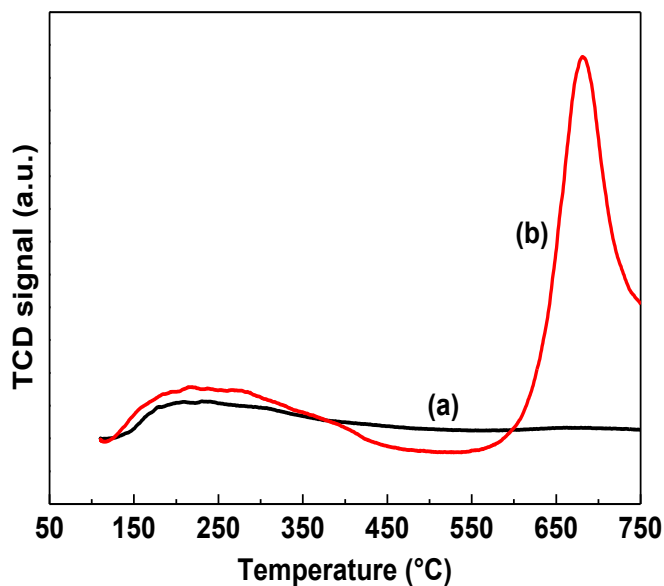
It is very interesting to observe that on incorporation of  $\text{Sm}^{3+}$  in  $\text{CeO}_2$  the reduction peaks merge into one broad peak (330–630°C) centered at 560°C as can be seen from Fig. 4.37b. The broad peak is deconvoluted into two peaks (see inset of Fig. 4.37b) centered at 495°C and 560°C attributed to surface and bulk oxygen reductions, respectively. Though there is no appreciable change in the peak position of the surface reduction peak but the peak area increased as compared with those of pure  $\text{CeO}_2$ . Surprisingly, the bulk reduction peak of  $\text{Sm}^{3+}$  doped  $\text{CeO}_2$  is shifted to lower temperature and the peak area is also drastically enhanced in comparison to the pure sample. This essentially suggests that the bulk reduction occurs with a lower activation barrier and quantitatively account for the oxygen enhancement. A decrease in the bulk reduction temperature that approaches the surface reduction peak indicates that the



incorporation of  $\text{Sm}^{3+}$  eases the formation of labile bulk oxygen vacancies.<sup>65</sup> As evident from XRD results that  $\text{Sm}^{3+}$  doping leads to an expansion of the  $\text{CeO}_2$  lattice, the related lower lattice strain and larger free volume in the  $\text{CeO}_2$  network then facilitates the equilibrium between the surface and bulk oxygen atoms.<sup>67</sup> The results of  $\text{H}_2$ -TPR profiles show that the total  $\text{H}_2$  consumption amount of  $\text{Sm}^{3+}$  doped  $\text{CeO}_2$  is much higher (69.16 mg/g) than that of pure  $\text{CeO}_2$  (14.42 mg/g). It is evident from these observations that a higher concentration of active oxygen vacancies in  $\text{Sm}^{3+}$  doped  $\text{CeO}_2$  leading to the formation of active oxygen species reducible by  $\text{H}_2$  at low temperature. The higher surface area and unique mesoporous structure also favour the gas diffusion.<sup>66</sup> Liu and coworkers pointed out that any processing condition which favors the formation of more desired oxygen vacancies (as we also observed from HRTEM) will result in enhanced reducibility.<sup>68</sup> As reported by previous study, the lower formation energy of oxygen vacancies could enhance the reducibility by the process (eqn. 1) :  $2\text{Ce}^{4+} + \text{O}^{2-} \rightarrow 2\text{Ce}^{3+} + \text{V}_\text{o}^{\bullet\bullet} + \frac{1}{2}\text{O}_2$  (1), where,  $\text{V}_\text{o}^{\bullet\bullet}$  represents an oxygen vacant site.<sup>69</sup> The presence of oxygen vacancy clustering (see HRTEM) facilitated the activation and transportation of active oxygen species, thus promoting reducibility.<sup>68</sup> The active oxygen species is found to contribute to high performances of ceria in oxygen storage, water–gas shift reaction, wet catalytic oxidation, etc.,<sup>66</sup> thus, high performances can be expected from mesoporous pure and  $\text{Sm}^{3+}$  doped  $\text{CeO}_2$  for applications in these areas.



**Fig. 4.37.**  $\text{H}_2$  consumption as a function of temperature for mesoporous  $\text{CeO}_2$  and  $\text{Sm}^{3+}$  doped  $\text{CeO}_2$  calcined at  $500^\circ\text{C}$ .

4.3.10. NH<sub>3</sub>-TPD analysis

**Fig. 4.38.** NH<sub>3</sub>-TPD profiles of the (a) CeO<sub>2</sub> and (b) Sm<sup>3+</sup> doped-CeO<sub>2</sub> calcined at 500°C.

The NH<sub>3</sub>-TPD profiles of the pure CeO<sub>2</sub> and Sm<sup>3+</sup> doped CeO<sub>2</sub> samples are shown in Fig. 4.38, which provide evidence of the presence of acid sites of different strengths on each sample. In this study, a wide desorption peak is observed in the range 100°C to 500°C, which is characterized as weak acid sites.<sup>70</sup> This broad peak is illustrating that the NH<sub>3</sub> adsorbed on multifold active sites in the outer and inner surface of the mesoporous materials. The strongest acid sites releasing NH<sub>3</sub> at higher temperature of 670°C are Lewis-acidic in nature, while weak acid sites desorbing NH<sub>3</sub> at lower temperature are attributed as Brønsted acidic sites.<sup>1</sup> When Sm<sup>3+</sup> dopant replaces one Ce<sup>4+</sup>, one of the oxygen atoms on Ce<sup>4+</sup> loses a bonding site and thereby a hydroxyl group (Brønsted acid site) is formed in CeO<sub>2</sub> lattice. The Sm<sup>3+</sup> doped CeO<sub>2</sub> show two major desorption peaks at 235, and 670°C, whereas pure CeO<sub>2</sub> show only one major peak at 235°C. The more prominent high temperature peak at 670°C for Sm<sup>3+</sup> doped CeO<sub>2</sub> sample suggests that higher number of stronger acidic sites. It is clear from the figure that the Sm<sup>3+</sup> incorporation into CeO<sub>2</sub> lattice induces an increase in the weak acidic sites and created more number of strong acidic sites as compared to pure CeO<sub>2</sub>. The larger number of oxygen vacancy, which can accept electron (Lewis acid site) may be the reason for the higher acidity of Sm<sup>3+</sup> doped CeO<sub>2</sub> sample.

### 4.3.10. Conclusion

Mesoporous and nanocrystalline (0.5, 2, 5, 10 and 20 mol%) Sm<sup>3+</sup> doped CeO<sub>2</sub> powders with cubic fluorite structure were synthesized through a facile aqueous solution-based chemical route using different surfactants. The prepared materials were characterized using DSC-TG, XRD, TEM, BET, UV-vis diffuse reflectance and, PL, XPS, TPR and TPR techniques. The as-synthesized hybrid and the sample calcined at 500°C exhibited high surface area and pore volume. The co-existence of mixed valence state, Ce<sup>3+</sup> and Ce<sup>4+</sup> was confirmed by XPS studies. Concentrations of Ce<sup>3+</sup> obtained from the XPS analysis are significantly larger than reported previously, which indicates the presence of higher original concentration of the oxygen vacancies in nano-CeO<sub>2</sub>. Sm<sup>3+</sup> doping in CeO<sub>2</sub> show improved structural features such as increased lattice volume, higher surface hydroxyl groups, specific surface area, pore volume, and Ce<sup>3+</sup> and oxygen vacancies concentrations. UV-vis diffuse reflectance spectra for mesoporous samples showed intense broad bands corresponding to the charge-transfer transitions from O<sub>2</sub> (2p) to the Ce<sup>4+</sup> or Ce<sup>3+</sup> (4f) orbitals in host cubic CeO<sub>2</sub>. The enhanced PL emission spectra of mesoporous Sm<sup>3+</sup> doped CeO<sub>2</sub> show narrow bands arising from the <sup>4</sup>G<sub>5/2</sub>→<sup>6</sup>H<sub>5/2</sub> and <sup>4</sup>G<sub>5/2</sub>→<sup>6</sup>H<sub>7/2</sub> transitions of Sm<sup>3+</sup> ion, and an intense broad band, typical for defective CeO<sub>2</sub> nanocrystals. The high surface area mesoporous Sm<sup>3+</sup> doped CeO<sub>2</sub> material having nanocrystalline framework, strong UV-visible absorption, and PL will have important applications in catalysis, and separation technology, and the possibility of these materials to be used as better UV blockers and nanoscale photoluminescent or nano-optoelectronic materials. These results suggest that high surface area, mesoporous and surface defects engineered Sm<sup>3+</sup> doped CeO<sub>2</sub> are very promising materials for multifunctional applications.

### References

1. A. Corma, P. Atienzar, H. García and J. Y. C. Ching, *Nature Mater.*, 2004, **3**, 394.
2. Y. P. Fu, S. B. Wen and C. H. Lu, *J. Am. Ceram. Soc.*, 2008, **91**, 127.
3. Q. Liu, F. Zhao, X. Dong, C. Yang and F. Chen, *J. Phys. Chem. C*, 2009, **113**, 17262.
4. T. Yu, B. Lim and Y. Xia, *Angew. Chem., Int. Ed.*, 2010, **49**, 4484.
5. Y. Ma, X Wang, S. Li, M.S Toprak, B. Zhu and M. Muhammed, *Adv. Mater.*, 2010, **22**, 1640.
6. A.D. Mayernick, R. Li, K.M. Dooley and M.J. Janik, *J. Phys. Chem. C*, 2011, **115**, 24178.
7. J. Li, A. Kalamb, A.S. Al-Shihrib, Q. Sua, G. Zhonga and G. Du, *Mater. Chem. Phys.*, 2011, **130**, 1066.
8. Z. Wang, Z. Quan and J. Lin, *Inorg. Chem.*, 2007, **46**, 5237.

9. S. Gupta, S.V.N.T. Kuchibhatla, M.H. Engelhard, V. Shutthanandan, P. Nachimuthu, W. Jiang, L.V. Saraf, S. Thevuthasan and S. Prasad, *Sens Actuators B.*, 2009, 139, 380.
10. Y. Yoshida and S Fujihara, *Eur. J. Inorg. Chem.*, 2011, 10, 1577.
11. S. Fujihara and M. Oikawa, *J. Appl. Phys.*, 2004, 95, 8002.
12. V.V. Ursaki, V. Lair, L. Zivkovic, M. Cassir, A. Ringuede and O. Lupan, *Opt. Mater.*, 2012, 34, 1897.
13. J. Liu, J. Ye, P. Liu, L. Chen and M. Zhang, *Mater. Lett.*, 2011, 65, 143.
14. E. C. C. Souza, H. F. Brito and E. N. S. Muccillo, *J. Alloys Comp.*, 2010, 491, 460.
15. M. K. Rath, S. K. Acharya, B. H. Kim, K. T. Lee and B. G. Ahn, *Mater. Lett.*, 2011, 65, 955.
16. K. Wang, R. Ran and Z. Shao, *J. Power Sources*, 2007, 170, 251.
17. R. Ran, Y. Guo, Y. Zheng, K. Wang and Z. Shao, *J. Alloys Comp.*, 2010, 491, 271.
18. S. Hao, J. Hou, P. Aprea and T. Lv, *Ind. Eng. Chem. Res.*, 2014, 53, 14617.
19. Y. Xu and R. Li, *RSC Adv.*, 2015, 5, 44828.
20. B. Ksapabutr, E. Gulari and S. Wongkasemjit, *Mater. Chem. Phys.*, 2006, 99, 318.
21. D. Ramimoghadam, M. Z. B. Hussein and Y. H. T. Yap, *Int. J. Mol. Sci.*, 2012, 13, 13275..
22. F. Zhang, N. Du, S. Song and W. Hou, *Mater. Chem. Phys.*, 2015, 152, 95.
23. P. W. Dunne, A. M. Carnerup, A. Węgrzyn, S. Witkowski and R. I. Walton, *J. Phys. Chem. C*, 2012, 116, 13435.
24. C. Tiseanu, B. Cojocar, D. Avram, V. I. Parvulescu, A. V. V. Gonzalez and M. S. Dominguez, *J. Phys. D: Appl. Phys.*, 2013, 46, 275302.
25. L. Zivkovic, V. Lair, O. Lupan and A. Ringuede, *Thin Solid Films.*, 2011, 519, 3538.
26. J. Wei, Z. Yang, H. Yang, T. Sun and Y. Yang, *Cryst. Eng. Comm.*, 2011, 13, 4950.
27. B. Chen, Z. Zhu, J. Hong, Z. Wen, J. Ma, Y. Qiu and J. Chen, *Dalton Trans.*, 2014, 43, 10767.
28. G. Zhang, Z. Shen, M. Liu, C. Guo, P. Sun, Z. Yuan, B. Li, D. Ding and T. Chen, *J. Phys. Chem. B*, 2006, 110, 25782.
29. P. Sudarsanam, K. Kuntaiah and B. M. Reddy, *New J. Chem.*, 2014, 38, 5991.
30. M. Guo, J. Lu, Y. Wu, Y. Wang and M. Luo, *Langmuir*, 2011, 27, 3872.
31. W. Huang, P. Shuk and M. Greenblatt, *Chem. Mater.*, 1997, 9, 2240.
32. E. K. Goharshadi, S. Samiee and P. Nancarrow, *J. Colloid Interface Sci.*, 2011, 356, 473.
33. L. Zhu, Q. Li, X. D. Liu, J. Y. Li, Y. F. Zhang, J. Meng and X. Q. Cao, *J. Phys. Chem. C*, 2007, 111, 5898.
34. H. Li, G. Lu, Q. Dai, Y. Wang, Y. Guo and Y. Guo, *ACS. Appl. Mater. & Inter.*, 2010, 2, 3, 838.
35. N. B. McKeown, P. M Budd, K. J. Msayib, B. S Ghanem, H. J. Kingston, C. E. Tattershall, S. Makhseed, K. J.Reynolds and D. Fritsch, *Chem. Eur. J.*, 2005, 11, 2610.
36. Y. Meng, D. Gu, F. Q. Zhang, Y. F. Shi, L. Cheng, D. Feng, Z. X. Wu, Z. X. Chen, Y. Wan, A. Stein and D. Y. Zhao, *Chem. Mater.*, 2006, 18, 4447.
37. J. G. Li, T. Ikegami and T. Mori, *Acta Mater.*, 2004, 52, 2221.

38. P. Nayak, B. B. Nayak and A. Mondal, *Mater. Chem. Phys.*, 2011, 127, 12.
39. D. Andreescu, E. Matijevic and D. V. Goia, *Colloids Surfaces A Physicochem. Eng. Asp.*, 2006, 291, 93.
40. L. Zhao and L. Gao, *J. Mater. Chem.*, 2004, 14, 1001.
41. T. S. Sreeremya, K. M. Thulasi, A. Krishnan and S. Ghosh, *Ind. Eng. Chem. Res.*, 2012, 51, 318.
42. B. Yan, H. X. Zhu, *J. Nanopart. Res.*, 2008, 10, 1279.
43. Z. Y. Ma, C. Yang, W. Wei, W. H. Li and Y. H. Sun, *J. Mol. Catal. A Chem.*, 2005, 227, 119.
44. S. E. Collins, J. M. Cies, E. del Rio, M. Lopez-Haro, S. Trasobares, J. J. Calvino, J. M. Pintado, and S. Bernal, *J. Phys. Chem. C*, 2007, 111, 14371.
45. S. Torbrügge, M. Reichling, A. Ishiyama, S. Morita and Ó. Custance, *Phys. Rev. Lett.*, 2007, 99, 056101.
46. Y. Namai, K. Fukui and Y. Iwasawa, *J. Phys. Chem. B*, 2003, 107, 11666.
47. K. Kuntaiah, P. Sudarsanam, B. M. Reddy and A. Vinu, *RSC Advances*, 2013, 3, 7953.
48. B. Choudhury, P. Chetri and A. Choudhury, *RSC Adv.*, 2014, 4, 4663.
49. P. Patsalas, S. Logothetidis, L. Sygellou and S. Kennou, *Phys. Rev. B.*, 2003, 68, 035104.
50. M. Y. Chen, X. T. Zua, X. Xiang and H. L. Zhang, *Physica B.*, 2007, 389, 263.
51. B. M. Reddy, P. Bharali, G. Thrimurthulu, P. Saikia, L. Katta and S. E. Park, *Catal. Lett.*, 2008, 123, 327.
52. S. Sakirzanovas, A. Katelnikovas, H. Bettentrup, A. Kareiva and T. Justel, *J. Lumin.*, 2011, 131, 1525.
53. U. S. Sias, E. C. Moreira and E. Ribeiro, *Nucl. Instrum. Methods B.*, 2004, 218, 405.
54. P. Ghosh, S. Sadhu, A. Patra, *Phys. Chem. Chem. Phys.*, 2006, 8, 3342.
55. R. H. Krishna, B. M. Nagabhushana, H. Nagabhushana, N. S. Murthy, S. C. Sharma, C. Shivakumara and R. P. S. Chakradhar, *J. Phys. Chem. C*, 2013, 117, 1915.
56. G. S. R. Raju, E. Pavitra, G. Nagaraju and J. S. Yu. *Dalton Trans.*, 2015, 44, 1790.
57. Z. Qing, M. Qingyu, T. Yue, F. Xiaohui, S. Jiangting and L. Shuchen, *J. Rare. Earths*, 2011, 29, 815.
58. W. Luo, R. Li, and X. Chen, *J. Phys. Chem. C*, 2009, 113, 8772.
59. S. K. Gupta, P. S. Ghosh, N. Pathak, A. Arya and V. Natarajan, *RSC Adv.*, 2014, 4, 29202.
60. E. D. Rosa, L. A. D. Torres, P. Salas and R.A. Rodriguez, *Opt. Mater.*, 2005, 27, 1320.
61. S. Deshpande, S. Patil, S. VNT Kuchibhatla and S. Seal, *Appl. Phys. Lett.*, 2005, 87, 133113.
62. A. Krishnan, T. S. Sreeremya, E. Murray, S. Ghosh, *J. Colloid Interface Sci.*, 2013, 389, 16.
63. S. Ahmad, K. Gopalaiah, S. N. Chandrudu and R. Nagarajan, *Inorg. Chem.*, 2014, 53, 2030.
64. S. K. Pahari, P. Pal, A. Sinhamahapatra, A. Saha, C. Santra, S. C. Ghosh, B. Chowdhury and A. B. Panda, *RSC Adv.*, 2015, 5, 45144.
65. A. G. M. Silva, T. S. Rodrigues, A. Dias, H. V. Fajardo, R. F. Gonçalves, M. Godinho and P. A. Robles-Dutenhefner, *Catal. Sci. Technol.*, 2014, 4, 814.
66. S. Chow, T. Fan, J. Ding and D. Zhang, *J. Am. Ceram. Soc.*, 2010, 93, 40.
67. W. Y. Hernandez, O. H. Laguna, M. A. Centeno and J. A. Odriozola, *J. Solid State Chem.*, 2011, 184, 3014.
68. X. Liu, K. Zhou, L. Wang, B. Wang and Y. Li, *J. Am. Chem. Soc.*, 2009, 131, 3140.
69. G. Hua, L. Zhang, G. Fei and M. Fang, *J. Mater. Chem.*, 2012, 22, 6851.
70. S. K. Meher and G. R. Rao, *J. Colloid Interface Sci.*, 2012, 373, 46.

## Chapter 5

# Characterization of High Surface Area $\text{Eu}^{3+}$ Doped $\text{CeO}_2$ Nanopowders

**Outline:** This chapter presents the results and discussion pertaining to the structural, microscopic and optical characteristics of the nanosized 0.5, 1, 2 and 5 mol%  $\text{Eu}^{3+}$ -doped  $\text{CeO}_2$  synthesized through a surfactant (SDS) assisted homogeneous precipitation route followed by conventional refluxing method. Extensive characterization of the nanopowders were investigated by means of simultaneous thermal analysis (TG-DSC), X-ray diffraction (XRD), BET surface area, field emission scanning electron microscopy (FESEM), high resolution transmission electron microscopy (HRTEM),  $\text{H}_2$ -TPR and TPD as a function of the dopant concentration ( $\text{Eu}^{3+}$ ) and calcination temperatures. At the same time the influence of microwave refluxing method on the structural properties were also evaluated. XRD studies along with HRTEM results confirmed the formation of mesoporous nanocrystalline  $\text{CeO}_2$  at a lower temperature as low as  $100^\circ\text{C}$ . A detailed analysis revealed that  $\text{Eu}^{3+}$  doping in to  $\text{CeO}_2$  has increased the lattice volume, surface area, mesopore volume and engineered the surface defects. The as-prepared 1 mol%  $\text{Eu}^{3+}$ -doped  $\text{CeO}_2$  sample possesses high surface area of  $234\text{ m}^2/\text{g}$  with average pore diameter of 4 nm. On thermal treatment at  $500^\circ\text{C}$ , a high-quality surfactant-free  $\text{Eu}^{3+}$  doped  $\text{CeO}_2$  nanoparticles with surface area of  $148\text{ m}^2/\text{g}$  and larger average pore sizes of 5.5 nm, respectively, were formed. The emission spectra of 1 mol%  $\text{Eu}^{3+}$  doped  $\text{CeO}_2$  nanocrystals exhibited three main peaks centered at 590, 608, and 630 nm corresponding to the  $^5\text{D}_0 \rightarrow ^7\text{F}_1$ ,  $^5\text{D}_0 \rightarrow ^7\text{F}_2$  and  $^5\text{D}_0 \rightarrow ^7\text{F}_3$  transitions, respectively, upon excitation at 335 nm.

## 5.1. Introduction

Rare-earth doped nanoparticles are considered as the best phosphors among other inorganic metal oxide nanoparticles.<sup>1-3</sup> They are widely applied for emissive displays, fluorescent lamps, and for optoelectronic devices.<sup>4</sup> The most attractive feature of the luminescence spectra of rare-earth oxide is their line like emission which leads to high color purity. The line like emission is basically due to their well shielded inter configurational f-f transition.<sup>5</sup> CeO<sub>2</sub> is a well-known functional material due to its wide range of applications, such as automotive three way catalysts,<sup>7</sup> ultraviolet absorbers,<sup>8</sup> hydrogen storage materials,<sup>9</sup> oxygen sensors,<sup>10</sup> optical devices<sup>11</sup> and polishing materials.<sup>12</sup> It also has been consider to use in many biomedical applications due to their nontoxic nature and excellent biocompatibility.<sup>13</sup> However, CeO<sub>2</sub> shows weak emission characteristics as Ce<sup>4+</sup> has no 4f electron,<sup>14</sup> which implies their potential use as photo luminescent host material. The luminescence properties of weakly emitting particles could be improved by various methods. Most commonly it is to attach a fluorescent dye, like a shell to the surface of the nanoparticle.<sup>15</sup> Although this approach provides reliable and consistent emission from the fluorescent tag, but it has some demerits as (a) it suffers from the fact that the modification of the surface may lead to illogical inactivity of the nanoparticle, (b) it also makes the material more bulky and thus limits the penetration of the cells by the nanoparticles. Another method is doping of the parent matrix with guest elements, which can emit upon excitation<sup>16</sup> in the UV-visible range of the spectrum would be a better alternative. Europium (Eu) show a strong red emission when doped in different matrices. Kumar *et al.*<sup>13</sup> reported the purpose of considering Eu as a suitable dopant for enhancing emission in ceria as (i) it can be excited from ultraviolet to visible light,<sup>17</sup> (ii) the ionic radius<sup>18</sup> of Eu<sup>3+</sup> (0.1066 nm), being close to that of cerium (Ce) (Ce<sup>3+</sup>: 0.1143 nm; Ce<sup>4+</sup>: 0.097 nm), favors extensive solubility with the ceria lattice, and (iii) it increases the trivalent state of Ce, which may further enhance the biological activity of ceria. Although lots of research on luminescence of Eu doped metal oxides, such as alkaline, transition, and lanthanide oxides and some sulfides, has been done but only few report are available on doping with ceria.<sup>19,20</sup> Earlier, Wang *et al.*<sup>1</sup> have shown that doping with Eu is not efficient in improving the photoluminescence (PL) properties of ceria. On the contrary, few studies have shown prominent emission upon doping Eu in ceria.<sup>21</sup> Li *et al.* using citrate and polyethylene glycol, synthesized 0.1-10% Eu-doped ceria and attributed the broad band.<sup>22</sup>

In this study, nanocrystalline Eu-doped ceria were successfully synthesized through a surfactant assisted method using cheaper inorganic precursors. The structural and optical properties of  $\text{Eu}^{3+}$  doped  $\text{CeO}_2$  nanoparticle annealed at different temperatures were investigated. The PL properties of  $\text{Eu}^{3+}$ -doped  $\text{CeO}_2$  systems are investigated with respect to dopant concentration and annealing temperature. The mechanism of efficient energy transfer has been correlated with the surface and defect structure.

## 5.2. Synthesis and characterization of $\text{Eu}^{3+}$ doped $\text{CeO}_2$ materials

The methodology for the preparation of  $\text{Eu}^{3+}$  doped  $\text{CeO}_2$  samples are discussed in chapter – II. The prepared materials were characterized by TG-DSC, XRD, FESEM, BET surface area, FTIR, UV-Vis DRS, PL,  $\text{H}_2$ -TPR and TPD measurements.

## 5.3. Results and discussion

This section describes the results obtained from the various characterization techniques used for studying the physical properties of mesoporous  $\text{Eu}^{3+}$  doped  $\text{CeO}_2$  samples for various compositions.

### 5.3.1. TG-DSC profiles of as-prepared $\text{Eu}^{3+}$ doped $\text{CeO}_2$ powders

#### 5.3.1.1. Effect of dopant concentration

In order to investigate the thermal decomposition behaviors of as-synthesized  $\text{CeO}_2$  samples doped with (a) 0.5, (b) 1, (c), 2, and (d) 5 mol%  $\text{Eu}_2\text{O}_3$  prepared through conventional refluxing method using SDS as surfactant, were subjected to TG and DSC analyses from room temperature to  $1000^\circ\text{C}$  in air atmosphere at a heating rate of  $10^\circ\text{C min}^{-1}$ , and the corresponding profiles are shown in Fig. 5.1 (a-d). The TG results of all the samples can be analyzed as four steps weight loss processes, which are assigned as AB ( $30$ - $150^\circ\text{C}$ ), BC ( $150$ - $400^\circ\text{C}$ ), CD ( $400$ - $690^\circ\text{C}$ ), and DE ( $690$ - $1000^\circ\text{C}$ ). The weight losses were correspond to the following processes: (i) elimination of physio-adsorbed water (AB region), (ii) decomposition of organic template (BC region) along with (iii) elimination of nitrates (CD region), and (iv) removal of  $\text{SO}_2$  group (DE region). Total weight losses for the samples are in the range of 19.6 to 25%, which indicate that the sample consisted of a mixture of more  $\text{CeO}_2$  than the undecomposed precursor of cerium oxyhydroxide/ hydroxide with surfactant.



Table 5.1 summarizes the % of mass losses obtained from TG curves of the samples. The DSC curves of all the samples show two endothermic peaks and two exothermic peaks. Endothermic peaks appeared  $\sim 50$ - $70^\circ\text{C}$ , and  $120$ - $150^\circ\text{C}$  are associated with the physisorbed water molecule. A sharp prominent exothermic peak occurring around  $186^\circ\text{C}$  along with an additional peak centering at  $250^\circ\text{C}$  are due to the decomposition of the cerium hydroxide to crystalline  $\text{CeO}_2$  and combustion of the template molecule, respectively. The difference in the amount of weight loss and the decomposition temperature attributed to the varied amounts of water or hydroxyl group and surfactant molecule in the precursor samples. The weight loss of 2.5 to 5.5% was observed in the DE region at higher temperatures above  $690^\circ\text{C}$ , which triggered the removal of  $\text{SO}_2$  group from precursor's surface.

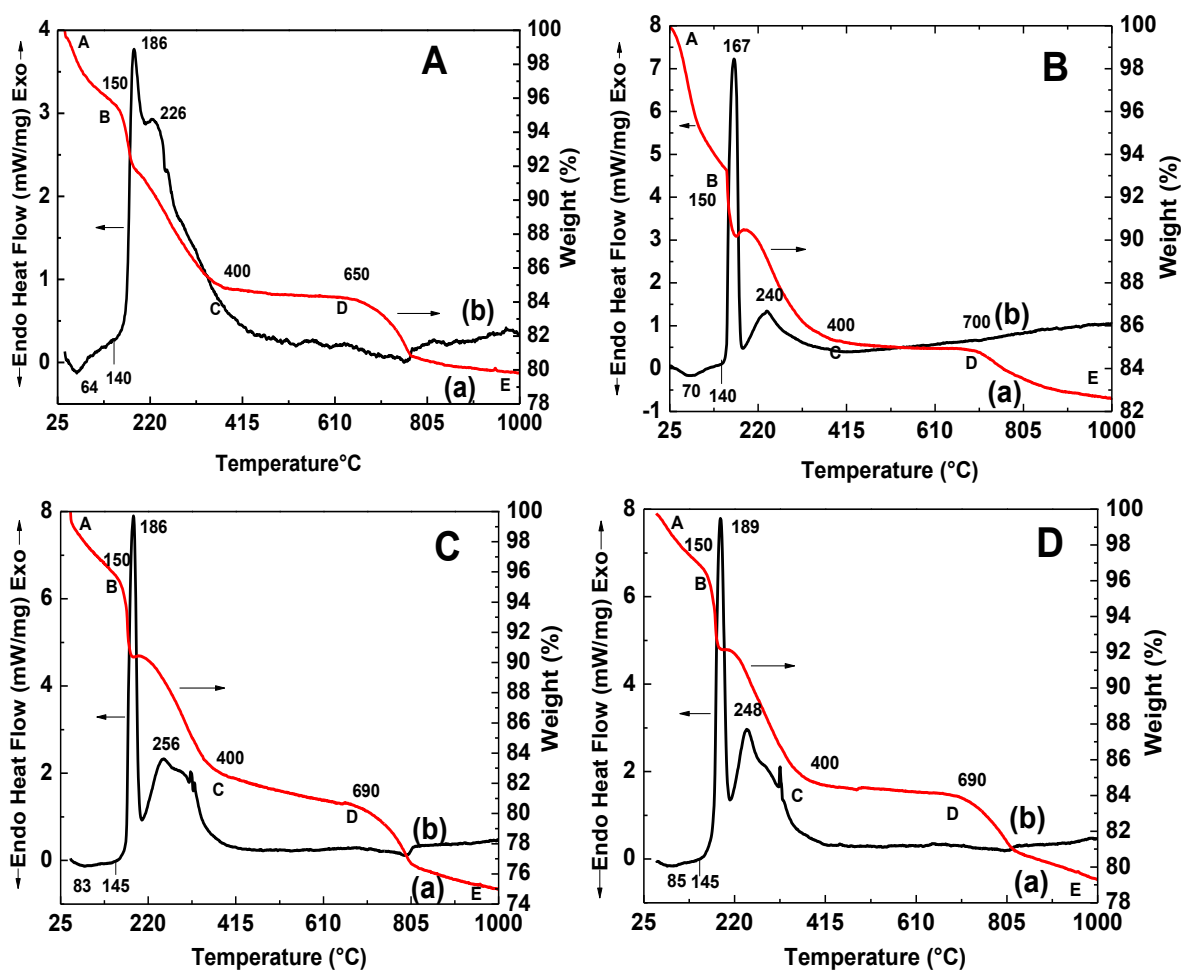


**Fig. 5.1.** (a) TG and (b) DSC profiles of as-prepared (A) 0.5, (B) 1.0, (C) 2.0, and (D) 5 mol%  $\text{Eu}^{3+}$  doped  $\text{CeO}_2$  sample obtained via conventional refluxing.

**Table 5.1.** Weight loss % of Eu<sup>3+</sup> doped CeO<sub>2</sub> samples.

Samples	TG results			
	Region	Temperature range (°C)	Weight loss (%)	Total weight loss (%)
0.5EuCeSDSasp	AB	30-150	4.5	20
	BC	150-400	10.7	
	CD	400-650	0.6	
	DE	650-1000	4.2	
1EuCeSDSasp	AB	30-150	6.7	17.5
	BC	140-430	7.9	
	CD	430-690	0.5	
	DE	690-1000	2.4	
2EuCeSDSasp	AB	30-150	4.3	25
	BC	150-400	13.2	
	CD	400-690	2	
	DE	690-1000	5.5	
5EuCeSDSasp	AB	30-150	3.3	20.8
	BC	150-400	12.1	
	CD	400-690	0.5	
	DE	690-1000	4.9	
1EuCeSDSMWasp	AB	30-150	5.7	19.6
	BC	150-400	10.3	
	CD	400-690	0.6	
	DE	690-1000	3	

### 5.3.1.2. Effect of microwave refluxing

TGA/DSC analysis was also performed to understand the influence of microwave heating during the synthesis on the thermal properties of as-synthesized 1 mol% Eu<sup>3+</sup> doped CeO<sub>2</sub> synthesized using SDS followed by microwave refluxing. Fig. 5.2 represents the TGA/DSC curves of the precursor obtained by microwave refluxing method. The sample synthesized via microwave refluxing exhibited more weight loss of 19.6% as compared to that of 17.4% observed in the sample via conventional refluxing and given in Table 5.1.

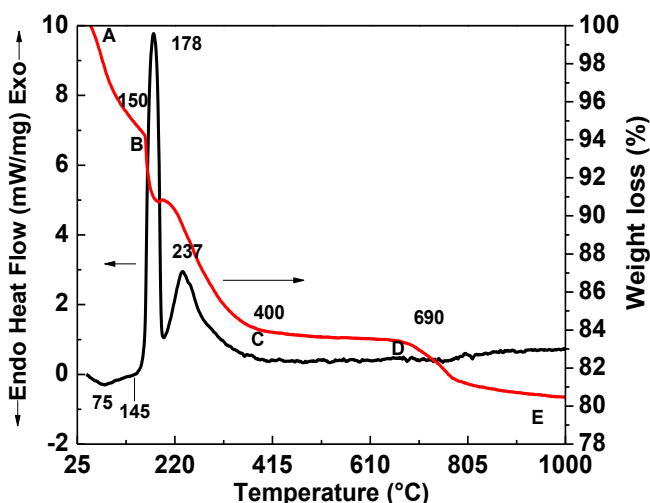


**Fig. 5.2.** TG-DSC profiles of the as-prepared 1 mol%  $\text{Eu}^{3+}$  doped  $\text{CeO}_2$  sample, obtained via microwave refluxing method.

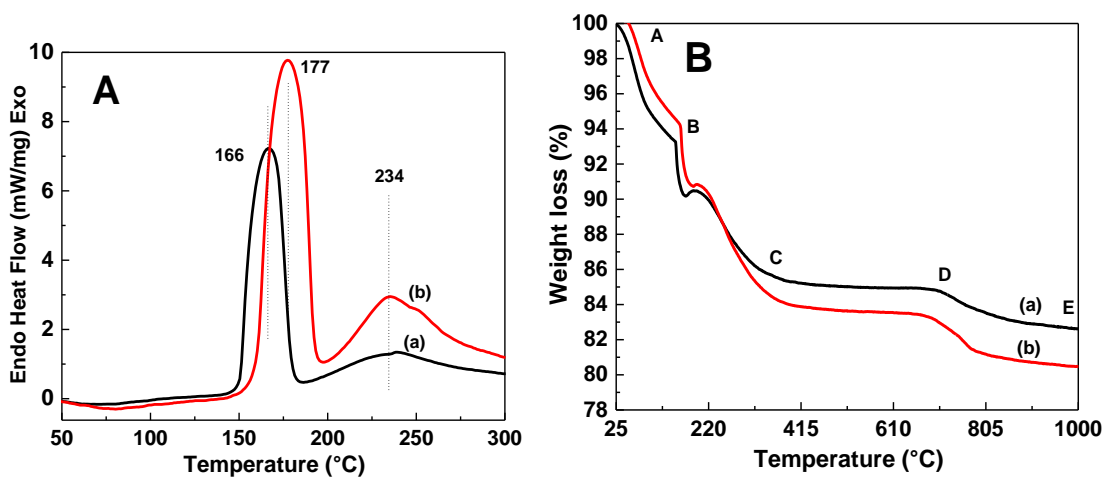


**Fig. 5.3.** Comparative (A) DSC and (B) TG profiles of the as-prepared 1 mol%  $\text{Eu}^{3+}$  doped  $\text{CeO}_2$  samples obtained via (a) conventional, and (b) microwave refluxing method.

It is clearly seen in Fig. 5.3(A) that the exothermic peak related to the thermal decomposition of the hydroxide precursors into their corresponding oxides of  $1\text{EuCeSDSasp}$  centered at  $166^\circ\text{C}$  are shifted to lower temperatures as compared to that of  $1\text{EuCeSDSMWasp}$ , suggesting that the conventional refluxing method accelerate the transformation of the amorphous to crystalline phase at lower temperatures than microwave refluxing. However, there was no changes in the position of second exothermic peak centered at  $234^\circ\text{C}$  related to the surfactant decomposition but it becomes stronger in case of  $1\text{EuCeSDSMWasp}$  than that of the  $1\text{EuCeSDSasp}$ , indicating the presence of more surfactant

molecule in the inorganic frame work in case of microwave refluxing method, which was further confirmed from the weight loss obtained in the BC region of their respective TG profiles as shown in Fig. 5.3(B).

### 5.3.2. XRD patterns of Eu<sup>3+</sup> doped CeO<sub>2</sub> nanopowders

#### 5.3.2.1. Effect of dopant concentrations

Fig. 5.4 shows the XRD patterns of the (a) 0.5, (b) 1, (c) 2, and (d) 5 mol% Eu<sup>3+</sup> doped CeO<sub>2</sub> nanopowders after calcining at 500°C. The XRD patterns of all the samples resemble the cubic fluorite phase of CeO<sub>2</sub> (JCPDS# 34-0394) and no diffraction peaks corresponding to either europium oxide or hydroxide were observed, indicating the formation of solid solution in the entire composition range. The crystallite size was calculated from the strongest XRD peak (111) plane broadening using the Scherrer equation.<sup>23</sup>

$$d = \frac{0.89\lambda}{\beta \cos \theta} \quad (5.1)$$

where  $d$  is the crystallite size,  $\lambda$  is the wavelength of CuK <sub>$\alpha$</sub>  radiation,  $\beta$  is the full-width at half-maxima (FWHM) of the diffraction peak, and  $\theta$  is the diffraction angle. It was found that the crystallite size decreases initially with increasing the dopant concentration from 0.5 to 1.0 mol% Eu<sup>3+</sup>, and then increases on further doping. The decrease in crystallite size for 1 mol% Eu<sup>3+</sup> could be attributable to the presence of significant lattice strain which reduces ion transport and sintering as noted previously for doped CeO<sub>2</sub>.<sup>24,25</sup> The lattice parameter for the (hkl) plane was calculated using the equation

$$a = d\sqrt{h^2 + k^2 + l^2} \quad (5.2).$$

The measured lattice parameters of Eu<sup>3+</sup> doped CeO<sub>2</sub> were found to be somewhat higher than that of pure CeO<sub>2</sub> (0.541 nm). This is due to the substitution of Ce<sup>4+</sup> with a smaller radius ( $r = 0.097$  nm) by Eu<sup>3+</sup> with a larger effective ionic radius ( $r = 0.1066$  nm). No significant change in the lattice parameters was found on increasing the concentration of Eu<sup>3+</sup>. The lattice parameters increases initially on increasing the Eu<sup>3+</sup> concentration from 0.5 to 1.0 mol% but decreases upon further doping to 2 mol% and then again increases on 5 mol% Eu<sup>3+</sup> doping. This anomaly can be ascribed to the combined effect of the lattice contraction due to surface tension which exceeds the small expansion due to europium addition and the existence of the many oxygen vacancies. A similar decrease in the lattice parameter has also

been reported in  $\text{Eu}^{3+}$  doped  $\text{CeO}_2$  nanoparticles synthesized by a single step simple solvothermal process.<sup>25,22</sup> Table 5.2 summarizes the variation of crystallite size and lattice parameters with europium concentrations.

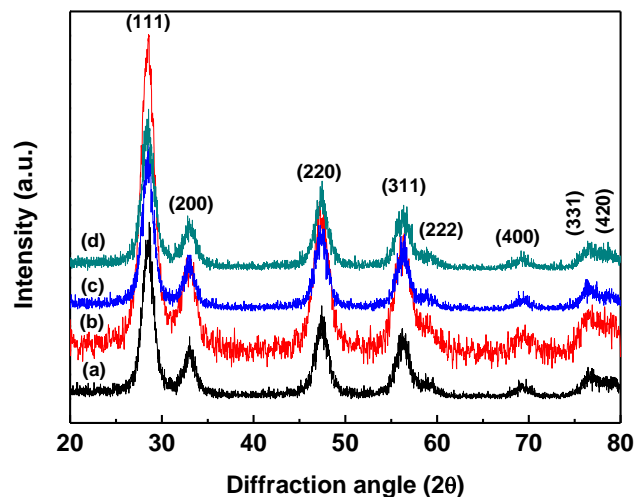


**Fig. 5.4.** XRD patterns of (a) 0.5, (b) 1.0, (c) 2.0, and (d) 5 mol%  $\text{Eu}^{3+}$  doped  $\text{CeO}_2$  obtained via conventional refluxing method and calcined at  $500^\circ\text{C}$  for 2 h.

**Table 5.2.** Crystallite size, lattice parameters and lattice volumes of (a) 0.5, (b) 1.0, (c) 2.0, and (d) 5 mol%  $\text{Eu}^{3+}$  doped  $\text{CeO}_2$  samples obtained via conventional refluxing method and calcined at  $500^\circ\text{C}$  for 2 h.

Sample	Crystallite size (nm)	Lattice parameter (nm)	Lattice volume ( $\text{nm}^3$ )
0.5EuCeSDS500	6.5	0.5428	0.1599
1EuCeSDS500	5.7	0.5432	0.1602
2EuCeSDS500	6.6	0.5430	0.1601
5EuCeSDS500	6.1	0.5432	0.1602

### 5.3.2.2. Effect of calcination temperature

Fig. 5.5 shows XRD patterns of 1 mol%  $\text{Eu}^{3+}$  doped  $\text{CeO}_2$  samples annealed at  $500^\circ\text{C}$ ,  $650^\circ\text{C}$  and  $800^\circ\text{C}$  for 2 h. The diffraction peaks of all the samples correspond to (111), (200), (220), (311), (222), (400), (331), and (420) could be indexed to pure cubic fluorite  $\text{CeO}_2$  structure, JCPDS (34-0394). No diffraction peaks related to the impurity phases was detected over the investigated temperature range. The results are suggesting that a solid solution was

formed and calcination did not lead to the segregation of the europium oxide phases as it occupies in the  $\text{CeO}_2$  lattice. Crystallite size and unit cell parameters of the calcined samples were calculated and listed in Table 5.3. On increasing the calcination temperatures, peak intensity increases with narrowing the diffraction peaks due to the crystal growth hence the crystallite size of 1 mol%  $\text{Eu}^{3+}$  doped  $\text{CeO}_2$  increases. A decrease in the lattice parameters is observed with increasing the calcination temperatures up to  $650^\circ\text{C}$ , which may be ascribable to the enhanced particle size upon calcination. According to Dhannia *et al.*<sup>26</sup> upon sintering oxygen vacancies are drastically reduced, which leads to an increase in the corresponding grain size, as a result the lattice parameter is found to decrease with annealing. In addition low-temperature  $\text{CeO}_2$  tends to exhibit higher lattice parameters due to the presence of defects and impurities.<sup>26</sup> Deshpande *et al.* studied the relationship between the crystallite size and lattice parameters of the synthesized  $\text{CeO}_2$  nanoparticles.<sup>27</sup> They pointed out that the variation in the lattice parameter is attributed to the lattice strain induced by the introduction of  $\text{Ce}^{3+}$  ions due to the formation of oxygen vacancies. The increase in lattice parameters of nanocrystalline  $\text{CeO}_2$  with decrease of particle size can also be explained in terms of grain surface relaxation.<sup>28</sup> Further increase of lattice parameters of  $\text{Eu}^{3+}$  doped  $\text{CeO}_2$  sample calcined at  $800^\circ\text{C}$  may be due to the reduction of  $\text{Ce}^{4+}$  ion to  $\text{Ce}^{3+}$ . Since the radius of  $\text{Ce}^{3+}$  ion (0.114 nm) is larger than that of  $\text{Ce}^{4+}$  ion (0.097 nm), the increase of  $\text{Ce}^{3+}$  ion in SDC solid solution would also lead to lattice expansion.<sup>29</sup>

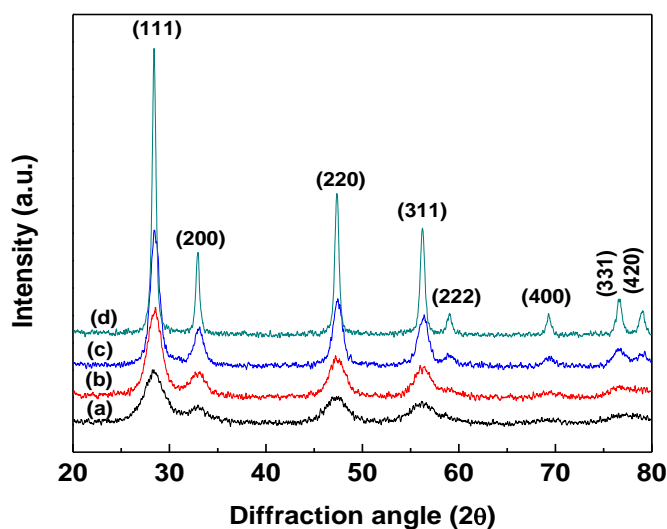


**Fig. 5.5.** XRD patterns 1 mol%  $\text{Eu}^{3+}$  doped  $\text{CeO}_2$  obtained via conventional refluxing method (a) as-prepared, and calcined at (b)  $500^\circ\text{C}$ , (c)  $650^\circ\text{C}$  and (d)  $800^\circ\text{C}$  for 2 h.

**Table 5.3.** Crystallite size, lattice parameters and lattice volume of 1 mol%  $\text{Eu}^{3+}$  doped  $\text{CeO}_2$  samples obtained via conventional refluxing method.

Sample	Crystallite size (nm)	Lattice parameter (nm)	Lattice volume ( $\text{nm}^3$ )
1.0EuCeSDSasp	4.5	0.5431	0.1602
1.0EuCeSDS500	5.7	0.5424	0.1596
1.0EuCeSDS650	8.6	0.5419	0.1591
1.0EuCeSDS800	19	0.5436	0.1606

### 5.3.2.3. Effect of microwave refluxing

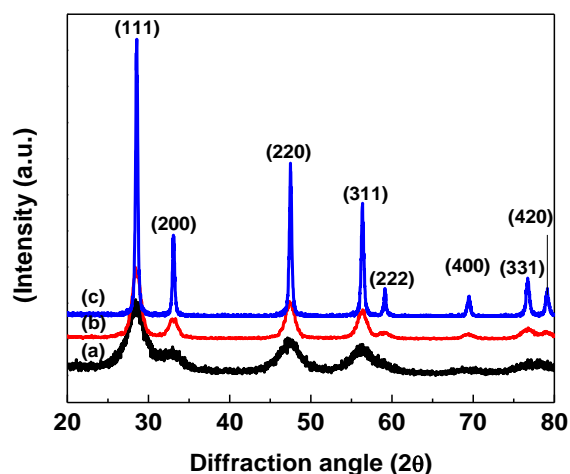


**Fig. 5.6.** XRD patterns of 1 mol%  $\text{Eu}^{3+}$  doped  $\text{CeO}_2$  obtained via microwave refluxing method (a) as-prepared, and the samples calcined at (b)  $500^\circ\text{C}$ , and (c)  $800^\circ\text{C}$  for 2 h.

Fig. 5.6 shows the XRD patterns of (a) as-prepared precursor powders of 1 mol%  $\text{Eu}^{3+}$  doped  $\text{CeO}_2$  obtained by microwave refluxing method and the powders calcined at (b)  $500^\circ\text{C}$ , and (c)  $800^\circ\text{C}$  for 2 h. All the peaks of the as-prepared as well as the calcined  $\text{Eu}^{3+}$ -doped  $\text{CeO}_2$  nanopowders, in  $20$ - $80^\circ$  range of  $2\theta$ -value, are indexed to their single crystalline cubic-fluorite structure of pure  $\text{CeO}_2$  (JCPDS 34-0394). Further, no diffraction peaks of any sample that could be attributed to cerium hydroxide or Europium oxide were observed. Unlike previous reports for the synthesis of ceria particles at low temperature, neither these are poorly crystalline, nor contain any appreciable amount of undecomposed precursor.<sup>22,28</sup> The results implies that the present aqueous based synthesis route is advantageous in preparing nanocrystalline  $\text{CeO}_2$  powders at lower temperatures as low as  $90^\circ\text{C}$ . These make this aqueous based microwave assisted route a low-cost and time saving one. With increase in

calcination temperatures, the peaks become narrower and their intensity increases due to the increase in crystallinity and agglomeration of  $\text{Eu}^{3+}$ -doped  $\text{CeO}_2$  crystallites. The average crystallite sizes of the  $\text{Eu}^{3+}$ -doped  $\text{CeO}_2$  samples were calculated from X-ray line broadening of the (111) reflections using Scherrer's equation.

**Table 5.4.** Crystallite size, lattice parameters and lattice volume of 1.0EuCeSDSMW, 1.0EuCeSDSMW500, and 1.0EuCeSDSMW800.

Sample	Crystallite size (nm)	Lattice parameter (nm)	Lattice volume (nm) <sup>3</sup>
1.0EuCeSDSMWasp	4.5	0.5420	0.1592
1.0EuCeSDSMW500	7.7	0.5415	0.1587
1.0EuCeSDSMW800	27.7	0.5409	0.1582

The calculated crystallite sizes are 4.5, 7.7 and 27.7 nm for the as-prepared sample and the samples heated at 500°C and 800°C, respectively, are given in Table 5.4. The lattice parameter ( $a$ ) value (0.5420 nm) of the as-prepared mesoporous  $\text{Eu}^{3+}$ -doped  $\text{CeO}_2$  sample is higher than that of the mesoporous as-prepared  $\text{CeO}_2$  sample ( $a = 0.53929$  nm), prepared under same experimental conditions, but very close to that of bulk cubic  $\text{CeO}_2$  (0.5411 nm). Due to the small size of the nanocrystallites, the formation energy of oxygen vacancy ( $V_{\text{O}}^{\bullet\bullet}$ ) is reduced and the two electrons from the oxygen atom are captured by two lattice site  $\text{Ce}^{4+}$  ions and hence favors the formation of reduce  $\text{Ce}^{4+}$  ions to the  $\text{Ce}^{3+}$  state. Using Kroger–Vink notation, the vacancy formation reaction is represented as  $\frac{1}{2}\text{O}_2 + 2\text{Ce}_{\text{Ce}}^{\times} \rightarrow V_{\text{O}}^{\bullet\bullet} + 2\text{Ce}'_{\text{Ce}} + \frac{1}{2}\text{O}_2$ . The presence of  $\text{Ce}^{3+}$  ions allows the increase of the lattice parameter due to the fact that  $\text{Ce}^{3+}$  ion has a larger ionic radius compared to  $\text{Ce}^{4+}$  and the concentration of  $\text{Ce}^{3+}$  ion decreases with increase in calcination temperature.<sup>21</sup> Again, the ionic radius of  $\text{Eu}^{3+}$  (0.1066 nm) is larger than  $\text{Ce}^{4+}$  (0.0971 nm), hence a little lattice expansion is expected due to incorporation of  $\text{Eu}^{3+}$  into  $\text{CeO}_2$  lattice, and results are in good agreement with previous reports.<sup>1,21</sup> In order to balance the charge compensation,  $\text{Eu}^{3+}$  additives create oxygen vacancies in the  $\text{CeO}_2$  lattice for example,  $\text{Eu}_2\text{O}_3 \xrightarrow{\text{CeO}_2} 2\text{Eu}'_{\text{Ce}} + 3\text{O}_{\text{O}}^{\times} + V_{\text{O}}^{\bullet\bullet}$ . A very negligible decrease in  $a$  value was observed upon increasing the calcination temperature up to 800°C. A continuous growth of the crystallite size was observed upon sintering. The consistency in the lattice parameter



infers that the introduction of  $\text{Eu}^{3+}$  ions into  $\text{CeO}_2$  can stabilize the host lattice at high temperatures and no new phase is formed.

### 5.3.3. $\text{N}_2$ -sorption analysis

#### 5.3.3.1. Effect of dopant concentration

The  $\text{N}_2$  adsorption–desorption measurements have been performed to investigate the textural properties of 0.5, 1, 2, and 5 mol%  $\text{Eu}^{3+}$  doped  $\text{CeO}_2$  obtained by using SDS as surfactant via conventional refluxing method. Fig. 5.7(A) shows their respective  $\text{N}_2$  adsorption–desorption isotherms and BJH pore size distribution graphs (Fig. 5.7B). The isotherm of all the samples, in spite of the amount of dopant content display very similar type IV isotherm patterns with distinct hysteresis loop which is associated with mesoporous materials. Hysteresis in the relative pressure ( $p/p_0$ ) region of 0.1–0.8 indicates the presence of mesopores in the samples.<sup>30</sup> The extended hysteresis loop arises due to the uptake of  $\text{N}_2$  at higher relative pressure ( $p/p_0 > 0.9$ ) implying the existence of macropores due to interparticle voids.<sup>31</sup> The calculated specific surface areas and other textural properties such as pore diameter and pore volume are listed in Table 5.5. No obvious trend in variation of surface area was observed with varying the dopant concentration. However, the 1 mol%  $\text{Eu}^{3+}$  doped  $\text{CeO}_2$  possesses highest specific surface area of  $148 \text{ m}^2 \text{ g}^{-1}$  along with pore volume of  $0.20 \text{ cm}^3 \text{ g}^{-1}$  as compared to the other samples. The BJH pore size distribution plots show wide monomodal profiles with the maximum at  $\sim 4 \text{ nm}$ .

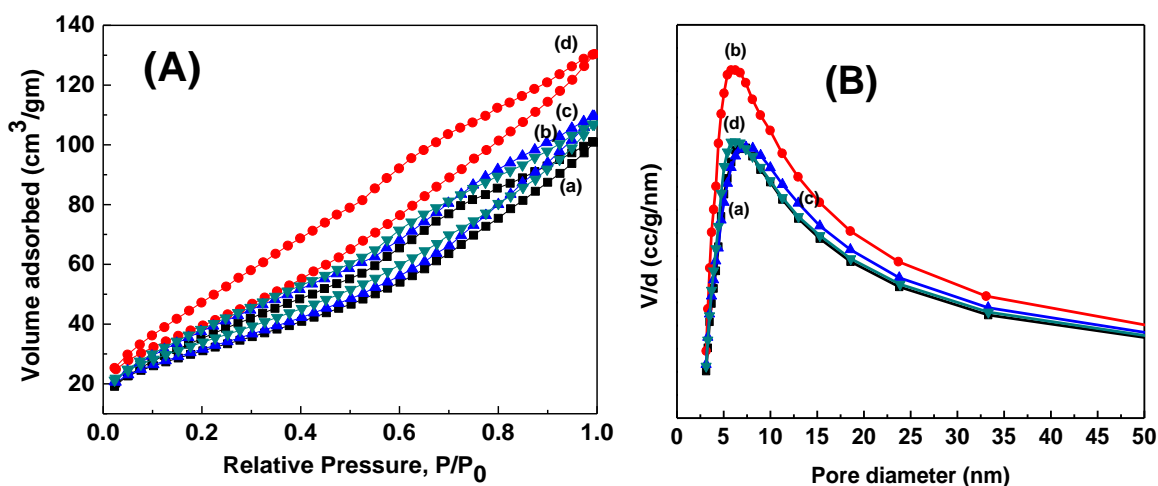


**Fig. 5.7.** (A)  $\text{N}_2$ -sorption isotherms, and (B) BJH pore size distribution curves of (a) 0.5, (b) 1.0, (c) 2.0, and (d) 5 mol%  $\text{Eu}^{3+}$  doped  $\text{CeO}_2$  obtained via conventional refluxing method and calcined at  $500^\circ\text{C}$  for 2 h.

**Table 5.5.** BET surface area, pore volume, and pore size of  $\text{Eu}^{3+}$  doped  $\text{CeO}_2$  samples obtained via conventional refluxing and calcined at  $500^\circ\text{C}$ .

Sample	Surface area ( $\text{m}^2/\text{g}$ )	Pore volume ( $\text{cm}^3/\text{g}$ )	Pore diameter (nm)
0.5EuCeSDS500	112	0.16	5.57
1EuCeSDS500	148	0.20	5.45
2EuCeSDS500	115	0.17	5.90
5EuCeSDS500	123	0.17	5.36

### 5.3.3.2. Effect of calcination temperature

The nitrogen adsorption–desorption isotherms of the 1 mol%  $\text{Eu}^{3+}$  doped  $\text{CeO}_2$  as-prepared and calcined at various temperatures are presented in Fig. 5.8 (A). It was found that all the samples showed an isotherm resemble with type-IV along with hysteresis loop representing the mesoporous structure. It should be also noted that with increasing calcination temperature the isotherms shift downward and the hysteresis loops gradually become small implying a decrease in BET surface area, which might be due to the formation of large interparticle pores. The presence of the hysteresis loop in the sample calcined at  $800^\circ\text{C}$  indicates that the mesoporosity remains intact even at high temperature.

Table 5.6 listed the textural parameters of the samples calculated from nitrogen adsorption–desorption isotherm data. It's notable that the total pore volume and specific surface area for samples decrease where the average pore diameter increased with increasing in the calcination temperature due to the collapse of the mesopores and the subsequent growth of crystallites by the effect of sintering occurring in the material. The surface area and pore volume of the as-prepared sample was  $234 \text{ m}^2\text{g}^{-1}$  and  $0.24 \text{ cm}^3\text{g}^{-1}$  after calcination at  $500^\circ\text{C}$  which slightly decrease to  $148 \text{ m}^2\text{g}^{-1}$  and  $0.21 \text{ cm}^3\text{g}^{-1}$ , but it dropped noticeably to  $59 \text{ m}^2\text{g}^{-1}$  and  $0.11 \text{ cm}^3\text{g}^{-1}$  at  $650^\circ\text{C}$ . With further increase in the calcination temperature to  $800^\circ\text{C}$ , surface area and pore volume of the nanotubes decreased to  $38 \text{ m}^2\text{g}^{-1}$  and  $0.07 \text{ cm}^3\text{g}^{-1}$ , respectively. Tiseanu *et al.* reported a similar trend in variation of surface area along with calcination temperatures in case of  $\text{Eu}^{3+}$ -impregnated  $\text{CeO}_2$  nanocrystals.<sup>32</sup> Fig. 5.8 (B) shows the corresponding pore size distributions of the powders calcined at different temperature. It can be seen that prior to calcination, the nanopowder exhibited a wide pore size distribution which gradually becomes narrower with increasing calcination temperature.

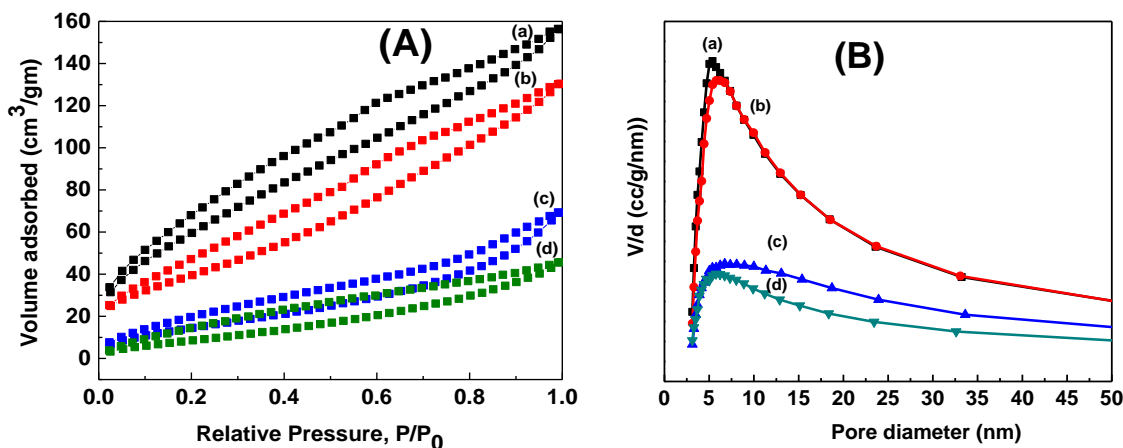


**Fig. 5.8.** (A)  $N_2$ -sorption isotherms and the (B) BJH pore size distribution curves of 1 mol %  $Eu^{3+}$  doped  $CeO_2$  samples, (a) as-prepared and calcined powders at (b)  $500^\circ C$ , (c)  $650^\circ C$ , and (d)  $800^\circ C$  for 2 h, obtained via conventional refluxing.

**Table 5.6.** BET surface area, pore volume, and pore diameter of 1 mol%  $Eu^{3+}$  doped  $CeO_2$  samples calcined at different temperatures.

Sample	Surface area ( $m^2/g$ )	Pore volume ( $cm^3/g$ )	Pore diameter (nm)
1EuCeSDSasp	234	0.24	4.13
1EuCeSDS500	148	0.20	5.45
1EuCeSDS650	59	0.11	7.23
1EuCeSDS800	38	0.07	7.37

### 5.3.3.3. Effect of microwave refluxing

Textural properties of the  $N_2$  adsorption–desorption measurements have been performed on representative samples of 1 mol%  $Eu^{3+}$  doped  $CeO_2$  prepared using SDS via microwave refluxing method and calcined at different temperatures. The corresponding sorption isotherms and pore size distribution curves are shown in Fig. 5.9 (A) and 5.9 (B). It is quite noteworthy to mention that 1EuCeSDSasp or 1EuCeSDS500 exhibited higher surface area value of 234 or  $148\ m^2/g$  than that of the 1EuCeSDSMWasp ( $156\ m^2/g$ ) or 1EuCeSDSMW500 ( $70\ m^2/g$ ). The sample obtained via conventional refluxing method showed the presence of more fractions of mesopores as compared to that of microwave refluxing method, which is reflected from the hysteresis in the relative pressure ( $p/p_0$ ) region of 0.1–0.8. The specific surface area, pore volume, and pore diameter of the nanopowders are given in Table 5.7.

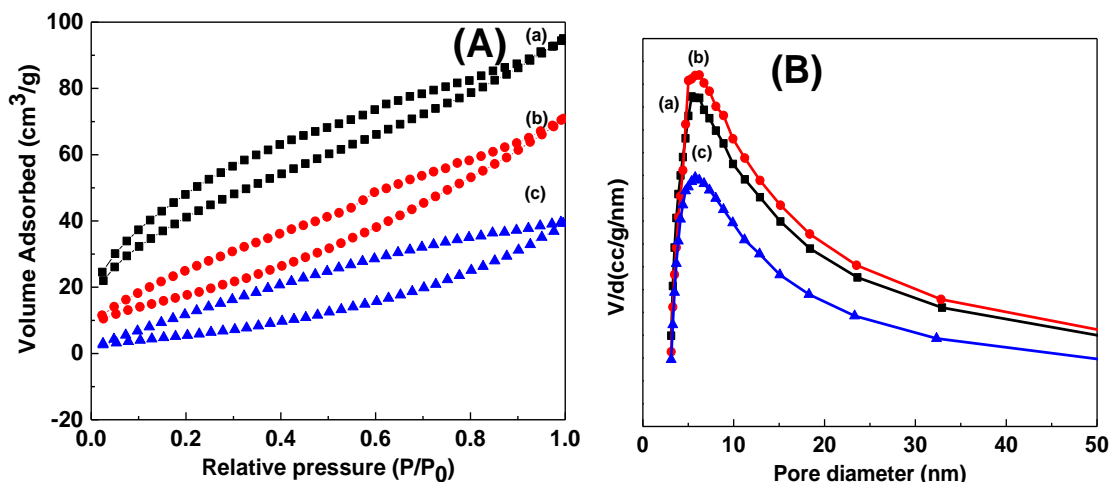


**Fig. 5.9.** (A)  $N_2$ -sorption isotherms, and (B) BJH pore size distribution curves of (a) 1EuCeSDSMWasp, (b) 1EuCeSDSMWasp, and (c) 1EuCeSDSMWasp.

**Table 5.7.** BET surface area, pore volume and pore diameter of 1 mol%  $Eu^{3+}$  doped  $CeO_2$  samples obtained microwave refluxing route.

Sample	Surface area ( $m^2/g$ )	Pore volume ( $cm^3/g$ )	Pore diameter (nm)
1EuCeSDSMWasp	156	0.15	3.77
1EuCeSDSMW500	70	0.11	6.31
1EuCeSDSMW800	53	0.06	9.98

#### 5.3.4. FTIR analysis

In order to find out the surface interaction between the synthesized nanopowder and surfactant molecule both the as-prepared and calcined nanopowders were subjected to Fourier transform infrared (FTIR) analysis. Fig. 5.10 shows FTIR spectra of 1 mol%  $Eu^{3+}$  doped  $CeO_2$  (a) as-prepared and the samples calcined at (b)  $500^\circ C$  and (c)  $650^\circ C$ , obtained via conventional refluxing method. As-prepared nanopowder showed a broad peaks at  $3402\text{ cm}^{-1}$  corresponding to the OH stretching frequency of the surface hydroxyl group and another band around  $1635\text{ cm}^{-1}$  is attributed to the bending vibration of absorbed molecular water. With increasing the calcination temperature, the intensity of the shoulder peaks at  $2922$  and  $2850\text{ cm}^{-1}$  are assigned to the symmetric and asymmetric stretching of the  $CH_2$  groups decreased. It is quite interesting to note that the stretching band of  $SO_4^{2-}$  at  $1245\text{ cm}^{-1}$  still can be observed even after calcination at  $500^\circ C$ . The peaks corresponding to the Ce–O–Ce vibration bands are

observed at 1040 and 1400  $\text{cm}^{-1}$ . The strong absorption band at  $\sim 500 \text{ cm}^{-1}$  is assigned to Ce–O stretching band. The  $\text{CeO}_2$  prepared in the presence of SDS on the other hand shows the typical C–H stretching (3000–2850  $\text{cm}^{-1}$ ) and deformation (1466 and 1380  $\text{cm}^{-1}$ ) bands of the anionic surfactant. The characteristics peaks below 900  $\text{cm}^{-1}$  are designated to Ce–O stretching vibrations for both the as-prepared and calcined nanopowders.

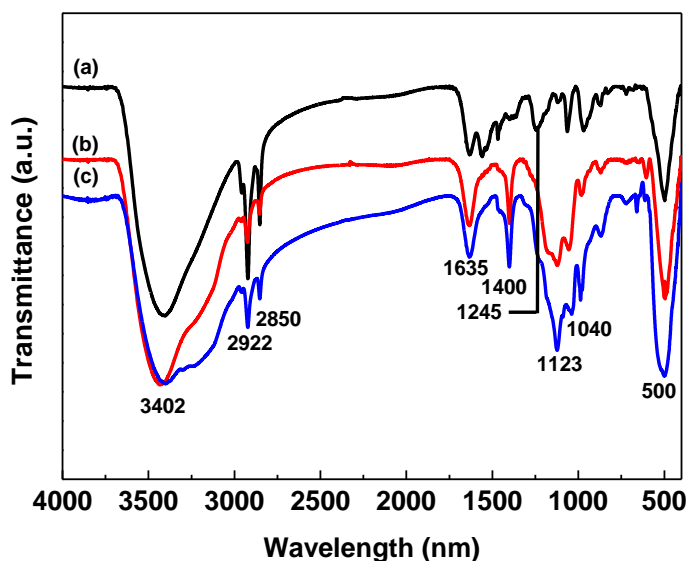


**Fig. 5.10.** FTIR spectra of 1 mol%  $\text{Eu}^{3+}$  doped  $\text{CeO}_2$  (a) as-prepared, and the samples calcined at (b) 500°C, and (c) 650°C.

### 5.3.5. Microstructure analysis

#### 5.3.5.1. FESEM images, EDAX analysis and elemental mapping

The surface morphology, size, and distribution of elements (EELS) of  $\text{Eu}^{3+}$  doped  $\text{CeO}_2$  were investigated using a field emission scanning electron microscope (FESEM). Representative FESEM images of 1 mol%  $\text{Eu}^{3+}$  doped  $\text{CeO}_2$  (a) asp, and the samples calcined at various temperatures of (b) 500°C, (c) 650°C, and (c) 800°C obtained via conventional refluxing methods are displayed in Fig. 5.11. The FESEM micrographs showed spherical-shaped nanoparticles with diameters of about 10-20 nm. The as-prepared nanopowders consist of agglomerated grains of irregular particles. Upon variation of the dopant concentration, no substantial change in the particle morphologies were observed. It is important to note that the particles were less agglomerated even after calcination at a higher temperature of 800°C. So, the present synthesis method is important in synthesizing the  $\text{Eu}^{3+}$  doped  $\text{CeO}_2$  nanoparticles with smaller particle sizes via conventional refluxing methods.

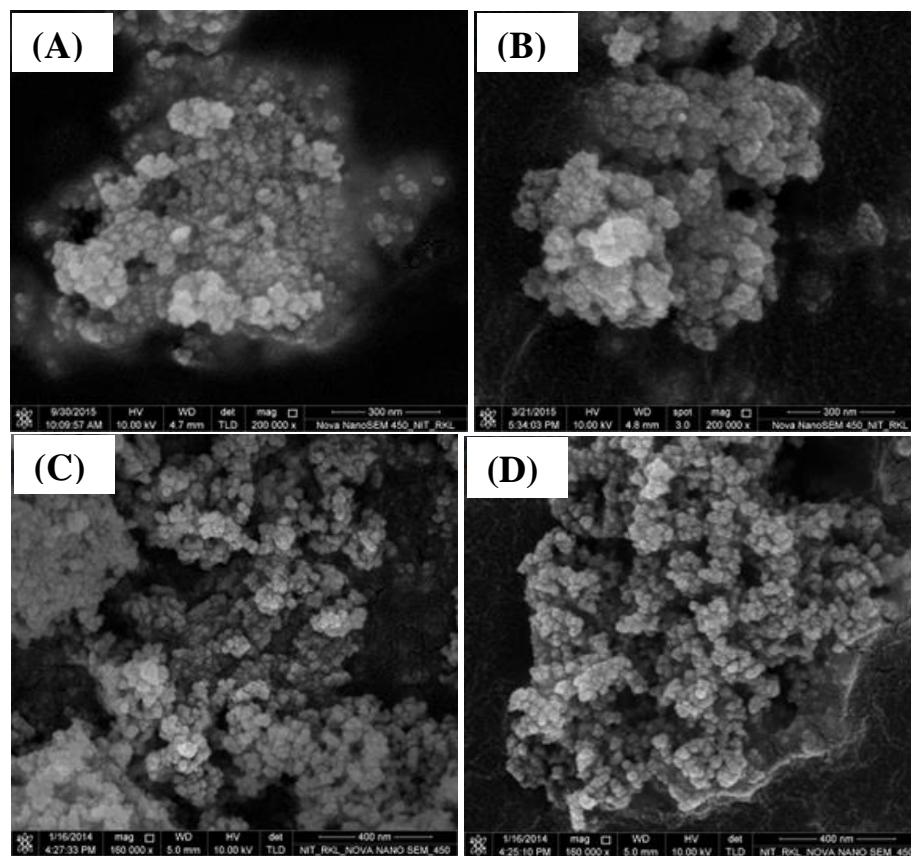


**Fig. 5.11.** FESEM micrographs of 1 mol%  $\text{Eu}^{3+}$  doped  $\text{CeO}_2$ , (A) as-prepared, and the samples calcined at (B) 500°C, (C) 650°C, and (D) 800°C.

Fig. 5.12 show the FESEM images of 0.5, 1.0, 2.0 and 5.0 mol%  $\text{Eu}^{3+}$  doped  $\text{CeO}_2$  calcined at 500°C. The particle sizes are in the range of 6 to 10 nm. To further investigate the morphology and size of the particles, TEM/HRTEM measurements were carried out. The result suggest that  $\text{Eu}^{3+}$  ions are incorporated into the crystal structure. The representative sample 1EuCeSDS500 was further subjected for elemental mapping analysis of selected area shown in Fig 5.13, which clearly depicts the homogeneous distribution of  $\text{Eu}^{3+}$  ions in the  $\text{CeO}_2$  matrix. The energy dispersive X-ray spectrum (EDS) shown in Fig. 5.14, confirms the presence of Ce, Eu, and O in the synthesized nanopowders. The average weight percentage (at.%) of the constituent elements of O, Ce and Eu in 5 mol%  $\text{Eu}^{3+}$  doped  $\text{CeO}_2$  were 15.94, 75.92 and 8.14%, respectively.

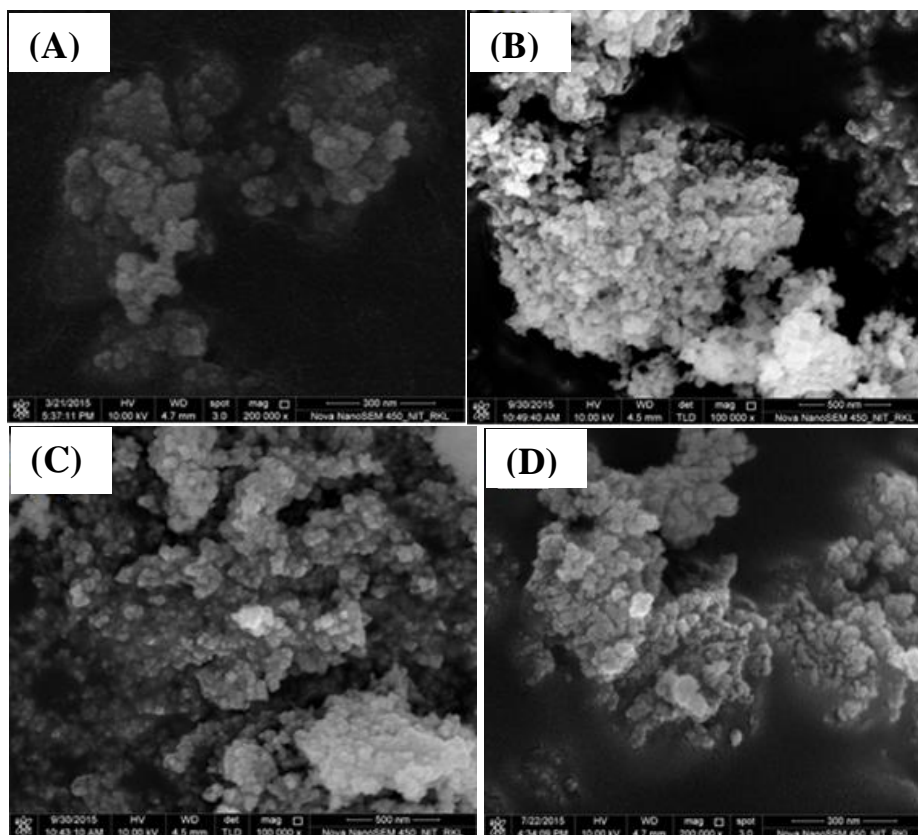


**Fig. 5.12.** FESEM micrographs of (A) 0.5, (B) 1.0, (C) 2.0, and (D) 5 mol% Eu<sup>3+</sup> doped CeO<sub>2</sub> samples obtained via conventional refluxing and calcined at 500°C.

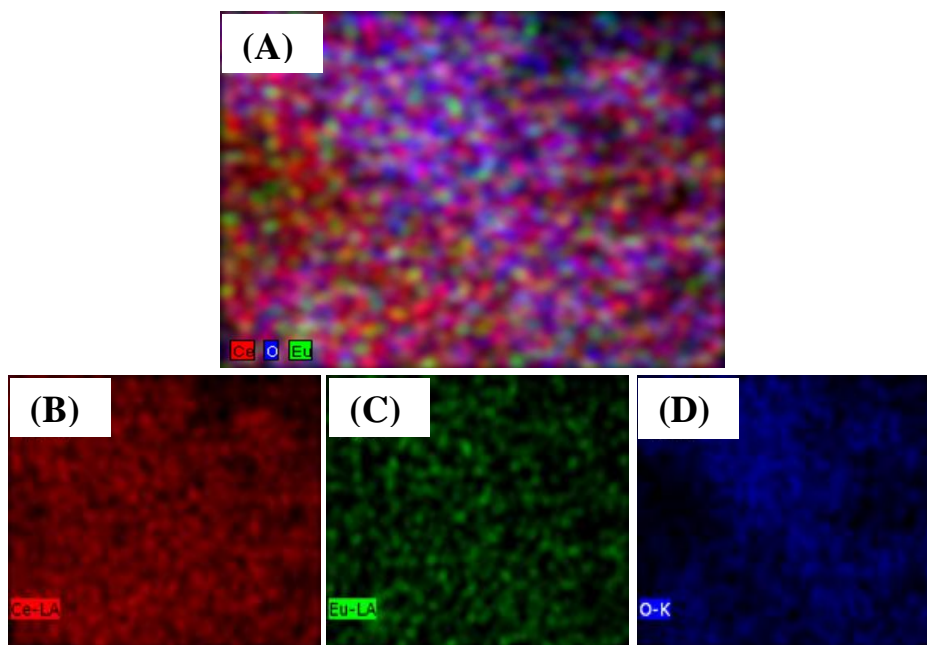


**Fig. 5.13.** Elemental mapping of 1 mol% Eu<sup>3+</sup> doped CeO<sub>2</sub> samples, (A) overall elemental mapping, (B) Ce, (C) Eu, and (D) O.

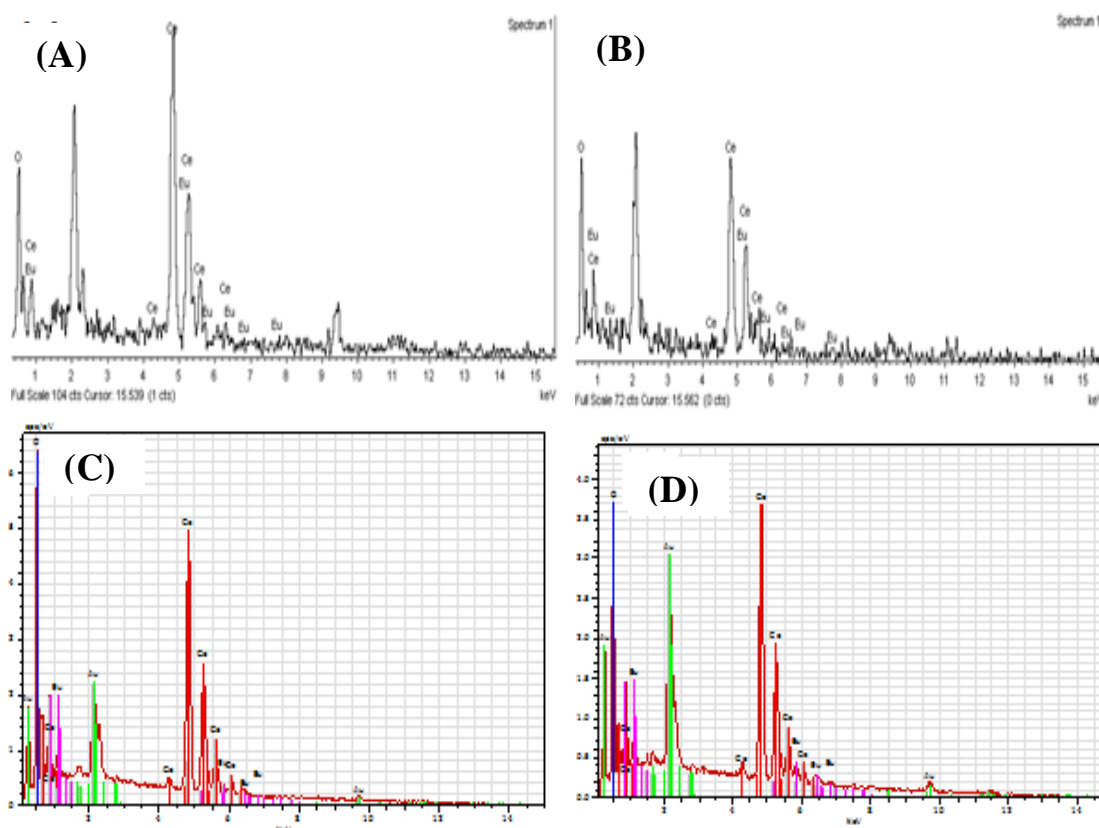


**Fig. 5.14.** EDS of (A) 0.5, (B) 1.0, (C) 2.0, and (D) 5 mol%  $\text{Eu}^{3+}$  doped  $\text{CeO}_2$  calcined at  $500^\circ\text{C}$ .

### 5.3.5.2. TEM and HRTEM image

TEM, and HRTEM image and the corresponding SAED patterns of the representative sample of 1 mol%  $\text{Eu}^{3+}$  doped  $\text{CeO}_2$  obtained via conventional refluxing method and calcined at  $500^\circ\text{C}$  are shown in Fig. 5.15. It was found that the particles are weakly agglomerated, ultrafine, and highly uniform in size with average particle size of 6 nm, which is comparable to the crystallite size calculated from XRD by using Scherer formula. It should be noted that the addition of anionic surfactant (SDS) leads to the reduction of surface tension of the precursor solution, which facilitates nucleation and allows its easier spreading as a result no apparent agglomeration between particles are observed. The high degree of crystallinity was further supported from the HRTEM image composed of well-defined lattice fringes. The HRTEM image clearly shows the existence of elongated and irregular particles along with wormhole like mesopores. A similar TEM image has been obtained by Li *et al.* for flowerlike  $\text{CeO}_2$  microspheres.<sup>33</sup> The “dark pits” observed in the HRTEM image may be due to the rough surface of the synthesized nanoparticle and more surface reconstruction happened in the structure transformation. It is worth noting that many previous reports show rougher



surface of CeO<sub>2</sub> nanostructures resulted in higher catalytic activity because of its increased surface area.<sup>34-36</sup> The interplanar spacing's of the nanoparticle were calculated from the lattice fringes about 0.30 nm, which is in good agreement with the *d*-value of (111) lattice plane obtained from XRD data. This indicates the presence of the (111) exposed faces in the materials. The shape and size of the particles are almost unchanged after calcination at 500°C. The corresponding selected area electron diffraction (SAED) image shows a ring pattern which indicate the highly crystalline nature of both as-synthesized and calcined nanopowder and also could be indexed to the cubic fluorite structure of CeO<sub>2</sub> (JCPDS #34-0394).

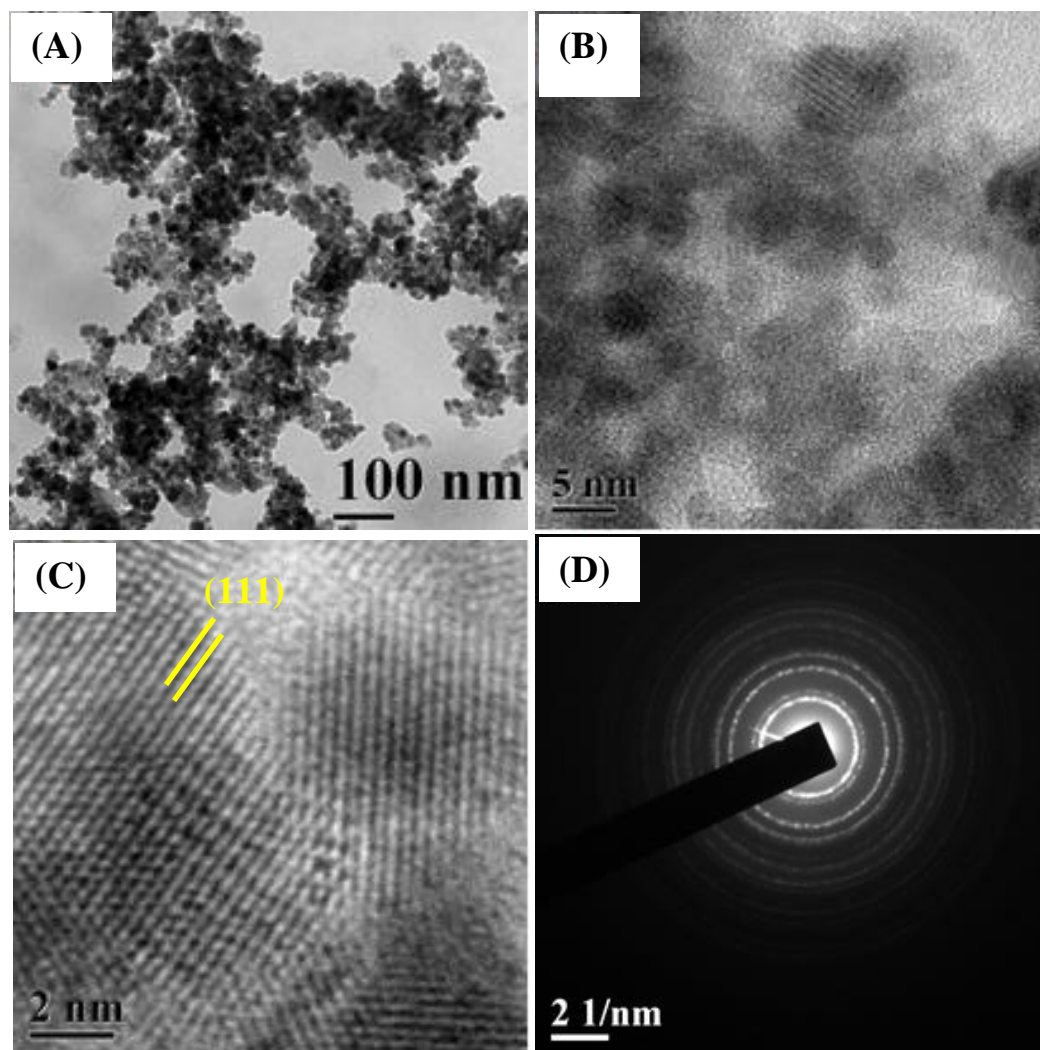


**Fig. 5.15.** (A) TEM, (B) HRTEM image, (C) lattice fringes, and corresponding (D) SAED pattern of 1EuCeSDS500°C.

Fig 5.16 shows the HRTEM image of the (A) 0.5, (B) 1, (C) 2 and (D) 5 mol% of  $\text{Eu}^{3+}$  doped  $\text{CeO}_2$  obtained via conventional refluxing method and calcined at  $500^\circ\text{C}$ . All the sample irrespective of their dopant concentration exhibit lattice fringes throughout the whole particle, which confirmed their highly crystalline nature. The microstructure of the 1 mol%  $\text{Eu}^{3+}$  doped  $\text{CeO}_2$  calcined at  $650^\circ\text{C}$  are shown in Fig. 5.16. It is clear from the figure that the mesoporosity is still well preserved even after calcination at  $650^\circ\text{C}$  temperature, which further confirming the high thermal stability of the mesoporosity. In addition it is also worth noting that the high temperature calcination leads to the more define close hexagonal shape nano particle of particle size 7 nm.

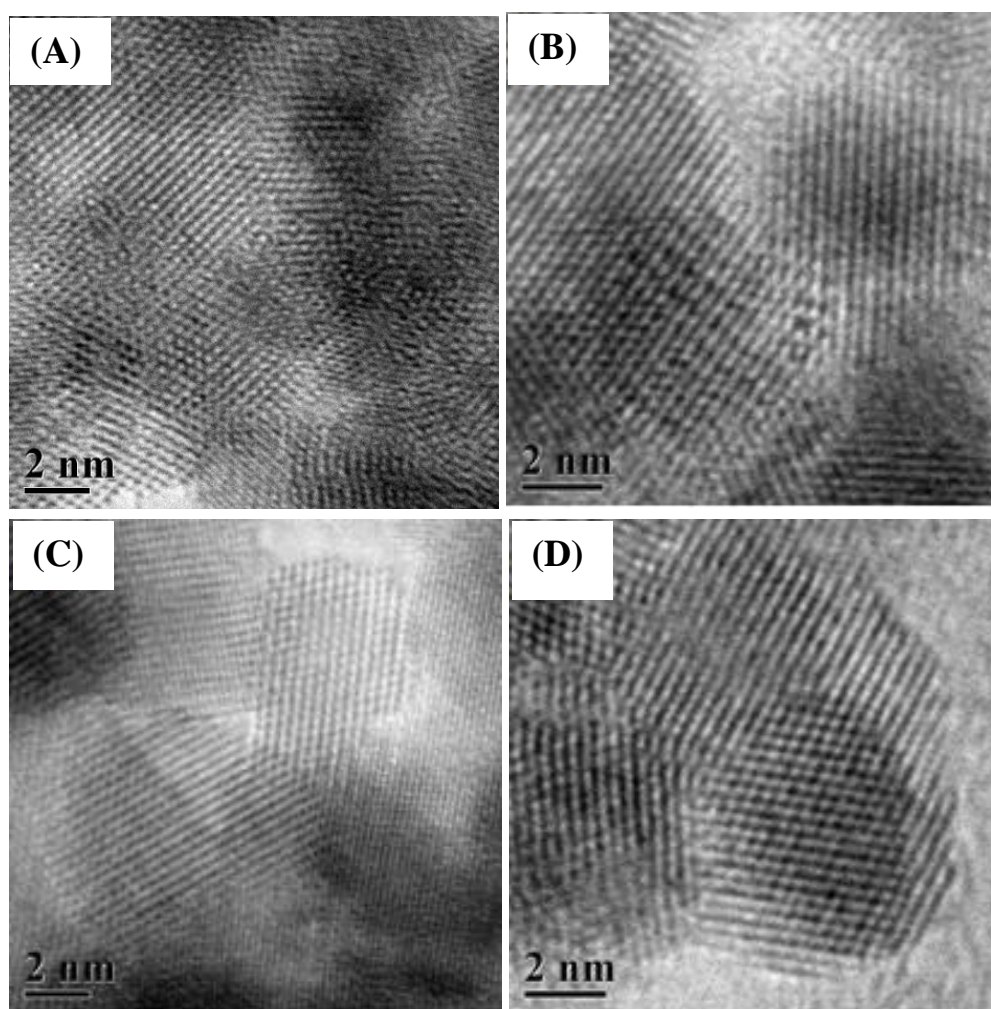


**Fig. 5.16.** HRTEM image and lattice fringes of (A) 0.5, (B) 1, (C) 2, and (D) 5 mol%  $\text{Eu}^{3+}$  doped  $\text{CeO}_2$  samples obtained via conventional refluxing and calcined at  $500^\circ\text{C}$ .

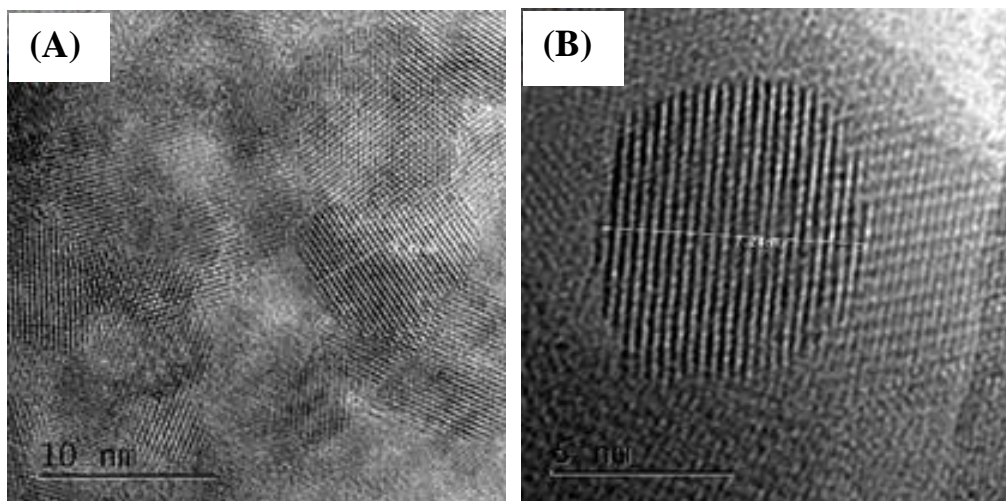


**Fig. 5.17.** HRTEM images of 1EuCeSDS650°C at different magnifications.

### 5.3.6. UV-Vis diffuse reflectance spectroscopic studies

#### 5.3.6.1. Effect of dopant concentration

UV-vis diffuse reflectance spectroscopic study has been conducted to various metal oxides to obtain the information on the surface coordination and different oxidation states of the metal ions. Fig. 5.18 shows the UV-Vis absorbance spectra of europium doped CeO<sub>2</sub> nanopowders by varying the europium concentration after calcination at 500°C for 2 h. All the nanopowders showed an excellent UV-absorption capacity and high transparency in the visible light region. The strong absorption may be due to a charge-transfer transition from O<sub>2</sub> (2p) to the Ce<sup>4+</sup> (4f) orbital in CeO<sub>2</sub>.<sup>37</sup> The absorption bands at 235, 276 nm and 347 nm are attributed to the O<sup>2-</sup>→Ce<sup>3+</sup> and O<sup>2-</sup>→Ce<sup>4+</sup> charge transfer (CT), and interband transitions, respectively.<sup>38,39</sup> It can be seen that 1 mol % Eu<sup>3+</sup> doped CeO<sub>2</sub> samples showed greater red shifts as compared to the other samples. This might be due to the presence of large numbers of oxygen vacancies, smaller particle size or smaller amount of Ce<sup>3+</sup> ions on the surface. Bandgap values for the 0.5, 1, 2 and 5 mol % Eu<sup>3+</sup> doped CeO<sub>2</sub> calcined at 500°C obtained via conventional refluxing method are 2.59, 2.64, 2.66 and 2.64 eV, respectively. Table 5.8 presents the corresponding band gap values calculated from Kubelkamonk plot, which showed that the energy gaps of all the materials are comparable.

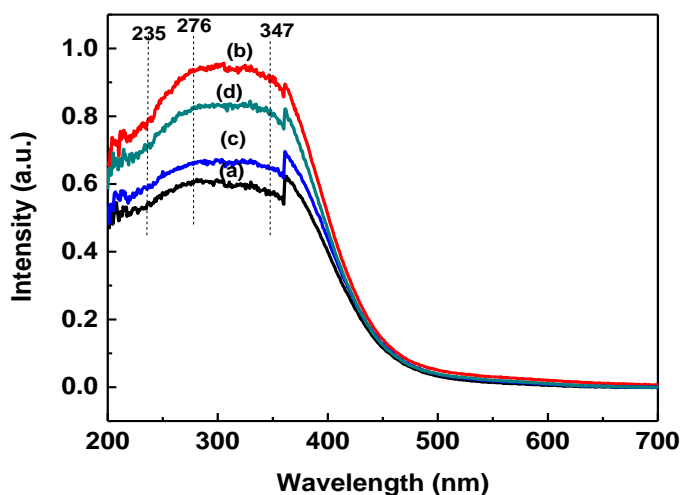


**Fig. 5.18.** UV-vis absorbance spectra of (a) 0.5, (b) 1, (c) 2 and (d) 5 mol %  $\text{Eu}^{3+}$  doped  $\text{CeO}_2$  calcined at  $500^\circ\text{C}$  for 2 h.

### 5.3.6.2. Effect of calcination temperatures

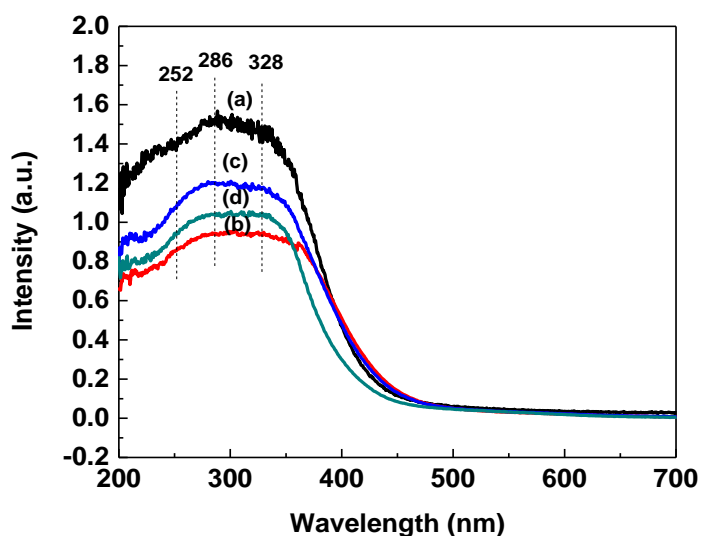


**Fig. 5.19.** UV-vis absorbance spectra of  $\text{Eu}^{3+}$  doped  $\text{CeO}_2$  powders obtained via conventional refluxing method, (a) as-prepared and calcined at (b)  $500^\circ\text{C}$  (c)  $650^\circ\text{C}$ , and (d)  $800^\circ\text{C}$  for 2 h.

**Table 5.8.** Bandgap energy of (a) 0.5, (b) 1, (c) 2 and (d) 5 mol %  $\text{Eu}^{3+}$  doped  $\text{CeO}_2$  obtained in conventional reflux method and calcined at  $500^\circ\text{C}$  for 2 h.

Eu dopant Conc.	Band gap energy (eV)
0.5	2.59
1	2.64
2	2.66
5	2.64

UV-vis absorption spectra of the  $\text{Eu}^{3+}$ -doped  $\text{CeO}_2$  samples as-prepared and calcined at different temperatures are shown in Fig. 5.19. All the samples have intense absorption in the UV region ( $<400$  nm), of the spectrum. The absorption of  $\text{CeO}_2$  in the UV-Vis region is due to the charge transfer transition between O 2p and Ce 4f bonds. The UV spectrum of all the samples exhibited three prominent peaks around 252, 286 nm and 328 nm. The absorption band at 252 nm corresponds to  $\text{Ce}^{3+}$  variety present which is caused by  $\text{Ce}^{3+} \leftarrow \text{O}^{2-}$  in the system. The peak at 328 nm arises due to inter band transition in ceria, and the band at 280 nm is assigned to  $\text{Ce}^{4+} \leftarrow \text{O}^{2-}$  charge transfer transitions.<sup>37</sup>

The bandgap energies were calculated to be 2.81, 2.64, 2.83, and 2.94 eV for  $\text{Eu}^{3+}$  doped  $\text{CeO}_2$  as-prepared, and calcined at 500, 650 and 800°C, respectively. These values are smaller than the values for the bulk  $\text{CeO}_2$  (3.08 eV),<sup>40</sup>  $\text{CeO}_2$  microspheres (2.81 eV), and  $\text{CeO}_2$  microflowers (3.08 eV).<sup>41</sup> This shows that  $\text{Eu}^{3+}$ -doping can shift the absorption edge of  $\text{CeO}_2$  to the visible light range and narrow the band-gap as can be seen from Table 5.9. This may be beneficial for improving the photoabsorption performance of  $\text{Eu}^{3+}$ -doped  $\text{CeO}_2$  and enhance its photocatalytic performance. The redshift of optical band gap of the cerium oxide ( $\text{CeO}_x$ ) films was correlated with the increase of  $\text{Ce}^{3+}$  content at the grain boundary.<sup>42</sup> Chen *et al.* also observed a blueshift of band gap due to the valence transition of  $\text{Ce}^{3+}$  - $\text{Ce}^{4+}$  induced by thermal annealing.<sup>43</sup> The quantum-size effect is expected to enhance the band gap of the materials with decreasing particle size due to the higher localization of energy bands.<sup>42</sup> The content of  $\text{Ce}^{3+}$  and oxygen vacancies decreased with growth of the  $\text{CeO}_2$  nanoparticles during annealing in air atmosphere. So, the blueshift of  $E_g$  in our  $\text{Eu}^{3+}:\text{CeO}_2$  samples with increasing calcination temperatures is due to the decrease in  $\text{Ce}^{3+}$  content, not due to the results of the quantum-size effect. The results also suggest that the  $\text{Eu}^{3+}$  doping in  $\text{CeO}_2$  has induced higher concentration of  $\text{Ce}^{3+}$ .

### 5.3.6.3. $\text{Eu}^{3+}$ doped $\text{CeO}_2$ obtained via microwave refluxing

The 1 mol%  $\text{Eu}^{3+}$  doped  $\text{CeO}_2$  particles obtained via microwave refluxing method also exhibited strong UV absorption below 400 nm. Fig. 5.20 show the UV-visible absorption spectra of both (a) asp and calcined nanopowders at various temperatures of (b) 500, (c) 650, and (d) 800°C for 2 h. It can be seen that a similar trend of bandgap variation with calcination temperatures were observed as in case of  $\text{Eu}^{3+}$  doped  $\text{CeO}_2$  obtained via conventional

refluxing method. It is to be noted that the absorbance spectra of 1 mol%  $\text{Eu}^{3+}$  doped  $\text{CeO}_2$  calcined at  $500^\circ\text{C}$  obtained via both conventional and normal refluxing methods exhibited red shifts as compared to the as-prepared and other calcined samples. The bandgap energies were 2.78, 2.66, 2.69, and 2.94 eV for  $\text{Eu}^{3+}$  doped  $\text{CeO}_2$  as-prepared, and calcined at 500, 650 and  $800^\circ\text{C}$ , respectively (see Table 5.9). Close similarities of the absorption spectra of 1 mol%  $\text{Eu}^{3+}$  doped  $\text{CeO}_2$  samples prepared via both the conventional and microwave refluxing methods revealed that there is no significant influence of the preparative methods on the UV-Vis absorption properties of the samples.

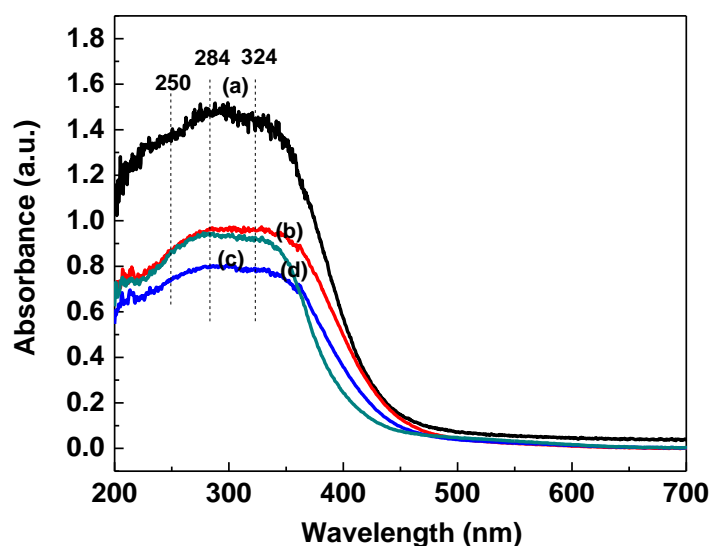


**Fig. 5.20.** UV-Vis absorbance spectra of 1 mol%  $\text{Eu}^{3+}$  doped  $\text{CeO}_2$  powders obtained via microwave refluxing method, (a) as-prepared and calcined at (b)  $500^\circ\text{C}$ , (c)  $650^\circ\text{C}$ , and (d)  $800^\circ\text{C}$  for 2 h.

**Table 5.9.** Bandgap energy of  $\text{Eu}^{3+}$  doped  $\text{CeO}_2$  powders obtained by conventional and microwave refluxing methods.

Asp and calcined samples at	Band gap energy (eV) of 1mol% $\text{Eu}^{3+}$ dope $\text{CeO}_2$	
	Conventional refluxing method	Microwave refluxing method
Asp	2.81	2.78
$500^\circ\text{C}$	2.64	2.66
$650^\circ\text{C}$	2.83	2.69
$800^\circ\text{C}$	2.94	2.94

### 5.3.7. PL analysis

#### 5.3.7.1. Effect of calcination temperature

The excitation and emission spectra of 1 mol%  $\text{Eu}^{3+}$  doped  $\text{CeO}_2$  nanocrystals (a) as-prepared, and calcined at (b) 500, (c) 650 (d) 800 and 1000°C are illustrated in Fig. 5.21 (A) and (B). Upon excitation at 335 nm, emission spectra exhibited three main peaks centered at 590, 608, and 630 nm, which corresponds to the  $^5\text{D}_0 \rightarrow ^7\text{F}_1$ ,  $^5\text{D}_0 \rightarrow ^7\text{F}_2$  and  $^5\text{D}_0 \rightarrow ^7\text{F}_3$  transitions, respectively. The dominance of the magnetic dipole allowed  $^5\text{D}_0 \rightarrow ^7\text{F}_1$  emission over the electric dipole  $^5\text{D}_0 \rightarrow ^7\text{F}_2$  emission indicate that the  $\text{Eu}^{3+}$  ions occupy lattice sites with inversion centers. It can be seen that the sharp peaks in the emission spectra for all the nanopowders are located in the same position irrespective of their calcination temperatures, but the relative peak intensities increases with increasing the calcination temperatures.

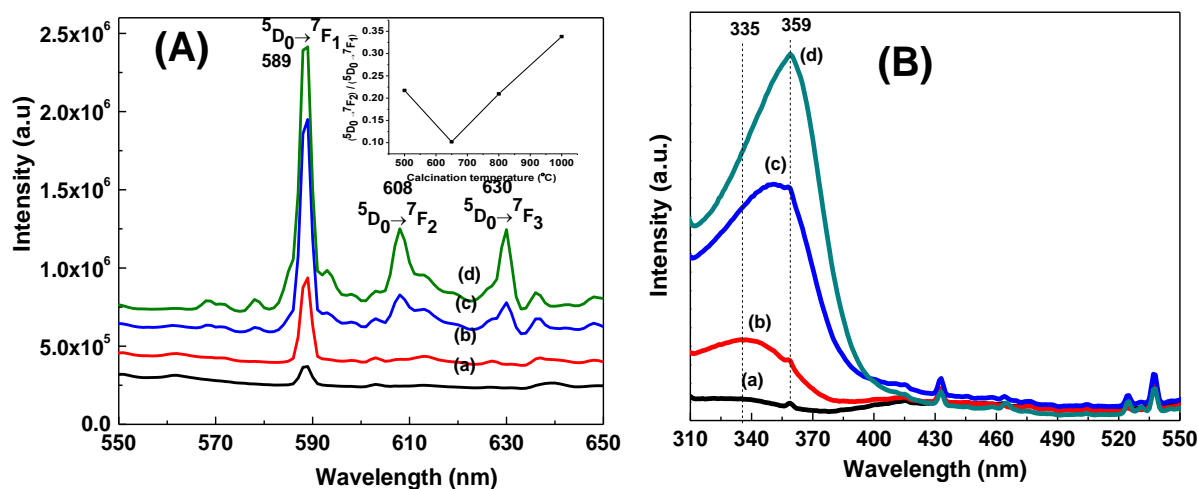


**Fig. 5.21.** PL (A) emission and (B) excitation spectra of  $\text{Eu}^{3+}$  doped  $\text{CeO}_2$  obtained in conventional refluxing method, and calcined at (a) 500°, (b) 650°C, (c) 800°C, and (d) 1000°C for 2 h.

The as-prepared sample showed very weak luminescence due to their high surface-to-volume ratio of nanoparticles which leads to the quenching defects on the surface. Upon increasing the calcination temperatures the crystallinity of the nanopowders is enhanced. As a result surface-to-volume ratio would be decreased and finally the luminescence quenching defects will be eliminated. The position and relative intensities of the two emission peaks indicate the local geometry of the guest ion ( $\text{Eu}^{3+}$ ) in the host molecule. The variation of asymmetry ratio  $I(^5\text{D}_0 \rightarrow ^7\text{F}_2)/I(^5\text{D}_0 \rightarrow ^7\text{F}_1)$  with the calcination temperatures are shown in the

inset of Fig. 5.21(A). It should be noted that asymmetric ratio initially decreased upon increasing the calcination temperatures from 500 to 650°C and then show a linear increase till 1000°C. This might be attributed to the change in symmetry of the crystal field around  $\text{Eu}^{3+}$  during calcination. A similar trend was found by Krishna *et al.* in case of  $\text{Y}_2\text{O}_3:\text{Eu}^{3+}$  nanophosphor.<sup>44</sup>

Fig. 5.21(B) shows the excitation spectra of the 1 mol%  $\text{Eu}^{3+}$  doped  $\text{CeO}_2$  samples calcined at different temperatures. The excitation spectra was obtained by monitoring the  $^5\text{D}_0 \rightarrow ^7\text{F}_1$  emission peak at 589 nm. It was found that all the nanopowders showed a broad excitation bands within 320-360 nm range, which may be arises due to the charge transfer transition from  $\text{O}^{2-}$  to  $\text{Ce}^{4+}$ .<sup>45-48</sup> In addition the absorption intensity of the broad band is increases gradually with increasing the calcining temperatures. At the same time it should be also noted that the peak position shifts toward the higher wavelength side with calcination temperature. This might be due to the change of local environment around the  $\text{O}^{2-}$  surroundings during the calcination. A similar peak shift was observed upon calcination for  $\text{Y}_2\text{O}_3:\text{Eu}^{3+}$  nanophosphor prepared by a low temperature solution combustion method.<sup>44</sup>

### 5.3.7.2. Effect of dopant concentration

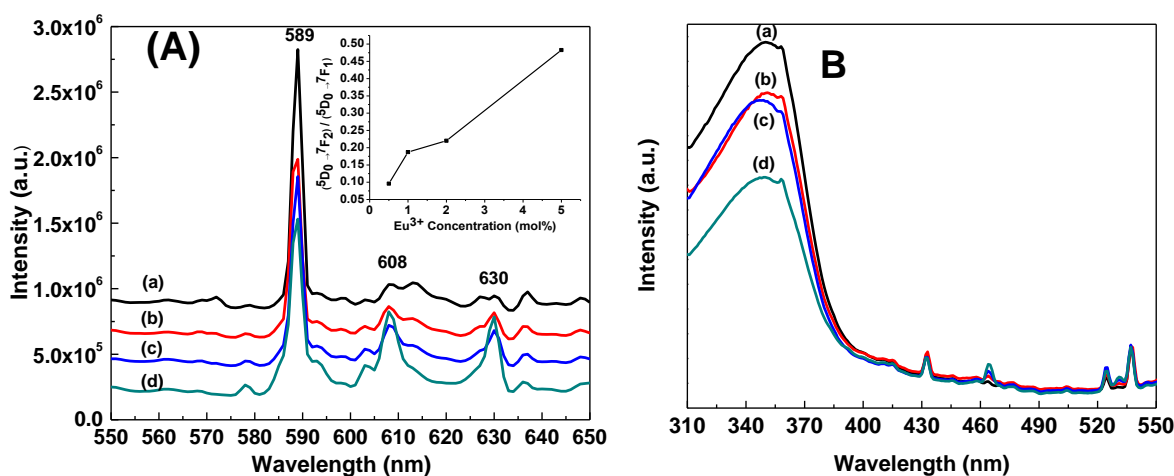


**Fig. 5.22.** PL (A) emission and (B) excitation spectra of (a) 0.5, (b) 1, (c) 2, and (d) 5 mol %  $\text{Eu}^{3+}$  doped  $\text{CeO}_2$  obtained via conventional refluxing method and calcined at 800°C for 2 h.

The emission spectra of 0.5%, 1.0%, 2.0% and 5%, and 10%  $\text{Eu}^{3+}$  doped  $\text{CeO}_2$  annealed at 800°C for 2 h were recorded upon excitation at 335 nm and shown in Fig. 5.22(A). It has been observed that the intensity of magnetic dipole transition  $^5\text{D}_0 \rightarrow ^7\text{F}_1$



centered at 589 nm decreases with increasing the  $\text{Eu}^{3+}$  concentrations, whereas the intensity of electric dipole  ${}^5\text{D}_0 \rightarrow {}^7\text{F}_2$  transition around 610–630 nm increases. The local symmetry around  $\text{Eu}^{3+}$  in the  $\text{CeO}_2$  host lattice were examined by the emission intensity ratio between the red emission transition  ${}^5\text{D}_0 \rightarrow {}^7\text{F}_2$  (608 nm) and the orange emission transition  ${}^5\text{D}_0 \rightarrow {}^7\text{F}_1$  (591 nm) (asymmetry ratio, R/O), and shown in the inset. It was found that the asymmetry ratio (R/O) increases with increasing the  $\text{Eu}^{3+}$  concentration. The results are in well accordance with the previous reports.<sup>46</sup> This is ascribed to the low  $\text{Eu}^{3+}$  doping concentrations and the  $\text{Eu}^{3+}$  ions mainly occupy the sites with inversion symmetry, while at high  $\text{Eu}^{3+}$  doping concentrations the % of the Eu occupying the sites without inversion symmetry is increased.

The PL excitation spectra of  $\text{Eu}^{3+}$  doped  $\text{CeO}_2$  phosphors calcined at  $800^\circ\text{C}$  for 2 h with different doping concentration of  $\text{Eu}^{3+}$  are illustrated in Fig. 5.22(B). The spectra were measured by monitoring the  ${}^5\text{D}_0 \rightarrow {}^7\text{F}_1$  transition at 589 nm. It can be seen that all the nanocrystals exhibited strong broad bands with a maximum at 330 nm which is attributed to the charge transfer from  $\text{O}^{2-}$  to  $\text{Ce}^{4+}$ .<sup>49,50</sup> From these spectra, it is clear that the  $\text{CeO}_2$  host lattice able to transfer the excitation energy to the emitted level of  $\text{Eu}^{3+}$  ions to cause the characteristic red emission of  $\text{Eu}^{3+}$  in the nanophosphors. With an increase in the  $\text{Eu}^{3+}$  doping concentration, it can be seen that the position of the absorption maxima remain unaltered. It is noteworthy that the intensity of the excitation bands decreases with increasing the  $\text{Eu}^{3+}$  concentration from 0.5 to 5 mol %, which may be due to the concentration quenching of  $\text{Eu}^{3+}$  emission caused by cross-relaxation and energy migration among  $\text{Eu}^{3+}$  ions.<sup>51</sup>

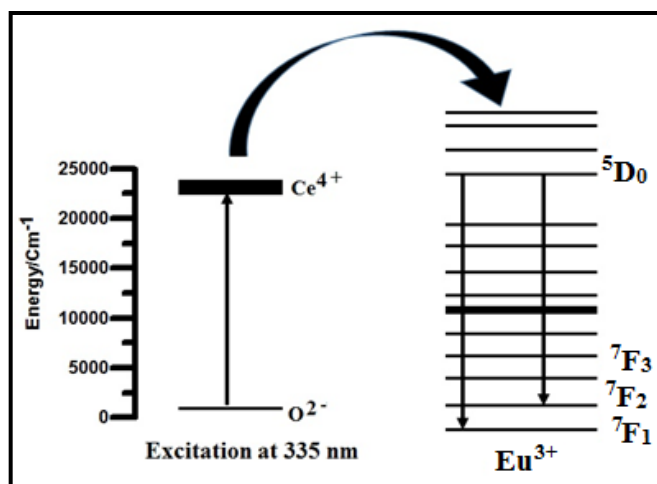
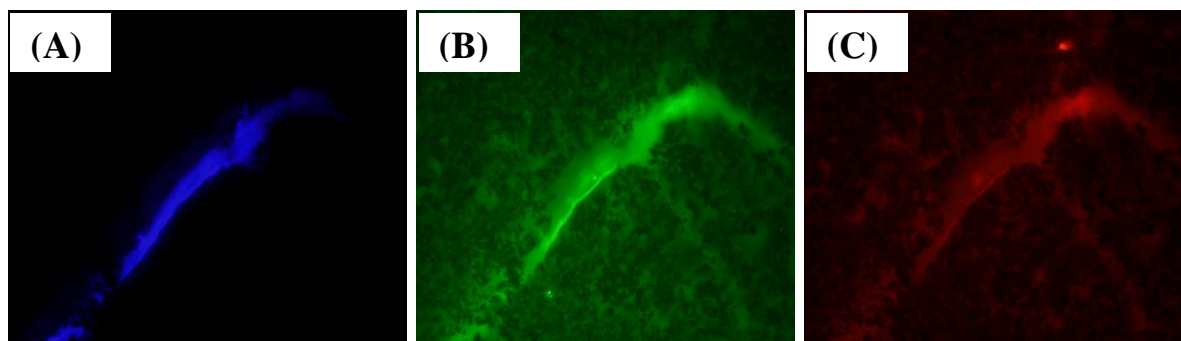


Fig. 5.23. Energy transfer mechanism from  $\text{CeO}_2$  host to  $\text{Eu}^{3+}$  ions.

The energy level scheme of the emissions of  $\text{Eu}^{3+}$  doped  $\text{CeO}_2$  nanocrystals is depicted as Fig. 5.23. On excitation by UV light, energy is absorbed by the host molecule of  $\text{CeO}_2$  via charge transfer transition from  $\text{O}^{2-}$  (2p) valence band to  $\text{Ce}^{4+}$  (4f). Then this energy is directly transferred to the 4f orbitals of the guest molecule of  $\text{Eu}^{3+}$ . Finally the characteristic emissions of  $\text{Eu}^{3+}$  are produced as a result of the population of  $^5\text{D}_0$  level.

### 5.3.7.3. Fluorescent microscopy images



**Fig. 5.24 (A-C)** Fluorescent microscope images of 1 mol%  $\text{Eu}^{3+}$  doped  $\text{CeO}_2$  obtained via conventional refluxing method, and calcined at  $800^\circ\text{C}$ , excited at wavelengths of (A) 350 nm, (B) 405 nm, and (C) 532 nm.

Optical properties of the representative sample of 1 mol%  $\text{Eu}^{3+}$  doped  $\text{CeO}_2$  obtained via conventional refluxing method and calcined at  $800^\circ\text{C}$  was further investigated under a fluorescent microscope upon exciting at various wavelengths. The fluorescent microscopy images [Fig. 5.24 A-C] of the sample exciting at three different wavelengths of 350, 405 and 532 nm exhibits distinct color emission upon excitation at different wavelength. So, the results indicate that the multicolored emissions from the prepared  $\text{Eu}^{3+}$  doped  $\text{CeO}_2$  can be achieved by exciting the material at different wavelengths.

### 5.3.8. XPS analysis

The chemical compositions of nano  $\text{CeO}_2$  were verified by means of XPS analysis which confirm the co-existence of both the oxidation states following the reactions of  $4\text{CeO}_2 \rightarrow 2\text{Ce}_2\text{O}_3 + \text{O}_2$  or  $\text{Ce}^{4+} + e^- \rightarrow \text{Ce}^{3+}$ .  $\text{Eu}^{3+}$  doped  $\text{CeO}_2$  samples calcined at  $500^\circ\text{C}$  were mounted on a carbon tape for XPS analysis and the peak positions were charge-corrected with respect to C 1s core level as a baseline (284.6 eV). The general XPS survey scan shown in Fig. 5.25, which revealed that no peaks of other elements except C, Ce, Eu and O were

observed. The high-resolution Ce 3d spectra of the nanopowder after deconvolution were fitted with ten peaks which arises from three doublets resulting from the  $\text{Ce}^{4+}$  state designated as  $u$ ,  $u''$ ,  $u'''$ ,  $v$ ,  $v''$ ,  $v'''$  and two doublets resulting from the  $\text{Ce}^{3+}$  state designated as  $u_0$ ,  $u'$ ,  $v_0$ ,  $v'$  are shown in Fig. 5.25. The Ce3d photoelectron spectra are complicated because of the hybridization involving in the final state of the Ce4f orbitals with O2p orbitals and fractional occupancy of the valence 4f orbitals. The amount of  $\text{Ce}^{3+}$  were calculated from the integrated area under the corresponding peak  $\text{Ce}^{3+}/(\text{Ce}^{3+}+\text{Ce}^{4+})$  ratio. By comparing these results with pure  $\text{CeO}_2$  shown in previous chapter, it was found that  $\text{Eu}^{3+}$  doping into the  $\text{CeO}_2$  host lattice leads to the more percentage of  $\text{Ce}^{3+}$ . Thorat *et al.* reported that the concentration of  $\text{Ce}^{3+}$  increases linearly with Eu addition for  $\text{Eu}^{3+}$  doped  $\text{CeO}_2$  nanocrystals synthesized by simple solvothermal process.<sup>52</sup>

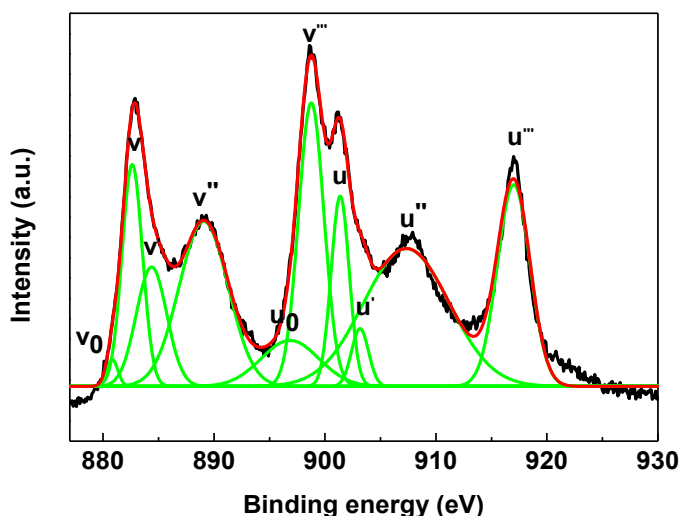


**Fig. 5.25.** High resolution XPS spectrum of the Ce 3d core level regions for the 1 mol%  $\text{Eu}^{3+}$  doped  $\text{CeO}_2$  obtained via conventional refluxing method and calcined at  $500^\circ\text{C}$  for 2 h.

From the XPS analysis of  $\text{Eu}^{3+}$  doped  $\text{CeO}_2$  nanoparticles, Kumar *et al.* observed that the concentration of  $\text{Ce}^{3+}$  increases from 18.3% for 1 mol%  $\text{Eu}^{3+}$  dopant to 23.5% for 30 mol%  $\text{Eu}^{3+}$  dopant and decreased with annealing temperature.<sup>13</sup> Babu *et al.* also pointed out that the concentration of  $\text{Ce}^{3+}$  increases on doping with  $\text{Eu}^{3+}$  but decreases on annealing.<sup>53</sup> In contrast many author has also report the decrease of the  $\text{Ce}^{3+}$  fraction on the surface of  $\text{CeO}_2$  upon doping as for example Wang *et al.* noticed that when  $\text{Eu}^{3+}$  was doped in the  $\text{CeO}_2$  nanocrystals the amount of  $\text{Ce}^{3+}$  ion decrease on the surface which might be due to the

replacement of  $\text{Ce}^{3+}$  by trivalent  $\text{Eu}^{3+}$  ions.<sup>1,54</sup> Hence, both the pure and europium doped ceria nanopowder obtained in our synthetic route, possess a relative large amount of  $\text{Ce}^{3+}$  21.3 and 22.9% respectively, which might be facilitated them for chemical and catalytic applications.

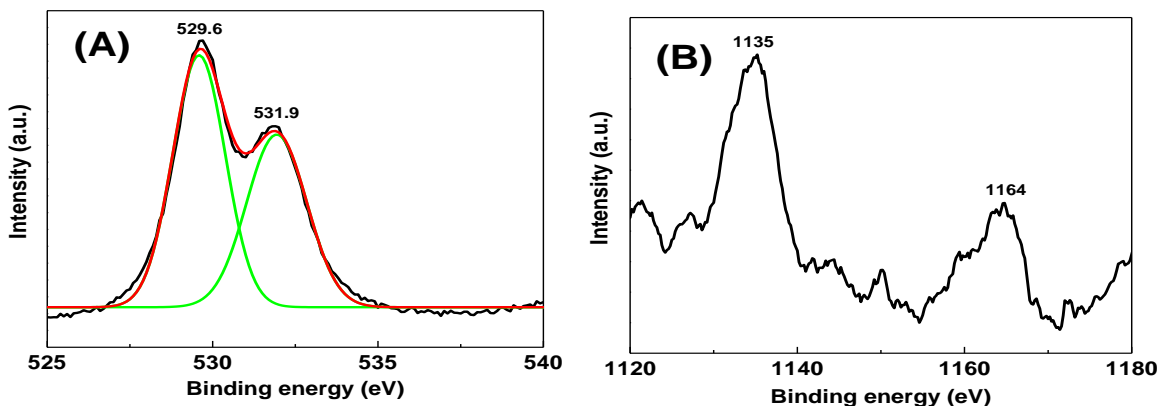


**Fig. 5.26.** High resolution XPS spectra of the (A) O1s and (B) Eu 3d core level regions for the 1 mol%  $\text{Eu}^{3+}$  doped  $\text{CeO}_2$  obtained via conventional refluxing and calcined at  $500^\circ\text{C}$  for 2 h.

The high resolution O1s core levels spectra derived after deconvolution by XPS curving fitting are shown in Fig. 5.26(a). The analysis revealed that the spectrum was decomposed into two separated peaks. The main peak at higher binding energy centered at 529.6 eV corresponds to the lattice oxygen of the  $\text{Eu}^{3+}$  doped  $\text{CeO}_2$  whereas the shoulder peak located at 531.9 eV could be attributed to surface hydroxyl species or ambient moisture.<sup>55</sup> When  $\text{Eu}^{3+}$  was doped into  $\text{CeO}_2$ , the XPS result of O1s spectra shows that the lattice oxygen peak position and its broadness are considerably different than that of pure ceria as shown in previous chapter, this can be attributed to the variation in the chemical environment of the Ce–O bond after the addition of dopant into the host lattice. It was also notably found that the oxygen peak at the higher binding energy for Eu doped sample was more intense than that of the pure  $\text{CeO}_2$ , which might be to its higher surface area and pore volume. The presence of  $\text{Eu}^{3+}$  ions in  $\text{Eu}^{3+}$  doped  $\text{CeO}_2$  nanocrystals were also recognized by xps analysis and the respective high resolution Eu 3d spectra are shown in Fig. 5.26(b). The characteristic peaks of  $\text{Eu}3d_{3/2}$  and  $\text{Eu}3d_{5/2}$  peaks are observed correspond to the binding energy at 1107.4 and 1080.45 eV, respectively. Hence, these XPS analysis clearly confirms that europium ions in the  $\text{CeO}_2$  lattices existed in the form of trivalent ions and no peak was observed in the region of  $1124\pm 1$  eV ( $\text{Eu}^{2+} 3d_{5/2}$ ) and  $1153\pm 1$  eV ( $\text{Eu}^{2+} 3d_{3/2}$ ), corresponding to the  $\text{Eu}^{+2}$ .

### 5.3.9. H<sub>2</sub>-TPR analysis

The reducibility of oxygen species present in the representative sample of 1 mol% Eu<sup>3+</sup> doped CeO<sub>2</sub> obtained via conventional refluxing method and calcined at 500°C for 2 h were extensively characterized by H<sub>2</sub>-TPR analysis and the corresponding profiles are shown in Fig. 5.27 (A). It was found that the deconvoluted H<sub>2</sub>-TPR profile of Eu<sup>3+</sup> doped CeO<sub>2</sub> showed two stages of reduction processes. A broad peak centered at 465°C followed by a sharp peak at 531°C is arising from the surface-capping oxygen and the bulk oxygen, respectively. H<sub>2</sub> -TPR values of 1 mol% Eu<sup>3+</sup> doped CeO<sub>2</sub> nanopowders are 9.29 and 54.64 mL/g. Comparison of the relative intensity of peak I to peak II, it is clear that the reduction of bulk oxygen at the higher temperatures are dominated compared to that of the reduction of surface oxygen at lower temperatures. The low-temperature H<sub>2</sub> consumptions was registered on the H<sub>2</sub> TPR profile for Eu<sup>3+</sup> doped CeO<sub>2</sub> as compared to that of the pure CeO<sub>2</sub>. In addition, the corresponding hydrogen consumption was far higher than that of pure CeO<sub>2</sub> and this improvement in the redox behavior might be due to the lattice distortion occurred in CeO<sub>2</sub> host lattice when Eu<sup>3+</sup> is incorporated. The generation of the reactive oxygen species is strongly facilitated, which could be reduced easily by hydrogen at low temperatures. This observation is consistent with many previous studies. For example, Han *et al.* also reported that the reducing temperature greatly decreased after the copper deposition on bare CeO<sub>2</sub>.<sup>56</sup>

According to Rao *et al.* when Ni<sup>2+</sup> is incorporated into the CeO<sub>2</sub> lattice caused to charge unbalance and lattice distortion. As a result, very reactive oxygen species are generated, which could be reduced easily by hydrogen at low temperatures.<sup>57</sup> Silva *et al.* also observed that the reduction peaks of Sm<sup>3+</sup> doped CeO<sub>2</sub> shift to lower temperatures with increasing Sm content.<sup>58</sup> Kuntaiah *et al.* found that the incorporation of Sm<sup>3+</sup> into the CeO<sub>2</sub> lattice strongly modified the reduction behaviour of CeO<sub>2</sub> by shifting the surface and bulk reduction to lower temperatures.<sup>59</sup> Reddy *et al.* noticed that the incorporation of Pr into the CeO<sub>2</sub> lattice creating a pathway for oxygen diffusion.<sup>60</sup> This would promote the oxygen ion diffusion from the bulk to the surface, enabling the bulk reduction at low temperatures. In our previous work discussed in chapter IV, we have also observed the same reducibility enhancement of CeO<sub>2</sub> by doping with Sm<sup>3+</sup> ion.<sup>61</sup> The XRD patterns also showed an increase of lattice parameter with Eu addition in fluorite structure of CeO<sub>2</sub> host lattice. This increase in lattice parameter contributed to the structural distortion, and these findings are well agreement with the H<sub>2</sub> TPR result.

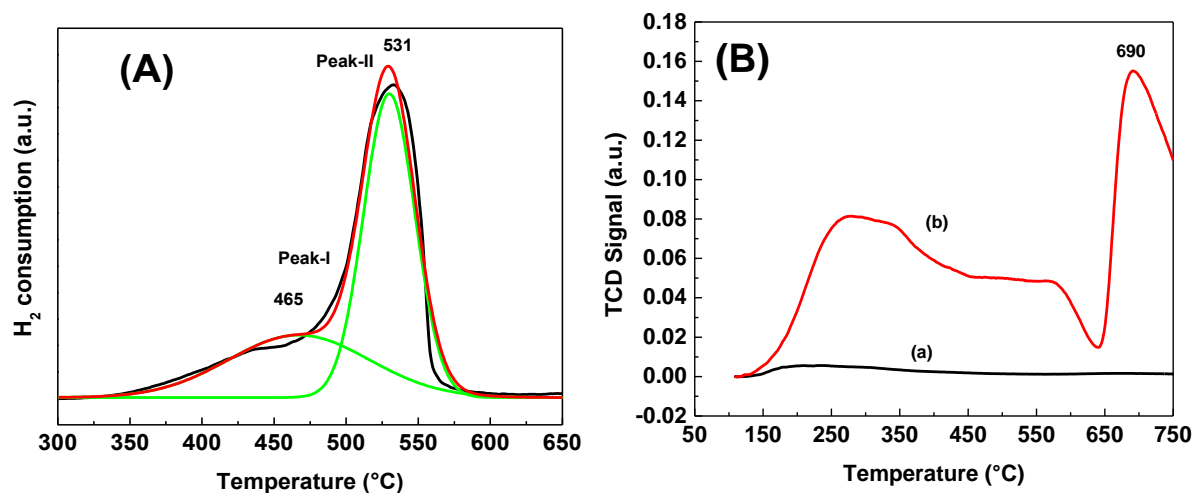


**Fig. 5.27.** (A) H<sub>2</sub> consumption as a function of temperature, and (B) NH<sub>3</sub>-TPD profiles for (a) pure CeO<sub>2</sub> and (b) 1 mol% Eu<sup>3+</sup> doped CeO<sub>2</sub> calcined at 500°C for 2 h.

### 5.3.10. NH<sub>3</sub>-TPD analysis

Surface acidity of the representative sample 1 mol% Eu<sup>3+</sup> doped CeO<sub>2</sub> obtained via conventional refluxing method and calcined at 500°C was investigated by means of NH<sub>3</sub>-TPD analysis and the corresponding pattern are shown in Fig. 5.27(B). The ammonia desorption proceeds via two stages signify that the presence of acid sites of different strength, a wide peak with a broad shape was found in the ammonia desorption patterns at the temperature range of 100–600°C, which mainly due to the successive desorption of physisorbed ammonia to weak Bronsted acidic sites.<sup>62</sup> The other sharp peak at 690°C assigned to the strong Lewis acid position.<sup>62</sup> It is also noticeable that the ammonia adsorption intensity at the Lewis acid sites was shown to be more prominent than the Brönsted acid sites. The comparative analysis along with the pure CeO<sub>2</sub> is shown in Fig. 5.27(B) revealed that the Eu doping induce the ammonia desorption peak area increase which suggests that the doping increase the acid strength in the nanocrystal.

## 5.4. Conclusion

CeO<sub>2</sub> nanopowders with 0.5%, 1.0%, 2.0%, and 5 mol% Eu<sup>3+</sup> were successfully synthesized by using inorganic precursors and sodium dodecyl sulphate as a template at a lower temperature of 100°C via both conventional and microwave refluxing methods. XRD data revealed that both the as-prepared as well as the calcined Eu<sup>3+</sup>-doped CeO<sub>2</sub> nanopowders are highly crystalline. The incorporation of Eu<sup>+3</sup> into CeO<sub>2</sub> was confirmed by EDS analysis.

N<sub>2</sub> sorption isotherm indicated mesoporous structure of the nanopowders with a high surface area and narrow pore size distribution. The FESEM micrograph showed spherical-shaped nanoparticles with diameters of about 10-20 nm. The results revealed that calcination temperature plays a significant role to create individual particles with less agglomeration. No substantial change in the particles morphologies and sizes were observed on varying the dopant concentration (Eu<sup>3+</sup>). The TEM, HRTEM image and the corresponding SAED pattern of the representative sample were also taken. It was found that the samples are weakly agglomerated, ultrafine, highly uniform nanocrystals with averaged particle size of 5–7 nm which is comparable to the crystallite size calculated from XRD by using Scherrer formula. The high degree of crystallinity was further supported from the HRTEM images composed of well-defined lattice fringes.

## References

1. Z. Wang, Z. Quan and J. Lin. *Inorg. Chem.*, 2007, 46, 5237.
2. G. K. Das and T. T. Y. Tan. *J. Phys. Chem. C*, 2008, 112, 11211.
3. M. Wang, J. L. Liu, Y. X. Zhang, W. Hou, X. L. Wu and S. K. Xu. *Mater. Lett.*, 2009, 63, 325.
4. S. S. Chang and M. S. Jo, *Ceramics International*, 2007, 33, 511.
5. K. Binnemans, *Chem. Rev.*, 2009, 109, 4283.
6. C. Sun, H. Li and L. Chen, *Energy Environ. Sci.*, 2012, 5, 8475.
7. M. Asadullah, K. Tomishige and K. Fujimoto. *Catal. Commun.*, 2001, 2, 63.
8. L. Qian, J. Zhu, W. Du and X. Qian. *Mater. Chem. Phys.*, 2009, 115, 835.
9. K. Sohlberg, S. T. Pantelides and S. F. Pennycook. *J. Am. Chem. Soc.*, 2001, 123, 6609.
10. P. Jasinski, T. Suzuki and H. U. Anderson. *Sensors Actuators B Chem.*, 2003, 95, 73.
11. F. Goubin, X. Rocquefelte, M. H. Whangbo, Y. Montardi, R. Brec and S. Jobic. *Chem Mat.*, 2004, 16, 662.
12. D. G. Shchukin and R. A. Caruso, *Chem Mat.*, 2004, 16, 2287.
13. A. Kumar, S. Babu, A. S. Karakoti, A. Schulte and S. Seal, *Langmuir*, 2009, 25, 10998.
14. G. Blasse and B.C. Grabmaier, *Luminescent Materials*, Springer, Berlin, 1994.
15. S. Patil, S. Reshetnikov, M. Haldar and S. Seal, *J. Phys. Chem. C*, 2007, 111, 8437.
16. L. Li, J. Tao, H. Pan, H. Chen, X. Wu, F. Zhu, X. Xu and R. Tang, *J. Mater. Chem.*, 2008, 18, 5363.
17. J. Wu, G. L. Wang, D. Y. Jin, J. L. Yuan, Y. F. Guan and J. Piper, *Chem. Commun.*, 2008, 3, 365.
18. R. D. Shannon, *Acta Crystallogr. Sect. A: Cryst. Phys., Diffraction, Theor. Gen. Crystallogr.* 1976, A32, 751.
19. P. F. Smet, J. E. V. Haecke, F. Loncke, H. Vrielinck, F. Callens and D. Poelman, *Phys. Rev. B - Condens. Matter Mater. Phys.*, 2006, 74, 035207.
20. M. Nogami and Y. J. Abe, *Non. Cryst. Solids*, 1996, 197, 73.
21. X. H. Liu, S. J. Chen and X. D. Wang, *J. Lumin.*, 2007, 127, 650.

22. L. Li, H. K. Yang, B. K. Moon, Z. Fu, C. Guo, J. H. Jeong, S. S. Yi, K. Jang and H. S. Lee, *J. Phys. Chem. C*, 2009, 113, 610.
23. B. D. Cullity, *Elements of X-ray Diffraction*, 2nd edition, Addison-Wesley, London, 1978,
24. K. M. Ryan, J. P. McGrath, R. A. Farrell, W. M. O'Neill, C. J. Barnes and M. A. Morris, *J. Phys. Condens. Matter.*, 2003, 15, L49.
25. V. Thorat, T. Ghoshal, P. Carolan, J. D. Holmes, and M. A. Morris, *J. Phys. Chem. C*, 2014, 118, 10700.
26. T. Dhannia, S. Jayalekshmia, M.C. S. Kumar, T. P. Rao and A. C. Bose, *J. Phy. Chem. Solids*, 2010, 71, 1020.
27. S. Deshpande, S. Patil, S. V. N. T. Kuchibhatla and S. Seal, *Appl. Phys. Lett.*, 2005, 87, 133113.
28. M. Leonim, R. D Maggio, S. Polizzi and P. J. Scardi, *J. Am. Ceram. Soc.*, 2004, 87, 1133.
29. R. Tiana, F. Zhaoa, F. Chen and C. Xia, *Solid State Ionics.*, 2011, 192, 580.
30. F. Rouquerol, J. Rouquerol and K. Sing, *Academic Press*, London, 1999.
31. M. Rose, W. Böhlmann, M. Sabo and S. Kaskel, *Chem. Commun.*, 2008, 2462.
32. C. Tiseanu, V. I. Parvulescu, M. S. Dominguez and M. Boutonnet, *J. Appl. Phys.*, 2012, 112, 013521.
33. H. Li, G. Lu, Q. Dai, Y. Wang, Y. Guo, and Y. Guo, *ACS Appl. Mater. Interfaces*, 2010, 2, 838.
34. X. Liang, X. Wang, Y. Zhuang, B. Xu, S. M. Kuang and Y. D. Li, *J. Am. Chem. Soc.*, 2008, 130, 2736.
35. X. Liu, K. Zhou, L. Wang, B. Wang and Y. Li, *J. Am. Chem. Soc.*, 2009, 131, 3140.
36. K. B. Zhou, X. Wang, X. Sun, Q. Peng and Ya. Li, *J. Catal.*, 2005, 229, 206.
37. Y. W. Zhang, R. Si, C. S. Liao, C. H. Yan, C. X. Xiao and Y. Kou, *J. Phys. Chem. B*, 2003, 107, 10159.
38. A. Bensalem, F. B. Verduraz, M. Delamar and G. Bugli, *Appl. Catal, A Gen.*, 1995, 121, 81.
39. K. N. Rao, P. Bharali, G. Thrimurthulu and B.M. Reddy, *Catal. Commun.*, 2010, 11, 863.
40. C. Ho, J. C. Yu, T. Kwong, A. C. Mak and S. Lai, *Chem. Mater.*, 2005, 17, 4514.
41. H. Wu and L. Wang, *Catal. Commun.*, 2011, 12, 1374.
42. P. Patsalas, S. Logothetidis, L. Sygellou and S. Kennou, *Phys. Rev. B: Condens. Matter Mater. Phys.*, 2003, 68, 35104.
43. M. Y. Chen, X. T. Zua, X. Xiang and H. L. Zhang, *Physica B*, 2007, 389, 263.
44. R. H. Krishna, B. M. Nagabhushana, H. Nagabhushana, N. S. Murthy, S. C. Sharma, C. Shivakumara, and R. P. S. Chakradhar, *J. Phys. Chem. C*, 2013, 117, 1915.
45. Y. Sohn, *J. Am. Ceram. Soc.*, 2013, 96, 3747.
46. S. Shi, M. Hossu, R. Hall and W. Chen, *J. Mater. Chem.*, 2012, 22, 23461.
47. L. Li, S. Zhou and S. Zhang, *Chem. Phys. Lett.*, 2008, 453, 283.
48. S. Fujihara and M. Oikawa, *J. Appl. Phys.* 2004, 95, 8002.
49. S. Tsunekawa, T. Fukuda and A. Kasuya, *J. Appl. Phys.*, 2000, 87, 1318
50. J. Liu, Z. Zhao, Y. S. Chen, C. M. Xu, A. J. Duan and G. Y. Jiang, *Catal. Today*, 2011, 175, 117.
51. A. J. Kenyon, *Quantum Electron.*, 2002, 26, 225.
52. A. V. Thorat, T. Ghoshal, P. Carolan, J. D. Holmes and M. A. Morris, *J. Phys. Chem. C*, 2014, 118, 10700.
53. S. Babu, A. Schulte, and S. Seal, *Appl. Phys. Lett.*, 2008, 92, 123112.
54. Z. L. Wang, G. R. Li, Y. N. Ou, Z. P. Feng, D. L. Qu, and Y. X. Tong, *J. Phys. Chem. C*, 2011, 115, 351.



55. E. Abiaad, R. Bechara, J. Grimblot and A. Aboukais, *Chem. Mater.*, 1993, 5, 793.
  56. J. Han, H. J. Kim, S. Yoon and H. Lee, *J. Mol. Catal. A: Chemical.*, 2011, 335, 82.
  57. P. V. R. Rao, V. P. Kumar, G. S. Rao and K. V. R. Chary, *Catal. Sci. Technol.*, 2012, 2, 1665.
  58. A. G. M. Silva, T. S. Rodrigues, A. Dias, H. V. Fajardo, R. F. Gonçalves, M. Godinhob and P. A. R. Dutenhofner, *Catal. Sci. Technol.*, 2014, 4, 814.
  59. K. Kuntaiah, P. Sudarsanam, B. M. Reddy and A. Vinu, *RSC Adv.*, 2013, 3, 7953.
  60. B. M. Reddy, G. Thrimurthulu, L. Katta, Y. Yamada and S.E. Park, *J. Phys. Chem. C.*, 2009, 113, 15882.
  61. B. Mandal, A. Mondal, S. S. Ray and A. Kundu, *Dalton Trans.*, 2016, 45, 1679.
  62. S. K. Mehera, M. Cargnello, H. Troiani, T. Montini, G. R. Rao and P. Fornasiero, *Appl. Catal. B Environ.*, 203, 130–131, 121.
-

## Chapter 6

# Applications of Pure and Doped CeO<sub>2</sub> Nanopowders for Environmental Remediation

**Outline:** This chapter examines an efficient adsorption process of the prepared high surface area mesoporous samaria doped ceria (CeO<sub>2</sub>:Sm<sup>3+</sup>) nanopowders for the removal of Cr(VI) ions from aqueous solutions. The effects of contact time, initial sorbate concentration, pH and dose of adsorbent on Cr(VI) adsorption were studied to optimize the conditions for maximum adsorption. The kinetics of the adsorption has been studied. Both Langmuir and Freundlich models were fitted well with the adsorption data. The mesoporous CeO<sub>2</sub>:Sm<sup>3+</sup> are demonstrated to be effective materials for removing toxic Cr(VI) ions from aqueous solutions. In addition, CeO<sub>2</sub>:Sm<sup>3+</sup> nanopowders were also successfully used as remarkably efficient new photocatalysts for degradation of a representative azo dye Acid Orange 7 (AO7) in aqueous medium under natural sunlight without addition of any external reagents like peroxides, acid or base. The effects of calcination temperature, pH of the medium, catalyst dosage and irradiation time on the decolorization of AO7 were investigated and discussed in this chapter. Sm<sup>3+</sup> doping in CeO<sub>2</sub> narrowed the band gap and significantly enhanced the photocatalytic degradation of the azo dye. The photocatalytic degradation of AO7 is also investigated by using certain radical scavengers and the results suggest that under solar-light irradiation predominantly positive holes and super oxide radicals (O<sup>2•-</sup>) act as the active species in the degradation process. We have also monitored the anti-oxidation performances with H<sub>2</sub>O<sub>2</sub> of mesoporous pure CeO<sub>2</sub> and defect engineered Sm<sup>3+</sup> doped CeO<sub>2</sub>. To evaluate the autocatalytic activity of the prepared mesoporous Sm<sup>3+</sup> doped CeO<sub>2</sub>, we have carried out UV-visible transmission spectroscopic studies both in the absence and in the presence of H<sub>2</sub>O<sub>2</sub> (an oxidant). Our results suggest these materials developed here are promising alternative solar light sensitive photocatalyst and also appears to be potential candidates for biomedical (antioxidant) applications.

## 6.1. Effective adsorption of hazardous Cr(VI) ions in aqueous environment

### 6.1.1. Introduction

Inorganic heavy metal ions and organic dyes removal have attracted great research attention due to their long term environmental toxicity and health hazard. Among heavy metal contaminants, chromium has been a major focus in wastewater management. Large quantities of chromium are discharged into the environment from a variety of industries such as electroplating, steel fabrication, paints and pigments, mining, leather tanning, textile dyeing, aluminum conversion coating operations, plants producing industrial inorganic chemicals and wood treatment units. Among three oxidation states of chromium [Cr(II), Cr(III) and Cr(VI)] in nature, only the last two species are stable.<sup>1,2</sup> Cr(VI) is known to be 500 times more toxic, mutagenic and carcinogenic than Cr(III) due to its solubility in water almost in the whole pH range and its larger mobility than that of Cr(III).<sup>3,4</sup> Many diseases such as epigastric pain, nausea, vomiting, severe diarrhea, corrosion of skin, respiratory tract and lungs carcinoma may causes from Cr(VI).<sup>5-8</sup> Its toxicity also include cancer as well as kidney, liver and gastric damages.<sup>9</sup> Due to environmental concern, discharge limits of Cr(VI) have been investigated by most industrial countries. The guideline for drinking water prescribed by the US environmental protection agency for Cr(VI) is 100 µg/L.<sup>10</sup> Conventional methods applied for Cr(VI) removal are mainly chemical precipitation, oxidation/ reduction, filtration, ion exchange, membrane separation and adsorption.<sup>11</sup> Chemical precipitation produces great amounts of mud, whilst ion exchangers and membrane separations are relatively of very high cost.<sup>11,12</sup> Adsorption is the most effective and versatile technique for removing chromium owing to its advantages, such as availability of varieties of adsorbent materials with high efficiency at a relatively lower cost.<sup>13</sup> Although activated carbon is one of the most popular adsorbents for removal of metal ions,<sup>11,13</sup> but enormous attention has been given towards achieving higher removal efficiencies with much cheaper and abundant materials. The development of new and more effective tailor-made adsorbents has become essential to suit these demanding applications.

Due to their high surface area and porosity nanoporous inorganic oxide based adsorbents like magnetic MCM-41, ZrO<sub>2</sub>, CeO<sub>2</sub>, etc., have been used for adsorption and removal of toxic heavy metal Cr(VI) from aqueous solutions. CeO<sub>2</sub> is one of the most

abundant and cost effective among rare earth metal oxides. CeO<sub>2</sub> possesses the lowest solubility against acid among the rare earth metal oxides and can be regenerated chemically with simultaneous quantitative recovery of the adsorbate material. The larger surface area of hetero structured CeO<sub>2</sub> may explain both higher removal capacities and faster adsorption rate. In particular, porous CeO<sub>2</sub> nanostructure enhances the spatial dispersion, which results in not only higher surface area but also facile mass transportation of molecules to the active sites. In many environmental remediation applications, CeO<sub>2</sub> had demonstrated a high adsorption capacity for hazardous anions, such as fluoride,<sup>14</sup> bichromate,<sup>15,16</sup> and arsenate.<sup>17,18</sup>

Recently, tremendous efforts have been focused on the excellent Cr(VI) ions removal capacities of CeO<sub>2</sub>. Xiao *et al.*<sup>16</sup> reported maximum Cr(VI) adsorption capacity of 6.76 mgg<sup>-1</sup> by the hierarchical CeO<sub>2</sub> nanocrystal microspheres with surface area of 65 m<sup>2</sup>g<sup>-1</sup>, prepared via a nonaqueous sol-gel method by reacting cerium nitrate hydrate with benzyl alcohol at 120°C. But the removal efficiency of these microspheres was not affected by the pH value. Recently, Zhong *et al.*<sup>17</sup> also reported the removal of toxic ions from water with higher removal capacity than bulk materials by flowerlike CeO<sub>2</sub>. However, their outstanding adsorption performance could only be exhibited in case of the low pH value (ca. pH 3). CeO<sub>2</sub> hollow nanospheres with a surface area of 72 m<sup>2</sup>g<sup>-1</sup> synthesized by a template-free microwave-assisted hydrothermal method showed an excellent adsorption capacity for Cr(VI) of 15.4 mg.g<sup>-1</sup>.<sup>18</sup> It can be seen from the previous reports that CeO<sub>2</sub> has been used as a good adsorbent for Cr(VI), however, there are only limited reports on its Cr(VI) removal effect and most of them possess lower surface area.<sup>16,17</sup>

Introduction of dopants in to the CeO<sub>2</sub> lattice enhances the adsorption capacity of the material.<sup>19,20</sup> Copper containing ceria adsorbents have also been developed in recent years for the removal of H<sub>2</sub>S and SO<sub>x</sub> from flue gas, natural gas and coal derived gas.<sup>19</sup> Li and Stephanopoulos<sup>21</sup> stated that the CuO-CeO<sub>2</sub> system, containing equal molar parts of CuO and CeO<sub>2</sub>, is efficient sorbent for high temperature gas desulfurization. Mayernick *et al.*<sup>22</sup> reported that the addition of La<sup>3+</sup> and Tb<sup>3+</sup> to CeO<sub>2</sub> results in the presence of stoichiometric oxygen vacancies and also lowers the energy to form additional oxygen vacancies (reduction of Ce<sup>4+</sup> to Ce<sup>3+</sup>) hence enhance the sulfur adsorption process. Oxygen vacancies may serve as active sites for surface adsorption and dissociation of H<sub>2</sub>S. Furthermore, Lim *et al.*<sup>23</sup> revealed that Sm-doped CeO<sub>2</sub> (SDC) coated Ni/YSZ may serve as a more effective sulphur adsorbent than

CeO<sub>2</sub>. It is well known that the concentration of oxygen vacancies can be remarkably enhanced after doping with Sm, due to Sm<sup>3+</sup> → Ce<sup>4+</sup> substitutions. The presence of adjustable porosity and high specific surface area of Sm<sup>3+</sup> doped CeO<sub>2</sub> would be beneficial for metal ion adsorption owing to the increase in the amount and density of the adsorption sites.

Herein, the application of high surface area (184 m<sup>2</sup>g<sup>-1</sup>) 1 mol% Sm<sup>3+</sup> doped CeO<sub>2</sub> nanoparticles (described in details in chapter IV), synthesized through a simple low temperature surfactant (sodium dodecyl sulphate; SDS) assisted chemical route, for Cr(VI) ion removal along with its adsorption mechanisms are discussed. We have investigated the chromium adsorption property as a function of contact time, pH, adsorbent dosage and adsorbate concentration.

### 6.1.2. Experimental condition of Cr(VI) adsorption

100 mgL<sup>-1</sup> of Cr(VI), stock solution was prepared by dissolving 0.2834 g of K<sub>2</sub>Cr<sub>2</sub>O<sub>7</sub> in 1000 mL of deionized water. Different Cr(VI) concentrations (20, 40, 60, and 80 mg L<sup>-1</sup>) were prepared by dilution of the stock K<sub>2</sub>Cr<sub>2</sub>O<sub>7</sub> standard solution with deionized water. The experiments were carried out in 100 mL borosil beaker by stirring 0.1 g of Sm<sup>3+</sup> doped CeO<sub>2</sub> nanopowders with 10 mL of the aqueous Cr(VI) solution of desired concentration at room temperature (25°C), and without any further pH adjustment. Adsorption isotherm study was carried out with different initial concentrations of Cr(VI) from 20 to 100 mg/L. The initial pH value was 5 for Cr(VI) solution without any adjustment of pH. The amount of Cr(VI) adsorbed per unit mass of the adsorbent was evaluated by using the mass balance equation:

$$q_t = (C_0 - C_t)V/W \quad (6.1),$$

Where  $q_t$  (mgg<sup>-1</sup>) is the amount adsorbed per gram of adsorbent at time  $t$  (min),  $C_0$  is the initial concentration of Cr(VI) in the solution (mg L<sup>-1</sup>),  $C_t$  is the concentration of Cr(VI) at time  $t$  of adsorption (mgL<sup>-1</sup>),  $W$  is the mass of the adsorbent used (g), and  $V$ (L) is the initial volume of the Cr(VI) solution. After reaction for 1 h, the reaction solution was centrifuged, and the supernatant liquid was used for Cr concentration analysis by UV-visible spectrophotometer immediately at 352.5 nm. The Cr(VI) concentration in the supernatant was

determined by monitoring the absorbance at 352.5 nm on a Shimadzu ultraviolet–visible-2450 spectrophotometer. The percentage of adsorption can be calculated by Eq. (6.2),

$$\text{Adsorption (\%)} = (C_0 - C_t) / C_0 \times 100. \quad (6.2)$$

The effect of pH on adsorption of Cr(VI) ions by SDC nanopowders were studied by varying pH of the solution over the range of 1.5-8, by addition of NH<sub>4</sub>OH and 1 M HNO<sub>3</sub> aqueous solution. Separate sets of experiments were conducted to test the time required to reach the equilibrium condition, by keeping the initial concentration of the test solution 100 mg/L, adsorbent dose 10 gL<sup>-1</sup> for Cr(VI) and without any adjustment of pH. The effect of adsorbent dosage on adsorption of Cr(VI) was performed by stirring 10 mL of 100 mgL<sup>-1</sup> stock solution for 1 h with different adsorbent doses (4 -12 gL<sup>-1</sup>) at room temperature.

### 6.1.3. Result and Discussion

#### 6.1.3.1 Effect of various adsorbent

The effect of dopant concentrations and processing routes on the Cr(VI) ion adsorption capacities from aqueous solution by the Sm<sup>3+</sup> doped CeO<sub>2</sub> nanopowders are compared with the performance of the pure CeO<sub>2</sub> at room temperature (25°C) for 1 h are given in Table 6.1. As the addition of dopant increased the surface area of Sm<sup>3+</sup> doped CeO<sub>2</sub> nanopowder, it exhibited greater adsorption capacity in comparison to the pure CeO<sub>2</sub> but no further significant enhancement was observed with increasing the dopant concentration beyond 1 mol%. Doping could increase the number of OH<sup>-</sup> groups attached on CeO<sub>2</sub> surface, thus increasing the adsorption capacity of Cr(VI) in the form of HCrO<sub>4</sub><sup>-</sup>, CrO<sub>4</sub><sup>-</sup> and Cr<sub>2</sub>O<sub>7</sub><sup>-</sup>.

**Table 6.1.** Comparison of Cr(VI) uptake by different pure and doped CeO<sub>2</sub> nanopowders.

Sample	Cr(VI) % adsorb
100CeSDSasp	67
0.5SmCeSDSasp	78
1SmCeSDSasp	83.5
2SmCeSDSasp	82
5SmCeSDSasp	83
1SmCeSDSMWasp	81
1SmCeSDSNRasp	62
1SmCeSDS500	70

In addition, it is also noteworthy that the 1SmCeSDSasp or 1SmCeSDSMWasp nanopowder showed comparable 84 or 81 % Cr(VI) adsorption capacity, but a lower amount of 62% Cr(VI) was adsorbed by the 1SmCeSDSNRasp nanopowder, which is obtained without refluxing. A decrease in adsorption capacity was observed for the calcined samples. Since the as-prepared 1 mol% Sm<sup>3+</sup> doped CeO<sub>2</sub> nanopowders obtained in conventional refluxing method shows maximum adsorption capacity it was subjected for further studies in order to find out the effect of other parameters on Cr(VI) adsorption capacities.

### 6.1.3.2. Effect of contact time

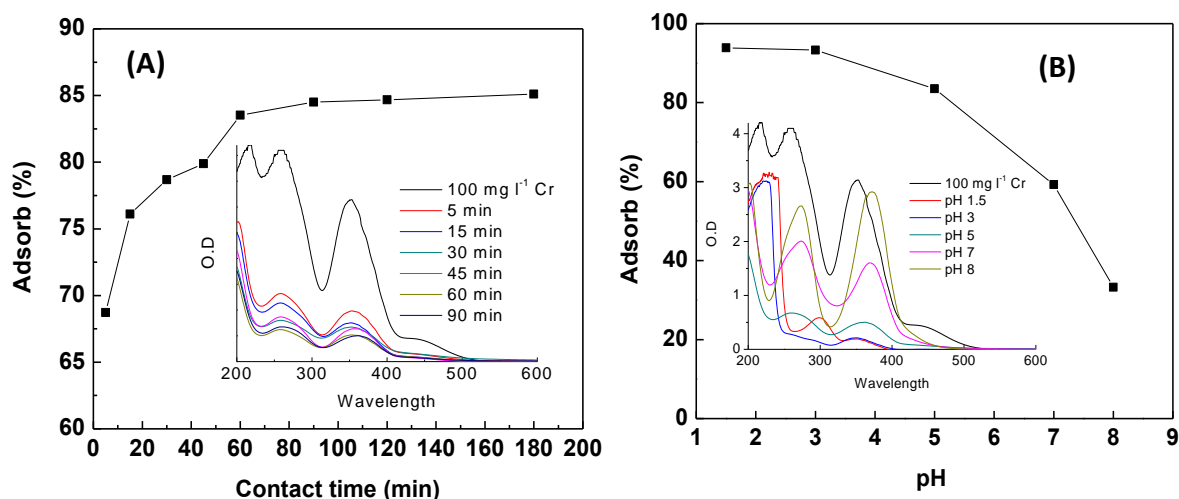


**Fig. 6.1.** (A) Time profile of Cr(VI) removal with 1SmCeSDSasp without adjustment of pH. The initial Cr(VI) concentration and the amount of adsorbent were 100 mgL<sup>-1</sup> and 10 gL<sup>-1</sup>, respectively. (B) Effect of pH (varied from 1.5 to 8) on the Cr(VI) adsorption by 1SmCeSDSasp (time = 60 min, initial Cr(VI) conc. = 100 mg L<sup>-1</sup>, and amount of 1SmCeSDSasp = 10 gL<sup>-1</sup>).

Effect of contact time is one of most important parameter which has significant influence on Cr(VI) adsorption capacity. To determine the equilibrium point, the adsorption processes as a function of time were carried out by dispersing 0.10 g nanopowder in 10 mL of 100 mgL<sup>-1</sup> Cr(VI) solution without any adjustment of pH i.e. at initial pH of 5 at room temperature. The results are shown in Fig. 6.1 (A). It can be seen from the Fig. 6.1(A), that the adsorption efficiency of Cr(VI) ions into nanopowders is gradually increasing from 69% to 83.5% with increasing the contact time from 5 min to 1 h. Stability reached within 1 h and no significant change in Cr(VI) adsorption was further observed. The complete adsorption equilibrium was reached after 1h between the two phases. The Cr(VI) adsorption capacity was

found to be reached maximum of  $8.35 \text{ mgg}^{-1}$  in 1 h of contact time. No further significant improvement in adsorption capacity was observed after 1h of contact time by placing the adsorbent in contact with the Cr(VI) solutions for 3 days. The rapid adsorption equilibrium could be attributed to the presence of large number of surface active sites due to high surface area and mesoporous structure of the adsorbent. This behavior shows that adsorption of Cr(VI) ions occurred in a single step. The slow adsorption before 1 h can be explained by ion exchange of the Cr(VI) ions on the surface of the nanopowders.

### 6.1.3.3. Effect of pH

The effect of initial pH on the adsorption of Cr(VI) ( $100 \text{ mgL}^{-1}$ ) from aqueous solution by the nanopowder (0.1 g dispersed in 10 mL solution) was examined by varying the pH of the solution over the range of 1.5 to 8 and contact time of 1 h. The pH of the solution was adjusted by adding  $\text{HNO}_3$  and  $\text{NH}_4\text{OH}$  solutions. The adsorption of metal ions on powder surfaces can be reduced or increased by varying the pH values of the medium, due to the weaker interactions of metal ions with adsorbed functional groups on the powder surfaces than the interactions with the surface hydroxyls of the mineral. The influence of initial pH on the adsorption of Cr(VI) ions ( $100 \text{ mgL}^{-1}$  solutions) is shown in Fig. 6.1(b). This nanopowder exhibits a typical metal anion adsorption behavior. It was found that the maximum adsorption occurs at lower pH, whereas negligible adsorption takes place at high pH. A sharp decrease in adsorption capacity in alkaline media was observed. With decreasing the pH value from 7 to 3, the % of Cr(VI) adsorption was increased from 59% to 93% and no significant increase in adsorption was observed on further decrease in the pH to 1.5. Whereas the increase in pH value from 7 to 8, the maximum percentage of adsorption significantly decrease to 33%. The maximum adsorption of Cr(VI) at lower pH values may be attributed due to the strong electrostatic interaction between the positively charged surface and the negatively charged hydrolyzed species of Cr(VI) ions. The most stable oxidation state of Cr(VI) in aqueous solution are the hexavalent, Cr(VI) and the trivalent, Cr(III). In solution at pH higher than 5, Cr(VI) exists in the form of  $\text{CrO}_4^{2-}$  ions, whereas at lower pH values, the Cr(VI) is present either as  $\text{HCrO}_4^{2-}$  or  $\text{Cr}_2\text{O}_7^{2-}$  depending on the Cr concentration, which is adsorbed onto the powder surface, thereby leading to high percentage of adsorption. At higher pH value, the surface group may partially be deprotonated and the surface become negatively charged which can in turn inhibit the adsorption of Cr(VI) due to the competition between Cr(VI) ion



and hydroxide ion resulting a decrease of Cr(VI). The increase of alkaline media also suppresses the hydrolysis of Cr(VI) ions leading to lower adsorption and the nano powders acts as ion exchanger.

#### 6.1.3.4. Effect of adsorbent dose

To investigate the amount of adsorbent dose on Cr(VI) adsorption capacity batch experiments were carried out by taking 10 mL 100 mgL<sup>-1</sup> Cr(VI) solution without adjustment of pH, contact time of 1h and varying the adsorbent amount from 0.04 g to 0.12 g. It can be seen from the Fig. 6.2 (A), that the adsorption capacity increases proportionally from 45% to 83.5% with increasing the amount of nanopowders from 0.04 to 0.10 g. On further increase in the adsorbent dose to 0.12 g, a very little increase in adsorption capacity to 86% was observed. So, 10 gL<sup>-1</sup> of adsorbent is the optimum quantity for the quantitative removal of Cr(VI) from wastewater. The increase in adsorption efficiency with the increase in adsorbent dose may be attributed to the availability of the more number of active sites for adsorption. On further increase in the adsorbent dose to 0.12 g, no significant increase in Cr(VI) removal was observed due to the saturation of the active sites.

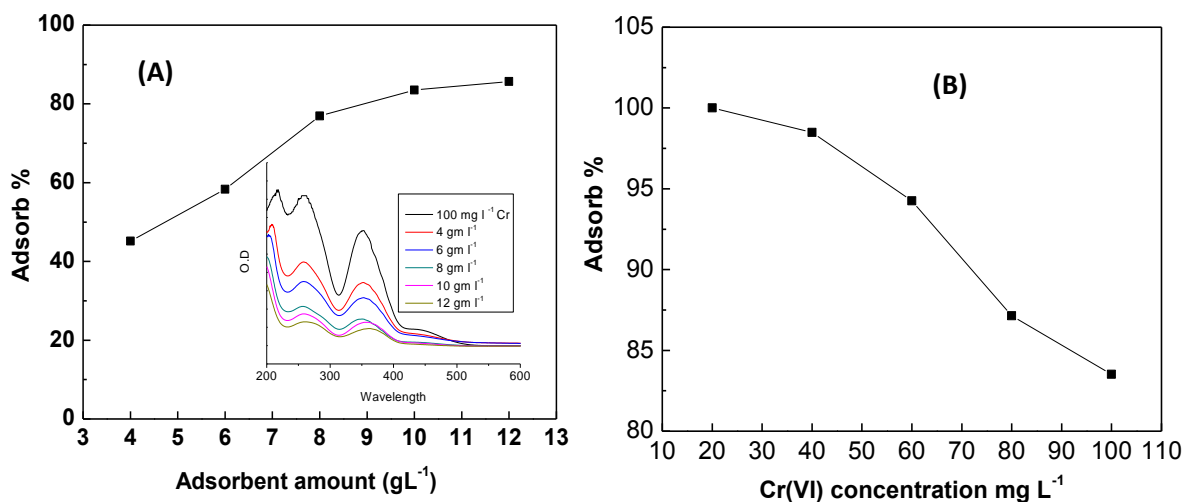


**Fig. 6.2.** Effect of (A) adsorbent dose and (B) adsorbate concentration on % Cr(VI) adsorption by 1SmCeSDSasp (time: 60 min, initial Cr(VI) conc. 100 mgL<sup>-1</sup>, and without any further pH adjustment).

### 6.1.3.5. Effect of initial concentration

Assessment of the effect of initial adsorbate concentration on the percentage uptake of the Cr(VI) adsorption on nanopowders was carried out by varying the adsorptive concentrations from  $20 \text{ mgL}^{-1}$  to  $100 \text{ mgL}^{-1}$  at room temperature for 1h with 0.1g of adsorbent in 10 mL solution and the results of the adsorption of Cr (VI) ions are shown in Fig. 6.2(B). It was found that the adsorption of Cr (VI) onto nanopowders was strongly dependent on initial metal ion concentration. As is seen in Fig. 6.2(b), the percentage of adsorption decreased from 100 to 83.5% when initial concentration of chromium ions increased from 20 to  $100 \text{ mgL}^{-1}$  respectively. The decrease of adsorption could be explained by the interaction of metal ions adsorbed onto the surfaces, by a mechanism that involves specific metal ion adsorption at a limited number of surface sites, because there are less number of surface active sites per gram of sorbent available for deposition at higher initial concentration.

### 6.1.3.6. Maximum adsorption capacity

In order to find out the maximum adsorption capacity, the adsorption study was performed by taking maximum initial Cr(VI) concentration ( $100 \text{ mg L}^{-1}$ ) and minimum amount of nanopowder  $2.0 \text{ g L}^{-1}$  of 1 mol%  $\text{Sm}^{3+}$  doped  $\text{CeO}_2$  at optimum  $\text{pH}=2$  and room temperature of  $25^\circ\text{C}$ . From Fig.6.3, it was found that the adsorption process almost finished within 8 h, and no significant change was observed from 8 to 12 h. The maximum adsorption capacity was found to be  $23.30 \text{ mg.g}^{-1}$ .

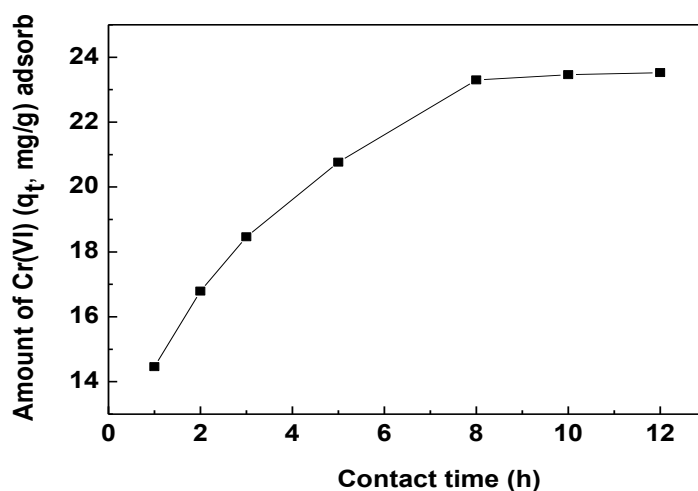


**Fig. 6.3.** Maximum adsorption capacity of 1SmCeSDSasp, variation with time (in h), initial Cr (VI) conc  $100 \text{ mg L}^{-1}$ , amount of 1SmCeSDSasp  $2 \text{ g L}^{-1}$ , at pH 2.

### 6.1.3.7. Adsorption isotherm study

Adsorption isotherm models were used to determine the relationship between the adsorbed species and their equilibrium concentrations. The obtained experimental data were fitted to the common isotherm models i.e. Langmuir and Freundlich isotherms.

#### 6.1.3.7.1. Langmuir isotherm

The Langmuir isotherm is assumed to be adsorption on homogeneous surfaces as well as monolayer adsorption. According to this isotherm, available sites on the adsorbent surface is constant. The linearized form of this isotherm is given by the equation 2.17 in chapter II. A linear relationship was observed among the plotted data which revealed the applicability of the Langmuir isotherm. Values of the Langmuir constants  $q_m$  and  $b$  were calculated from the slopes and intercepts, respectively, by plotting  $C_e/q_e$  versus  $C_e$  (Fig. 6.4a) and are given in Table 6.2. The values of  $q_m$  and  $b$  for the removal of Cr(VI) were found to be  $8.344 \text{ mg g}^{-1}$  and  $1.154 \text{ L mg}^{-1}$ , respectively.

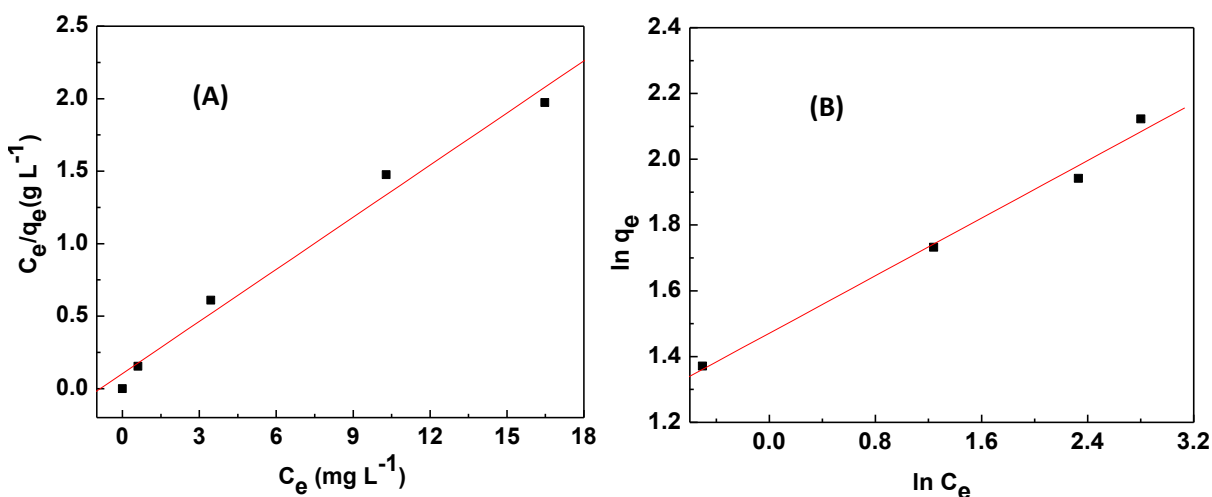


**Fig. 6.4.** (A) Langmuir and (B) Freundlich adsorption isotherms for Cr(VI) adsorption by 1SmCeSDSasp.

Langmuir isotherm can be expressed in terms of dimension less separation factor,  $R_L$ , which describes the type of isotherm;

$$R_L = 1/(1 + bC_0) \quad (6.3)$$

Where  $C_0$  is the initial concentration of Cr(VI) ( $\text{mg.L}^{-1}$ ) and  $b$  ( $\text{L.mg}^{-1}$ ) is Langmuir constant. The magnitude of  $R_L$  determines the feasibility of the sorption process. If  $R_L > 1$ ,

the sorption is unfavourable; if  $R_L = 1$ , the sorption is linear; if  $R_L < 1$ , the sorption is favorable and if  $R_L = 0$ , the sorption is irreversible. The values for  $R_L$  listed in Table 6.2 were calculated for the initial concentration of  $100 \text{ mg.L}^{-1}$ . The value of  $R_L$  in the present investigation has been found  $0 < R_L < 1$ . Hence the sorption process was very favorable and the adsorbent employed exhibited a good potential for the removal of Cr(VI) from aqueous solution.

### 6.1.3.7.2. Freundlich isotherm

The Freundlich isotherm is based on a non-ideal multilayer adsorption on heterogeneous surface. The linear form of Freundlich isotherm has been given by equation 2.19 in chapter II. Where  $q_e$  is the amount adsorbed ( $\text{mg g}^{-1}$ ) at equilibrium,  $C_e$  is the equilibrium concentration ( $\text{mg.L}^{-1}$ ), and  $K_f$  and  $1/n$  are related to the adsorbent capacity and sorption intensity of the adsorbent, respectively. The values of the Freundlich constants  $K_f$  and  $n$  were determined from the intercept and slope, respectively, by plotting  $\ln q_e$  vs  $\ln C_e$  and the plot is shown in Fig. 6.4 (b). The values of  $K_f$  and  $n$  for removal of Cr(VI) from aqueous solutions are found to be  $4.354 \text{ mg g}^{-1}$ , and  $4.573 \text{ Lg}^{-1}$ , respectively (Table 6.2). Since the  $1/n$  value is less than unity which signify the better adsorption at lower Cr(VI) concentration. The  $R^2$  values for the parameters of the two isotherm models were calculated, and these values suggest that both models fit the equilibrium data.

**Table 6.2.** Langmuir and Freundlich isotherm parameters for Cr(VI) adsorption by 1SmCeSDSasp.

Langmuir isotherm model				Freundlich isotherm model		
$q_m$ (mg/g)	$b$ (L/mg)	$R_L$	$R^2$	$K_f$ (mg/g)	$n$	$R^2$
8.344	1.1547	0.00859	0.9827	4.354	4.573	0.9897

### 6.1.3.8. Adsorption kinetics

#### 6.1.3.8.1. The pseudo first-order equation

The kinetics of the Cr(VI) adsorption was studied by pseudo first order rate equation as given in equation 6.4. Where  $q_e$  is the sorption capacity at equilibrium ( $\text{mg g}^{-1}$ ),  $q_t$  is the sorption capacity at time  $t$  ( $\text{mg g}^{-1}$ ), and  $K_1$  is the pseudo first-order kinetic constant ( $\text{min}^{-1}$ ).

$$\log (q_e - q_t) = \log q_e - \left( \frac{k_1}{2.303} \right) t \quad (6.4)$$

The values of  $\log(q_e - q_t)$  were plotted with  $t$ . The plot of  $\log(q_e - q_t)$  versus  $t$  do not follow a linear relationship, (with  $R^2$  value 0.922) as can be seen from the Fig. 6.5(A), indicating the mechanism do not follow a first order kinetics. In addition the calculated value of  $q_e$  (1.468) obtained from the plot of  $\log (q_e - q_t)$  versus  $t$  are (Table 6.3) quite different from the theoretical  $q_e$  (8.351) value, which further confirmed that the adsorption process did not follow the pseudo first order adsorption kinetics.

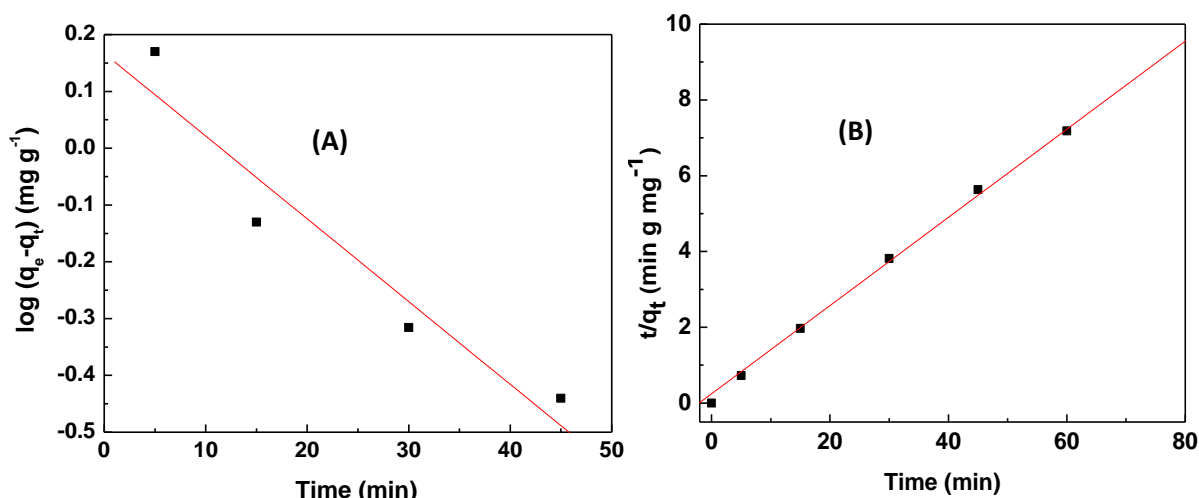


**Fig. 6.4.** (A) Pseudo-first and (B) pseudo-second order kinetics for Cr(VI) adsorption by 1SmCeSDSasp.

#### 6.1.3.8.2. The pseudo second-order equation

In contrast, the adsorption data were well fitted with the pseudo second-order equation as expressed in equation 6.5

$$\frac{t}{q_t} = \frac{1}{k_2 q_e^2} + \frac{1}{q_e} t \quad (6.5)$$

and resulted very good straight line as shown in Fig. 6.5(b), with  $R^2$  value 0.99932. The  $q_e$  i.e. the amount of Cr(VI) adsorbed at equilibrium and  $K_2$  the rate constant, values were calculated from the linear plot of the  $t/q_t$  versus  $t$  and summarized in Table 6.3. It is noteworthy that the calculated  $q_e$  (8.597) value obtained from the graph are in well agreement with the theoretical  $q_e$  (8.3518) value which suggest that the kinetics of the adsorption process followed pseudo-second-order kinetics.

**Table 6.3.** Kinetic parameters for pseudo-first order and pseudo-second order kinetic models.

pseudo-first order				pseudo-second order			
Calculated $q_e$ (mg g <sup>-1</sup> )	Theoretical $q_e$ (mg g <sup>-1</sup> )	$K_2$ (min <sup>-1</sup> )	$R^2$	Calculated $q_e$ (mg g <sup>-1</sup> )	Theoretical $q_e$ (mg g <sup>-1</sup> )	$K_2$ (min <sup>-1</sup> )	$R^2$
1.4689	8.351853	0.0335	0.9228	8.59771	8.351853	0.05457	0.99932

#### 6.1.4. Conclusion

The high surface area and mesostructured as-prepared 1 mol% Sm<sup>3+</sup> doped CeO<sub>2</sub> adsorbent obtained in conventional reflux method could effectively remove 84 % of toxic Cr(VI) metal ions from aqueous solution within a short period of 1 h and without any adjustment of pH. Kinetic studies confirmed that the adsorption process obeys pseudo-second-order kinetics. The adsorption isotherm data were fitted to both Freundlich and Langmuir models. The material was prepared through a simple and cost-effective method so the adsorbents are suitable for large scale waste water treatment.

## 6.2. Evaluation of Photo degradation of Acid Orange 7 under natural sunlight

### 6.2.1. Introduction

Now a days, tremendous efforts have been dedicated in water treatment researches to ensure sufficient water supply as the global consumption of water is increasing. Wastewater generated from textile, leather, paper, plastics, pharmaceutical and food industries are extensively containing azo dyes, which are largely non-biodegradable and toxic under aerobic conditions and reduced to potential carcinogenic aromatic amines under anaerobic conditions, and regarded as a major source of ecological and environmental problems.<sup>24,25</sup> Acid Orange 7 [*p*-(2-hydroxy-1-naphthylazo) benzene sulfonic acid] (AO7) that has a –N=N– unit as chromophore in their molecular structure, is a popular water-soluble dye that poses a severe health threat to humans includes eye, skin, mucous membrane, and upper respiratory tract irritation; severe headaches, nausea, methemoglobinemia, tumors, water-borne diseases such as dermatitis etc.<sup>26</sup> Therefore, development of a simple and effective technology for the purification of dye-containing wastewater is imperative.

For degrading organics and toxic materials, many treatment methods require high pressure (0.5–20 MPa) and high temperature (80–320°C),<sup>27</sup> which limit the practical application. To resolve this problem, in particular, heterogeneous photocatalysis using most preferred TiO<sub>2</sub> and ZnO photocatalysts have emerged as a promising advanced oxidation processes for the purification of the dye-containing wastewater and also provides solutions to many problems related to environmental pollution.<sup>28-30</sup> Mostly these processes involve UV/H<sub>2</sub>O<sub>2</sub>, UV/O<sub>3</sub> for the oxidative degradation of dyes.<sup>29-31</sup> Although H<sub>2</sub>O<sub>2</sub> is an environmentally friendly oxidant and widely used for environmental remediation, disinfection, etc. but the current industrial process for H<sub>2</sub>O<sub>2</sub> production requires toxic solvents and high energy input, which is not environmentally benign.<sup>32,33</sup> Photo assisted oxidation by solar irradiation has been found to be a most cost effective and ideal approach, as it is readily available and free that can be used directly to oxidize or degrade hazardous organic chemicals.<sup>28</sup> The advantage of CeO<sub>2</sub> (band gap  $E_g \sim 2.9$  eV) in comparison with TiO<sub>2</sub> ( $E_g \sim 3.0$  to 3.2 eV for anatase and absorbs less than 5% UV light of the sunlight) is that it absorbs over a larger fraction of UV spectrum and the onset of absorption of CeO<sub>2</sub> is  $\sim 440$  nm.<sup>34</sup> CeO<sub>2</sub> nanopowder has been reported to be more efficient photocatalyst than commercial TiO<sub>2</sub> P25.<sup>34-36</sup> So recently, CeO<sub>2</sub> is gaining immense interest as photocatalysts for photocatalytic degradation of various dyes as it is chemically stable, inexpensive and can be easily synthesized through various reproducible solution based synthesis routes.<sup>37-41</sup> It has already been used in various catalytic applications such as fluid cracking, purification of harmful gases in three way automotive catalytic converters, water splitting for the generation of H<sub>2</sub> gas, as well as in biomedicine, solar cell, and inorganic phosphors.<sup>42-46</sup>

The key to the wide ranges of catalytic applications of ceria based materials is that CeO<sub>2</sub> by shifting some Ce<sup>4+</sup> to Ce<sup>3+</sup> ions can easily produce oxygen vacancies, which act as sources for the oxygen involved in reactions taking place on the catalyst surface.<sup>38,41,47</sup> The effectiveness of CeO<sub>2</sub> photocatalyst can be enhanced by introducing other metal ions into it by forming solid solution.<sup>39,41</sup> It has been also reported that the lanthanide ion including La<sup>3+</sup>, Nd<sup>3+</sup>, Pr<sup>3+</sup>, Sm<sup>3+</sup>, or Eu<sup>3+</sup> doped in TiO<sub>2</sub> photocatalysts improve the separation rate of photo-induced charge carriers and greatly enhance the photocatalytic activity of TiO<sub>2</sub> than that of pure TiO<sub>2</sub>.<sup>48</sup> Cai *et al.* observed improved degradation of AO7 in the dark as well as under the visible light irradiation in the CeO<sub>2</sub>–H<sub>2</sub>O<sub>2</sub> system after Fe<sup>3+</sup> doping.<sup>41</sup>

It is well known that the concentration of oxygen vacancies can be remarkably enhanced after doping with Sm, due to  $\text{Sm}^{3+} \rightarrow \text{Ce}^{4+}$  substitutions.<sup>43</sup>  $\text{Sm}^{3+}$  doping also induces the least distortion of the parent lattice when oxygen vacancies are created in the  $\text{CeO}_2$  lattice for charge compensation. Many studies have reported on  $\text{Sm}_{0.2}\text{Ce}_{0.8}\text{O}_{1.9}$  system showing the highest electrical conductivity (specific to ionic conductivity) required for solid oxide fuel cell application.<sup>45</sup> Also samarium doped ceria nanoparticles are very important in developing new luminescence devices.<sup>43</sup> But no investigation on  $\text{Sm}^{3+}$  doped  $\text{CeO}_2$  as photocatalyst has been reported. Therefore, in this study, we aimed to obtain an efficient photocatalyst by doping  $\text{CeO}_2$  with  $\text{Sm}^{3+}$  ions.

Recently, Sun *et al.* reported 97.6% degradation efficiency of AO7 by nitrogen-doped  $\text{CeO}_2$  (N:Ce molar ratio of 0.3) nanoparticles synthesized solvothermally at  $120^\circ\text{C}$  for 24 h in an autoclave.<sup>37</sup> They investigated degradation of 20 mg/L AO7 solution (at pH = 3.0) containing 1 g/L of the as-synthesized sample, which had air bubbled through it at  $60^\circ\text{C}$  at a flow rate of 300 mL/min, using a domestic 10 W compact fluorescent lamp.<sup>37</sup> Salker *et al.* reported low solar light assisted photocatalytic activity of  $\text{CeO}_2$  for the degradation of textile dye Naphthol Blue Black.<sup>49</sup> But a significant increase in the photocatalytic activity was observed by substitution of 30 mol%  $\text{Mn}^{4+}$  in  $\text{CeO}_2$  crystal lattice due to the enhancement of the redox couple  $\text{Ce}^{4+}\text{-Ce}^{3+}$  and decrease in band gap energy.<sup>49</sup> Few studies have also demonstrated the potential use of  $\text{CeO}_2$ ,<sup>35,36,38</sup> or doped  $\text{CeO}_2$ <sup>39-41</sup> for photocatalytic degradation of dyes under visible light irradiation (mostly  $\lambda > 420$  nm).<sup>36,39,41</sup> However, in most cases they are successful in the presence of high concentrations of oxidizing agents,<sup>38,41</sup> and/or under specific pH conditions.<sup>37</sup> These conditions limit the industrial application of nanomaterials in environmental remediation. There is a need to develop general, simple and economical routes for designing novel nanomaterials which can efficiently remove various contaminants in the environment under solar illumination. Due to the higher reaction rate and selectivity, microwave chemistry has recently been shown to be a fast-growing research area with immense potential.<sup>50-52</sup> Microwave-assisted methods are effectively employed to synthesize a great many novel nanostructures with various shapes.<sup>50-52</sup>

However, the application of microwave heating with addition of surfactants to synthesize mesostructured nanomaterials has hardly been exploited until now. Here, we used surfactant



assisted microwave heating method, which enables the convenient low temperature preparation of efficient CeO<sub>2</sub> photocatalysts with higher surface area and higher crystallinity. In the present study, we demonstrate a new photochemical remediation method for dye-polluted waters by using samarium doped ceria nanoparticles and natural sunlight only. The effect of the calcination temperature, pH and the amount of nanopowders were also investigated. Though several studies on mechanistic details of dye degradation on TiO<sub>2</sub> have been reported under UV as well as visible light but some insight of active species for photodegradation process on CeO<sub>2</sub> under solar light irradiation is given here for the first time.

### 6.2.2. Experimental details

The photocatalytic efficiency of the CeO<sub>2</sub>:Sm<sup>3+</sup> samples were evaluated by the extent of degradation of Acid orange 7 (AO7) in an aqueous solution under solar light irradiation. In a typical experiment, a 20 mL of AO7 solution (concentration:  $2 \times 10^{-4}$  M, i.e. 70 mg/L) was taken in a 100 mL beaker to which photocatalysts of 20 mg (1 g/L) were added separately. To achieve adsorption-desorption equilibrium, suspension were stirred in dark for 30 min, after that exposed to sunlight at room temperature with vigorous stirring to ensure mixing of catalysts. The experiments using solar light were carried out between 7.00 am and 5.00 pm at a location of 22°25'N 84°00'E during the months of May and June and stirred for a period ranging from 1 h to 10 h without any adjustment of pH and then centrifuged. Sample aliquots were withdrawn from the reaction mixture at a regular time interval and centrifuged and then dye concentration in the residual solution was analyzed by using a Shimadzu UV-2450 spectrophotometer. Changes in the concentration of AO7 were observed from its characteristic absorption band maximum at 484 nm. The decolorization efficiencies of the dyes were estimated by the equation:  $\left[ \frac{C_i - C_t}{C_i} \right] \times 100$ , where  $C_i$  and  $C_t$  represent the concentration of dye in solution before and after irradiation for time  $t$ , respectively. To find out the effect of the pH on the photocatalytic degradation efficiency the pH value of the obtained suspension was adjusted in the range of 3 to 9 using dilute NH<sub>4</sub>OH and HNO<sub>3</sub>. Effects of calcination temperatures, dosage concentration on the decolorization of AO7 were also investigated. To investigate the mechanism of the photodegradation processes, different chemical scavengers - isopropanol (90 mM, •OH scavenger), CrO<sub>3</sub> (1.5 mM,  $e^-$  scavenger), sodium oxalate (60 mM,  $h^+$  scavenger), and 1,4-benzoquinone (2.0 mM, O<sub>2</sub><sup>•-</sup> scavenger) were used.

To determine the adsorption behavior of  $\text{Sm}^{3+}$  ion doped and pure  $\text{CeO}_2$  catalyst, adsorption tests in the dark was performed. 20 mg of photocatalysts was added to 20 mL of  $2 \times 10^{-4}$  M AO7 solution. The mixture was well dispersed, and put in the dark for 10 h. The AO7 concentration in the suspension before and after the adsorption tests was analyzed and the adsorbed amount of AO7 on the catalysts was calculated.

### 6.2.3. Result and discussion

#### 6.2.3.1. Effect of various photocatalysts

In order to find out the best performing photocatalyst, the photocatalytic degradation of AO7 by using different nanopowders were evaluated by using 20 mL  $2 \times 10^{-4}$  M stock solution of AO7 and 0.02 g nanopowder under natural sunlight for 1 h and the results are summarized in Table 6.4.

**Table 6.4.** Comparison of photocatalytic degradation % of AO7 by different  $\text{CeO}_2$  nanopowders during the decolorization process at solar irradiation time of 1 h. pH neutral.

Sample	Degradation % of AO7
100CeSDS500	55
100CeSDSMW500	60
0.5SmCeSDSMW500	71
1SmCeSDSMW500	82.5
2SmCeSDSMW500	77
5SmCeSDSMW500	70
10SmCeSDSMW500	62
1SmCeSDS500	75

It was found that  $\text{Sm}^{3+}$  doping significantly enhanced the photocatalytic activity. In addition it is also notable that the nanopowder obtained in microwave assisted route showed higher photodegradation efficiency than the nanopowder obtained in conventional route. Furthermore, the effects of different amount of dopants were also examined under the same experimental conditions and the results revealed that the 1 mol%  $\text{Sm}^{3+}$  doped  $\text{CeO}_2$  exhibits highest photocatalyst efficiency. Hence, 1 mol%  $\text{Sm}^{3+}$  doped  $\text{CeO}_2$  obtained in microwave

assisted route and calcined at 500°C was subjected to further analysis to find out the effect of other parameters on the photodegradation process.

### 6.2.3.2. Effect of catalyst dosage

In order to study the effect of  $\text{Sm}^{3+}$  doped  $\text{CeO}_2$  catalyst dosage on the photodegradation efficiency we have carried out experiments by varying the amount of nanopowders from 1 to 4 g/L using  $2 \times 10^{-4}$  M stock solution of AO7 over a period of 1 h of sunlight irradiation and without any further adjustment of pH of the solutions and at atmospheric conditions. As can be seen from the Fig. 6.6(A), the photodegradation efficiency increases from 82% to 94% with increasing catalyst dosage from 1 g/L to 4 g/L at 1 h solar irradiation time. This is due to the increased number of adsorption and active sites available on the catalyst surface, which in turn increased the number of hydroxyl, and superoxide radicals. The total active surface area increases with increasing catalyst dosage. At the same time, due to an increase in the turbidity of the suspension, there is a decrease in sunlight penetration as a result of increased light scattering and screening effect and hence the photo activated volume of suspension decreases.<sup>53</sup> When catalyst dosage varied between 1 g/L and 2 g/L, the dye removal performance varied only ~ 6%. As it is important to keep the treatment expenses low when it goes to industrial use and also taking the operational error of photocatalytic test into consideration, we regarded 1 g/L as the optimum catalyst dosage in the present work.

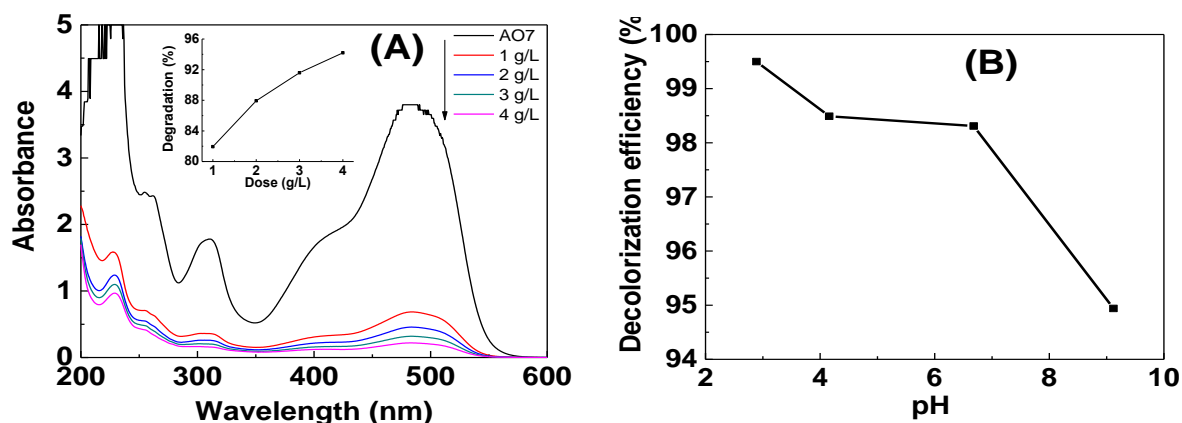


**Fig. 6.6.** (A) Effect of 1SmCeSDSMW500 catalyst amount on UV–Vis spectra of AO7 (photodegradation % in the inset) (B) Effect of initial pH value on the photocatalytic degradation efficiency of AO7 in 10 h. during the decolorization process at solar irradiation time of 1 h. pH neutral.

### 6.2.3.3. Effect of pH of the medium

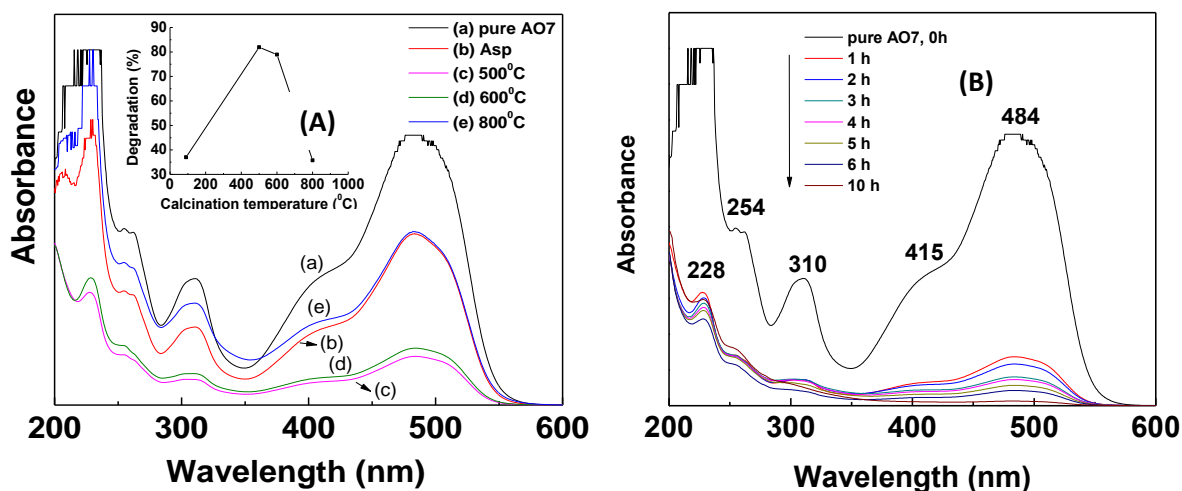
The solution pH is an important parameter in photocatalytic degradation reactions and the wastewaters from textile industries usually have a wide range of pH values. It has significant influence on the surface charge of the metal oxide catalyst and therefore the adsorption ability of pollutants onto the surface of the catalyst. Higher adsorption of dye could lead to a higher degree of degradation. The effect of pH of the medium on the photocatalytic degradation efficiency of AO7 under sunlight irradiation for 10 h was examined in the pH range of 2.9 to 9.1 at a fixed dose of  $\text{Sm}^{3+} : \text{CeO}_2$  (1g/L) and keeping all other experimental parameters constant.

Fig. 6.6(B) shows a direct influence of the initial solution pH values of 2.9, 4.2, 6.9, and 9.1 on the degradation efficiency of dyes on the catalyst. It is interesting to observe that the  $\text{Sm}^{3+} : \text{CeO}_2$  photocatalyst was very efficient in degrading (99.5 % to 95 %) the dye over the pH range from 2.9 to 9.1. At neutral pH of 6.9, photodegradation of AO7 was 98 %. The photodegradation efficiency of AO7 is slightly higher in acidic solutions than that in alkaline solutions. The zero point charge of ceria is at pH 4.2, which is close to the neutral pH of 6.9 of the solution. AO7 dye act as a Lewis base due to the presence of negatively charged acidic sulfonate group on it and can easily adsorb on the positively charged  $\text{Ce-OH}_2^+$  catalyst surface in acidic pH, and hence increasing the degradation rate. In alkali medium may be due to the increased  $\text{OH}^-$  ion concentration with increased pH, there is a competitive adsorption by hydroxyl groups and the dye molecule in addition the negatively charged catalyst surface repels the dye, thereby undergoes a bit slower degradation.

### 6.2.3.4. Effect of calcination temperature

Calcination temperature is a vital parameter in the preparation of catalyst and has prominent influence on the activity of the prepared photocatalysts. Fig.6.7 (A) shows the effect of temperature ranging from 90 (as-prepared) to 800°C of the catalyst on the photocatalytic activity under sunlight irradiation for 1 h at normal pH condition. The results revealed that the photocatalytic activity rapidly increased from 37 % to 82 % as the calcination temperature increased from 90 (as-prepared) to 500°C and was optimum at 500°C. A reduced photodegradation of 79 % and 36 % were observed for the catalysts calcined at 600

and 800°C, respectively. Therefore, the catalyst calcined at 500°C has the most favorable physical properties for optimal photo activity.

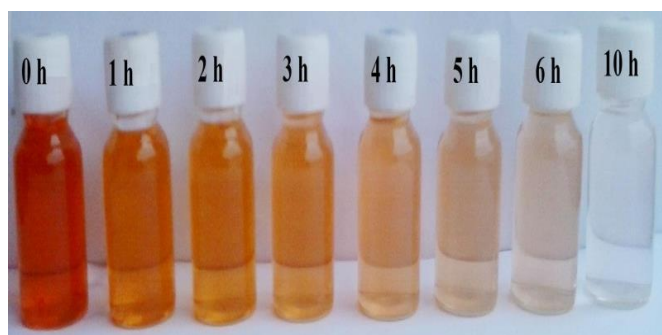


**Fig. 6.7.** (A) Effect of calcination temperatures of 1SmCeSDSMW catalyst on UV–Vis spectra of AO7 (photodegradation % in the inset) during the decolorization process at solar irradiation time of 1 h. pH neutral. (B) Evolution of the UV–vis spectra with irradiated time for the photocatalytic degradation of AO7 in aqueous solution in the presence of 1SmceSDSMW500, pH neutral.

Generally, the specific surface area, surface states and crystallinity play key roles in the degradation efficiency.<sup>53</sup> The catalyst calcined at 600°C possesses lower surface area than the as-prepared catalyst though showing prominently 42% higher photodegradation efficiency. This indicates that surface area is not the only determining factor to cause the different efficiencies seen in this study. The as-prepared catalyst also contains certain amount of SDS molecules, which is attached to the inorganic framework and is difficult to remove just by simple washing process. The  $\text{SO}^{4-}$  ions of SDS molecules present in the as-prepared sample also decrease the adsorption of the negatively charged dye on its surface, thereby decrease the photodegradation efficiency. Carbonaceous species formed during the sunlight irradiation and low crystallinity could be possible reasons for the unusually low activity of as-prepared catalyst despite having high surface area. Wang *et al.* found that organic impurities (carbonaceous species) present in the well-known photocatalyst  $\text{TiO}_2$  diminishes the photocatalytic activities by accelerating the electron and hole recombination by acting as intermediate levels under UV light.<sup>54</sup>

As the decomposition temperature of SDS is  $\sim 210^{\circ}\text{C}$ , the catalyst calcined at  $500^{\circ}\text{C}$  is surfactant free as was also evident from IR analysis (not shown here). This calcination temperature is high enough to develop well crystalline structure of the catalyst. The highest photocatalytic activity of the catalyst calcined at  $500^{\circ}\text{C}$  may be attributed to the high surface areas, pore volume and mesoporous morphology. Also the catalyst can absorb light in the near UV and also absorbs larger fraction of the solar spectrum than the others. As the temperature reaches above  $500^{\circ}\text{C}$ , the crystallites grows larger and the surface area and total pore volume goes down, leading to the poor performance of the samples. The photocatalytic activity reduction for the catalyst calcined at  $800^{\circ}\text{C}$  may be attributed to the extensive decreases of specific surface area and its nonporous morphology.

#### 6.2.3.5. Effect of irradiation time



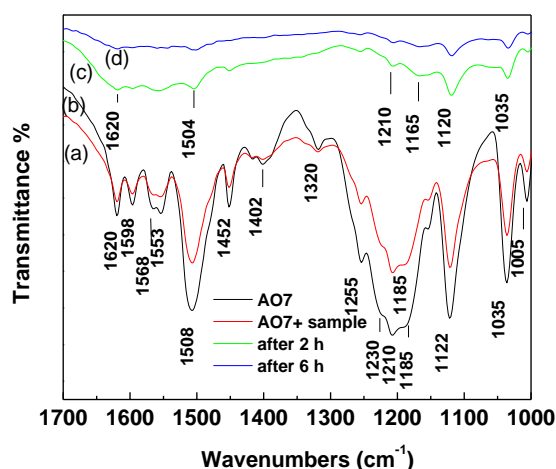
**Fig. 6.8.** The photo of AO7 solutions in the presence of 1SmCeSDSMW500 as catalyst under solar irradiation at different time intervals (h) as marked therein.

Figure 6.7 (B) displays the evolution of the UV-Vis absorption spectra of the AO7 solution prior to and during photocatalytic degradation using 100CeSDSMW500 as catalyst under solar irradiation as a function of irradiation time at natural pH conditions. The absorption spectrum of AO7 has three characteristic absorption peaks at 228, 310, and 484 nm, and two shoulders at 254 nm and 415 nm, respectively. The peaks at 228 and 310 nm, and the shoulder at 254 nm are attributed to the  $\pi \rightarrow \pi^*$  transition of benzene and naphthalene ring, respectively. The peak at 484 nm and the shoulder at 415 nm corresponds to the  $n \rightarrow \pi^*$  transition of the hydrazone form and azo, respectively.<sup>24</sup> In the photo decoloration process, it was found that the major absorption band at 484 nm declined rapidly until no peak was further observed with increasing irradiation time. This indicates that the cleavage of the

chromophore (N=N or C–N bond) responsible for characteristic color of the AO7 and the representative photograph (Fig. 6.8) for the AO7 solution using the catalyst clearly shows the decoloration process of AO7 solutions along with irradiation time.

It is observed that after the first 1 h of solar irradiation the absorbance peaks including the shoulder in the visible region decreased over 82% from their initial value and almost complete decolorization (98%) was achieved after 10 h of photocatalysis. The peaks at 228, 254 and 310 nm decreased significantly. This indicates that benzene and naphthalene rings of AO7 are broken into smaller species.

### 6.2.3.6. FT-IR study on dye before and after photodegradation



**Fig. 6.9.** FT-IR spectra of AO7 (a) isolated, (b) adsorbed on catalyst, and after photodegradation at (c) 2 h, and (d) 6 h of irradiation.

Degradation of the dye solution was further confirmed with FT-IR spectroscopy. Fig. 6.9 presents FT-IR spectra of pure dye (AO7), and AO7 adsorbed over the 1SmCeSDSMW500 catalyst and finally after photocatalytic treatment under solar irradiation for 2 and 6 h. The IR spectrum between 1000 and 1900 cm<sup>-1</sup> in the fingerprint area of the pure AO7 molecule exhibited several characteristic intense and prominent peaks at 1005, 1035, 1122, 1185, 1210 and 1508 cm<sup>-1</sup>.<sup>55</sup> The IR spectrum of AO7 exhibits characteristic bands of aromatic skeletal vibrations at 1620, 1598, 1568, 1553 and 1452 cm<sup>-1</sup>. The intense band at 1508 cm<sup>-1</sup>, which is attributed to the vibrations of the –N=N– bond or aromatic ring sensitive to the interaction with the azo bond, or to the N–H bending vibration mode  $\delta(\text{N–H})$  of the

hydrazone form of the azo dye, nearly disappears after 6 h of degradation indicating the breakdown of the azo-chromophore. The most striking feature is that after 2 h of degradation, the important band of  $\nu_{\text{as}}(\text{SO}_3)$  at  $1185 \text{ cm}^{-1}$  is shifted to  $1165 \text{ cm}^{-1}$ , while the band of  $\nu_{\text{s}}(\text{SO}_3)$  at  $1122 \text{ cm}^{-1}$  is slightly shifted to  $1120 \text{ cm}^{-1}$ . It is interesting to observe that the two weak bands at  $1035$  and  $1122 \text{ cm}^{-1}$  due to the coupling between benzene mode and  $\nu_{\text{s}}(\text{SO}_3)$  can still be detected by FTIR, when 94.5% dye was already degraded after 6 h of photodegradation. During photodegradation all the peaks decrease in intensity until they almost disappear after 6 h of solar irradiation, indicating destruction of the AO7 dye molecule adsorbed over the catalyst. Even after 30 h irradiation, a certain amount of chemicals containing phenyl and sulfo groups still exist on the surface of  $\text{CeO}_2$  powder prepared by the precipitation method.<sup>36</sup>

### 6.2.3.7. Active species to attack dye molecule

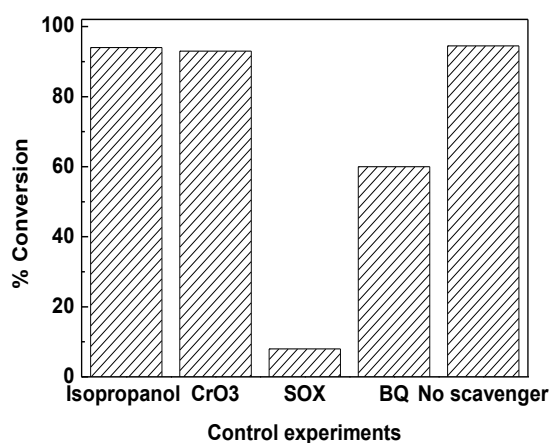


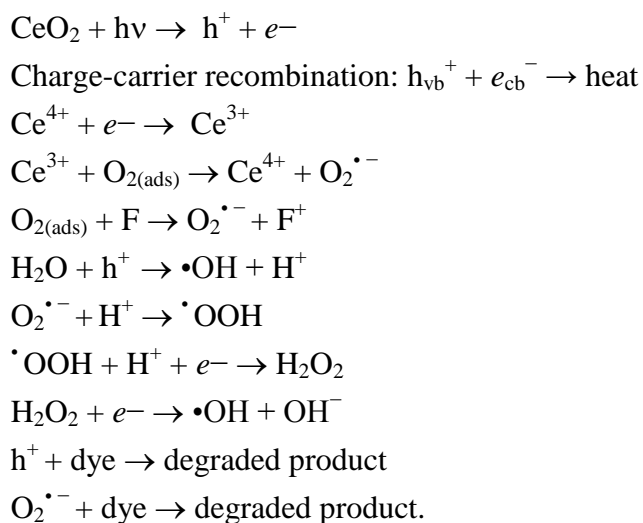
**Fig. 6.10.** Control experiments of photocatalytic degradation of AO7 with the addition of different radical scavengers: Isopropanol (scavenger for hydroxyl radicals),  $\text{CrO}_3$  (scavenger for electrons), sodium oxalate (SOX, scavenger for holes), and benzoquinone (BQ, scavenger for superoxide radicals), over the optimum 1SmCeSDSMW500 under solar light irradiation for 6 h.

Chemical scavengers were employed to understand the role of photogenerated radical species for the photocatalytic oxidation of AO7 over the 1SmceSDSMW500 under solar light irradiation. We have performed a series of control experiments with adding different scavengers: isopropanol for  $\bullet\text{OH}$ , sodium oxalate (SOX) for holes ( $h^+$ ),  $\text{CrO}_3$  for electron ( $e^-$ ), 1,4-benzoquinone (BQ) for superoxide radicals ( $\bullet\text{OOH}/\text{O}_2^{\bullet-}$ ). As shown in Fig. 6.10, the



$e^-$  and  $\bullet\text{OH}$  scavengers do not affect the photodegradation experiments. However, when BQ is added to the reaction system, a significant inhibition effect on the decolorization of the AO7 solution was observed. A remarkable inhibition effect on photodegradation of AO7 was also observed when sodium oxalate scavenger for holes was used. The experiments clearly suggest that the  $h^+$  play predominant role in the photocatalytic destruction of AO7. It worth noting that though  $e^-$  in bulk solution plays negligible role in photodegradation but superoxide radicals appear to play secondary roles in the photocatalytic destruction of AO7 (as depicted in Fig.6.11).

A tentative photocatalytic reaction mechanism for degradation of AO7 over the 1SmCeSDSMW500 can be proposed as the following. Under solar light irradiation, the electron-hole pairs are generated from  $\text{CeO}_2$ . Part of the photogenerated  $e^-$  also gets trapped by the oxygen vacancies (F centres) before moving to conduction band.<sup>46</sup> Adsorbed surface oxygen first interact with the  $\text{Ce}^{3+}$  and oxygen vacancies to generate superoxide radical and then form  $\text{H}_2\text{O}_2$ ,  $\bullet\text{OOH}$  and  $\bullet\text{OH}$ . Due to the short lifetime of the resulting  $\bullet\text{OH}$  on the photocatalyst, the contribution of the oxidizing species in the bulk solution could be insignificant. Active  $h^+$  and  $\text{O}_2^{\bullet-}$  generated in bulk solution is accepted to be produced by the following equations:



Adsorption experiment indicated that AO7 adsorbed strongly on  $\text{CeO}_2$  surface. Two oxygen atoms from sulfonate group of AO7 are linked with two Ce surface and forms an inner-sphere complex. AO7 molecules, being strong electron donors due to oxygen atoms of  $\text{SO}_3^{2-}$ , are able to direct interact with valence band holes. The valence band hole primarily

captured by the adsorbed AO7 molecules rather than by the adsorbed water or hydroxyl groups as the oxidative potential of AO7 (0.76 V versus NHE),<sup>56</sup> is much lower than that of photogenerated hole. The pathway for photodegradation under solar light as presented in our study is different from the dye self-sensitization pathway implicated during visible light irradiation ( $\lambda > 420$  nm) using pure CeO<sub>2</sub> as photocatalyst.<sup>39</sup> Other study reported that the active h<sup>+</sup> play a major role in AO7 degradation using P-25 under UV irradiation.

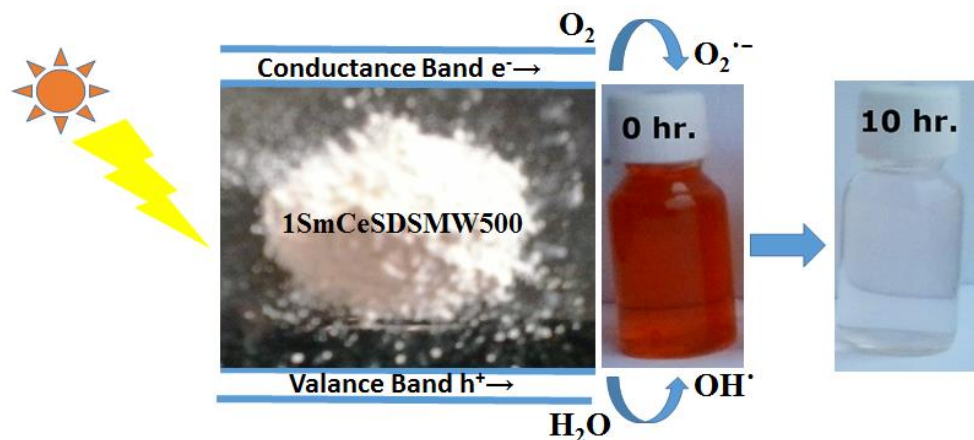


**Fig. 6.11** Proposed pathways for photocatalytic AO7 degradation.

Kondarides and coworkers have reported that it takes about 50 h to totally decolorize AO7 solution with concentration up to 100 mg/L by TiO<sub>2</sub> under visible light irradiation.<sup>57</sup> Cu<sub>2</sub>O/CeO<sub>2</sub> composites photocatalyst (1g/L) with surface area 53 m<sup>2</sup>/g degrades about 96.2% of AO7 (35 mg/L) after 4 h visible light irradiation.<sup>39</sup> When the 0.05 g of Co doped CeO<sub>2</sub> nanocubes (catalyst) was added with 15 mL of AO7 (0.3 mmol) and exposed under UV illumination ( $\lambda_{\text{max}}=365$  nm) for 8 h, specific change in the color of the dye was observed due to its decomposition.<sup>58</sup> In particular, it is interesting to evoke some reasons why the mesoporous 1SmCeSDSMW500 prepared through microwave exhibited the enhanced solar light photocatalytic activities. The first explanation is that the shifts of the absorption edge of CeO<sub>2</sub> to the visible-light range and narrow the band gap and have strong absorption in the UV region as well as definite absorptions in the visible region. This decrease in band gap may help to facilitate the propagation of electron to conduction band initiating photolysis reaction.<sup>59</sup> Ceria mesoporous structures with high specific surface area, large pore size and thermal stability have several advantages in high adsorption, which is a key factor for the

degradation rate and photocatalysis. The mesoporous structure space effectively enhances the spatial dispersion, which results in higher surface area and also mass transportation of molecules both into and out of the pore structure.<sup>60</sup> It has been suggested that the degradation of organic dye in ceria/H<sub>2</sub>O<sub>2</sub> system relies significantly on its adsorption on the surface of CeO<sub>2</sub>.<sup>38</sup> We found that the adsorption effects of AO7 in the dark after 11 h by pure CeO<sub>2</sub> and 1 mol% Sm<sup>3+</sup> doped CeO<sub>2</sub> are 52.7 and 65%, respectively. The very high adsorption of AO7 by CeO<sub>2</sub> is attributed to high surface area and pore volume of the mesoporous catalysts, high oxygen vacancies on the surface originating from facile Ce<sup>3+</sup>/Ce<sup>4+</sup> redox cycle,<sup>38</sup> and to the ability of cerium ion to form complexes with the electron-rich sulfonate group (SO<sub>3</sub><sup>-</sup>) of AO7.<sup>36</sup> Xiao *et al.* also demonstrated that Sm<sup>3+</sup>-TiO<sub>2</sub> had a higher methylene blue adsorption capacity than undoped TiO<sub>2</sub>.<sup>61</sup> Sm<sup>3+</sup> doping further improved the concentration of Ce<sup>3+</sup> or in other words concentrations of oxygen vacancy in CeO<sub>2</sub> samples as well as enhanced the adsorption capacity of AO7, which resulted in better catalytic performances. Tang *et al.* reported that the oxygen vacancy can not only act as impurity levels in the band structure of ZnO but can also work as electron traps to accept the photogenerated electrons.<sup>62</sup> Oxygen vacancy on the CeO<sub>2</sub> catalyst surface can easily trap the photo-generated electrons and efficiently benefit for the separation of excited electron-hole pairs and thus can play a more functional and effective role in photocatalytic application.

In our study, the optimum Sm<sup>3+</sup> concentration in the CeO<sub>2</sub> was 1.0 mol%, at which the recombination of photo-induced electrons and holes could be effectively inhibited, and thereby the highest photocatalytic activity was achieved. At natural pH conditions, the photodegradation of AO7 under 1 h of solar light irradiation by the CeO<sub>2</sub> photocatalysts (calcined at 500 °C) with 0, 0.5, 1.0, 2.0 and 5.0 mol% Sm<sup>3+</sup> doping were 60, 66, 82, 78, and 72%, respectively. It is well documented that a higher adsorption capacity with a higher Sm<sup>3+</sup> content does not lead to a higher photocatalytic activity in TiO<sub>2</sub>.<sup>61</sup> Cai *et al.* also showed that doping Fe<sup>3+</sup> improved the defect concentration and thus favored the catalytic activity of CeO<sub>2</sub> at low levels, but retarded the degradation of AO7 at high levels, with an optimal Fe/Ce ratio of 1/100.<sup>41</sup> Probably at higher Sm<sup>3+</sup> concentrations the Sm may be present at the surface of particles and form clusters, which are detrimental for photocatalytic activity carried out at the surface.<sup>63</sup>

#### 6.2.4. Conclusions

In summary,  $\text{Sm}^{3+}$  doped  $\text{CeO}_2$  mesoporous photocatalysts with high crystallinity and high surface area have been successfully synthesized by a facile and low-cost surfactant-assisted microwave heating method using  $(\text{NH}_4)_2\text{Ce}(\text{NO}_3)_6$  and  $\text{Sm}_2\text{O}_3$  and SDS. Structural, spectroscopic, and electron microscopy techniques were used to characterize the photocatalysts. The resultant  $\text{Sm}^{3+}$  doped  $\text{CeO}_2$  exhibits excellent photocatalytic activities for degradation of Acid Orange 7 (AO7) under natural sunlight irradiation in absence of any oxidising agents and over a broad range of pH values from 2.9 to 9.1. The results indicated that the degree of AO7 degradation was influenced by calcination temperature and the amount of photocatalyst. The main features those are responsible for making 1SmCeSDSMW500 a promising material for use as an active solar light sensitive photocatalyst are its specific surface area, crystallinity, enhanced dye adsorption capacity, importantly, high Uv-vis absorption capability and reduced band gap of the material due to the presence of higher concentration of  $\text{Ce}^{3+}$  in  $\text{CeO}_2$ . It was found that besides holes, which are the main active species in the photocatalytic destruction of AO7,  $\text{O}_2^{\bullet -}$  played secondary roles in the photocatalytic degradation process. This new material is a promising candidate as a robust solar-light active photocatalyst over a broad pH range of the dye polluted water without addition of any oxidizing agents.

### 6.3. Autocatalytic activity

#### 6.3.1. Introduction

The reversibly switching capability from  $\text{Ce}^{3+}$  to  $\text{Ce}^{4+}$  of mixed valence state  $\text{CeO}_2$  nanoparticles has also driven interest in biomedical applications as antioxidants.<sup>64-66</sup> Some reports suggest that a large amount of  $\text{Ce}^{3+}$  ions on the particle surface could enhance their radical scavenging activity.<sup>67-69</sup> The autoregeneration of the active  $\text{Ce}^{3+}$  oxidation state for radical scavenging is an unique property of nanoceria, which separates it from other antioxidant nanoparticles such as hydroxylated C-60 and SWCNTs.<sup>70</sup> Zhang *et al.* investigated antioxidant activity for nano- $\text{CeO}_2$  with different morphologies synthesized by a hydrothermal process.<sup>71</sup> Prompted by the mesoporous structure, high surface area, pore volume and mixed valence ( $\text{Ce}^{3+}$  and  $\text{Ce}^{4+}$ ) state, we anticipated that these mesoporous  $\text{Sm}^{3+}$  doped  $\text{CeO}_2$  could be promising candidates for antioxidant application if they undergo autocatalytic property. Here, for the first time, we monitored the anti-oxidation performances

with H<sub>2</sub>O<sub>2</sub> of mesoporous pure CeO<sub>2</sub> and defect engineered 1SmCeSDS500. To evaluate the autocatalytic activity of the prepared mesoporous 1SmCeSDS500, we have carried out UV-visible transmission spectroscopic studies both in the absence and in the presence of H<sub>2</sub>O<sub>2</sub> (an oxidant).

### 6.3.2. Evaluation of autocatalytic behaviour

Autocatalytic activity was assessed by treating 20 mg mesoporous 1SmCeSDS500 samples dispersed in 10 mL of deionized water with 100 µl H<sub>2</sub>O<sub>2</sub> solution. The transmission spectra were recorded for these samples in the absence and presence of H<sub>2</sub>O<sub>2</sub> at different time intervals up to 10 days.

### 6.3.3. Toxicity analysis

Both mesoporous 100CeSDS500 and 1SmCeSDS500 were assessed to determine the potential of toxicity. Cell viability utilizing MTT (3-(4,5-dimethylthiazol-2-yl)-2,5-diphenyltetrazolium bromide) (Sigma-Aldrich) assays were evaluated for up to 5 days using MG-63 cells cultured in DMEM (Dulbecco's Modified Eagle's Medium), 10% FBS (Fetal Bovine Serum) and 1% antibiotic solution. The cells were seeded in 96-well plates at a concentration of 10000 cells per well and were allowed to adhere at 37°C in 5% CO<sub>2</sub> for 24 h. The next day the cells were treated with 100 µg mL<sup>-1</sup> mesoporous ceria samples. As a control group, cells were cultured in the same media (without ceria particles). Following 24 h of incubation with mesoporous ceria, the original media was removed from each well and 100 µL of fresh MTT reagent (1: 10 ratio with cell culture media) was added to each well and incubated for 3 h. At the end of incubation purple color formazan crystals were formed, and those were dissolved in DMSO and the absorbance of each well was measured (using a Systronic double beam spectrophotometer 2203) at 590 nm. The experiment was done in triplicate. A similar procedure was repeated after 3 and 5 days of treatment with mesoporous ceria. The viability graphs were plotted by normalizing the data with respect to the control group of the experiment of each day.

### 6.3.4. Results and discussion

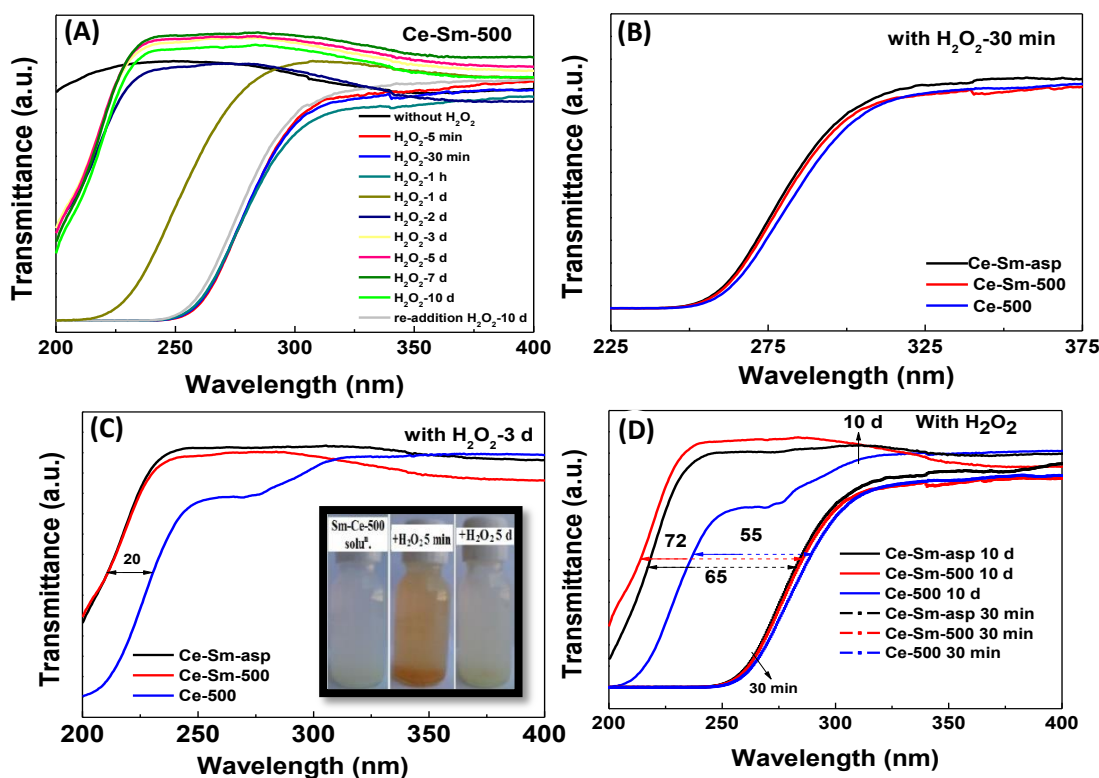
#### 6.3.4.1. Autocatalytic properties

Fig. 6.12a presents the UV-Vis transmittance spectra of the mesoporous 1SmCeSDS500 powder dispersing in deionized water both in absence and in presence of hydrogen peroxide

H<sub>2</sub>O<sub>2</sub> as an oxidizer. After the addition of H<sub>2</sub>O<sub>2</sub>, a large red shift ( $\Delta\lambda \sim 73$  nm) in the resulting UV/Vis transmittance spectrum was observed as compared with the untreated sample may be due to the change in the oxidation state from Ce<sup>3+</sup> to Ce<sup>4+</sup> induced by the hydroxyl free (OH<sup>•</sup>) radical.<sup>72</sup> The magnitude of the red-shifted wavelength of the UV-vis band ( $\Delta\lambda$ ) was measured between the untreated (235 nm) and the redshifted band position at transmittance value  $\sim 60$ . Corresponding color change from light yellow to orange can be observed visually as shown in the inset of Fig. 6.12c, upon addition of H<sub>2</sub>O<sub>2</sub>. During the next 10 consecutive days, at the given time intervals, transmittance spectra of the H<sub>2</sub>O<sub>2</sub> treated solution were recorded and a gradual blue shift in the spectra was observed over time. The solution color also changed and then turned back to its original light yellow color. The blue shift reflects the auto-regeneration of the cerium oxide nanoparticles (Ce<sup>4+</sup>  $\rightarrow$  Ce<sup>3+</sup>) as the H<sub>2</sub>O<sub>2</sub> decomposed from the suspension.<sup>72</sup> Again end of the 10 days, re-addition of H<sub>2</sub>O<sub>2</sub> to the solution leads to the same red shift in the corresponding transmission spectrum. This reversible behavior suggests their possible application as an antioxidant.

Earlier, it has been reported that the surface Ce<sup>3+</sup> in nano CeO<sub>2</sub> can be stoichiometrically oxidized to Ce<sup>4+</sup> and the extent of red shift in transmission spectra is closely related to antioxidant performance.<sup>67</sup> Interestingly, we observed that after 30 min of addition of H<sub>2</sub>O<sub>2</sub> there was no significant change in the red shift values for the doped and undoped CeO<sub>2</sub> samples (see Fig. 6.12b). However, the auto regeneration of Ce<sup>3+</sup> from Ce<sup>4+</sup> after 3 days (as can be seen from Fig. 6.12c) was much faster in the case of Sm<sup>3+</sup> doped CeO<sub>2</sub> samples. The difference in the blue shift values observed after 3 days of H<sub>2</sub>O<sub>2</sub> addition in the pure and doped sample is  $\sim 20$  nm as marked in Fig. 6.12c. The total shift difference values between the blue shift after 10 days and the red shift after 30 min is 55, 65 and 72 nm, for 100CeSDS500, 1SmCeSDSasp, and 1SmCeSDS500, respectively. So, the autocatalytic ability after 10 days of these materials is in the following order: 100CeSDS500 < 1SmCeSDSasp < 1SmCeSDS500. Thus, it can be stated that the regeneration of Ce<sup>3+</sup> from the Ce<sup>4+</sup> is much more difficult than the counter process in pure CeO<sub>2</sub> sample. In contrast, Sm<sup>3+</sup> doped CeO<sub>2</sub> is able to regenerate Ce<sup>3+</sup> easily, returning to its original values for Ce<sup>3+</sup> and Ce<sup>4+</sup> in the initial sample. A faster regeneration of Ce<sup>3+</sup> can reduce the time lag for CeO<sub>2</sub> to be active repeatedly for radical scavenging.<sup>73</sup> The more Ce<sup>3+</sup> is converted back from Ce<sup>4+</sup>, the higher the extent of OH<sup>•</sup> radicals that can be scavenged in the following cycles. Therefore, the

ability of regeneration of  $\text{Ce}^{3+}$  from the  $\text{Ce}^{4+}$  of nano- $\text{CeO}_2$ , is the rate-determining step in the auto-catalytic cycle.



**Fig. 6.12.** Transmittance spectra showing autocatalytic behavior of (A)  $\text{Sm}^{3+}$  doped  $\text{CeO}_2$  calcined at  $500^\circ\text{C}$ . Photographs [in the inset of (C)] of the aqueous solution of the sample in absence and presence of  $\text{H}_2\text{O}_2$  showing characteristic reversible color changes. Transmittance spectra showing blue shift for the  $\text{CeO}_2$  (blue line) and  $\text{Sm}^{3+}$  doped  $\text{CeO}_2$  samples (black: as-prepared; and red: calcined at  $500^\circ\text{C}$ ) after addition of  $\text{H}_2\text{O}_2$  (B) 30 min, (C) 3 days, and (D) 30 min and 10 days (showing shift difference).

#### 6.3.4.2. Effect of type of dopant

The effect of the dopant on the auto-catalytic properties were also examined. All the samples treated with hydrogen peroxide were then kept in the dark for 3 days. After 3 days of hydrogen peroxide treatment UV–visible transmittance spectra of these samples were taken. It was found that  $\text{Sm}^{3+}$  doped  $\text{CeO}_2$  nanopowder exhibits maximum shift in the spectrum shown in Fig. 6.13(A). This result indicates that the  $\text{Sm}^{3+}$  doped  $\text{CeO}_2$  nanopowder had a significantly higher peroxide detoxification ability than pure  $\text{CeO}_2$  and  $\text{Eu}^{3+}$  doped  $\text{CeO}_2$ .

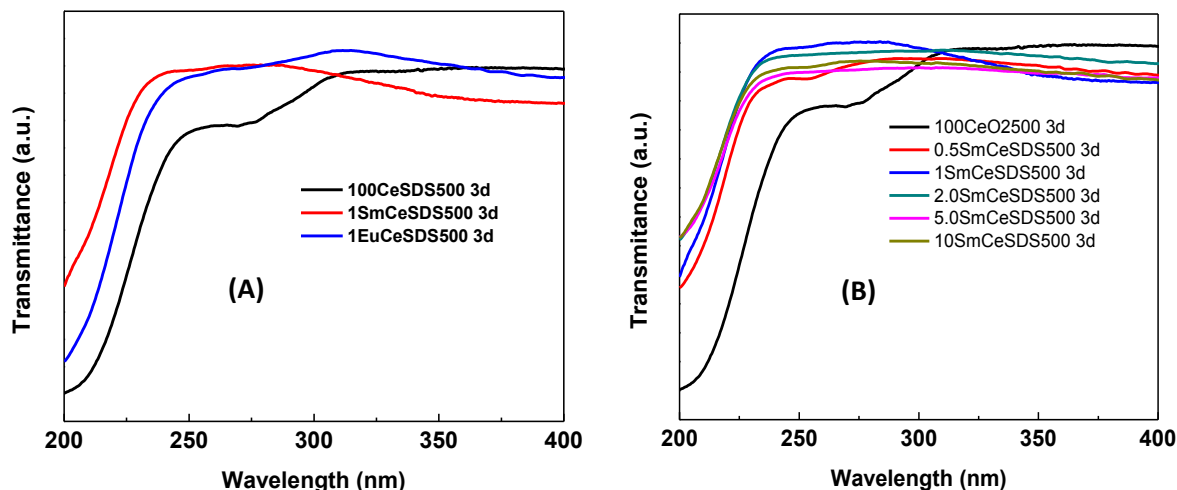


**Fig. 6.13.** UV-visible transmittance spectra of (A) pure,  $\text{Sm}^{3+}$  and  $\text{Eu}^{3+}$  doped  $\text{CeO}_2$  calcined at  $500^\circ\text{C}$  for 2 h, after 3 days of  $\text{H}_2\text{O}_2$  treatment, and (B) 0 to 10 mol%  $\text{Sm}^{3+}$  doped  $\text{CeO}_2$  calcined at  $500^\circ\text{C}$  for 2 h.

#### 6.3.4.3. Effect of dopant concentration

To demonstrate the effect of dopant concentration on autocatalytic property we have carried out the UV-visible transmission spectroscopic studies on a series of 0.5 to 10 mol%  $\text{Sm}^{3+}$  doped  $\text{CeO}_2$  nanopowders calcined at  $500^\circ\text{C}$ . All the samples after treated with hydrogen peroxide were preserved in the dark for 3 days. After 3 days corresponding transmission spectra of all the experimental solution were taken. The resulting spectrum of the doped sample showed a large blue shift as compared with the spectrum of the pure  $\text{CeO}_2$ , as can be seen from Fig 6.13(B). It is also notable that the no significant blue shift in the spectrum was found above 1 mol%  $\text{Sm}^{3+}$  doping. The fast autogenerative catalytic behavior of the 1 mol%  $\text{Sm}^{3+}$  doped  $\text{CeO}_2$  suggests that these materials could be efficiently used as an antioxidant.

It is interesting to evoke some reasons why the mesoporous  $\text{Sm}^{3+}$  doped  $\text{CeO}_2$  exhibited the enhanced autocatalytic activities. As the autocatalytic experiment was performed under the same conditions and size of the pure and doped  $\text{CeO}_2$  nanoparticles were also almost equal, hence the concentration and size of the particles are not the key factor here. Xue *et al.* observed a size dependent  $\text{OH}\cdot$  radicals scavenging activity as the concentration of  $\text{Ce}^{3+}$  is determined by the size of the nanocrystal.<sup>74</sup> XPS data also revealed that the  $\text{Sm}^{3+}$  doping improved slightly the percentage of  $\text{Ce}^{3+}$  on the surface. So, the  $\text{Ce}^{3+}$  concentration on



the surface is also not the dominating factor here. The factors influencing the regeneration of  $\text{Ce}^{3+}$  with excess  $\text{H}_2\text{O}_2$  would be the key step in the catalytic cycle.<sup>75</sup> Higher surface area and pore volume of mesoporous  $\text{Sm}^{3+}$  doped  $\text{CeO}_2$  increased the adsorption of extra peroxide species available in the solution. Higher oxygen vacancy in doped  $\text{CeO}_2$  increased the coordination capability of adsorbed peroxide species and thus improves the reaction possibility of the  $\text{H}_2\text{O}_2$  decomposition.<sup>75</sup> The pH of the mesoporous  $\text{Sm}^{3+}$  doped  $\text{CeO}_2$  solution changed from 6.6 to 3.6 after adding  $\text{H}_2\text{O}_2$  due to the generation of  $\text{H}^+$  according to the equation given by Wang *et al.*<sup>75</sup>:  $\text{H}_2\text{O}_2 (\text{ad}) + 2\text{Ce}^{4+} = \text{O}_2 (\text{g}) + 2\text{H}^+ + 2\text{Ce}^{3+} + \text{V}_\text{O}$ ; where  $\text{V}_\text{O}$  denotes oxygen vacancy. The increased surface hydroxyl group on mesoporous  $\text{Sm}^{3+}$  doped  $\text{CeO}_2$  (also evident from XPS and TPD results as discussed in chapter-IV) also enhances the catalytic ability of decomposing  $\text{H}_2\text{O}_2$  as compared to that of pure  $\text{CeO}_2$ . XRD results indicated that the  $\text{Sm}^{3+}$  doping leads to an expansion of the  $\text{CeO}_2$  lattice and larger free volume in the sample facilitated the required expansion to form  $\text{Ce}^{3+}$  from  $\text{Ce}^{4+}$  (auto-regeneration). Oxygen vacancy clustering as observed from the HRTEM also contributed to the enhanced reducibility. It is evident from the  $\text{H}_2$ -TPR results that a  $\text{Sm}^{3+}$  doping in  $\text{CeO}_2$  increased the concentration of active oxygen vacancies, which leads to the formation of active oxygen species reducible by  $\text{H}_2$  at lower temperature and thus promoting reducibility i.e. the process of  $\text{Ce}^{4+} \rightarrow \text{Ce}^{3+}$  (regeneration of  $\text{Ce}^{3+}$ ). Therefore, we present a robust method to accelerate the reduction of  $\text{Ce}^{4+}$  in the catalytic cycle by modifying the defect state and reducibility of  $\text{CeO}_2$  by doping with  $\text{Sm}^{3+}$ .

Wang *et al.* observed that the ability to decompose  $\text{H}_2\text{O}_2$  is highest when 20%  $\text{Gd}^{3+}$  was doped as compared to that of 10%  $\text{Gd}^{3+}$  doped  $\text{CeO}_2$  or pure  $\text{CeO}_2$ .<sup>75</sup> The anti-oxidation performance of  $\text{CeO}_2$  nanoparticles after  $\text{Gd}^{3+}$  doping was improved by increasing the oxygen vacancies and through the modulation of reducibility. On the contrary, Chaudhary *et al.* observed poor auto-regeneration in the case of a 2 at%  $\text{Gd}$  doped  $\text{CeO}_2$  sample as compared to 0.5 and 1.0 at%  $\text{Gd}$  doped  $\text{CeO}_2$  samples as the higher doping level (i.e. 2%) is probably stabilizing the fluorite structure of  $\text{CeO}_2$  by replacing  $\text{Ce}^{4+}$  with  $\text{Gd}^{3+}$ .<sup>69</sup> So, there are some contradictory results in the previous studies on the effect of rare earth dopant concentration on the anti-oxidation process of  $\text{CeO}_2$  nanoparticles. Seal and coworkers have emphasized that the synthesis routes can have a dramatic influence on the physico-chemical properties of  $\text{CeO}_2$  nanomaterials, and hence their behaviors differ at the biological interfaces.<sup>76</sup> It should

be noted that the effect of  $\text{Sm}^{3+}$  concentration on different properties and their correlation with antioxidant activity would be an interesting and important topic of research, which will require further investigation and will be addressed in future work.

#### 6.3.4.4. Cytotoxicity test

Earlier reports have shown that  $\text{CeO}_2$  and  $\text{Gd}^{3+}$  doped  $\text{CeO}_2$  are nontoxic and biocompatible.<sup>73,75</sup> Here, the cytotoxicity of the prepared mesoporous pure and  $\text{Sm}^{3+}$  doped  $\text{CeO}_2$  was evaluated with MG-63 cells. The viability of cells using the MTT assay is shown in Fig. 6.14. There was no obvious decrease in cell viability upon addition of the mesoporous ceria in a concentration as high as  $100 \mu\text{g mL}^{-1}$  over an incubation period of 120 h. Under the same treatment, the cell viability of the pure  $\text{CeO}_2$  approaches 100% compared with the control group, and the cell viability of the  $\text{Sm}^{3+}$  doped  $\text{CeO}_2$  is slightly higher than that of the pure  $\text{CeO}_2$ . Thus the results confirm that the prepared mesoporous  $\text{Sm}^{3+}$  doped  $\text{CeO}_2$  is also nontoxic and biocompatible, and can be explored for antioxidant application.

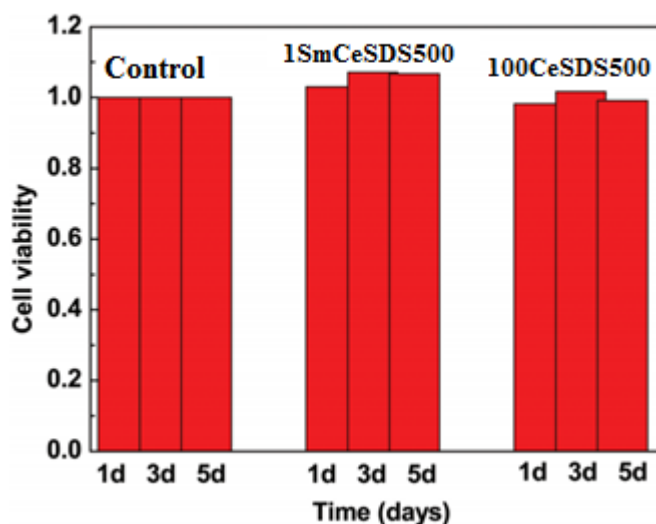


**Fig. 6.14.** Cell viability by MTT assay of mesoporous  $\text{CeO}_2$  and  $\text{Sm}^{3+}$  doped  $\text{CeO}_2$  calcined at  $500^\circ\text{C}$  after 1, 3 and 5 days incubation in MG-63 cell lines.

#### 6.3.5. Conclusion

In summary, for the first time autocatalytic activity of mesoporous high surface area 1SmCeSDS500 was evaluated.  $\text{Sm}^{3+}$  doping in  $\text{CeO}_2$  show improved structural features such as increased lattice volume, higher surface hydroxyl groups, specific surface area pore

volume, and  $\text{Ce}^{3+}$  and oxygen vacancies concentrations, and enhanced the reduction behaviour of  $\text{CeO}_2$  which has been already discussed in Chapter (IV), leading to enhanced autocatalytic activity.  $\text{Ce}^{4+}/\text{Ce}^{3+}$  recycle is easier for 1SmCeSDS500 sample than that for the 100CeSDS500 or 1EuCeSDS500 sample, which results in an improved autocatalytic activity. These results suggest that high surface area, mesoporous and surface defects engineered  $\text{Sm}^{3+}$  doped  $\text{CeO}_2$  are very promising materials for multifunctional applications including waste water treatment and antioxidant application.

## References

1. M. C. Golonka, *Polyhedron*, 1995, 15, 3667.
2. C. Raji and T.S. Anirudhan, *Water Res.*, 1998, 32, 3772.
3. V. Sarin and K. K. Pant, *Bioresour. Technol.*, 2006, 97, 15.
4. Y. Zeng, H. Woo, G. Lee, and J. Park, *Microporous Mesoporous Mater.*, 2010, 130, 83.
5. B. C. Schneider, Constant, L. Stephanie, Patierno, R. Steven, R. A. Jurjus, and S. M. Ceryak, *Toxicol. Appl. Pharm.*, 2012, 259, 38.
6. B. D. Kerger, W. J. Butler, D. J. Paustenbach, J. Zhang, and S. Li, *J. Toxicol. Environ. Health A.*, 2009, 72, 329.
7. A. K. Kopec, S. Kim, A. L. Forgacs, T. R. Zacharewski, D. M. Proctor, M. A. Harris, L. C. Haws, and C. M. Thompson, *Toxicol. Appl. Pharmacol.*, 2012, 259, 13.
8. H. Dai, J. Liu, L. H. Malkas, J. Catalano, S. Alagharu, and R. J. Hickey, *Toxicol. Appl. Pharmacol.*, 2009, 236, 154.
9. D. Mohan, K.P. Singh and V. K. Singh, *Ind. Eng. Chem. Res.*, 2005, 44, 1027.
10. WHO, 2nd ed., *Guidelines for Drinking Water Quality*, vol. 1, World Health Organization, Geneva, 1993.
11. D. Mohan and C. U. Pittman Jr., *J. Hazard. Mater. B.*, 2006, 137, 762.
12. S. M. Nomanbhay and K. Palanisamy, *Elect. J. Biotechnol.*, 2005, 8, 43.
13. S. Babel and T.A. Kurniawan, *J. Hazard. Mater. B.*, 2003, 97, 219.
14. A. M. Raichur and M.J. Basu, *Sep. Purif. Technol.*, 2001, 24, 121.
15. S. Recillas, J. Colon, E. Casals, E. González, V. Puentes, A. Sánchez and X. Font, *J. Hazard. Mater.*, 2010, 184, 425.
16. H. Y. Xiao, Z. H. Ai and L. Z. Zhang, *J. Phys. Chem. C*, 2009, 113, 16625.
17. L. S. Zhong, J. S. Hu, A. M. Cao, Q. Liu, W. G. Song and L. J. Wan, *Chem. Mater.*, 2007, 19, 1648.
18. C. Y. Cao, Z. M. Cui, C. Q. Chen, W. G. Song and W. Cai, *J. Phys. Chem. C*, 2010, 114, 9865.
19. M. Kobayashi and M. F. Stephanopoulos, *Ind. Eng. Chem. Res.*, 2002, 41, 3115.
20. S. Watanabe, S. Velu, X. Ma and C. Song, *Prepr. Pap. Am. Chem. Soc., Div. Fuel Chem.* 2003, 48, 695.
21. Z. Li and M. Stephanopoulos, *Ind. Eng. Chem. Res.*, 1997, 36, 187.
22. A. D. Mayernick, R. Li, K. M. Dooley and M. J. Janik, *J. Phys. Chem. C*, 2011, 115, 24178.

23. D. H. Lim, H. S. Kim, S. P. Yoon, J. Han, C.W. Yoon, S. H. Choi, S. W. Nam and H. C. Ham, *Phys. Chem. Chem. Phys.*, 2014, 16, 10727.
24. F. S. Freyria, B. Bonelli, R. Sethi, M. Armandi, E. Belluso and E. Garrone, *J. Phys. Chem. C*, 2011, 115, 24143.
25. A. Ozcan, M. A. Oturan, N. Oturan and Y. S<sup>ˆ</sup>ahin, *J. Hazard. Mater.*, 2009, 163, 1213.
26. V. K. Gupta, A. Mittal, V. Gajbe and J. Mittal, *Ind. Eng. Chem. Res.*, 2006, 45, 1446.
27. G. Neri, A. Pistone, C. Milone and S. Galvagno, *Appl. Catal., B*, 2002, 38, 321.
28. B. Qiu, M. Xing and J. Zhang, *J. Am. Chem. Soc.*, 2014, 136, 5852.
29. Y.-G. Peng, J.-L. Ji, Y.-L. Zhang, H.-X. Wan and D.-J. Chen, *Environ. Prog. Sustainable Energy*, 2013, 33, 123.
30. J. B. Joo, I. Lee, M. Dahl, G. D. Moon, F. Zaera and Y. Yin, *Adv. Funct. Mater.*, 2013, 23, 4246.
31. P. V. Nidheesh, R. Gandhimathi and S. T. Ramesh, *Environ. Sci. Pollut. Res.*, 2013, 20, 2099.
32. G. Moon, W. Kim, A. D. Bokare, N. Sung and W. Choi, *Energy Environ. Sci.*, 2014, 7, 4023.
33. S. Shibata, T. Suenobu and S. Fukuzumi, *Angew. Chem., Int. Ed.*, 2013, 52, 12327.
34. P. Ji, J. Zhang, F. Chen and M. Anpo, *J. Phys. Chem. C*, 2008, 112, 17809.
35. T. Feng, X. Wang and G. Feng, *Mater. Lett.*, 2013, 100, 36.
36. P. Ji, J. Zhang, F. Chen and M. Anpo, *Appl. Catal., B*, 2009, 85, 148.
37. D. Sun, M. Gu, R. Li, S. Yin, X. Song, B. Zhao, C. Li, J. Li, Z. Feng and T. Sato, *Appl. Surf. Sci.*, 2013, 280, 693.
38. F. Chen, X. Shen, Y. Wang and J. Zhang, *Appl. Catal., B*, 2012, 121–122, 223.
39. S. Hu, F. Zhou, L. Wang and J. Zhang, *Catal. Commun.*, 2011, 12, 794.
40. S. Yuan, Q. Zhang, B. Xu, Z. Jin, Y. Zhang, Y. Yang, M. Zhang and T. Ohno, *RSC Adv.*, 2014, 4, 62255.
41. W. Cai, F. Chen, X. Shen, L. Chen and J. Zhang, *Appl. Catal., B*, 2010, 101, 160.
42. A. L. Gal and S. Abanades, *J. Phys. Chem. C*, 2012, 116, 13516.
43. V. V. Ursaki, V. Lair, L. Zivkovi<sup>ˆ</sup>c, M. Cassir, A. Ringuede and O. Lupan, *Opt. Mater.*, 2012, 34, 1897.
44. N. Sutradhar, A. Sinhamahapatra, S. Pahari, M. Jayachandran, B. Subramanian, H. C. Bajaj and A. B. Panda, *J. Phys. Chem. C*, 2011, 115, 7628.
45. Y.-P. Fu, S.-B. Wen and C.-H. Lu, *J. Am. Ceram. Soc.*, 2008, 91, 127.
46. J. Chen, S. Patil, S. Seal and J. F. McGinnis, *Nat. Nanotechnol.*, 2006, 1, 142.
47. X. Liu, K. Zhou, L. Wang, B. Wang and Y. Li, *J. Am. Chem. Soc.*, 2009, 131, 3140.
48. Y. Q. Wang, H. M. Cheng, Y. Z. Hao, J. M. Ma, W. H. Li and S. M. Cai, *Thin Solid Films*, 1999, 349, 120.
49. P. Borker and A. V. Salker, *Mater. Chem. Phys.*, 2007, 103, 366.
50. C.-Y. Cao, Z.-M. Cui, C.-Q. Chen, W.-G. Song and W. Cai, *J. Phys. Chem. C*, 2010, 114, 9865.
51. M. Godinho, C. Ribeiro, E. Longo and E. R. Leite, *Cryst. Growth Des.*, 2008, 8, 384.
52. M. M. Natile, G. Boccaletti and A. Glisenti, *Chem. Mater.*, 2005, 17, 6272.
53. U. G. Akpan and B. H. Hameed, *J. Hazard. Mater.*, 2009, 170, 520.
54. J. Wang, J. Wang, Q. Sun, W. Wang, Z. Yan, W. Gong and L. Min, *J. Mater. Chem.*, 2009, 19, 6597.
55. C. Bauer, P. Jacques and A. Kalt, *Chem. Phys. Lett.*, 1999, 307, 397.
56. K. Vinodgopal and P. V. Kamat, *Environ. Sci. Technol.*, 1995, 29, 841.

57. M. Styliidi, D. I. Kondarides and X. E. Verykios, *Appl. Catal., B*, 2004, 47, 189.
  58. N. S. Arul, D. Mangalaraj, P. C. Chen, N. Ponpandian and C. Viswanathan, *Mater. Lett.*, 2011, 65, 3320.
  59. J. Schneider, M. Matsuoka, M. Takeuchi, J. Zhang, Y. Horiuchi, M. Anpo and D. W. Bahnemann, *Chem. Rev.*, 2014, 114, 9919.
  60. H. Song, G. Zhou, C. Wang, X. Jiang, C. Wu and T. Li, *Res. Chem. Intermed.*, 2013, 39, 747.
  61. Q. Xiao, Z. Si, J. Zhang, C. Xiao and X. Tan, *J. Hazard. Mater.*, 2008, 150, 62.
  62. Y. Tang, H. Zhou, K. Zhang, J. Ding, T. Fan and D. Zhang, *Chem. Eng. J.*, 2015, 262, 260.
  63. D. de la Cruz, J. C. Arevalo, G. Torres, R. G. Bautista Margulis, C. Ornelas and A. Aguilar-Elguezabal, *Catal. Today*, 2011, 166, 152.
  64. I. Celardo, J. Z. Pedersen, E. Traversa and L. Ghibelli, *Nanoscale*, 2011, 3, 1411.
  65. M. Li, P. Shi, C. Xu, J. S. Ren and X. G. Qu, *Chem. Sci.*, 2013, 4, 2536.
  66. A. Karakoti, S. Singh, J. M. Dowding, S. Seal and W. T. Self, *Chem. Soc. Rev.*, 2010, 39, 4422.
  67. J. M. Perez, A. Asati, S. Nath and C. Kaittanis, *Small*, 2008, 5, 552.
  68. S. Kar, C. Patel and S. Santra, *J. Phys. Chem. C*, 2009, 113, 4862.
  69. Y. S. Chaudhary, S. Panigrahi, S. Nayak, B. Satpati, S. Bhattacharjee, and N. Kulkarni, *J. Mater. Chem.*, 2010, 20, 2381.
  70. F. Muhammad, A. Wang, W. Qi, S. Zhang and G. Zhu, *ACS Appl. Mater. Interfaces*, 2014, 6, 19424.
  71. Y. Zhang, K. Zhou, Y. Zhai, F. Qin, L. Pan and X. Yao, *RSC Adv.*, 2014, 4, 50325.
  72. M. Das, S. Patil, N. Bhargava, J. F. Kang, L. M. Riedel, S. Seal and J. J. Hickman, *Biomaterials*, 2007, 28, 1918.
  73. A. S. Karakoti, S. Singh, A. Kumar, M. Malinska, S. V. N. T. Kuchibhatla, K. Wozniak, W. T. Self and S. Seal, *J. Am. Chem. Soc.*, 2009, 131, 14144.
  74. Y. Xue, Q. Luan, D. Yang, X. Yao and K. Zhou, *J. Phys. Chem. C*, 2011, 115, 4433.
  75. Y.-J. Wang, H. Dong, G.-M. Lyu, H.-Y. Zhang, J. Ke, L.-Q. Kang, J.-L. Teng, L.-D. Sun, R. Si, J. Zhang, Y.-J. Liu, Y.-W. Zhang, Y.-H. Huang and C.-H. Yan, *Nanoscale*, 2015, 7, 13981.
  76. A. Kumar, S. Das, P. Munusamy, W. Self, D. R. Baer, D. C. Saylee and S. Seal, *Environ. Sci.: Nano*, 2014, 1, 516.
-

## Chapter 7

# Conclusion and Recommendation for Future Works

### Outline

*This is the last chapter of the thesis that discusses the summary of the outcomes of this research work, frameworks precise conclusions drawn from both the experimental and investigative efforts and proposes ideas and directions for future research scope as follows.*

### 7.1. Summary and Conclusion

The chapter wise summary and conclusion of the thesis is given below

#### Chapter 1:

This chapter comprised a general introduction and thorough literature survey on cerium oxide and its composite oxides including structural, properties, synthesis strategies and potential applications. A short introduction of nanomaterials also includes. Synthesis and application of mesoporous materials has also been discussed. Synthesis of mesoporous CeO<sub>2</sub> and CeO<sub>2</sub>-based mixed oxides via templating method particularly, both the soft-templating and hard templating methods are reviewed. Applications of mesoporous CeO<sub>2</sub> and CeO<sub>2</sub>-based oxides were also briefed with prominence to adsorption and removal of organic pollutants from aqueous solution. The main objectives of the present work are summarized towards the end of this chapter.

**Chapter 2:**

This chapter deals with the synthetic methodology adopted for the synthesis of pure as well as samarium ( $\text{Sm}^{3+}$ ) and europium ( $\text{Eu}^{3+}$ ) doped ceria ( $\text{CeO}_2$ ) and their characterization by various sophisticated instrumental techniques employed in the present study to understanding a complete structural, optical and spectroscopic properties such as thermogravimetric analysis/differential scanning calorimetry (TGA/DSC), X-ray diffraction (XRD), BET-BJH-surface area and pore size analysis, Fourier transform-infra red spectroscopy (FTIR), UV-visible diffuse reflectance spectroscopy (UV-vis DRS), X-ray photoelectron spectroscopy (XPS), field emission scanning electron microscopy (FESEM), high resolution transmission electron microscopy (HRTEM), temperature programmed reduction (TPR) and temperature programmed desorption (TPD).

**Chapter 3:**

This chapter focuses on the synthesis of pure ceria using surfactants as structure-directing agents and analysis of the samples using various characterization techniques. Effect of surfactant on the crystallization behavior, thermal properties, phase stability and morphology of  $\text{CeO}_2$  has been investigated. The mesoporous  $\text{CeO}_2$  samples showed broad and intense visible PL emission spectra when excited with light of wavelength 325 nm ascribed to surface defects or oxygen vacancies. Thermal analysis showed that as-synthesized  $\text{CeO}_2$  samples obtained in surfactant mediated route showed a lower % of weight loss than nano powder obtained in surfactant free route which revealed that the surfactant molecule promote the crystalline phase transformation in as synthesized nano powder even at low temperature at  $100^\circ\text{C}$ . The better formation of cubic phase nanocrystal ceria in surfactant mediated route was further supported by XRD results. The surfactant mediated synthesized  $\text{CeO}_2$  samples showed significantly better control over the reduction in the surface area that occurred during the heat treatments than the  $\text{CeO}_2$  sample synthesized by surfactant free method. XPS analysis confirms the existence of mixed valence states ( $\text{Ce}^{3+}$  and  $\text{Ce}^{4+}$ ) in the nanocrystals.

**Chapter 4:**

This chapter focuses on the characterization of formation of nanocrystalline and high surface area mesoporous samarium doped  $\text{CeO}_2$  samples with varying samarium content (0.5, 1, 2 and 5 mol %) prepared by co-precipitation of  $[(\text{NH}_4)_2\text{Ce}(\text{NO}_3)_6]$  and  $\text{Sm}_2\text{O}_3$  using

NH<sub>4</sub>OH as precipitating agent and SDS as template. Characterization of the synthesized samples using several characterization techniques was also discussed in detail. For the purpose of comparison, the representative sample 1 mol% Sm<sup>3+</sup> doped CeO<sub>2</sub> were also synthesized by dodecyl amine (DDA) and polyethylene glycol (PEG) assisted route. In addition the influence of microwave reflux method on the structural and optical properties of the representative sample 1 mol% Sm<sup>3+</sup> doped CeO<sub>2</sub> nanopowder were also evaluated. XRD studies along with HRTEM results confirmed the formation of mesoporous nanocrystalline CeO<sub>2</sub> at a lower temperature as low as 100°C. UV-vis absorption spectra of the samples showed strong absorption in the UV region and good transmittance in the visible region. The enhanced PL emission spectra of mesoporous Sm<sup>3+</sup> doped CeO<sub>2</sub> show narrow bands arising from the 4G<sub>5/2</sub>→6H<sub>5/2</sub> and 4G<sub>5/2</sub>→6H<sub>7/2</sub> transitions of Sm<sup>3+</sup> ion. The results of H<sub>2</sub>-TPR profiles show that the total H<sub>2</sub> consumption amount of Sm<sup>3+</sup> doped CeO<sub>2</sub> is much higher (69.16 mg/g) than that of pure CeO<sub>2</sub> (14.42 mg/g). It is clear from the NH<sub>3</sub>-TPD profiles that the Sm<sup>3+</sup> incorporation into CeO<sub>2</sub> lattice induces an increase in the weak acidic sites and created more number of strong acidic sites as compared to pure CeO<sub>2</sub>. High-resolution XPS spectrum confirms the doping of Sm<sup>3+</sup> in CeO<sub>2</sub>.

### Chapter 5:

This chapter focuses on the characterization of formation of nanocrystalline and high surface area mesoporous europium doped CeO<sub>2</sub> samples with 0.5, 1, 2, and 5 mol% europium content obtained in a SDS assisted homogeneous precipitation route followed by conventional reflux method. At the same time the influence of microwave reflux method on the structural properties were also evaluated. BET sorption isotherms displaying type IV adsorption isotherm indicative of mesoporous structure containing some micropores. A detailed analysis revealed that Eu<sup>3+</sup> doping in to CeO<sub>2</sub> has increased the lattice volume, surface area, mesopore volume and engineered the surface defects. The as-prepared sample of 1 mol% europium doped ceria possesses high surface area of 234 m<sup>2</sup>.g<sup>-1</sup> with average pore diameter of 4 nm. On thermal treatment at 500°C, a high-quality surfactant-free nanoparticles with surface area of 148 m<sup>2</sup>.g<sup>-1</sup> and larger average pore sizes of 5.5 nm, respectively, were formed. The high degree of crystallinity was further supported from the HRTEM images composed of well-defined lattice fringes. All the nanopowder exhibit sharp peaks in the emission spectra upon



excitation at 325 nm. The presence of  $\text{Eu}^{3+}$  ions in  $\text{Eu}^{3+}$  doped  $\text{CeO}_2$  nanocrystals was also recognized by xps analysis.

### Chapter 6:

This chapter discusses the application of synthesized nanopowder for environmental remediation such as adsorption of Cr(VI) from aqueous solution photocatalytic degradation of the organic dye (AO7). In order to study the adsorption behavior, high surface area, mesoporous samaria doped ceria (1SmCeSDSasp) nanopowders were used for the removal of Cr(VI) ions from aqueous solutions. The effects of contact time, initial sorbate concentration, pH and dose of adsorbent on Cr(VI) adsorption were studied to optimize the conditions for maximum adsorption. The kinetics of the adsorption has been studied. The sorption characteristics have been modeled using Langmuir and Freundlich isotherms. In addition samaria doped ceria (1SmCeSDSMW500) nanopowders were also successfully used as remarkably efficient new photocatalysts for degradation of a representative azo dye Acid Orange 7 (AO7) in aqueous medium under natural sunlight without addition of any external reagents like peroxides, acid or base. The effects of calcination temperature, pH of the medium, catalyst dosage and irradiation time on the decolorization of AO7 were investigated and discussed in this chapter.  $\text{Sm}^{3+}$  doping in  $\text{CeO}_2$  narrowed the band gap and significantly enhanced the photocatalytic degradation of the azo dye. The photocatalytic degradation of AO7 is also investigated by using certain radical scavengers and the results suggest that under solar-light irradiation predominantly positive holes and super oxide radicals ( $\text{O}_2^{\cdot -}$ ) act as the active species in the degradation process. Our results suggest these materials developed here are promising alternative solar light sensitive photocatalyst. The auto-catalytic anti-oxidant behavior of all the nano powder pure  $\text{CeO}_2$  (100CeSDS50) and  $\text{Sm}^{3+}$  doped  $\text{CeO}_2$  (1SmCeSDS500) and  $\text{Eu}^{3+}$  doped  $\text{CeO}_2$  (1EuCeSDS500) were evaluated by treating with  $\text{H}_2\text{O}_2$ .

### 7.2. New Achievements and Implications

The major achievements and implications achieved from this research work are as follows:

- Simple chemical routes have been developed using cheaper metal inorganic precursor to derive a high quality mesoporous pure  $\text{CeO}_2$  as well as  $\text{Sm}^{3+}$ , and  $\text{Eu}^{3+}$  doped  $\text{CeO}_2$ .

- XRD results showed that even as-prepared material have cubic fluorite structure of CeO<sub>2</sub> with no crystalline impurity phase. Thereby, confirming the ability of the present aqueous based synthetic approach to prepare mesoporous crystalline CeO<sub>2</sub> at 100°C.
- Both the mesoporous pure CeO<sub>2</sub> and rare earth (Sm<sup>3+</sup>, and Eu<sup>3+</sup>) doped CeO<sub>2</sub> possess high BET surface area and surfactant assisted route retard the decrease of surface area during calcination as well as mesoporosity of the samples well retained up to 650°C.
- Substantially high content of Ce<sup>3+</sup> was found in CeO<sub>2</sub>.
- These high surface area materials exhibited notable adsorption and effective removal of Cr(VI) from aqueous solutions at room temperature and without any adjustment of pH.
- 1SmCeSDSMW500 samples could effectively photodegrade AO7 dye under natural sunlight.
- Mesoporous 1SmCeSDS500 samples also exhibited excellent autocatalytical properties.
- Both pure and doped CeO<sub>2</sub> nanocrystals possesses strong absorption properties near the ultraviolet region revealed the possibility of these materials to be used as better UV blockers.
- Sm<sup>3+</sup> and Eu<sup>3+</sup> doped CeO<sub>2</sub> nanopowder showed enhanced photoluminescence.
- These novel high surface area CeO<sub>2</sub> materials developed in this work are important for a variety of applications in catalysts, membranes, optical materials, structural devices, sensors, adsorbents, environmental pollution control, and other applications.

### 7.3. Further scope of the work

The novel piece of the research work carried out in this investigation have tremendous scope of future research. Some of these points may be mentioned as follows.

- Applications of the prepared material for various catalysis reactions.
- Electrical, optical, and dielectric properties in pure, Sm<sup>3+</sup> or Eu<sup>3+</sup> doped CeO<sub>2</sub> samples.
- The prepared materials in the present study have good optical properties, which may be utilized in various optical applications in future. The photoluminescence property of doped CeO<sub>2</sub> with various morphologies can also be explored.
- The potential use of ceria based oxides in the field of SOFC can be analyzed.
- To find out the potential use of synthesized nanoparticle for biomedical applications.
- These mesoporous CeO<sub>2</sub> materials can find remarkable environmental applications in adsorption and removal of other toxic heavy metals e.g., As(III), As(V), Co(II), Cd(II), etc. along with degradation of toxic organic compounds like dyes.
- Extent the practical applications of the synthesized nanopowders in the bioremediation of various dye effluents.

**Bappaditya Mandal**

26<sup>th</sup> July, 1983

Nationality: Indian

Permanent address:

Vill-Bagdiha, PO-Bhuri

Dist-Burdwan, Pin-713378

West-Bengal

Present address:

Department of Chemistry

National Institute of Technology, Rourkela

Odisha-769008

Email: [bappa.chemistry@gmail.com](mailto:bappa.chemistry@gmail.com)

call@ +918908048510(Odisha)

call@ +917550813726(WB)



### Academic profile:

**Ph.D. (pursuing):** In Materials Chemistry, Department of Chemistry, National Institute of Technology, Rourkela, Odisha.

Thesis title: Surfactant Assisted Synthesis and Characterization of High Surface Area Mesoporous Nanocrystalline Pure, Eu<sup>3+</sup> and Sm<sup>3+</sup> doped Ceria for Novel Applications

**M.Sc (2007):** Sambalpur University, Odisha, Spl: Organic Chemistry 1<sup>st</sup> Class.

**B.Sc (2005):** The University of Burdwan, West Bengal, Spl: Chemistry (Honors), physics (pass), Math (pass), 2<sup>nd</sup> Class.

**12<sup>th</sup> (2001):** WBCHSE, West Bengal, Spl: Science, 1<sup>st</sup> Division.

**10<sup>th</sup> (1999):** WBBSE, West Bengal, 1<sup>st</sup> Division.

### Pre Doctoral Research Experience:

Project Assistant, CSIR-NML Jamshedpur, 26<sup>th</sup> November 2007 to 30<sup>th</sup> April 2010.

Project title: Recycling and Reuse of Electronic Waste.

### Expertise/Techniques:

#### Instruments Handle:

- ❖ Simultaneous thermal analysis (TG-DSC)
- ❖ X-ray diffraction (XRD)
- ❖ Fourier transform infrared spectroscopy (FTIR)
- ❖ UV-visible spectroscopy(UV)
- ❖ Photoluminescence spectroscopy (PL)
- ❖ BET surface area analyzer (BET)
- ❖ H<sub>2</sub> temperature programmed reduction (TPR)
- ❖ NH<sub>3</sub> temperature programmed deposition (TPD)

### Instruments Uses:

- ❖ X-Ray Photo Electron Spectroscopy (XPS)
- ❖ Field emission Scanning electron Microscope (FESEM)
- ❖ High Resolution Transmitted Electron Microscope (HRTEM)

### Publications:

- ❖ Bappaditya Mandal and Aparna Mondal, “Solar Light Sensitive Samaria Doped Ceria Photocatalysts: Microwave Synthesis, Characterization and Photodegradation of Acid Orange 7 at Atmospheric Condition and in Absence of Any Oxidizing Agents” **RSC Adv.**, **2015**, **5**, **43081–43091**.
- ❖ Bappaditya Mandal, Aparna Mondal, Sirshendu Sekhar Ray and Amar Kundu “Sm Doped Mesoporous CeO<sub>2</sub> Nanocrystals: Aqueous Solution-Based Surfactant Assisted Low Temperature Synthesis, Characterization and Their Improved Autocatalytic Activity” **Dalton Trans.**, **2016**, **45**, **1679–1692**.
- ❖ Bappaditya Mandal, Aparna Mondal “Effect of Surfactant on the Structural and Optical Properties of Nanocrystalline Ceria” Under Preparation.

### Conference:

- ❖ Bappaditya Mandal, Priyadarshini Nayak, and Aparna Mondal, “Surfactant Assisted Synthesis and Characterization of High Surface Area Samaria doped Ceria Nanoparticles for Novel Applications” National Seminars on Recent Trends in Condensed Matter Physics Including Laser Application (FNSCMPLA 2012), March 6-7, 2012. Department of Physics Centre of Advanced Study The University of Burdwan, Golapbag, Burdwan.
- ❖ Bappaditya Mandal, Dayanidhi Mohanta, and Aparna Mondal, “Synthesis of Visible Light Responsive Titania Photocatalyst” (ICMAT-2013), 7<sup>th</sup> International Conference On Materials for Advance Technologies 30<sup>th</sup> June To 5<sup>th</sup> July 2013, **Suntecity**, **Singapore**.
- ❖ Bappaditya Mandal, Bibhuti bhusan Nayak, and Aparna Mondal, “Effect of Surfactant on the Structural and Optical Properties of Nanocrystalline Ceria” International Conference on Functional Materials(ICFM-2014) February 5–7, 2014 Materials Science Centre Indian Institute of Technology, Kharagpur, 721 302.
- ❖ Bappaditya Mandal and Aparna Mondal, “Structural And Optical Properties Of Well-Crystallized Samaria Doped Ceria Nanophosphor Prepared By Surfactant Assisted Route” Advance in Chemistry and Their Biological and Industrial Relevance (ACBIR-2014), January 10-11, 2014, Department of chemistry NIT Rourkela.